

The author of the doctoral dissertation: **Damian Koszelow**  
Scientific discipline: **Materials engineering**

## **DOCTORAL DISSERTATION**

Title of doctoral dissertation: **High-temperature corrosion of porous ferritic stainless steel**

Title of doctoral dissertation (in Polish): **Wysokotemperaturowa korozja porowatych stali ferrytycznych**

Supervisor
<i>signature</i>
Ph.D., D.Sc., Eng. Sebastian Molin

Gdańsk, 2025



## STATEMENT

The author of the doctoral dissertation: **Damian Koszelow**

I, the undersigned, declare that I am aware that in accordance with the provisions of Art. 27 (1) and (2) of the Act of 4<sup>th</sup> February 1994 on Copyright and Related Rights (Journal of Laws of 2021, item 1062), the university may use my doctoral dissertation entitled:

**“High-temperature corrosion of porous ferritic stainless steel”**

for scientific or didactic purposes.<sup>1</sup>

Gdańsk, 27.01.2025

.....  
*signature of the PhD student*

Aware of criminal liability for violations of the Act of 4<sup>th</sup> February 1994 on Copyright and Related Rights and disciplinary actions set out in the Law on Higher Education and Science (Journal of Laws 2021, item 478), as well as civil liability, I declare, that the submitted doctoral dissertation is my own work.

I declare, that the submitted doctoral dissertation is my own work performed under and in cooperation with the supervision of Ph.D., D.Sc., Eng. Sebastian Molin

This submitted doctoral dissertation has never before been the basis of an official procedure associated with the awarding of a PhD degree.

All the information contained in the above thesis which is derived from written and electronic sources is documented in a list of relevant literature in accordance with Art. 34 of the Copyright and Related Rights Act.

I confirm that this doctoral dissertation is identical to the attached electronic version.

Gdańsk, 10.03.2025

.....  
*signature of the PhD student*

I, the undersigned, agree to include an electronic version of the above doctoral dissertation in the open, institutional, digital repository of Gdańsk University of Technology.

Gdańsk, 10.03.2025

.....  
*signature of the PhD student*

---

<sup>1</sup> Art 27. 1. Educational institutions and entities referred to in art. 7 sec. 1 points 1, 2 and 4–8 of the Act of 20 July 2018 – Law on Higher Education and Science, may use the disseminated works in the original and in translation for the purposes of illustrating the content provided for didactic purposes or in order to conduct research activities, and to reproduce for this purpose disseminated minor works or fragments of larger works.

2. If the works are made available to the public in such a way that everyone can have access to them at the place and time selected by them, as referred to in para. 1, is allowed only for a limited group of people learning, teaching or conducting research, identified by the entities listed in paragraph 1.



## **DESCRIPTION OF DOCTORAL DISSERTATION**

**The Author of the doctoral dissertation:** Damian Koszelow

**Title of doctoral dissertation:** High-temperature corrosion of porous ferritic stainless steel

**Title of doctoral dissertation in Polish:** Wysokotemperaturowa korozja porowatych stali ferrytycznych

**Language of doctoral dissertation:** English

**Supervisor:** Ph.D., D.Sc., Eng. Sebastian Molin

**Date of doctoral defense:**

**Keywords of doctoral dissertation in Polish:** porowata stal, wysokotemperaturowe utlenianie, okres trwałości, tlenkowe ogniwa paliwowe, stopy metali tworzących tlenek chromu

**Keywords of doctoral dissertation in English:** porous steel, high-temperature oxidation, lifespan prediction, solid oxide cells, chromia-forming alloys

### **Summary of doctoral dissertation in English:**

In recent years, scientists have taken an avid interest in porous alloys, which offer unique properties, including a large specific surface area, high formability and electrical conductivity. The purpose of this thesis was to determine the kinetics of the high-temperature oxidation process and the morphology changes resulting from that process for porous ferritic alloys. As part of the conducted research a lifespan prediction model for porous ferritic chromia-forming alloys was proposed and validated. Synchrotron X-Ray tomography was used to analyze three-dimensional images of the oxidized samples. Moreover, introducing a pre-oxidation process was proven to extend the possible lifespan of the porous alloys in high-temperatures. The results described herein provide a strong foundation for further research into the applications of porous alloys in the demanding operating conditions of solid oxide cells.

### **Summary of doctoral dissertation in Polish:**

W ostatnich latach szczególną uwagę naukowców przykuły porowate stopy metali, które oferują unikalne właściwości jak duża powierzchnia właściwa, łatwa formowalność oraz wysoka przewodność elektryczna.

Celem niniejszej rozprawy było określenie kinetyki utleniania wysokotemperaturowego oraz zmian morfologicznych zachodzących w jego wyniku dla porowatych stopów ferrytycznych. W ramach przeprowadzonych badań opracowano i zwalidowano model określający trwałość porowatych stopów ferrytycznych w wysokich temperaturach. Przeanalizowano również morfologię utlenianych próbek za

pomocą synchrotronowej tomografii rentgenowskiej pozwalającej na uzyskanie trójwymiarowego obrazu materiału. Co więcej, udowodniono, że możliwe jest przedłużenie trwałości porowatych stopów ferrytycznych w wysokich temperaturach przez zastosowanie procesu preoksydacji. Wyniki uzyskane w ramach niniejszej rozprawy stanowią obiecującą podstawę do dalszych badań nad zastosowaniem porowatych stopów metali w wymagających warunkach pracy tlenkowych ogniw paliwowych.

## Acknowledgements

Na wstępie chciałbym podziękować mojemu promotorowi, profesorowi Sebastianowi Molinowi, bez którego ta praca by nie powstała, za jego merytoryczny wkład oraz cenne wskazówki.

Ogromny wkład w napisanie tej pracy miała również doktor Małgorzata Makowska. Serdecznie dziękuję jej za możliwość przeprowadzenia badań synchrotronowych w Instytucie Paula Scherrera w Szwajcarii oraz za nieocenione wsparcie w pisaniu publikacji, które wchodzi w skład niniejszej rozprawy.

Podziękowania należą się także całej Katedrze Inżynierii Materiałów Funkcjonalnych Wydziału Elektroniki, Telekomunikacji i Informatyki, a w szczególności Bartłomiejowi Lemieszkowi za współpracę w laboratorium oraz pomoc w najtrudniejszych momentach pisania rozprawy.

Podczas doktoratu otrzymywałem wsparcie od przyjaciół i znajomych, za które również serdecznie dziękuję. Szczególnie chciałbym wyrazić wdzięczność Kacprowi Konopskiemu za długie dyskusje, które pozwoliły mi rozwiązać wiele naukowych problemów, Krzysztofowi Hope i Danielowi Jaworskiemu za wsparcie od początku mojej ścieżki naukowej oraz Joannie i Arturowi Borowskim za inspirowanie mnie przez cały okres studiów doktoranckich.

Za nieocenione wsparcie w pisaniu niniejszej rozprawy chciałbym podziękować mojej żonie Teresce, która motywowała mnie do działania aż do ostatniego akapitu i wspierała mnie w wychwytywaniu błędów językowych. Mam nadzieję, że w przyszłości nie będziesz ich szukać.

Na koniec pragnę wyrazić wdzięczność moim rodzicom za niezachwianą wiarę we mnie oraz wsparcie w podjęciu trudnej decyzji o rozpoczęciu studiów doktoranckich – bez Was nigdy nie podjąłbym się tego trudnego zadania.

## Table of contents

Abstract.....	10
Streszczenie .....	11
List of abbreviations and symbols.....	13
1. Introduction .....	15
1.1. Historical introduction .....	15
1.2. Mechanisms of the high-temperature corrosion.....	17
1.2.1. Thermodynamics of high-temperature oxidation .....	17
1.2.2. Laws of oxidation kinetics.....	19
1.2.3. Inward and outward corrosion .....	23
1.3. Microstructure influence on high-temperature oxidation .....	25
1.3.1. Ferritic and austenitic alloys .....	25
1.3.2. Grain and grain boundary diffusion fluxes .....	29
1.3.3. Porous and bulk alloys .....	32
1.4. Applications of porous alloys .....	33
1.5. Lifespan prediction model .....	37
2. Objectives and hypotheses .....	41
3. List of publications included in the dissertation .....	43
4. Experimental techniques and analysis methods .....	45
4.1. Porous alloy characterization.....	45
4.2. Oxidation tests .....	46
4.3. Post-mortem analysis .....	48
4.3.1. XRD measurements.....	48
4.3.2. SEM/EDX imaging .....	48
4.3.3. TEM imaging .....	49



4.3.4.	Synchrotron tomography analysis.....	49
4.3.5.	Chromium evaporation .....	50
4.4.	Glass-ceramics joints .....	51
4.4.1.	Glass and glass-ceramic preparation .....	52
4.4.2.	Oxidation tests and post-mortem analysis .....	53
5.	Overview of the relevant publications .....	55
5.1.	High temperature corrosion evaluation and lifetime prediction of porous Fe22Cr stainless steel in air in temperature range 700°C-900°C.....	55
5.2.	Morphology changes in Fe-Cr porous alloys upon high-temperature oxidation quantified by X-ray tomographic microscopy .....	68
5.3.	High-temperature corrosion of ~ 30 Pct porous FeCr stainless steels in air: long-term evaluation up to breakaway .....	88
5.4.	Pre-oxidation of porous ferritic Fe22Cr alloys for lifespan extension at high temperature.....	109
5.5.	Glass-ceramic joining of Fe22Cr porous alloy to Crofer22APU: interfacial issues and mechanical properties .....	128
6.	Conclusions .....	139
7.	References .....	141
8.	List of figures .....	150

## Abstract

Designing new materials is a complex process which requires taking into consideration many aspects, such as potential applications, mechanical and chemical properties, as well as the materials' durability in operating conditions. In recent years, scientists have taken an avid interest in porous alloys, which offer unique properties, including a large specific surface area, high formability and electrical conductivity. Such features suggest that these materials have a considerable potential to be applied, for example, in solid oxide cells – an important branch of the energy industry.

In this thesis, the research on porous ferritic chromia-forming alloys was presented. The alloys were considered as materials that can be potentially applied as parts in solid oxide cell interconnectors. The purpose of the research described herein was to determine the kinetics of the high-temperature oxidation process and the morphology changes resulting from that process for porous ferritic alloys.

As part of the conducted research:

- A lifespan prediction model that can be applied for porous ferritic chromia-forming alloys was proposed based on short-term (up to 100 h) oxidation tests.
- A validation of the model was performed based on long-term (up to 6000 h) exposure experiments.
- Synchrotron X-Ray tomography was used to analyze three-dimensional images of the oxidized samples
- Introducing a pre-oxidation process was proven to extend the possible lifespan of the porous alloys in high-temperatures.
- Glass-ceramic joints consisting of the dense Crofer 22 APU and pre-oxidized Fe22Cr porous alloy were fabricated and tested in terms of their application as components of solid oxide cells.

The results described herein provide a strong foundation for further research into the applications of porous alloys in the demanding operating conditions of solid oxide cells.

## Streszczenie

Projektowanie nowych materiałów jest złożonym procesem, który wymaga uwzględnienia wielu czynników, takich jak ich potencjalne zastosowania, własności mechaniczne, termiczne i chemiczne, a także trwałość w warunkach roboczych. W ostatnich latach szczególną uwagę naukowców przykuły porowate stopy metali, które oferują unikalne właściwości jak duża powierzchnia właściwa, łatwa formowalność oraz wysoka przewodność elektryczna, co sprawia, że są one obiecującymi materiałami do zastosowań w przemyśle energetycznym, w tym technologii ogniw paliwowych.

W niniejszej rozprawie zaprezentowane zostały badania nad porowatymi stalami ferrytycznymi, które w procesie utleniania formują tlenek chromu na swojej powierzchni. Stopy te są rozpatrywane jako materiały, które potencjalnie mogą być stosowane jako struktura wspierająca interkonektory w tlenkowych ogniwach paliwowych. Celem przeprowadzonych badań zawartych w niniejszej rozprawie było określenie kinetyki utleniania wysokotemperaturowego oraz zmian morfologicznych zachodzących w jego wyniku dla porowatych stopów ferrytycznych.

W ramach przeprowadzonych badań:

- Opracowano model określający trwałość porowatych stopów ferrytycznych w wysokich temperaturach na podstawie krótkookresowych testów korozyjnych trwających do 100 godzin.
- Zwalidowano model, wykonując długookresowe (trwające do 6000 godzin) badania w warunkach wysokich temperatur.
- Przeanalizowano morfologię utlenianych próbek za pomocą synchrotronowej tomografii rentgenowskiej pozwalającej na uzyskanie trójwymiarowego obrazu materiału
- Udowodniono, że możliwe jest przedłużenie trwałości porowatych stopów ferrytycznych w wysokich temperaturach przez zastosowanie procesu preoksydacji
- Wytworzono złącza szklano-ceramiczne, łączące gęstą stal Crofer 22 APU oraz porowatą stal Fe22Cr i przetestowano je pod kątem przydatności w roli komponentów tlenkowych ogniw paliwowych.

Wyniki uzyskane w ramach niniejszej rozprawy stanowią obiecującą podstawę do dalszych badań nad zastosowaniem porowatych stopów metali w wymagających warunkach pracy tlenkowych ogniw paliwowych.

## List of abbreviations and symbols

BCC	– body centered cubic
C	– integration constant
CTE	– coefficient of thermal expansion [ppm K <sup>-1</sup> ]
D	– density of oxide scale [g cm <sup>-3</sup> ]
D <sub>eff</sub>	– effective diffusion coefficient [m <sup>2</sup> s]
D <sub>gb</sub>	– grain boundary diffusion coefficient [m <sup>2</sup> s]
D <sub>l</sub>	– lattice diffusion coefficient [m <sup>2</sup> s]
G	– Gibbs free energy [J]
G <sup>0</sup>	– Gibbs free energy at thermodynamical equilibrium [J]
GDC	– gadolinium doped ceria
FCC	– face centered cubic
H	– enthalpy [J]
IOZ	– internal oxidation zone
J <sub>x</sub>	– diffusion flux of x species [mol m <sup>-2</sup> s <sup>-1</sup> ]
k <sub>l</sub>	– linear rate constant [g cm <sup>-2</sup> s <sup>-1</sup> ]
k <sub>p</sub>	– parabolic rate constant [g cm <sup>-2</sup> s <sup>-1</sup> ]
m	– mass [g]
MS-SOC	– metal-supported solid oxide cell
p	– pressure [Pa]
q	– grain shape parameter
Q	– activation energy of oxidation process [eV]
R	– gas constant equal to ~8.314 J mol <sup>-1</sup> K <sup>-1</sup>
R <sub>v</sub>	– ratio of the metal oxide volume to the metal
S	– entropy [J] or surface [cm <sup>2</sup> ]
SEM	– scanning electron microscope
SOC	– solid oxide cell
SSA	– specific surface area [m <sup>2</sup> g <sup>-1</sup> ]
t	– time [s]
T	– temperature [K]
W	– molecular weight of oxide scale [g mol <sup>-1</sup> ]
w	– molecular weight of metal/alloy [g mol <sup>-1</sup> ]
YSZ	– yttria stabilized zirconia

$\delta$  – grain boundary width [nm]

$\rho$  – density of metal/alloy [ $\text{g cm}^{-3}$ ]

## 1. Introduction

Corrosion process is a phenomenon of material degradation caused by environmental conditions, such as temperature, pressure, or surrounding gas. Depending on the considered material, corrosion can manifest as a chemical reaction, an electrochemical process, or a physical interaction. While corrosion can occur in a variety of materials, including polymers, glasses, concrete, and wood, it is most commonly observed in metals and alloys. One specific type of corrosion process is the high-temperature oxidation process that leads to the formation of an oxide scale on the surface of oxidized material at elevated temperatures Figure 1. Other types of corrosion processes also cause degradation of the material in a corrosive environment; however, they might be connected with the hydrogen atmosphere (hydrogen embrittlement) or mechanical surface interactions (fretting corrosion). The threshold temperature that determines the high-temperature oxidation process is 500°C [1]. In this thesis, the terms “high-temperature corrosion process” and “high-temperature oxidation” will be used interchangeably.

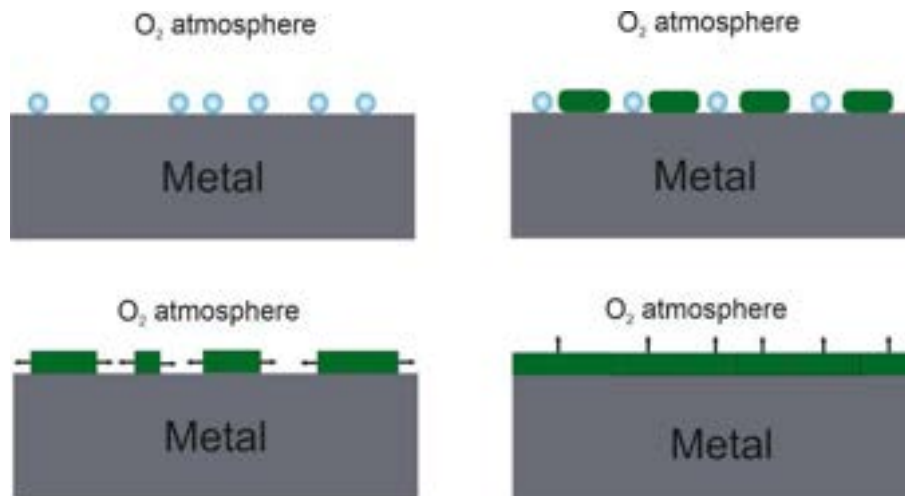


Figure 1. Schema of the oxide scale growth at high-temperature in oxygen atmosphere. Blue circles are assigned to oxygen and green rectangles are assigned to oxide scale.

### 1.1. Historical introduction

The roots of high-temperature corrosion research can be traced back to the industrial revolution, when the increasing demand for efficiency in steam engines exposed materials to harsh and corrosive conditions. Engineers and scientists

observed the accelerated degradation of boiler components, leading to reduced operational lifespans and increased maintenance costs [2].

In the late nineteenth century, internal combustion engines were employed in industrial systems, causing the necessity to find materials that could operate for long periods of time exposed to high temperatures in the combustion gas environment. One of the first alloys that was employed to operate at those conditions was Co – 10 %, Ni – 35 %, Cr – 7 %, W – 5 %, C – 0.5 %, Fe balanced [2]. The next challenge appeared at the beginning of the twentieth century due to the advent of industrial electric heating systems. This necessitated the search for a material to produce wires suitable for a radiant heater with a surface temperature of approximately 850°C. The issue was subsequently addressed through the development of Ni20Cr austenitic alloys, which offer adequate oxidation resistance and creep strength at such high temperatures [3].

The need to develop a corrosion-resistant alloy became apparent in 1940 because of the introduction of the aviation gas turbine in Germany and the United Kingdom [4]. A material for such gas turbine applications had to provide not only excellent corrosion resistance at temperatures over 1350°C but also high-temperature mechanical properties [5]. These demands initialized the application of protective coatings to the alloys to ensure sufficient corrosion resistance at high temperatures.

The first scientific paper about high-temperature oxidation was published by Gustav Tammann in 1920 [6]. He articulated that the rate of oxidation of metal decreases as the oxide scale thickness increases. In 1922, he expressed the logarithmic law of the oxidation of metals [7]. Nevertheless, the first paper about high-temperature oxidation, defined as the oxidation at which the transport of the reactive components through the protective layer determines the oxidation reaction, was published in 1923 by N. B. Pilling and R. E. Bedworth [8]. They showed that the oxide scale that forms at high temperatures might be cracked due to the volume changes of the metal–oxide scale systems. In 1929, Leonard B. Pfeil postulated that besides the inward oxygen diffusion, the outward cation movement in the oxide scale should also be analyzed when considering the high-temperature oxidation process [9]. Finally, in 1933, Wagner's equation, which determined the kinetics of high-temperature oxidation for numerous ferritic and austenitic steels, was expressed [10]. Subsequently, in 1934, the discovery that the transport process within the oxide scale is determined by the motion of the lattice defects permitted the implementation of quantitative techniques to describe high-temperature oxidation. In the early 1940s, the addition of a minor quantity of



reactive elements to the alloy composition was found to markedly enhance its oxidation resistance at elevated temperatures. The nature of this phenomenon remains a topic of scientific debate [4].

The issue of high-temperature corrosion has gained significant importance in recent years, particularly in complex environments that include mixed gases with low oxygen levels and high carbon or sulfur levels, or conditions in which molten alkali salts can accumulate on the surface of the alloy. There have been advancements in developing theoretical models for certain parts of these scenarios [11,12]. Nevertheless, a complete understanding of high-temperature corrosion processes, particularly in polyphase materials, has not been achieved yet.

## **1.2. Mechanisms of the high-temperature corrosion**

In order to determine the mechanism of the high-temperature oxidation process, it is necessary to describe the thermodynamics of this phenomenon. In this section, the growth of the oxide scale will be defined in terms of thermodynamic equilibrium. Moreover, the linear and parabolic laws of oxidation will be presented and discussed.

### **1.2.1. Thermodynamics of high-temperature oxidation**

The formation of the oxide scale at high temperatures is described by the reaction:



where  $M$  is metal,  $MO$  is an oxide scale, and  $O$  is oxygen [13]. The Gibbs free energy ( $G$ ) of the reaction determines the formation of oxide scale (if  $G < 0$ ) or oxide scale dissociation (if  $G > 0$ ). If  $G = 0$  the system is in equilibrium. The equilibrium Gibbs free energy of the oxidation reaction ( $G^0$ ) can be expressed using oxygen partial pressure ( $p_{O_2}$ ), temperature ( $T$ ), and universal gas constant  $R$  [14]:

$$G^0 = RT \ln(p_{O_2}). \quad (1.2)$$

The oxygen partial pressure directly influences the oxidation process at a particular temperature. A change of Gibbs free energy of the oxidation reaction can be also found out by the relation:

$$\Delta G = \Delta H - T\Delta S, \quad (1.3)$$

where  $\Delta H$  is enthalpy change, and  $\Delta S$  is entropy change at the particular temperature  $T$ . The Ellingham diagram (Figure 2) shows a set of curves that represent the temperature dependence of Gibbs free energy for oxidation reaction for different metals [15,16]. The curves show a linear dependence, where an intercept is enthalpy of the oxidation process  $\Delta H$  and a slope is change of the entropy caused by the oxidation reaction  $\Delta S$ .

Gibbs free energy of the oxidation process is dependent upon the oxygen partial pressure (Equation 1.2). The equilibrium partial pressure of oxygen at a specific temperature can be determined by employing the Ellingham diagram. The equilibrium partial pressure of oxygen for a given reaction can be determined by extrapolating a line from the “0 point” (upper left corner of the diagram) to intersect the oxidation reaction curve of the selected metal at the desired temperature. The point of intersection of the line with the  $p_{O_2}$  scale on the right side of the diagram determines the equilibrium partial pressure of oxygen. Moreover, the Ellingham diagram shows the ease of reduction for metals. The position of the oxidation reaction curves on the diagram indicates the stability of the oxides. Oxide scales that form from the reactions closer to the top of the diagram are less stable and more readily reduced than oxide scales of metals placed lower than them. For instance, chromia ( $Cr_2O_3$ ) is more stable than FeO, so the reduction of FeO is easier than the reduction of chromia.

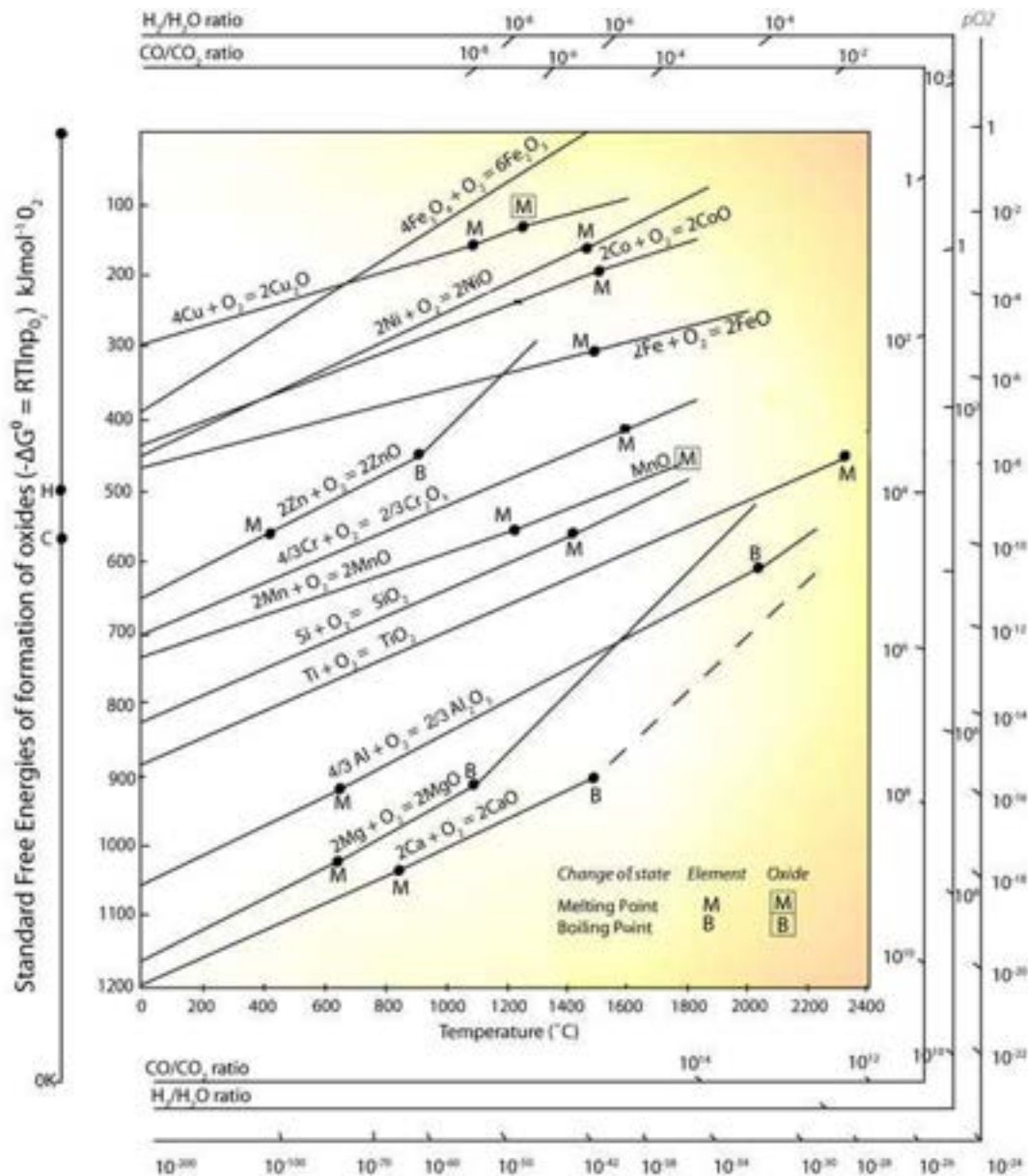


Figure 2. Ellingham diagram [17].

### 1.2.2. Laws of oxidation kinetics

The thermodynamics of high-temperature oxidation determines the formation of an oxide scale at elevated temperatures. However, the rate of growth of the oxide scale is described by the laws of oxidation kinetics:

#### a) Linear law

Linear law of oxidation is followed when

$$\frac{d\left(\frac{\Delta m}{S}\right)}{dt} = k_l, \quad (1.4)$$

where  $\Delta m$  is weight gain caused by oxidation process,  $S$  is surface area of the considered material,  $t$  is time, and  $k_l$  is linear rate constant [13]. Based on the Equation 1.4 it can be stated that materials that follow the linear oxidation law form an oxide scale whose thickness is gradually increasing at the same growth rate. The oxidation process that is determined by linear law is typical for metals with porous or cracked oxide films. According to the Pilling and Bedworth diffusion theory, the oxide scale formation is a consequence of the diffusion of reactant ions from the environment (i.e. oxygen in the air) that occurs at faster rates than the chemical reaction of oxidation [18]. Pilling and Bedworth divided metals into two groups in their work.

The first group contains “light metals which form porous oxides” with a smaller volume than that of the metals that constitute them. The ratio of the metal oxide volume to the metal ( $R_v$ ) can be calculated using the following formula:

$$R_v = \frac{W\rho}{wD}, \quad (1.5)$$

where  $W$  is molecular weight of the oxide,  $D$  its density,  $w$  the weight of the metal atoms in this oxide, and  $\rho$  the density of the metal. The exemplary metals from this group are potassium, calcium, and magnesium with  $R_v$  values equal to 0.88, 0.64, and 0.79, respectively.

#### **b) Parabolic law**

The second group consists of “aluminum and all of the heavier metals”. The metals from this group are characterized by  $R_v > 1$ , as exemplified by nickel and tungsten ( $R_v$  equal to 1.60, and 3.59 respectively). However, the oxidation process for these metals cannot be described by the linear law. Instead, the parabolic law has to be applied. The oxide scale growth that is determined by the parabolic law can be expressed by the following formula:

$$\frac{d\left(\frac{\Delta m}{S}\right)}{dt} = \frac{k_p}{\frac{\Delta m}{S}} \Rightarrow \left(\frac{\Delta m}{S}\right)^2 = k_p t + C, \quad (1.6)$$

where  $k_p$  is parabolic rate constant of oxidation process,  $S$  is the surface of the alloy,  $\Delta m$  its weight gain,  $t$  is the time, and  $C$  is the integration constant. Parabolic law of corrosion process was proposed by Carl Wagner in 1933, as a consequence of his theory of oxidation [10]. The theory can be applied when [13]:

- The oxide scale is compact and adherent

- The oxide scale growth is controlled by migration of charged species (i.e. cations or anions)
- Thermodynamic equilibrium is established at both the metal/oxide scale and oxide scale/corrosive environment interfaces
- The formed oxide scale is stoichiometric
- Oxygen solubility in the metal (or alloy) may be neglected.

There are also different laws of oxidation process such as cubic law [19], logarithm law [20], and inverse logarithm law [21]. Nevertheless, these laws typically describe the oxidation process of materials at temperatures below 500°C, thus they will not be considered in this work.

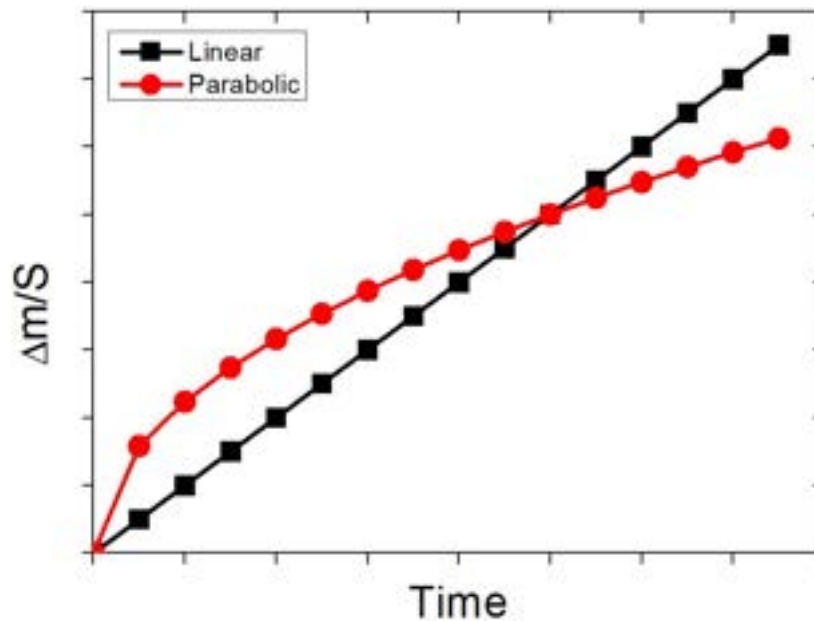


Figure 3. Comparison of oxide scale growth that follow linear and parabolic rate law.

The comparison of linear and parabolic laws of oxidation is presented in Figure 3. From Figure 3 it is clear that at the beginning of the oxidation process, the oxide scale growth is more rapid for materials which follow the parabolic law. However, when a longer time of oxidation is considered, the oxide scale growth is faster for materials which follow linear law.

Based on the parabolic rate law and Wagner's theory, the activation energy of the oxidation process can be calculated. For this purpose, a set of weight gain measurements at different temperatures has to be performed. Then, based on as-obtained data, parabolic rate constant  $k_p$  can be calculated for each considered temperature as a slope of  $\Delta m/S$  in time dependence (as shown in Figure 4 A). The

high-temperature oxidation process is a thermal-activated phenomenon determined by the diffusion of charged species (for the materials that follow parabolic law), thus the Arrhenius dependence (Equation 1.7) can be applied:

$$k_p = k_0 e^{\left(\frac{-Q}{RT}\right)}, \quad (1.7)$$

where  $Q$  is activation energy of the oxidation process, and  $k_0$  is pre-exponential factor (or Arrhenius factor). Finally, the slope of the  $\log(k_p)$  with  $1/T$  curve allows to calculate the activation energy of the oxidation process for the considered alloy, as shown in Figure 4 B).

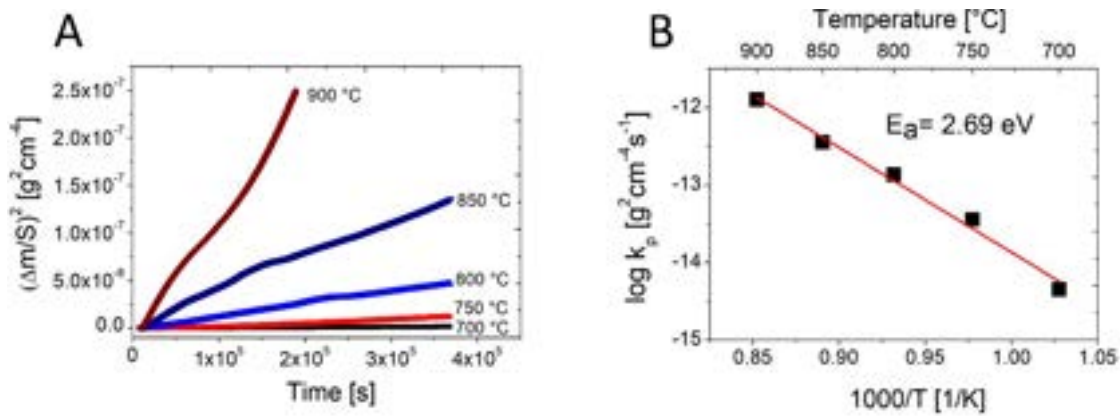


Figure 4. A) Weight gain data presented as square weight change with respect to the initial surface area, B) Arrhenius plot.

While Wagner's theory of oxidation has provided valuable insights into the kinetics of high-temperature oxidation processes, it is imperative to acknowledge its limitations, particularly concerning microstructural changes. The theory, based on the parabolic rate law, predominantly emphasizes the outward diffusion of metal cations. However, the intricate interplay between inward and outward diffusion, as well as microstructural alterations can significantly influence the overall oxidation kinetics. The role of microstructure in high-temperature oxidation will be discussed in next sections.

The parabolic and linear parabolic laws describe an idealized situation in which a single process is responsible for high-temperature oxidation. However, in many cases, multiple processes must be considered to fully describe the kinetics of oxidation.

The change in weight gain relative to the initial surface area over time can be expressed using the following generalized expression:

$$\log\left(\frac{\Delta m}{S}\right) = n \log t + C, \quad (1.8)$$

where  $\Delta m$  is the weight gain of the sample,  $S$  its surface area,  $t$  is the time,  $n$  is the power parameter, and  $C$  is the integration constant. The power parameter  $n$  is a slope of linear curve that determines the kinetics of the oxidation process. In order to determine the kinetics law of the oxidation process the double logarithmic plot can be used, as presented in Figure 5. For example, in the case of an oxidation process that follows the parabolic law, the slope of log-log plot (and thus the  $n$  value) is equal to 0.5. Conversely, the linear plot is expressed when  $n$  is equal to 1.

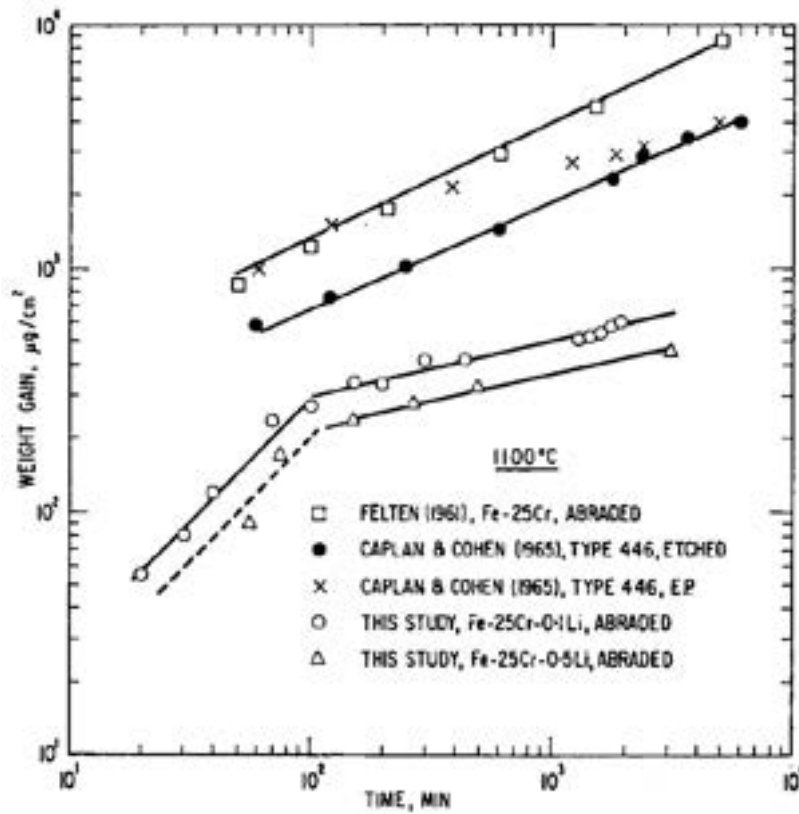


Figure 5. Comparison of oxidation behavior of Fe-Cr-Li and Fe-Cr alloys at 1100°C [22].

### 1.2.3. Inward and outward corrosion

In order to characterize the high-temperature corrosion process, three components have to be considered: the reacting material, the oxide scale, and the corrosive environment. A schematic representation of the high-temperature corrosion components is shown in Figure 6.

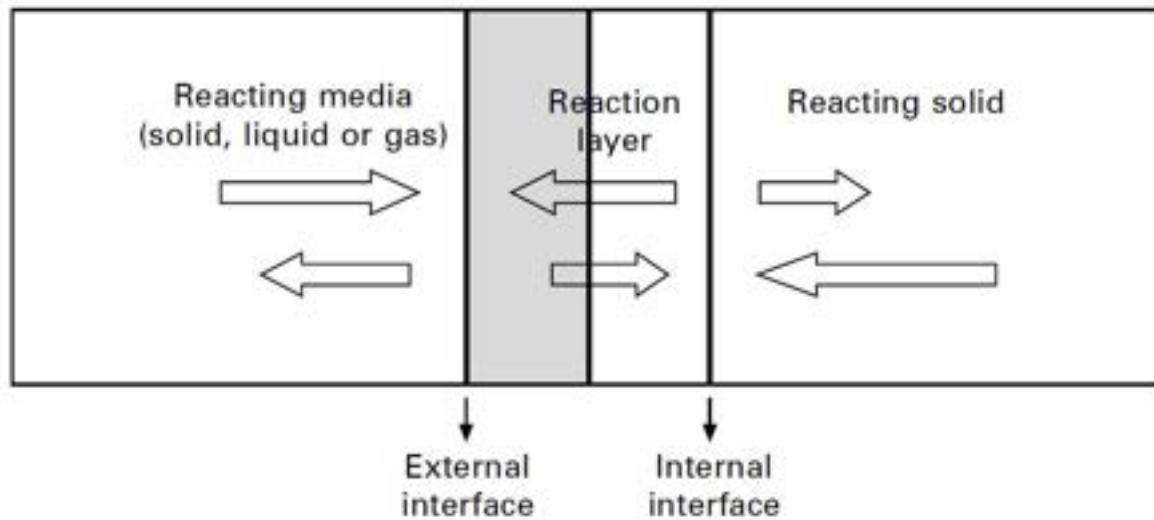


Figure 6. A schematic representation of the high-temperature corrosion components [23].

To gain a comprehensive understanding of high-temperature corrosion, it is essential to consider not only the processes occurring within each component of the system, but also the reactions occurring at both the internal interface (between the reacting solid and oxide scale) and the external interface (between the oxide scale and the reacting environment).

In accordance with the parabolic law of corrosion, the oxidation process is contingent upon the diffusion of ions within the oxide scale. Therefore, the oxide scale formation can be attributed to two distinct processes. One such process is the movement of oxygen anions from the external interface between the oxide scale and the surrounding environment to the internal interface between the oxide scale and the alloy (or metal). This process is designated as inward oxidation. Conversely, the movement of metal cations from the alloy/oxide scale interface to the oxide scale/external environment is referred to as the outward oxidation process [24].

Inward corrosion is typically regarded as an undesirable phenomenon, as it describes the penetration of oxygen into the material, leading to internal oxidation or the formation of subscale oxides. In contrast, the result of outward corrosion can be the formation of a protective oxide scale on the alloy's surface, which acts as a barrier, inhibiting further penetration of oxygen and other corrosive species into the alloy. Therefore, the outward corrosion mechanism is highly desirable in alloy design for applications in which maintaining structural integrity and preventing material degradation at elevated temperatures are paramount concerns. A schematic model that compares inward and outward corrosion processes is presented in Figure 7.



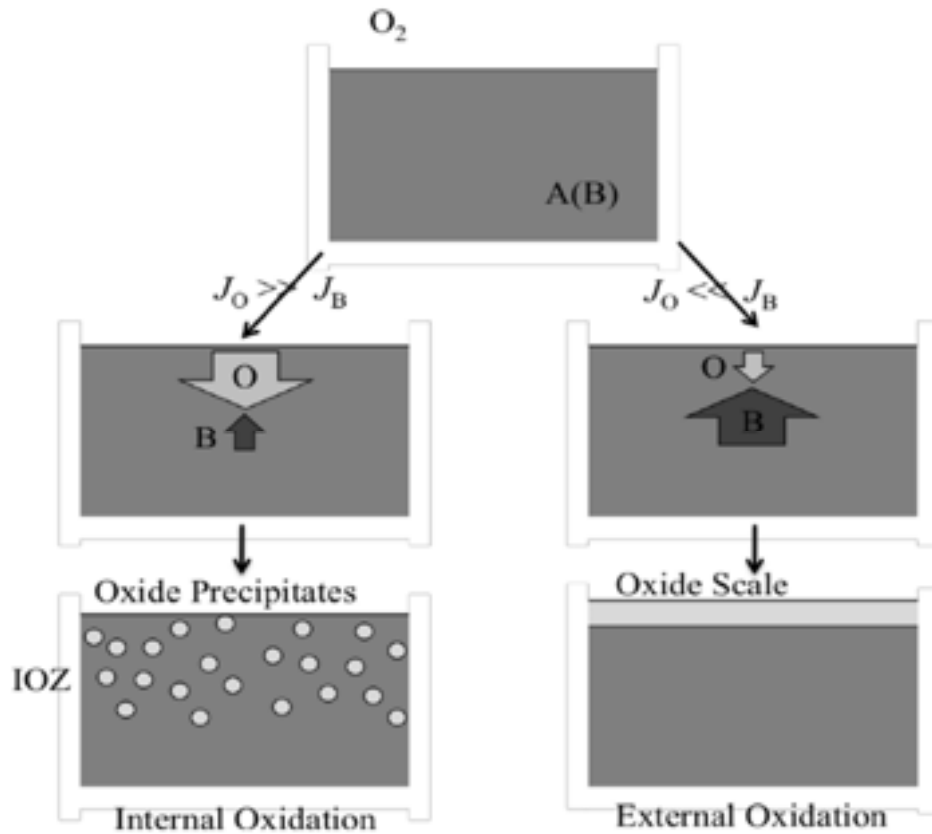


Figure 7. Schematic model of inward and outward oxidation process. IOZ is internal oxidation zone, A(B) is alloy consisting of solvent A and solute B, and  $J_x$  is diffusion flux of x species [25].

### 1.3. Microstructure influence on high-temperature oxidation

In order to determine the corrosion properties of an alloy at high temperatures a detailed analysis of their microstructure is necessary. The influence of crystal structure, grain size, porosity, and a number of grain boundaries to oxide scale growth at high temperatures has been confirmed for last decades.

#### 1.3.1. Ferritic and austenitic alloys

Ferritic alloys have a body-centered cubic (BCC) crystal structure and they are typically composed of iron and chromium, with varying amounts of other alloying elements. Because of the high chromium content, ferritic alloys form a protective chromia layer on the surface at high temperatures, providing good corrosion resistance.

The impact of the chemical composition on the resistance to oxidation at high temperatures is not limited solely to the austenitic and ferritic crystal structure. For an

enhanced understanding how the chemical and phase compositions determine corrosion properties, the analysis of the phase diagrams has to be considered.

The analysis of the Fe-Cr phase diagram (Figure 8) reveals a presence of sigma phase at the temperatures above 600°C for the alloy containing more than 25 % of Cr. The sigma phase is a mixed FeCr oxide that is brittle and exhibits increased coefficient of thermal expansion (CTE) [26]. Despite the protective feature of chromia in the context of high-temperature oxidation, ferritic alloys consisting of more than 26 % of Cr are often avoided in devices which operate at temperatures above 650°C.

The alloy's physical and chemical properties are influenced by its chemical composition, which goes beyond merely altering the phase composition. Various components are used to enhance the corrosion resistance or increase the stress resistance of the alloy. Manganese (Mn) is frequently used in FeCr systems to form a protective spinel layer that hinders the oxidation process. Experiments have revealed that the addition of around 0.4 % of Mn to the FeCr alloy has a substantial impact on enhancing its resistance to corrosion [27,28]. As a result, this modification effectively extends the lifespan of the alloy.

Adding Si to the alloy can improve the adherence of chromia by forming a SiO<sub>2</sub> subscale between Cr<sub>2</sub>O<sub>3</sub> and the alloy [29–31]. The incorporation of Al enhances the alloy's capacity to resist oxidation by creating a protective layer of Al<sub>2</sub>O<sub>3</sub> on its surface [32–34]. Nevertheless, the low electrical conductivity of both Al<sub>2</sub>O<sub>3</sub> and SiO<sub>2</sub> renders Al and Si unsuitable as modifiers for alloys used in electronic devices that operate at high temperatures [35].

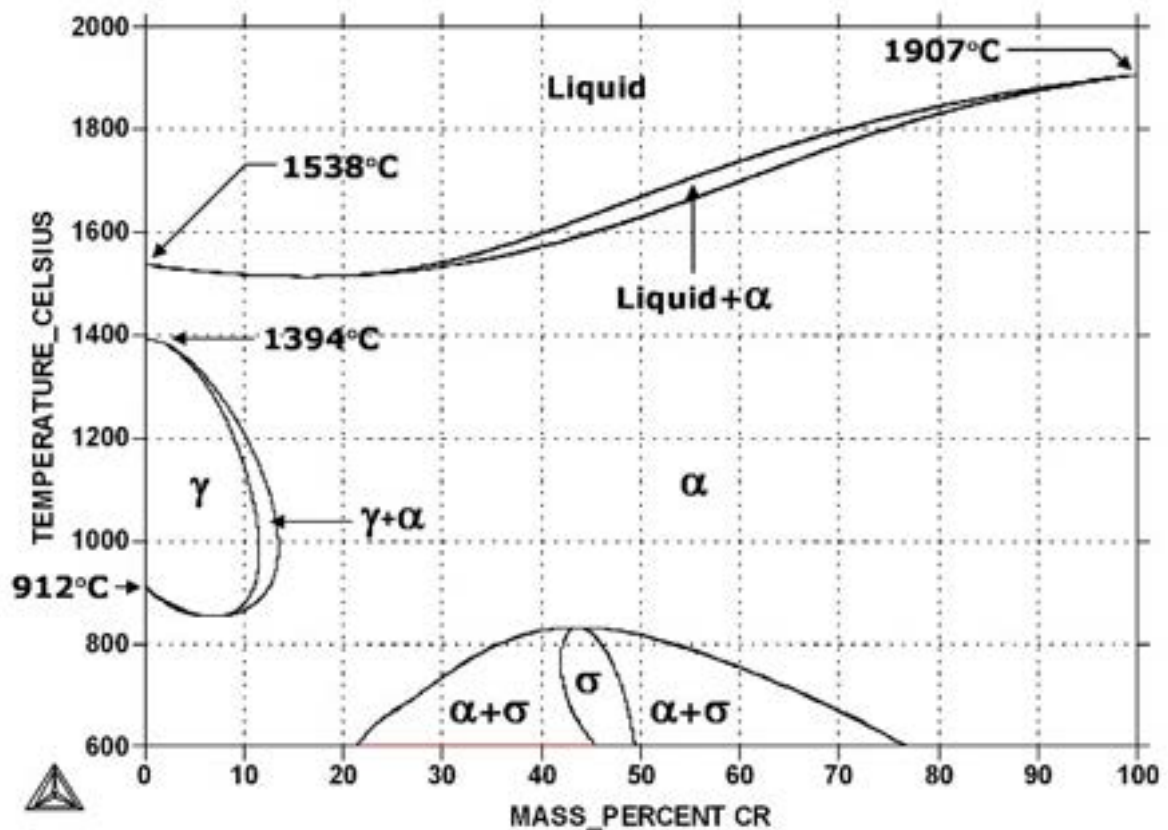


Figure 8. Fe-Cr phase diagram [36].

On the other hand, austenitic alloys have a face-centered cubic (FCC) crystal structure. Typically, the composition of the austenitic alloys is based on iron, chromium and nickel and other alloying elements. Austenitic alloys are known for their excellent corrosion resistance, making them suitable to use in aggressive environments at temperatures above 1000°C. One of the possible ways to transform ferritic alloy into austenitic one is to apply nickel coating to the ferritic alloy and treat as-prepared structure at an elevated temperature causing incorporation of Ni species in the alloy. Then, an austenitic microstructure is formed. The schema of this process is shown in Figure 9.

Other differences between austenitic and ferritic alloys are described in Section 1.4. of the thesis where possible applications and material restrictions are provided.

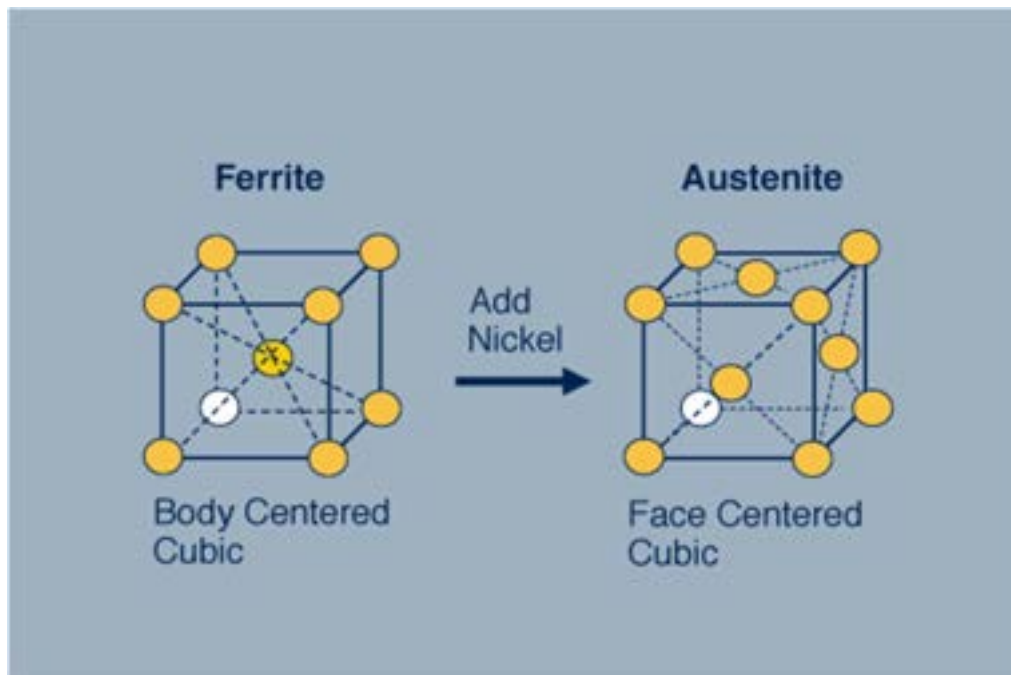


Figure 9. Crystal structure of ferritic and austenitic alloys [37].

The alloys which are employed in high-temperature operating conditions are often austenitic FeCrNi compositions or ferritic FeCr systems. In the case of austenitic FeCrNi alloys, it has been demonstrated that they are chromia-forming alloys that exhibit excellent oxidation resistance at the temperature range from 1000°C to 1300°C because of formation of protective  $\text{Cr}_2\text{O}_3$  on their surface [38,39]. However, in the temperature range from 500°C to 1000°C, the Cr diffusion is significantly lower and it allows for the formation of mixed FeCr oxides (Ni is not oxidized) [40]. On the other hand, the ferritic alloys which are typically the FeCr systems only form chromia at high-temperatures [41]. Then, a Cr concentration profile is flat within the alloy at temperatures above 500°C because of higher diffusivity of Cr in the ferritic crystal structure [42].

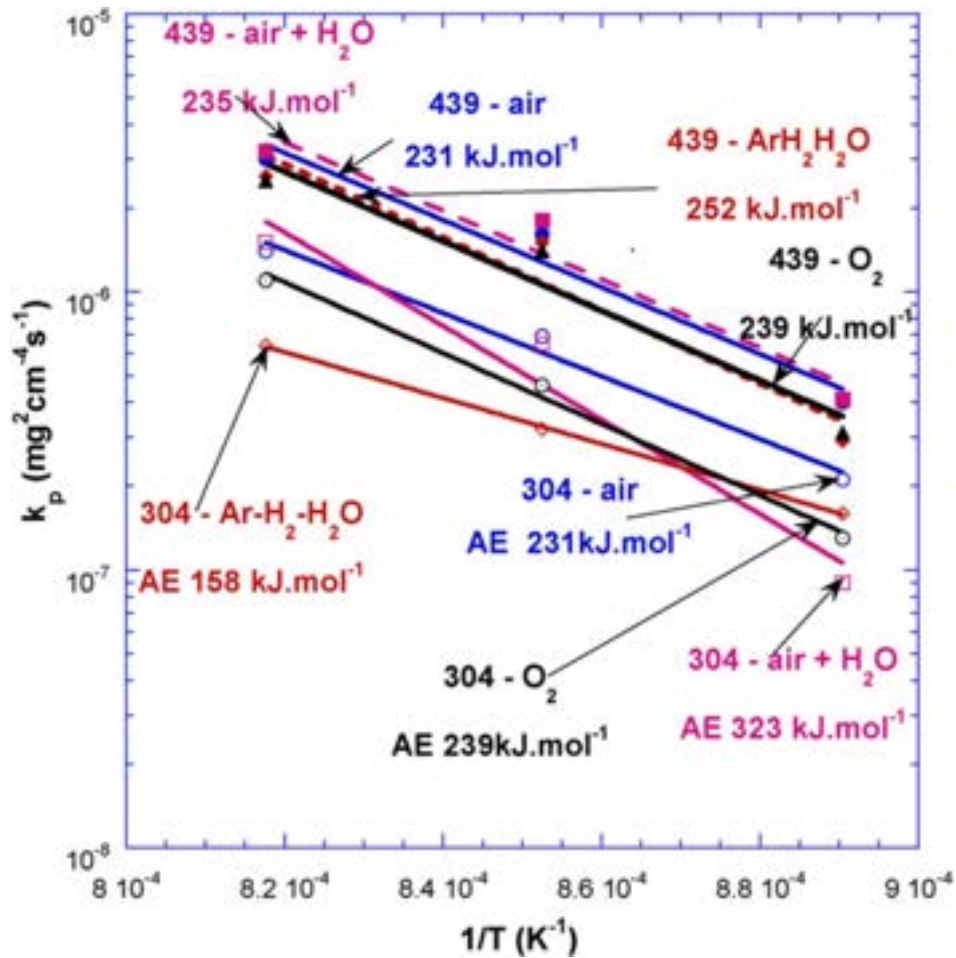


Figure 10. Arrhenius plot of oxidation for 439 and 304 steel [43].

The influence of the phase composition on the corrosion resistance at high-temperatures was investigated for chromia-forming austenitic and ferritic alloys. Huntz et al. researched corrosion resistance of ferritic 439 and austenitic 304 alloys which have similar Cr content ( $\sim 17 - 18$  wt. %) [44]. The oxidation tests performed for both alloys at temperature ranging from  $850^\circ\text{C}$  to  $950^\circ\text{C}$  in air revealed that the oxide scale growth rate is higher for ferritic 439 alloy when compared with austenitic 304 alloy (Figure 10).

### 1.3.2. Grain and grain boundary diffusion fluxes

The presence of structural defects in both oxide scale and the alloy, such as dislocations or grain boundaries, leads to an increase in the effective diffusion coefficient, so it influences the high-temperature properties of the alloy. The lattice diffusion coefficient and grain boundary diffusion coefficient constitute the effective diffusion coefficient as presented in the Hart's equation:

$$D_{eff} = \frac{q\delta}{d} D_{gb} + \left(1 - \frac{q\delta}{d}\right) D_l, \quad (1.9)$$

where  $D_{eff}$  is effective diffusion coefficient,  $D_{gb}$  is grain boundary diffusion coefficient,  $D_l$  is lattice diffusion coefficient,  $q$  is a grain shape parameter (its value is 1 for parallel grains, 3 for square grains),  $d$  is average grain size and  $\delta$  is grain boundary width [45]. The lattice diffusion, grain boundary diffusion, and surface diffusion are schematically presented in Figure 11.

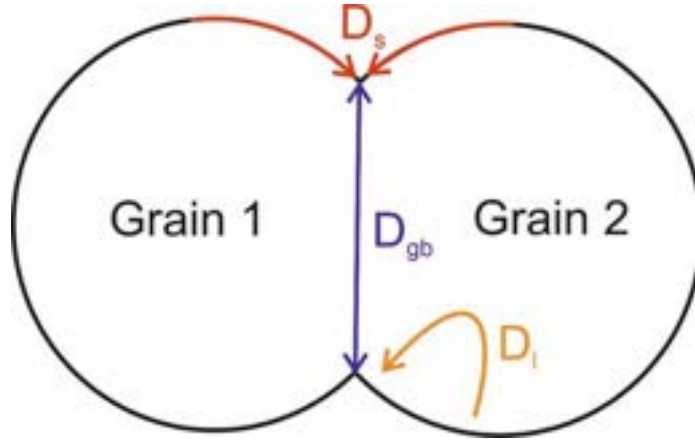


Figure 11. Different diffusion routes in two neighboring grains at high temperature.

The diffusion influence on the high-temperature oxidation can be considered in the following contexts:

#### a) Diffusion within the oxide scale

Suzuoka et al. created a model that allows for estimation of the lattice diffusion coefficient and grain boundary diffusion coefficient for the polycrystalline materials [46]. Lobnig et al. applied this model for the calculation of the grain boundary diffusion coefficient and lattice diffusion coefficient of the Cr cations in the oxide scale that formed in high temperature conditions [47]. They proved that the lattice-diffusion coefficient of Cr is 3 to 5 orders of magnitude smaller than the grain-boundary diffusion coefficient of Cr in chromia when the ferritic Fe20Cr alloy is oxidized at 900°C.

Chromia-forming alloys are widely used at high-temperatures because of protective properties of  $\text{Cr}_2\text{O}_3$  in harsh environments. In order to understand those features of chromia, the diffusivity of the Cr and O within the oxide scale formed at 800°C and 900°C was investigated [48,49]. It was confirmed that chromium lattice diffusion is close to that of oxygen, and chromium grain boundary diffusion is faster than that of oxygen, especially at 900°C. At this temperature the lattice diffusion coefficient of O is

$4.4 \times 10^{-17} \text{ cm}^2 \text{ s}^{-1}$  and the grain boundary diffusion coefficient of O is  $1.6 \times 10^{-12} \text{ cm}^2 \text{ s}^{-1}$ . The Cr lattice and grain boundary diffusion coefficient is  $2.0 \times 10^{-17} \text{ cm}^2 \text{ s}^{-1}$  and  $9.3 \times 10^{-12} \text{ cm}^2 \text{ s}^{-1}$ , respectively [48]. In this case, the diffusion rate of chromium within the oxide scale is relatively fast compared to the rate of oxygen diffusion. It leads to the formation of a dense, continuous, and protective oxide scale, which effectively isolates the underlying alloy from further oxidation. On the other hand, if the diffusion rate of chromium within the oxide scale is relatively slow compared to the rate of oxygen diffusion through the scale, this can lead to the depletion of chromium near the metal-oxide scale interface, resulting in the formation of a porous or non-protective oxide scale. The grain boundary diffusion of Cr is the fastest process among considered ones – thus it has a decisive influence on the oxidation resistance of the chromia-forming alloy.

The difference between Cr diffusivity in monocrystalline and polycrystalline chromia was extensively studied. It was confirmed that for polycrystalline materials the diffusion coefficient is several orders of magnitude larger than for single crystals, and this is probably due to much faster grain boundary diffusion in polycrystalline material [50]. Thus, one of the possible ways to improve the corrosion resistance of chromia-forming alloys is to employ pre-oxidation process. The pre-oxidation process is the oxidation performed at a high temperature in order to form a large-grained oxide scale. In consequence, the relative number of chromia grain boundaries decreases, causing an altering in the diffusion fluxes of Cr species through chromia. This in turn enhances the alloy's corrosion resistance at temperatures which are high, but lower than the ones applied during the pre-oxidation process. The beneficial effect of the pre-oxidation process on high-temperature corrosion resistance of chromia-forming alloys was confirmed by Kim et al [51].

#### **b) Diffusion within the alloy**

The diffusion of the elements within the alloy determines the possible application of the alloy, as it was mentioned in Section 1.3.1. For the chromia-forming alloys, the diffusion of chromium within the alloy structure influences the possible reservoir of this element in the region close to the oxide scale. Tőkei et al. investigated both lattice and grain boundary diffusion of Cr inside the austenitic and ferritic alloys [40]. Their research revealed that the slight change of Cr content in the alloy (from 9 wt. % to 12 wt. %) affects neither the lattice, nor the grain boundary diffusion coefficients for ferritic alloys. At  $\sim 900^\circ\text{C}$  the lattice diffusion coefficient is  $1.13 \times 10^{-16} \text{ m}^2 \text{ s}^{-1}$  and  $2.50 \times 10^{-16}$

$\text{m}^2 \text{s}^{-1}$  for ferritic alloy that contains 9 wt. % of Cr and 12 wt. % of Cr, respectively. The grain boundary diffusion coefficient at  $\sim 900^\circ\text{C}$  is  $6.74 \times 10^{-12} \text{ m}^2 \text{s}^{-1}$  and  $8.12 \times 10^{-12} \text{ m}^2 \text{s}^{-1}$  for 9 wt. % of Cr and 12 wt. % of Cr alloys, respectively (with the assumption that grain boundary thickness is  $5 \text{ \AA}$ ).

### **1.3.3. Porous and bulk alloys**

As the corrosion properties have been studied for decades, there is a considerable number of studies on the subject, including research on the influence of ferritic and austenitic alloy's grain size and chemical composition on the corrosion resistance of bulk alloys [52,53]. Based on those studies, a change in geometrical dimensions in particular can severely impact the corrosion properties of alloys. Therefore, porous alloys have recently become of greater interest as engineering materials employed in oxidation environments. Typical cross-section images of the porous and dense alloys are shown in Figure 12.

In the case of the porous alloy, a much larger specific surface area is exposed to the oxidation environment, leading to the formation of an oxide scale on top of the alloy's surface. For the alloy in Figure 12 A, the specific surface area (SSA) is  $\sim 0.022 \text{ m}^2 \text{g}^{-1}$ , whereas for the dense alloy shown in Figure 12 B it is only  $0.0008 \text{ m}^2 \text{g}^{-1}$  (28x difference). Limited protective element reservoir (in this case Cr) will lead to a much shorter lifetime of the porous samples due to its depletion and to breakaway oxidation of the alloy, as presented in Figure 13 B. This issue will be described in the next sections.



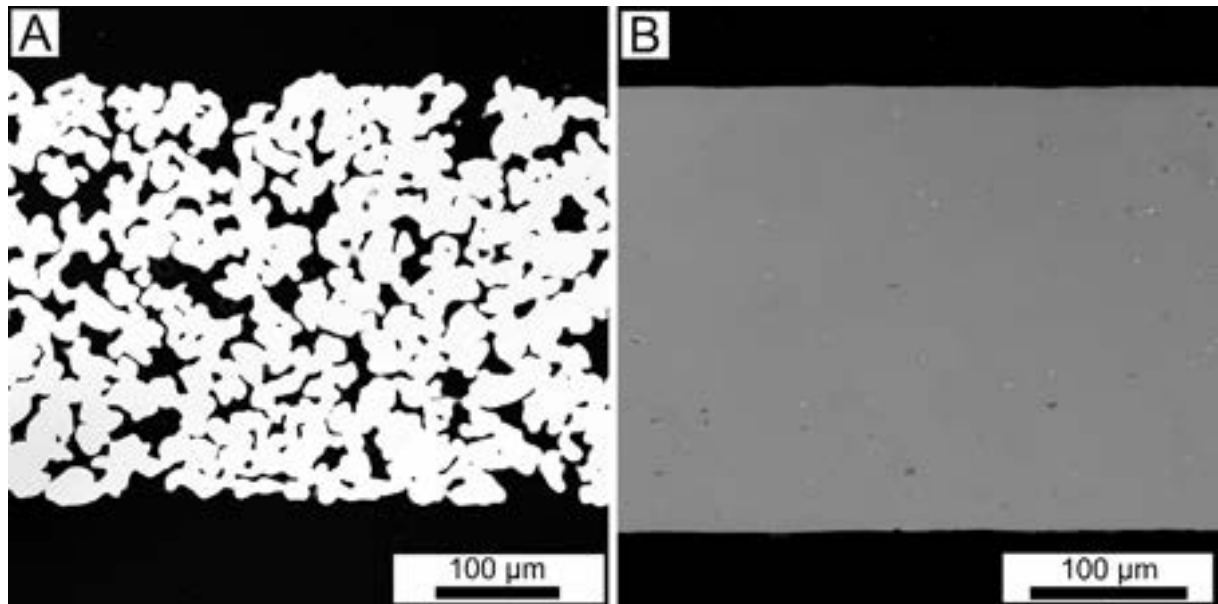


Figure 12. SEM image of A) porous, B) dense chromia-forming alloy cross-section.

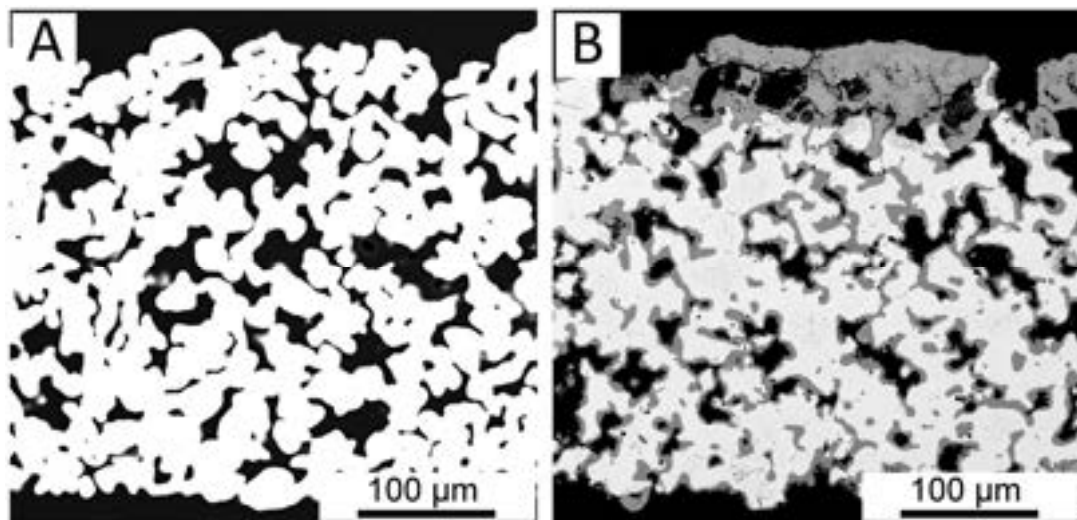


Figure 13. SEM image of porous Fe<sub>22</sub>Cr alloy A) before oxidation, B) after oxidation at 900°C for 30 h.

#### 1.4. Applications of porous alloys

Porous materials are utilized in several industries as a substitute for their bulk counterparts due to the potential advantageous characteristics of their microstructure. Porous alloys can be made into filters, fluid separators [54], heat exchangers [55], sound absorbers [56], or metal-supported solid oxide cells [35]. In this section, the application of porous alloys in solid oxide cells will be described in the context of material requirements which are crucial to their efficient usage.

Solid oxide cells (SOCs) are devices that are capable of operating in two distinct modes. The first mode is that of a solid oxide fuel cell (SOFC), which is able to transform the chemical energy of gases into electrical current. In contrast, a solid oxide electrolysis cell (SOEC) employs electrical energy to facilitate the conversion of chemical energy into gas species. The typical operating temperature range for SOCs is above 750°C. However, the intermediate-temperature solid oxide cells (IT-SOCs), which operate at temperatures ranging from 500°C to 750°C, have been extensively studied for the last decade [57]. One of the IT-SOC types that has attracted renewed interest in recent years is a metal-supported solid oxide cell (MS-SOC). In MS-SOCs, the alloys are considered not only as support components but also as interconnectors. The replacement of advanced ceramic materials with metallic components allows for a decrease in the cost of the device and provides tolerance to rapid thermal excursions. The drawback of using alloys at typical IT-SOC operating temperatures in an oxidizing environment is the unavoidable formation of metal oxide scales, which limits the potential lifespan of the device.

The most promising alloys that are considered in MS-SOC systems are chromia-forming alloys because they form a passive layer of oxide scale on their surface in typical SOC operating conditions. This layer acts as a barrier, decreasing the oxygen diffusion rate and limiting further oxidation process. Moreover, chromium oxide ( $\text{Cr}_2\text{O}_3$ ) has relatively high electrical conductivity among transition metal oxides. Therefore, chromia-forming alloys ensure sufficient electrical current conduction under IT-SOCs operating conditions. The electrical conductivity of the  $\text{Cr}_2\text{O}_3$  at 600°C - 800°C is  $\sim 1 - 10 \text{ mS cm}^{-1}$  [58]. On the other hand, the electrical conductivity of the aluminum oxide ( $\text{Al}_2\text{O}_3$ ) is  $\sim 10^{-8} - 5 \times 10^{-3} \text{ mS cm}^{-1}$  at 500°C - 1000°C [59], and for silicon oxide ( $\text{SiO}_2$ ) the electrical conductivity is  $\sim 10^{-5} - 2 \times 10^{-3} \text{ mS cm}^{-1}$  at 500°C - 1000°C [59].

Considering the operational temperature of IT-SOCs, it is necessary to make adjustments to the microstructure of the alloys to suit the corrosive environmental conditions. As it was mentioned in Section 1.3.1, austenitic alloys have excellent corrosion resistance at high temperatures. However, at the operating temperature of IT-SOC, the diffusion rate of alloying elements (such as Cr) is significantly lower in austenitic alloys, by the order of magnitude. This results in the formation of the Cr-depletion region beneath the oxide scale, which in turn leads to the synthesis of the mixed Fe-Cr oxides [42]. These mixed oxides reduce both the mechanical strength and electrical conductivity of the material. Therefore, chromia-forming ferritic alloys such

as Crofer 22 APU [60–63], Crofer 22 H [64–66], or SUS 430 [67–69] are employed in MS-SOC systems.

In recent years, an increasing number of scientists have worked on the application of porous ferritic stainless steel as a substrate for MS-SOCs. The structure of the porous alloy can provide sufficient gas permeability, which is an important feature in the context of SOC applications. The schematic representation of electrolyte-supported solid oxide cell, anode-supported solid oxide cell, and metal-supported solid oxide cell with porous alloy component is shown in Figure 14.

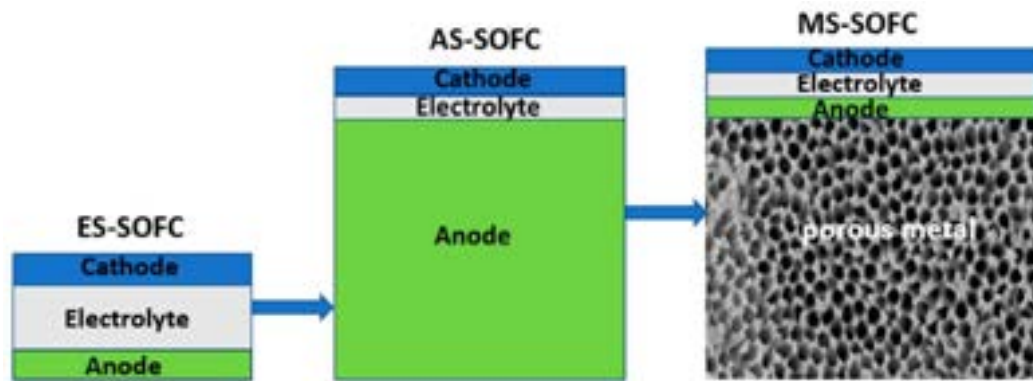


Figure 14. Schematic representation of electrolyte-supported solid oxide cell, anode-supported solid oxide cell and metal-supported solid oxide cell [70].

The important factor that has to be considered in the context of alloy application in MS-SOC systems is the coefficient of thermal expansion (CTE). It is essential to align the coefficient of thermal expansion (CTE) of the alloy with that of electrolyte in order to provide adequate mechanical stability during operational cycles. A typical CTE value of the electrolyte materials such as yttrium-stabilized zirconia (YSZ) or gadolinium-doped ceria (GDC) is in the range 10 – 12 ppm K<sup>-1</sup> [71–73]. Among the metallic compounds the 400-series stainless steels, Crofer 22 APU, and Crofer 22 H, which are ferritic chromia-forming alloys, have the CTE ~ 11 pm K<sup>-1</sup> [74,75].

The available literature about the corrosion process of porous alloys in the context of MS-SOC applications is still very limited. The corrosion properties of porous alloys for SOC systems have been researched by Molin et al, who investigated porous 430L stainless steel (~45 % - 55 % of total porosity) in air and in humidified hydrogen at 400 °C and 800 °C [76,77]. They confirmed that the mass gain for porous samples follows the parabolic law, similarly to dense samples. The area-specific resistance (ASR) of the oxide scale formed on 430L in the air at 800°C reached the limit of 100 mΩ cm<sup>-2</sup>

after 75 h of oxidation. The higher ASR means that the sample cannot be further used as a substrate in the SOC system because it is not able to provide sufficient current flow.

M.C. Tucker fabricated symmetric-structure metal-supported solid oxide fuel cell using porous ferritic P434L alloy as support material on both anode and cathode sides (Figure 15). The electrodes were obtained by infiltration of lanthanum strontium manganite (LSM) and samarium doped ceria mixed with Ni (SDCN) into the porous YSZ in cathode and anode side, respectively. Peak power density of as-fabricated cells was  $0.44 \text{ W cm}^{-2}$ ,  $1.1 \text{ W cm}^{-2}$ , and  $1.9 \text{ W cm}^{-2}$  at  $600^{\circ}\text{C}$ ,  $700^{\circ}\text{C}$ , and  $800^{\circ}\text{C}$ , respectively [78].

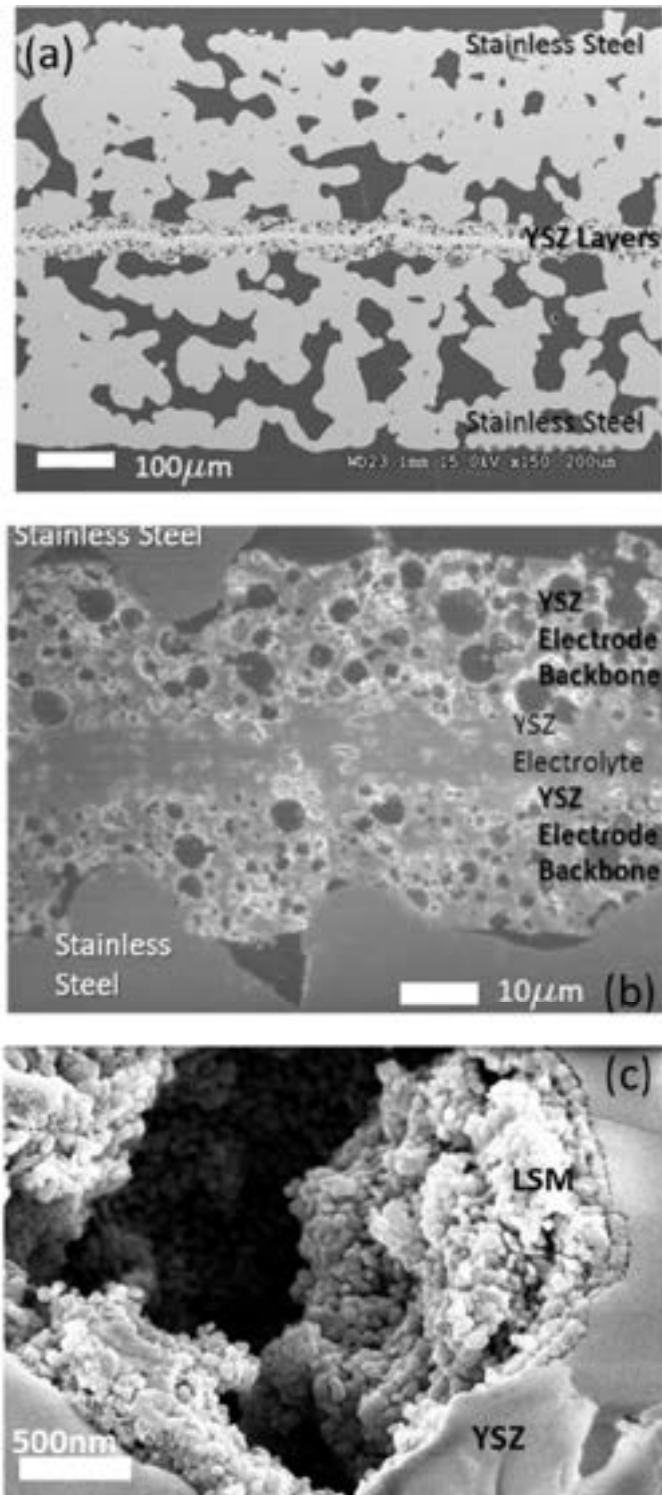


Figure 15. SEM image of a, b) polished cross-section of MS-SOFC structure after sintering and before catalyst infiltration, and c) cathode pore after infiltration of LSM [78].

### 1.5. Lifespan prediction model

The lifespan of an alloy can be defined in the context of high-temperature corrosion as the time that the considered material can withstand at a particular temperature

without significant deterioration of its mechanical (or other desired) properties. The lifespan of an alloy at high temperatures is limited due to the unavoidable formation of an oxide scale. Below several methodologies of assessing the threshold value of the alloy's lifespan are described.

The first methodology is the estimation of the time for the occurrence of breakaway oxidation, which is a Fe-rich oxide scale formed in the case of depletion of the scale-forming element in the alloy. Young et al. proposed a simple expression to calculate the threshold time for the breakaway corrosion formation based on the numerical analysis of different parameters' influence on the alloy's lifespan [79]. This expression is the function of the oxidation rate, the concentration and diffusivity of the solute element, and the oxide scale thickness. However, the presented model takes into consideration only the planar geometry of the alloy, so it cannot be applied to evaluate the possible lifespan of porous alloys. Moreover, for the austenitic alloys, the concentration profile of the chromium varies in the region beneath the oxide scale. Therefore, a lifespan prediction model for austenitic alloys has to be more complex than the proposed one.

The second approach focuses on analyzing the change in specimen thickness. This model employs the extrapolation of the log-log curve that shows a specimen thickness versus time to breakaway corrosion formation at high-temperatures [80–82]. The model was validated only for ferritic alloys like Crofer 22 APU and ZMG232. However, the model assumes that the considered alloy has the form of a flat sheet or plate. Therefore, it cannot be applied to porous alloys.

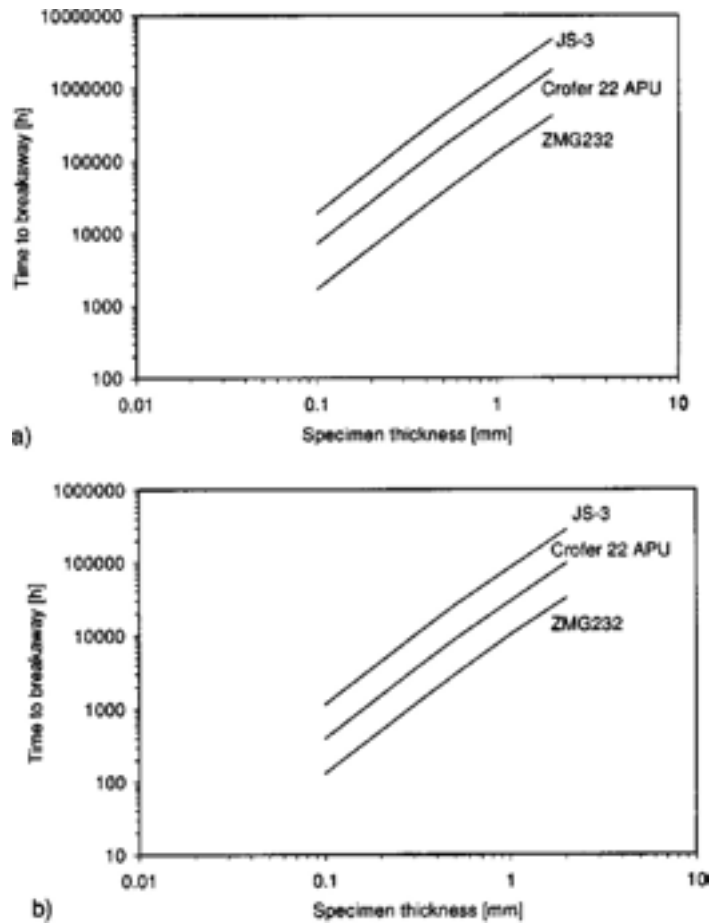


Figure 16. The lifespan prediction model applied for ferritic alloys based on the specimen thickness at a) 800°C, b) 900°C [80].

For the ferritic alloys, it was confirmed that their lifespan is directly correlated with the Cr reservoir within the sample. Huczowski et al. revealed that the minimum Cr content in the ferritic alloy required to maintain its protective properties was found to be ~15 wt. % [80]. When the Cr level within the alloy drops below this threshold, the oxidation of Fe begins, and the formation of breakaway corrosion regions is observed.

Tucker et al. observed that the porous ferritic Fe22Cr alloy exposed to a 9:1 H<sub>2</sub>: H<sub>2</sub>O environment at 850°C for 500 h exhibited the formation of a ~3 µm oxide scale layer on its surface [83]. Consequently, the investigated sample is unsuitable for use as a support in the MS-SOC system.

The lifespan of the alloy in other forms than bulk was studied by Chyrkin et al [84]. The lifespan of the INCONEL 625 foam obtained by the slip-reaction-foam-sinter process at temperatures ranging from 700°C to 900°C was investigated. A proposed lifespan prediction model was developed based on the calculation of Cr-depletion in the alloy at the oxide/metal interface of each individual foam particle. The model

assumed that the foam consists of spherical particles, that the oxidation process follows the parabolic rate law, and that interface displacement due to Cr consumption is not taken into account. The influence of the particle radius on the alloy's lifespan was then determined, as illustrated in Figure 17. The predicted lifespans were found to be in good agreement with the experimental results.

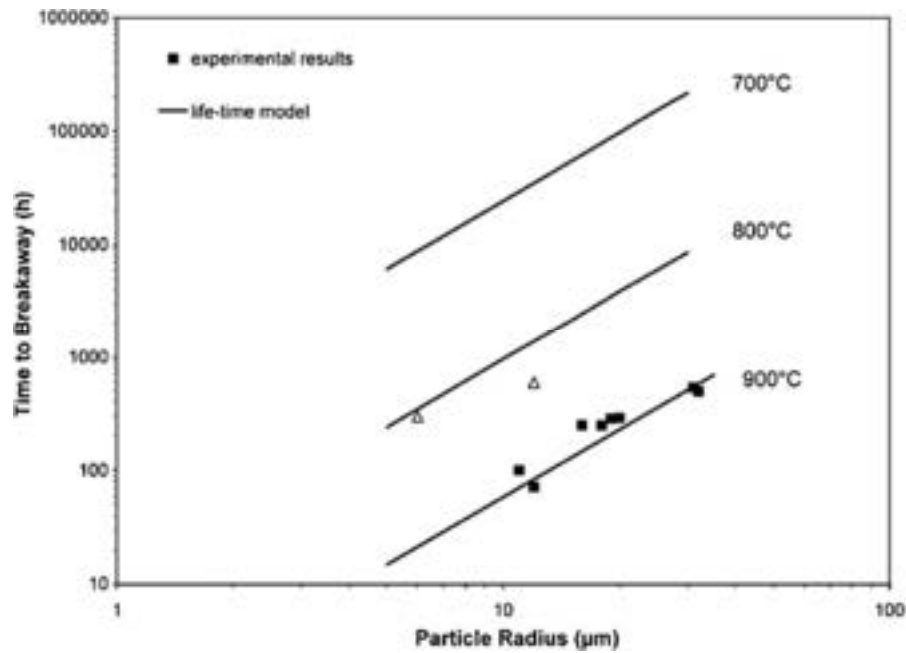


Figure 17. Calculated lifespan for various metal foams based on the average particle radius at different temperatures compared with experimental data [84].

Nevertheless, there is still missing data about the high-temperature oxidation of the porous alloys in the air, which is also typical of the SOC operating environment. Moreover, the influence of porosity on the possible lifespan was not determined based on a mathematical or experimental model.



## 2. Objectives and hypotheses

The high-temperature oxidation process is the main challenge for porous alloys' application in devices that operate at elevated temperatures, e.g. solid oxide cells. Although the corrosion resistance of bulk alloys has been studied for many decades and their properties are well described, there is still a limited number of publications regarding the porous alloys' oxidation resistance. **The aim of this dissertation is to describe the oxidation properties of porous ferritic alloys and formulate a practically relevant lifespan prediction model.**

The chemical composition of the investigated alloys was selected based on the material requirements that have to be fulfilled for metal-supported solid oxide cell applications. For this reason, chromia-forming porous alloys with Cr content ranging from 20 wt. % to 26 wt. % were considered in this work.

There is a very limited number of publications that evaluate the lifespan of porous alloys. Typically, the lifespan of the alloy at particular oxidizing conditions is determined via long-term exposure experiments. However, according to the current knowledge ferritic chromia-forming alloys reach their lifespan limit when the Cr content decreases to ~15 wt. % due to the formation of chromium oxide. In addition, the Cr concentration profile inside such alloys is flat. Basing on that, the scientific hypothesis has been formulated:

- 1) It is possible to create a lifespan prediction model for porous ferritic chromia-forming alloys based on short-term oxidation exposure experiments at high-temperatures.**

Such lifespan prediction model was proposed in [DK1]\* based on information obtained via 100 h oxidation exposure of porous Fe22Cr alloy at temperatures ranging from 700°C to 900°C. The microstructural changes of the porous Fe22Cr alloy at 850°C and 900°C were assessed via synchrotron tomography measurements described in [DK2].

The experimental validation of the proposed model was shown in [DK3] where the long-term exposure to temperatures from 600°C to 900°C was performed for three selected chemical compositions: Fe20Cr, Fe22Cr, and Fe27Cr.

The typical value of solid oxide cell lifespan is ~40 000 h. Therefore, the lifespan of the porous alloys at high temperatures has to be extended for ceramic element

\*notation used for papers listed in Section 3

replacement. As it has been proven that altering the grain and grain boundary diffusion fluxes of Cr species within the chromia scale can improve the corrosion resistance of dense alloys, the second hypothesis is postulated:

**2) It is possible to extend the lifespan of porous ferritic chromia-forming alloys operating at high temperatures by performing an initial pre-oxidation process.**

The influence of the pre-oxidation process (performed at 850°C and 900°C) on the corrosion properties of the porous Fe22Cr alloy was investigated [DK4]. In this work, the possible lifespan extension of the pre-oxidized porous alloys further oxidized at 700°C was studied and compared with samples that were not pre-oxidized.

Based on the results presented in [DK4], porous Fe22Cr to dense Crofer 22 APU joints were fabricated in the conditions that correspond with the beneficial effect of the pre-oxidation process on the porous alloy lifespan. This structure is comparable to the sealing system of MS-SOCs. The comprehensive study of the MS-SOC sealing system that consists of the pre-oxidized porous Fe22Cr alloy is presented in [DK5]. The aging tests of the as-fabricated system were performed at 700°C which is an operating temperature of IT-SOCs.

### 3. List of publications included in the dissertation

The chapter presents scientific publications that are part of the doctoral dissertation. Each of the attached articles is preceded by a summary of the work, including a justification for undertaking a given research problem and a short description of the obtained results. Then, the original version of the article published in the journal and a description presenting the author's independent contribution to the publication are attached.

The publications that consist of this dissertation:

[DK1] D. Koszelow, M. Makowska, F. Marone, J. Karczewski, P. Jasinski, S. Molin

**High temperature corrosion evaluation and lifetime prediction of porous Fe22Cr stainless steel in air in temperature range 700–900 °C**

Corrosion Science 189 (2021) <https://doi.org/10.1016/j.corsci.2021.109589>.

[DK2] D. Koszelow, S. Molin, J. Karczewski, F. Marone, M. Makowska

**Morphology changes in Fe-Cr porous alloys upon high-temperature oxidation quantified by X-ray tomographic microscopy**

Materials & Design 215 (2022) <https://doi.org/10.1016/j.matdes.2022.110492>.

[DK3] D. Koszelow, M. Makowska, A. Drewniak, G. Cempura, P. Jasiński, S. Molin

**High-temperature corrosion of ~ 30 Pct porous FeCr stainless steels in air: long-term evaluation up to breakaway**

Metallurgical and Materials Transactions A (2023)

<https://doi.org/10.1007/s11661-023-07005-z>.

[DK4] D. Koszelow, M. Makowska, F. Marone, G. Cempura, M. Tomas, J. Froitzheim, S. Molin

**Pre-Oxidation of Porous Ferritic Fe22cr Alloys for Lifespan Extension at High Temperature**

Corrosion Science (2024)

[DK5] F. D'Isanto, M. Salvo, S. Molin, D. Koszelow, H. Javed, S. Akram, A. Chrysanthou, F. Smeacetto

**Glass-ceramic joining of Fe22Cr porous alloy to Crofer22APU: interfacial issues and mechanical properties**

Ceramics International 48 (2022)

<https://doi.org/10.1016/j.ceramint.2022.06.166>.

## 4. Experimental techniques and analysis methods

In this section the experimental techniques and analysis methods which were used throughout the thesis work are presented. Those activities include the investigation of the porous alloy before oxidation tests, sample preparation, high-temperature oxidation measurements and post-mortem analysis.

### 4.1. Porous alloy characterization

Porous Fe22Cr ferritic alloy sheets were supplied by Hoganas AB, Sweden. A size of each sheet was  $\sim 10 \text{ cm} \times 10 \text{ cm}$ , and its thickness was  $\sim 0.35 \text{ mm}$ . The chemical composition provided by the producer is presented in Table. 1.

Table. 1. The composition of the porous Fe22Cr alloy provided by the producer.

Element	Fe	Cr	Mn	Mo	Cu	Si	Ni	C	Nb
wt. %	Bal.	22	0.23	0.01	0.02	0.08	0.03	0.01	0.02

The produced declared 30 % porosity of the alloy. In order to validate it, the Archimedes liquid displacement measurement was applied with kerosene as the medium. To calculate the porosity, the following expression was used:

$$P = \left( \frac{\rho_{teo}(m_s - m_m) - \rho_k m_d}{(m_s - m_m)\rho_{teo}} \right) * 100 \%, \quad (4.1)$$

where  $P$  is the porosity of the sample,  $\rho_{teo}$  is its theoretical density,  $\rho_k$  is the density of kerosene,  $m_s$  is the mass of soaked sample,  $m_m$  is the mass of merged sample, and  $m_d$  is mass of dry sample.

Another technique that was used in order to determine the sample's porosity was analysis of SEM images. This method as well as EDX analysis of the chemical composition will be described in Section 4.3.2.



Figure 18. A balance prepared for Archimedes liquid displacement measurements.

The porous alloy sheet was cut into  $\sim 1$  cm edge squares, as presented in Figure 19. In order to avoid a higher oxidation rate at the edges (due to higher microstructural defects concentration), as-prepared samples were diligently polished using P800 abrasive silicon carbide (SiC) paper (median diameter of SiC grit equal to  $21.8 \mu\text{m}$ ). Then, the samples were cleaned in isopropanol followed by ethanol using ultrasonic bath. The time of cleaning in each solvent was  $\sim 5$  min. As-prepared samples were dried for  $\sim 15$  min at  $80^\circ\text{C}$  to remove any residual liquid from the pores.

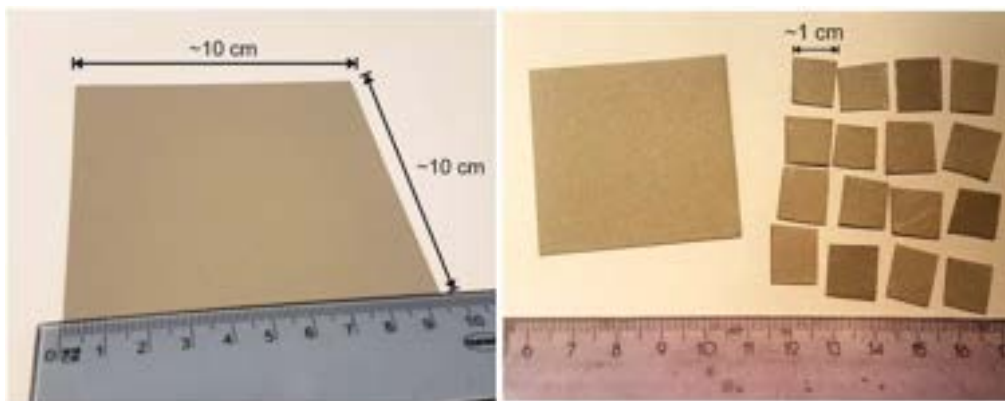


Figure 19. Fe22Cr alloy sheet (left) and set of samples obtained by cutting the 1 cm edge squares (right).

## 4.2. Oxidation tests

The oxidation tests can be performed in two ways: isothermal or cyclic. The isothermal oxidation is the continuous weight gain measurement with time, typically

performed in a thermogravimetric machine. The starting point of the measurement is typically established as the time of reaching a desired temperature at which the test is performed. In isothermal oxidation process the airflow (or other gas) is applied to provide uniform heat distribution in the system.

In the short-term (up to 100 h) exposure tests the isothermal oxidation was performed for the Fe22Cr samples at temperature ranging from 700°C to 900°C [85]. The heating and cooling rate were 3°C/min and the airflow was 30 ml/min. For the oxidation test performed at 900°C the time of the experiment was shortened to 40 h due to instability of microbalance.

The cyclic oxidation test is the type of exposure that is performed in a furnace. In contrast to the isothermal oxidation, there are several heating and cooling process in the cyclic oxidation measurements. The time of heating and cooling is typically not included in the final time of exposure. The cyclic oxidation measurements are usually applied for long-term exposures, so the heating and cooling time can be neglected as a relatively short time when compared with total exposure time. The most important advantage of cyclic oxidation test is a possibility of simultaneous exposure performed for set of samples at one process providing a statistical data from the experiment. However, a disadvantage of the cyclic oxidation is possible change of sample position in the furnace that may occur when sample is put out for the weight measurement, resulting in slightly different temperature of oxidation in next exposure stage.

Due to slightly different exposure conditions, i.e. gas flow rate, the results of isothermal oxidation and cyclic oxidation tests cannot be directly compared to each other.

The cyclic oxidation was applied to investigate long-term oxidation resistance of porous Fe20Cr, Fe22Cr, and Fe27Cr alloys and for the synchrotron tomography measurements. Finally, the effect of pre-oxidation process as well as glass-ceramics joints exposure were also performed in as the cyclic processes. All the cyclic exposures were performed with heating and cooling rate of 3°C/min.

The weight gains obtained via both isothermal and cyclic oxidation processes were plotted as a function of time. Moreover, based on the SSA information (from the tomography measurements described in Section 3.4.4) the weight gain results were also plotted as relative weight change, with respect to the initial surface area. It allowed for determining the kinetics of the oxidation process and  $k_p$  calculations. Then the

activation energy of the high-temperature oxidation for porous alloys was assessed from the Arrhenius dependence.

### **4.3. Post-mortem analysis**

In order to evaluate the morphological as well as phase compositional changes, the post-mortem analysis that includes XRD, imaging via SEM and TEM, synchrotron microtomography, and chromium evaporation measurements was performed.

#### **4.3.1. XRD measurements**

The investigation of phase composition of samples before and after oxidation was carried out using X-ray diffractometry (XRD) with a Bruker D2 Phaser equipped with an XE-T detector. The XRD measurements were performed using a Cu anode ( $K\alpha = 1.5405 \text{ \AA}$ ), with a  $2\theta$  range of  $10 - 90^\circ$ . The step size was  $0.02^\circ$ , and each step took 1 second to complete.

#### **4.3.2. SEM/EDX imaging**

Scanning electron microscopy (SEM) imaging was performed using the Phenom XL (Thermo Fisher Scientific, Netherlands) instrument for observation of sample surfaces and polished cross-sections. All scanning electron microscope (SEM) measurements have been carried out using a backscattered electron detector (BSE). The elemental maps of the materials were obtained using energy-dispersive X-ray (EDX) spectroscopy with an integrated analyzer (Thermo Fisher Scientific, 25 mm<sup>2</sup> Silicon Drift Detector).

In order to assess the porosity of the investigated samples before and after oxidation tests, the PoroMetric Software (Thermo Fischer Scientific) was employed. A set of 20 images taken at 2000 x magnification were analyzed. The images were binarized based on their histograms to distinguish pores from alloy and oxide scale phases. The resulted porosity was calculated as the mean value of percentage area assigned to pores for 20 images and the measurement uncertainty was determined as a standard deviation of these values.



#### **4.3.3. TEM imaging**

The samples for the TEM investigations were prepared as lamellae obtained by sputtering the sample surface with Ga<sup>+</sup> ions emitted from a liquid metal ion source (FIB). A thin Pt layer was deposited on the region of interest to minimize the curtain effect while thinning the sample with the ion beam. The lamellae were finished with thinning down to a level of several dozen nanometers after being mounted in a TEM-dedicated copper grid.

The TEM/STEM analyses were performed using a Cs probe-corrected Titan Cubed G2 60-300 microscope (FEI) equipped with the ChemiSTEM™ system. High-resolution STEM (HRSTEM) images were acquired using a high-angle annular dark-field (HAADF) detector.

TEM/STEM analyses were performed in cooperation with Grzegorz Cempura from the Centre of Electron Microscopy for Materials Science at AGH University of Krakow.

#### **4.3.4. Synchrotron tomography analysis**

X-ray tomographic microscopy offers a comprehensive understanding of the three-dimensional structure, whereas SEM is restricted to two-dimensional pictures. Electron microscopy, unlike  $\mu$ CT method, has the ability to resolve features of dimensions that are smaller than its spatial resolution. Thus, the synchrotron tomography analysis was performed for samples before and after oxidation process as a complementary technique to SEM imaging.

X-ray tomographic microscopy characterization of samples was performed by Federica Marone and Małgorzata Makowska at the TOMCAT beamline of the Swiss Light Source (SLS) at the Paul Scherrer Institute, Villigen, Switzerland. The detector configuration included a scintillator that converted X-rays into visible light, an objective lens, and a sCMOS camera with settings that produced a field of view (FOV) of around 0.8 mm × 0.8 mm and an image pixel size of 0.325  $\mu$ m. A total of 1001 projections over 180° were recorded, each with 1600 ms exposure, resulting in scans lasting about 26 min.

The reconstruction of the acquired tomograms was performed using the in-house developed pipeline at the beamline that provides complete tomographic volumes immediately after data acquisition. It allows for quick adjustment of measurement and reconstruction algorithm parameters. The obtained projections were tomographically

reconstructed after dark- and flat-field correction and phase retrieval (according to the Paganin method [86]). Signal-to-noise and contrast-to-noise ratios were improved with the use of phase retrieval. Material segmentation was rendered with the commercial software Avizo 9.4 by the author of this thesis during his internship at the Paul Scherrer Institute. The phases were discerned basing on the contrast achieved in the reconstructed images generated by this method. The intensity ranges assigned to the alloy, porosity, and oxide scale were determined based on the histogram minima for one of the samples with a significant degree of oxidation. The identical intensity ranges were subsequently applied to the measured tomograms for phase segmentation.

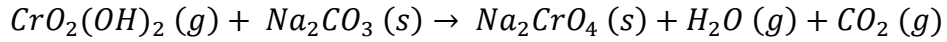
The detailed morphology changes analysis of porous Fe<sub>22</sub>Cr alloy before and after oxidation process allows for distinguishing the objects of ~1  $\mu\text{m}$  size in the reconstructed volume. Therefore, 1  $\mu\text{m}$  was further considered as a spatial resolution of the analyzed images. On the other hand, data from the experiment that revealed the pre-oxidation effect on the porous alloy microstructural changes allows to detect the oxide scale of thickness about 1.5  $\mu\text{m}$  (due to the presence of air blower near the investigated samples).

In addition to assessing the grain size distribution, the Avizo software was utilized to carry out alloy grain separation and evaluate the oxide scale thickness distribution. Furthermore, an exhaustive porosity analysis was performed, enabling the estimation of oxidation-induced alterations in the mean pore channel cross-section, open, closed, and total porosity. By localizing and analyzing the exact same region in the measured volumes of both oxidized and unoxidized states of the samples, it was feasible to directly compare and observe microstructural changes between the two states.

#### **4.3.5. Chromium evaporation**

Cr vaporization is a significant issue in terms of the longevity of the fuel cell stack because of poisoning process. The poisoning is the oxygen electrode degradation throughout the Cr volatiles that react with oxygen (or moisture) and form Cr-containing vapor species like  $\text{CrO}_3$  or  $\text{CrO}_2(\text{OH})_2$ . These compounds can move in the cathode and deteriorate its performance [87]. Therefore, it is necessary to quantify the rate of Cr evaporation of metallic interconnector material at the high-temperature oxidation conditions.

Cr vaporization was measured for the samples using the denuder technique. The measurements were carried out in horizontal tube furnaces using an air-flow of 6 000 sl·min<sup>-1</sup> for up to 500 h. A flow restrictor made of porous SiC was positioned 10 mm upstream of the samples to reduce spontaneous convection. The gas passed through the silica glass denuder tube with an inner diameter of 6 mm after the samples. The inside of the denuder tube had been coated with Na<sub>2</sub>CO<sub>3</sub>, which interacted with the volatile Cr (VI) and formed Na<sub>2</sub>CrO<sub>4</sub>:



The denuder tubes were periodically replaced and cleaned with pure water. The Cr content of the solution was measured using a spectrophotometer Genesys 10UV, Thermo Scientific. A schema of the experimental configuration, encompassing the denuder tube and a reactor containing a sample is presented in Figure 20. At least two sets of three samples were exposed, and Cr (VI) evaporation measurements were performed at regular intervals.

Chromium evaporation measurements were performed in cooperation with professor Jan Froitzheim and doctor Matthieu Tomas at Chalmers University of Technology in Sweden.

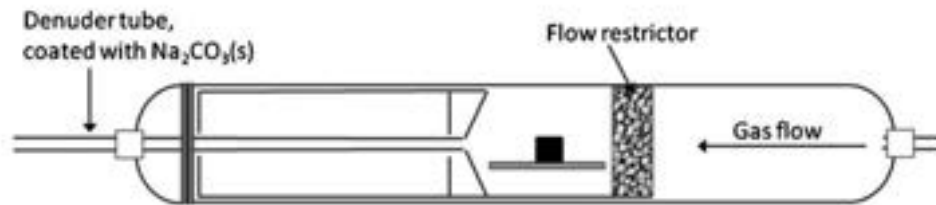


Figure 20. Diagram of the experimental setup featuring the reactor containing a sample and the denuder tube [88].

#### 4.4. Glass-ceramics joints

As the glass-ceramics are widely used as sealants in SOCs, one of the challenging issues is matching the desired properties of metallic interconnector with the joining material. Based on state-of-the-art knowledge in the context of glass-ceramics joints applied in bulk metallic systems, the Si-based sealant was chosen for the Fe22Cr porous alloy to Crofer 22 APU joints investigation. The chemical composition of the selected glass-ceramic is presented in Table. 2.

Table. 2. Glass-ceramic composition.

Molar %	SiO <sub>2</sub>	B <sub>2</sub> O <sub>3</sub>	Al <sub>2</sub> O <sub>3</sub>	CaO	BaO
GC2	55	8	4	7	26

The fabrication of glass-ceramics joints as well as the post-mortem analysis was performed by the author of this thesis during his 3-month internship (granted by Polish National Agency for Academic Exchange) at Politecnico di Torino in Italy in cooperation with scientific group of professor Federico Smeacetto.

#### 4.4.1. Glass and glass-ceramic preparation

In order to cast the glass, the precursors: SiO<sub>2</sub>, B<sub>2</sub>O<sub>3</sub>, Al<sub>2</sub>O<sub>3</sub>, CaCO<sub>3</sub>, and Ba<sub>2</sub>CO<sub>3</sub> were weighted and mixed for 24 h. Then, as-prepared powder was melted in a Pt-Rh crucible in a furnace (LHT418PN2, Nabertherm GmbH, Lilienthal/Bremen, Germany) in air at 1500°C for 1 h. After 30 min of the sintering, the crucible lid was removed from the furnace. The melt was cast onto a brass plate and the glass was obtained. The glass was ball-milled and sieved (particle size < 38 µm).

In order to determine the thermo-mechanical properties of the glass-ceramic that can be fabricated from the as-obtained glass powder the Hot Stage Microscopy (HSM) and dilatometry measurements were performed.

The HSM imaging was performed using Hesse Heating Microscope (Germany) with a heating rate of 5 °C/min starting from the room temperature. The measurement lasts up to reaching a melting temperature that is recognized by the instrument based on the specimen's shape change. The HSM tests were performed using both alumina and porous Fe22Cr alloy as a substrate. Then, based on the shrinkage-temperature curve the temperatures can be determined: first shrinkage (T<sub>fs</sub>), temperature of maximum shrinkage (T<sub>ms</sub>), first softening temperature (DT), sphere temperature (ST), half-sphere temperature (HT) and flow temperature (FT).

The dilatometric tests of the as-cast glass and glass-ceramic (obtained by sintering of glass at 950°C for 1 h) were performed using Netzsch, DIL 402 PC dilatometer in order to calculate the CTE of these materials. The glass and glass-ceramic that was used in the dilatometric tests was obtained by uniaxial pressing of 12 MPa. The heating rate of 5°C/min was applied. An alumina sample holder provided constant compressive force of 0.25 N between the specimen and the piston during the measurement. The

desired value of CTE is between  $10.0 \times 10^{-6} \text{ K}^{-1}$  and  $12.0 \times 10^{-6} \text{ K}^{-1}$  because of matching thermos-mechanical properties of sealant with other SOC components.

A small amount of a slurry consisting of glass powder (30 wt. %) and ethanol (70 wt. %) was applied manually between the two metal alloys (squared specimens -11 mm  $\times$  11 mm). The first experiments performed with various configurations determined that the most efficient joint consisted of pre-oxidized (at 900°C for 2h with a 5°C/min heating and cooling rate) dense Crofer22APU attached on top. The joining procedure was conducted for one hour at 950 °C in air using a muffle furnace (L5/13/P330, Nabertherm GmbH, Lilienthal/Bremen, Germany) with a heating/cooling rate of 5 °C/min. A weight made of stainless steel was positioned on top of the sandwich structure during the thermal treatment in order to exert an approximate pressure of 1.5 kPa.

A Computed Tomography (CT) scan was conducted using a Fraunhofer IKTS machine in Hermsdorf, Germany. The scan provided morphological and qualitative density information of the sample. The settings utilized were 9.25  $\mu\text{m}$  resolution, 280 kV acceleration voltage, and 1s exposure time for each projection. The joint reconstruction involves generating a three-dimensional model of the scanned volume using CT software.

#### **4.4.2. Oxidation tests and post-mortem analysis**

As-prepared joints were oxidized at 700°C for 500 h in a muffle furnace (Carbolite Gero, Hope Valley, UK). The heating and cooling rate was 5°C/min.

In order to evaluate morphological changes of the joints the samples before and after oxidation tests were investigated using SEM technique. SEM imaging was performed using a field-emission scanning electron microscope (FESEM; SupraTM 40, Zeiss, Oberkochen, Germany) equipped with an energy dispersive X-ray analyzer (EDS, Bruker, Germany). Before the imaging the samples were polished using SiC papers (grit size from 600 to 4000) and coated with Cr layer in order to provide the sufficient electrical conductivity.

The phase composition of the fracture surface of joints samples (Crofer 22APU side) after oxidation tests was investigated using X'Pert Pro MRD diffractometer, with Cu K $\alpha$  radiation (PANalytical X'Pert Pro, Philips, Almelo, The Netherlands). The phases were

identified using the JCPDS database provided by PDF-4 ICDD (International Centre for Diffraction Data, Newton Square, Pennsylvania, the USA).

The mechanical properties of the joints were determined for samples before and after oxidation tests via tensile strength measurements. The procedure of the test was modified from the ASTM C633-01 standard. The experiments were conducted using Syntech 10/D machine (MTS Systems Corporation, Minnesota, USA). The joints were attached to two loading fixtures using Araldite® 2015 epoxy resin and then thermally treated at 85 °C for 1 hour to crosslink. The cross-head speed was adjusted to 0.5 mm/min. The tensile strength was determined by dividing the greatest force by the area of the joint, which was 11 mm × 11 mm.

## 5. Overview of the relevant publications

### 5.1. High temperature corrosion evaluation and lifetime prediction of porous Fe22Cr stainless steel in air in temperature range 700°C-900°C

In this work, short-term isothermal oxidation tests of porous chromia-forming Fe22Cr alloys were performed. Based on as-obtained data the kinetics of the high-temperature oxidation process was determined. It was proven that the weight gain curves follow the parabolic law of corrosion and the  $k_p$  value is comparable to the  $k_p$  value of bulk chromia-forming alloys with similar chemical composition. Moreover, the activation energy of the high-temperature oxidation was determined to be ~2.7 eV which is also comparable to the results of bulk alloys like Crofer 22 APU or Crofer 22 H.

A lifespan prediction model for the porous ferritic chromia-forming alloys was proposed. The threshold weight gain level (6 wt. %) that determines the breakaway corrosion formation was assessed based on the change of slope in relative weight gain curve for sample oxidized at 900°C. This threshold value was recalculated in order to connect the breakaway corrosion formation with Cr reservoir within the alloy particles. Finally, the threshold band (between 10 wt. % and 12 wt. % of Cr content within the alloy) was determined. The lifespan of the porous Fe22Cr alloy obtained via the proposed model application were 3000 h, 400 h, and 150 h, for samples oxidized at 700°C, 750°C, and 800°C, respectively.

My original contribution in this work was:

- Determining the high-temperature corrosion kinetics of ferritic chromia-forming porous alloys
- Developing the high-temperature corrosion model for porous alloys based on the short-term oxidation experiments
- Defining the boundary conditions of the proposed model

Statement of the co-authors' contribution to the publication entitled 'High temperature corrosion evaluation and lifetime prediction of porous Fe22Cr stainless steel in air in temperature range 700–900 °C':

Name and surname	Contribution to the publication	Signature
Damian Koszelow	Conceptualization, Methodology, Formal Analysis, Investigation, Writing – Original Draft	
Małgorzata Makowska	Investigation – synchrotron tomography analysis, Writing – Review & Editing	
Federica Marone	Investigation – synchrotron tomography analysis, Writing – Review & Editing	
Jakub Karczewski	Investigation – SEM imaging	
Piotr Jasiński	Supervision, Resources	
Sebastian Molin	Conceptualization, Supervision, Project administration, Funding acquisition, Writing – Review & Editing	





# High temperature corrosion evaluation and lifetime prediction of porous Fe22Cr stainless steel in air in temperature range 700–900 °C

D. Koszelow<sup>a,\*</sup>, M. Makowska<sup>b</sup>, F. Marone<sup>b</sup>, J. Karczewski<sup>c</sup>, P. Jasiński<sup>a</sup>, S. Molin<sup>a</sup>

<sup>a</sup> Advanced Materials Centre, Faculty of Electronics, Telecommunications and Informatics, Gdańsk University of Technology, 80-233, Gdańsk, Poland

<sup>b</sup> Photon Science Division, Paul Scherrer Institut, Forschungsstrasse 111, 5232, Villigen, Switzerland

<sup>c</sup> Advanced Materials Centre, Faculty of Applied Physics and Mathematics, Gdańsk University of Technology, 80-233, Gdańsk, Poland

## ARTICLE INFO

### Keywords:

Stainless steel  
High temperature corrosion  
SEM  
X-ray diffraction

## ABSTRACT

This work describes a high temperature corrosion kinetics study of ~30 % porous Fe22Cr alloys. The surface area of the alloy (~0.02 m<sup>2</sup> g<sup>-1</sup>) has been determined by tomographic microscopy. The weight gain of the alloys was studied by isothermal thermogravimetry in the air for 100 h at 700–900 °C. Breakaway oxidation was observed after oxidation at 850 °C (~100 h) and 900 °C (~30 h). The lifetime prediction shows the investigated porous alloy can be used for >3000 h at temperatures <700 °C. At temperatures ≥700 °C, the lifetime of the porous alloy is limited by the available chromium reservoir.

## 1. Introduction

High temperature reactors and devices such as supercritical reactors, superheaters, turbines, and engines [1] rely on advanced alloys. For these applications, the most important properties of metallic alloys are their relatively low cost (in comparison to advanced ceramics), manufacturability, and the possibility to form complex shapes. In addition, high intrinsic electronic and heat conductivities can be beneficial for specific applications. For example, interconnects for high temperature (>600 °C) fuel cells require high electronic conductivity for efficient current collection and high heat conductivity to decrease thermal gradients. Ferritic stainless steels (FSSs), which are based on Fe and Cr, are the most common and cost-effective engineering alloys, being used in many room temperature and elevated temperature components (e.g. 430 alloy) [2]. For these reasons, the FSSs have been used as replacements for expensive and difficult to manufacture ceramic interconnects of the fuel cells [3–5]. To form a continuous chromia scale, the alloy should contain at least 10.5 wt.% Cr. Alloys with high chromium content (20–24 wt.%, e.g. Crofer 22 APU, Sanergy) have been designed to offer long term stable operation of the interconnects. Further increase of Cr content above ~26 wt.% is not beneficial, as it leads to a brittle sigma phase formation at high temperatures.

The drawback of using alloys at high temperatures in oxidising as well as in reducing (e.g. in H<sub>2</sub>/H<sub>2</sub>O) conditions is the unavoidable formation of metal oxide scales [6,7]. The most popular ferritic steels

belong to the group of chromia formers, as they form chromium oxide (Cr<sub>2</sub>O<sub>3</sub>) on their surface [8]. The oxide has a protective function due to slow cation Cr<sup>3+</sup> diffusion in the oxide, protecting the metallic core from rapid oxidation. Chromia has a satisfactory level of electrical conductivity (~1–10 mS cm<sup>-1</sup> at 600–800 °C) [9] for applications requiring electrical current conduction, e.g. sensors, fuel cells, membranes. Silica or alumina forming ferritic alloys are typically less prone to high temperature oxidation, but they have negligible electronic conductivity, resulting in high electrical resistance of the oxide scale [10–13].

High temperature corrosion of alloys in the dense form has been studied for many decades and their properties are well described. More recently, porous metallic alloys became of greater interest as engineering materials for use at high temperatures. Due to open porosity, the porous alloys allow for gas transport, which is an important engineering feature. Porous ferritic stainless steels have been proposed as support structures for high temperature ceramic fuel cells [14–16] and gas separation membranes [17].

The porous structure of the alloy is characterized by a high surface area available for oxidation. The specific alloy powder particle size distribution determines the porosity and surface and thus it has a strong influence on the corrosion behavior of the porous components. The large area of the alloy available for oxidation, on which Cr<sub>2</sub>O<sub>3</sub> will form, can cause relatively fast depletion of Cr from the bulk. Chromium depletion below a specific level will lead to breakaway oxidation. The threshold level of bulk Cr content for maintaining its protective action was

\* Corresponding author.

E-mail address: [damian.koszelow@pg.edu.pl](mailto:damian.koszelow@pg.edu.pl) (D. Koszelow).

<https://doi.org/10.1016/j.corsci.2021.109589>

Received 27 November 2020; Received in revised form 8 February 2021; Accepted 10 May 2021

Available online 27 May 2021

0010-938X/© 2021 The Authors. Published by Elsevier Ltd. This is an open access article under the CC BY license (<http://creativecommons.org/licenses/by/4.0/>).

determined by Huczowski et al. to be  $\sim 12$  wt.% [18,19].

Several studies about the oxidation processes of the porous ferritic steels have been reported [20–26]. The existing studies point to relatively fast corrosion of porous alloys at high temperatures ( $\geq 800$  °C), but the specific effects of the particle size, porosity, and surface area still remain open. The data is very limited in comparison to the number of studies of corrosion of the dense alloys.

The lifetime prediction for protective oxide scale forming alloys has also been already addressed by several authors with respect to different aspects. For example, Tucker et al. have discussed the lifetime as the time required to grow a  $\sim 3$   $\mu\text{m}$  thick oxide scale. Based on the reported corrosion values, the acceptable corrosion rates/temperatures have been mapped out [12]. Geometry-specific lifetime limitations for metallic alloys have been discussed by [18,27,28]. For example, Young et al. have devised a simple expression for lifetime prediction of austenitic (FCC) alloys [28]. Huczowski et al. studied the effects of alloy sheet thickness on their lifetime [18].

This study describes the oxidation behavior of a sintered porous Fe22Cr alloy in the air at temperatures of 700 °C, 750 °C, 800 °C, 850 °C, and 900 °C. After the isothermal exposures, the sample microstructures were analyzed in detail. The results were used to propose a simple approach for the lifetime prediction of the porous alloy.

## 2. Experimental

The porous alloy substrates were obtained from the company: Höganäs AB (experimental product MW2, Höganäs, Sweden). Porous steel sheets were prepared by proprietary tape-casting of steel particle slurry, drying, debinding, and sintering. Before the corrosion exposures, an alloy sheet with dimensions of  $100 \times 100 \times 0.4$  mm<sup>3</sup> was cut into smaller pieces. For continuous thermogravimetric analysis, samples were cut into pieces with approximate dimensions of  $\sim 3 \times 3 \times 0.35$  mm<sup>3</sup>, where 3–4 pieces were placed simultaneously in the crucibles. For tomography, samples were cut into elongated samples with approximate dimensions of  $\sim 6 \times 1 \times 0.35$  mm<sup>3</sup>. Before further use, samples were cleaned in an ultrasonic bath of ethanol followed by acetone.

High-temperature corrosion exposures were performed using a Netzsch TG 209 F3 Tarsus thermobalance. Measurements were carried out in air with a flow rate of 50 mL min<sup>-1</sup>. Used heating and cooling rates were 180 °C h<sup>-1</sup>. An isothermal hold was maintained for 100 h at 700 °C, 750 °C, 800 °C, 850 °C and  $\sim 40$  h at 900 °C (due to instabilities of the thermobalance for long measurements at high temperatures). Results were plotted as relative weight change, with respect to the weight of the samples before the oxidation. The typical initial weight of the samples was  $\sim 200$  mg. The prediction of the alloy lifetime was based on the extrapolation of the weight gain data presented in the double logarithmic plot (which allowed fitting by linear regression). The confidence interval was determined by the prediction band method, assuming a 95 % confidence level.

Post-mortem characterizations were performed on samples prepared by ex-situ oxidation at conditions corresponding to isothermal exposures, i.e. the additional samples were oxidised continuously for 100 h at 700 °C, 750 °C, 800 °C, 850 °C, and 900 °C in parallel to thermogravimetric measurements. The characterization methods included scanning electron microscopy (SEM) evaluation using a Phenom XL (Thermo Fisher Scientific, Netherlands) instrument for observation of sample surfaces and polished cross-sections. A backscattered electron detector (BSE) was used for all SEM measurements. The qualitative elemental maps of the investigated samples were determined via energy-dispersive X-ray (EDX) spectroscopy using an integrated analyzer (Thermo Fisher Scientific, 25 mm<sup>2</sup> Silicon Drift Detector). Maps of Cr and Mn were made based on Cr K and Mn L lines. EDX “spot” analyses of the chemical composition, were performed by scanning a small area (maximum  $\sim 5 \times 5$   $\mu\text{m}^2$ ) to improve signal. The error bars of the EDX (in the case of chromium content data) were calculated as the standard deviation of the mean of 15 measurements carried out in different regions for each

sample. Phase analysis was performed by X-ray diffractometry (XRD) using a Bruker D2 Phaser with an XE-T detector. XRD measurements were done using Cu anode ( $K\alpha = 1.5405$  Å), with  $2\theta$  range 10 – 90° (step 0.02°, integration time 1 step s<sup>-1</sup>). Cross-sections for SEM observations were prepared by embedding the samples in epoxy (EpoFix, Struers) and polishing them down to a 1  $\mu\text{m}$  finish (Struers consumables).

X-ray tomographic microscopy characterization of samples was performed at TOMCAT beamline [29] of the the Swiss Light Source (SLS) at the Paul Scherrer Institute Villigen, Switzerland at the. Tomography scans of a reference (non-oxidised) sample and samples with different degrees of oxidation were performed using a parallel X-ray beam with energy of 40 keV. The detector setup consisted of a scintillator converting X-rays into visible light, an objective lens, and a sCMOS camera with settings providing a field of view (FOV) of about 0.8 mm x 0.8 mm with an image pixel size of 0.325  $\mu\text{m}$ . 1001 projections over 180° were acquired with 1600 ms exposure time each, resulting in about 26 min scans.

The tomographic reconstruction pipeline [30] developed at the Tomcat group delivers full tomographic volumes immediately after data acquisition completion, which allows for prompt optimization of measurement and reconstruction algorithm parameters. The used reconstruction algorithm allows for partial phase retrieval according to the Paganin algorithm [31], which improves signal-to-noise and contrast-to-noise ratios. Reconstructed 3D volumes were analyzed using the commercial software Avizo 9.4 [32]. The information about sample porosity (open, closed, and total) and surface area was retrieved.

The porosity of porous alloys has also been determined experimentally by Archimedes principle (liquid displacement) and by image analysis. For image analysis, 20 pictures taken at a magnification of 2000x were analyzed using Phenom PoroMetricSoftware.

## 3. Results and discussion

### 3.1. Characterisation of the raw porous alloy

The surface morphology and cross-sectional microstructure of the “raw” sintered porous alloy are shown in Fig. 1A, B. The porous steel substrates used for the experiments were manufactured by Höganäs AB for potential application as support structures for high temperature fuel cells [33]. The main role of the relatively thick support is to provide mechanical strength for the much thinner (10–20x) ceramic layers and to enable good gas access to the electrodes. The presented porous metal sheet has a thickness of  $\sim 400$   $\mu\text{m}$ , similar to the ceramic/cermet supports used in traditional solid oxide cells [3]. The alloy particles used for the tape preparation were the -53 powder fraction (used sieve with 53  $\mu\text{m}$  opening), resulting in particle sizes in the range of 10–50  $\mu\text{m}$ . As seen in Fig. 1B, the particles are well connected and sintering necks between the particles are visible. The porosity of the metal sheet determined by the Archimedes method was  $\sim 30$  % ( $\pm 2$  %), similar to the porosity of porous ceramic/cermet components used in fuel cells. Image analysis of the cross-section SEM image revealed a porosity of 31 % ( $\pm 2\%$ ), which is in agreement with the Archimedes method.

The alloy is a ferritic (BCC crystallographic structure) stainless steel. As given by the alloy producer, the alloy contains  $\sim 22$  wt.% of Cr, 0.23 wt.% Mn and 0.08 wt.% Si. Other elements include Ni, Cu, and Mo in amounts  $< 0.03$  wt.%. The chemical composition of the alloy, as given by the producer, is presented in Table 1. It is also confirmed by EDX analysis that shows  $\sim 21.3$  wt.% Cr and 0.26 wt.% Mn plus iron as balance. At high temperatures, the metallic core is protected from heavy oxidation by a compact, slowly growing chromium oxide layer. High chromium content ( $\sim 22.0$  wt.%) should lead to an increased lifetime of the alloy due to an increased Cr reservoir available for the formation of the oxide scale. The addition of Mn can lead to the formation of the external Mn-Cr oxide spinel, which results in lower Cr evaporation [34, 35]. Similar alloys, produced by Höganäs AB were used in other studies [24,25,33]. The alloy composition is quite similar to the state-of-the-art

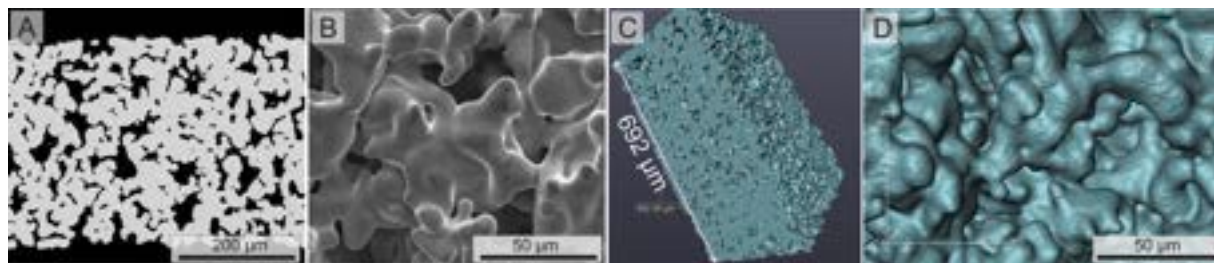


Fig. 1. SEM images of A) alloy cross section, B) surface and C, D) surface of the as-produced alloy generated from the tomographic reconstruction.

Table 1

Chemical composition of the alloy.

Target composition	Fe	Analyzed chemical composition, %										
		Cr	Ni	Mo	Mn	Cu	Si	Nb	C	O	N	S
Fe22Cr	Bal.	22.0	0.03	0.01	0.23	0.02	0.08	0.02	0.04	0.58	0.07	0.01

high temperature fuel cell alloys: Crofer 22 APU/H (VDM Metals, Germany) or Sanergy (Sandvik, Sweden).

To describe the complex microstructure of the non-oxidised porous alloys in more detail, tomographic microscopy was performed. The 3D microstructure of the alloy reconstructed from the series of projections is presented in Fig. 1C–D. Comparing Fig. 1B and D, the surface morphology obtained from tomography seems well reconstructed and is similar to that obtained via SEM. The porosity of the reference sample, obtained by the Avizo software is  $\sim 32.2\%$  and consists almost purely of open pores, which is in good agreement with the Archimedes-method and SEM measurements ( $\sim 30\%$ ). In the addition to porosity, the tomography allows for a calculation of the specific surface area, which is critical for the full assessment of corrosion properties at high temperatures. The specific surface area value obtained for the studied alloy was determined to be  $0.022 \text{ m}^2 \text{ g}^{-1}$ . The values can be compared with the available literature data. For example, Brandner has reported detailed processing of porous FeCr alloys in his PhD report [36]. He has obtained the surface area of  $\sim 0.02 \text{ m}^2 \text{ g}^{-1}$  for raw powders (gas atomized, SF 20–53\_B2 – particle fraction 20–53  $\mu\text{m}$ ) used for sintering of porous alloys and a surface area of  $0.007 \text{ m}^2 \text{ g}^{-1}$  for the  $\sim 18\%$  porous sintered product (sintering at  $1250^\circ\text{C}$  for 3 h). Increasing the sintering temperature to  $1350^\circ\text{C}$  led to a decrease of porosity to  $\sim 4\%$  and surface area to a level of  $\sim 0.001 \text{ m}^2 \text{ g}^{-1}$ . In our work, the powders have been produced by a water atomization process (as evidenced by the irregular shape of the particles), which results in lower green density, thus higher resulting porosity and surface area after sintering. Stefan et al. have studied a porous FeCr alloy from the same producer, Höganäs AB. The authors analyzed the surface area by nitrogen absorption (BET) and reported a value of  $\sim 0.017 \text{ m}^2 \text{ g}^{-1}$ , in line with our work [25]. Due to the relatively small amount of alloy availability, it was not possible to determine the BET area for our alloy. Rose et al. have also pointed out difficulties in determining the surface area of porous 430 alloys with the BET technique [37]. Due to the relatively low surface area of the porous alloys, the area determination is not simple due to the small amount of the adsorbed gas. In contrast to BET, tomography can be used on relatively small samples with good reproducibility, but its availability is much smaller and the data requires tedious post-processing.

In general, information about the specific surface area of the alloy is not easily obtainable. For comparison, a similar (chemical composition, thickness) dense alloy has a surface area of  $\sim 8 \text{ cm}^2 \text{ g}^{-1}$ , a factor of  $\sim 28\times$  smaller. This shows a striking difference in the surface area available for

oxide formation on porous alloys.

### 3.2. Corrosion exposures of porous alloys

The as-produced alloys were subjected to isothermal oxidation exposures in the air at temperatures of  $700^\circ\text{C}$ ,  $750^\circ\text{C}$ ,  $800^\circ\text{C}$ ,  $850^\circ\text{C}$ , and  $900^\circ\text{C}$ . Weight gain measurement results are shown in Fig. 2. The weight gain is shown as a relative weight gain (with respect to the initial sample weight) as well as is recalculated for the surface area, using the specific surface value determined by tomography. As the determination of the specific surface area (SSA) of porous alloys is troublesome, many research works only report the relative weight gain (% change). This data is, however, only relevant to the specific microstructure and a comparison between different publications, working with different materials is not possible quantitatively. Only a few works report surface specific weight gain data for porous alloys, which also makes it possible to compare the obtained oxidation kinetics data with the data available from oxidation of dense alloys.

The results presented in Fig. 2 show that the exposure temperature has a strong effect on the oxidation kinetics. Oxidation at  $900^\circ\text{C}$  progresses very fast. After only  $\sim 25$  h the slope of the weight gain curve changed (Fig. 2A), the oxidation process accelerated, whereby suggesting that a breakaway oxidation process started. Sample oxidised ex-situ at  $900^\circ\text{C}$  for 100 h showed a weight gain of  $\sim 43\%$ , which corresponds to oxidation of all Fe and Cr. For the oxidation at  $850^\circ\text{C}$ , the weight gain is initially following a parabolic-type (weight gain  $\sim$  square root of time) curve, which after  $\sim 40$  h seems to become linear. The weight gain curves obtained at  $800^\circ\text{C}$ ,  $750^\circ\text{C}$  and  $700^\circ\text{C}$  seem to follow the parabolic rate law. The weight gain at  $700^\circ\text{C}$  after 100 h of oxidation is the only  $1/10^{\text{th}}$  of the weight gain obtained at  $800^\circ\text{C}$ .

In order to determine the oxidation mechanism in more detail, Fig. 2B shows a double logarithmic plot (log-log plot) of the weight gain as a function of time. For the diffusion limited corrosion kinetics, the slope of the log-log plot should be 0.5. The rate determining factor, in this case, is typically outward cation diffusion. Our data shows good agreement throughout the measured time range. For all temperatures, the slopes are similar, confirming that the parabolic rate law  $\left(\frac{\Delta m}{A}\right)^2 = k_p \cdot t$ , where A is surface of the sample,  $\Delta m$  is a change of sample's mass,  $k_p$  is the parabolic rate constant and t is a time of oxidation) can be used for the description of corrosion kinetics.

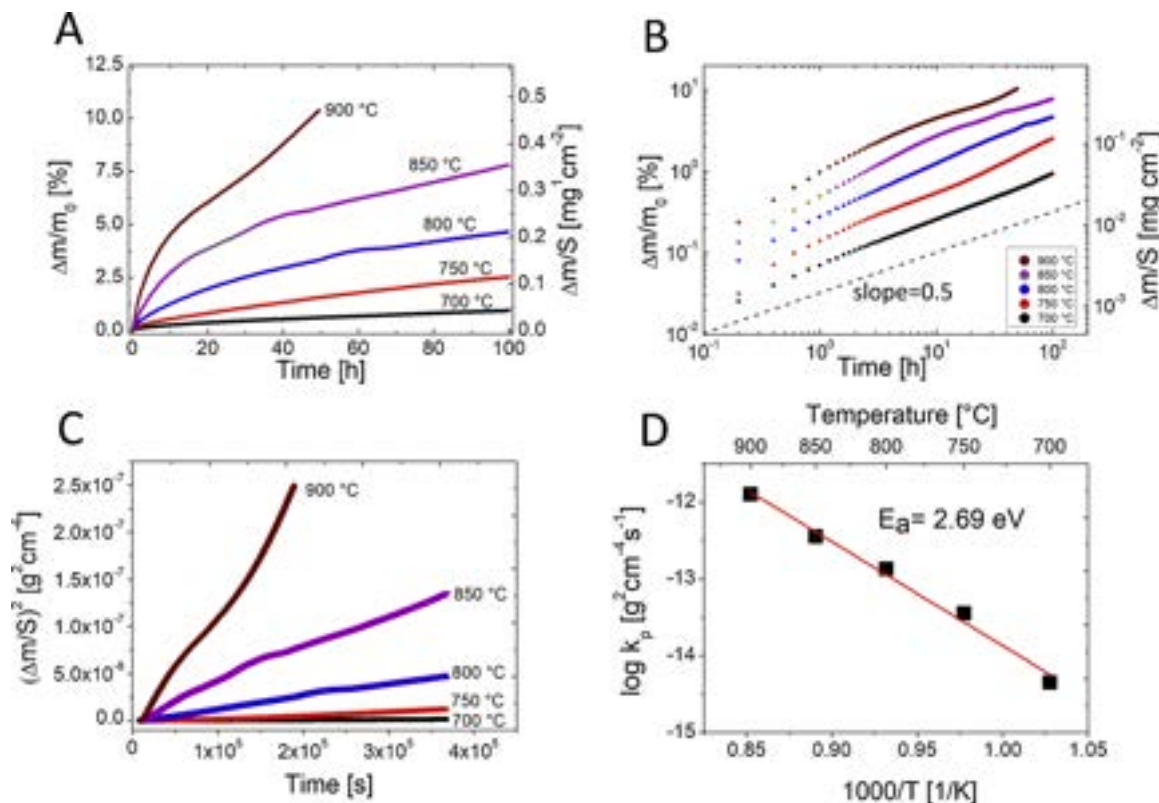


Fig. 2. Weight gain data presented as A) linear weight change, B) log-log plot, C) square weight change with respect to the initial surface area and D) Arrhenius plot.

Table 2  
Corrosion parameters after oxidation at different temperatures.

Temperature °C	Weight gain @ 100 h		Corrosion rate – $k_p$ g <sup>2</sup> cm <sup>-4</sup> s <sup>-1</sup>	$k_p$ temp / $k_p$ 700 °C	Activation energy eV
	%	mg cm <sup>-2</sup>			
900 (40 h)	10.4	0.50	$1.3 \times 10^{-12}$	289	2.69
850	7.80	0.37	$3.7 \times 10^{-13}$	82	
800	4.65	0.22	$1.3 \times 10^{-13}$	28	
750	2.52	0.11	$3.6 \times 10^{-14}$	8	
700	0.94	0.04	$4.5 \times 10^{-15}$	1	

Based on the assumption of the parabolic rate law, Fig. 2C shows parabolic weight gain plots (per surface area) for the alloys. The calculated corrosion rates ( $k_p$  values - slopes of the curves) are presented in Table 2. For comparison, for the FeCr porous alloy studied by Stefan et al., the  $k_p$  values of  $8 \times 10^{-15}$  g<sup>2</sup> cm<sup>-4</sup> s<sup>-1</sup> at 700 °C and  $1 \times 10^{-12}$  g<sup>2</sup> cm<sup>-4</sup> s<sup>-1</sup> at 800 °C were obtained [25]. The values are typical, as reported for chromia forming ferritic stainless steels [2]. The obtained values can be compared with a porous Al-forming alloy. In the case of FeCrAlY porous alloy (with comparable particle size) studied by Glasscock et al., the corrosion rate obtained at 850 °C was  $\sim 4 \times 10^{-16}$  g<sup>2</sup> cm<sup>-4</sup> s<sup>-1</sup>. The corrosion rate of the Al-former is thus  $\sim 3$  orders of magnitude lower than for the Cr-former. Unfortunately, the former cannot be used in applications where electronic conduction of the support is required. In other applications, like in oxygen transport membranes (OTM), alumina forming alloys have a clear advantage. For comparison with the results reported for dense alloys, Gavrilov et al. determined the parabolic rate constant for the Crofer 22 APU to be  $5.6 \times 10^{-14}$  g<sup>2</sup> cm<sup>-4</sup> s<sup>-1</sup> after 100 h oxidation at 800 °C [38]. Skilbred et al. calculated this parameter for Sandvik Sanergy HT at 800 °C as  $5.4 \times 10^{-14}$  g<sup>2</sup> cm<sup>-4</sup> s<sup>-1</sup> [39]. For Crofer 22 H alloy, the values are  $4.5 \times 10^{-16}$ ,  $1.1 \times 10^{-14}$  and  $3.3 \times 10^{-13}$  g<sup>2</sup> cm<sup>-4</sup> s<sup>-1</sup> for 650, 750 and 850 °C, respectively [40].

Overall the weight gain and corrosion kinetics  $k_p$  values obtained for the porous alloys in our work are in good agreement with the available corrosion data for chromia forming alloys. Due to minor compositional differences (e.g. Cr content, reactive elements, etc.), some variation of  $k_p$  values between different alloys is possible [41].

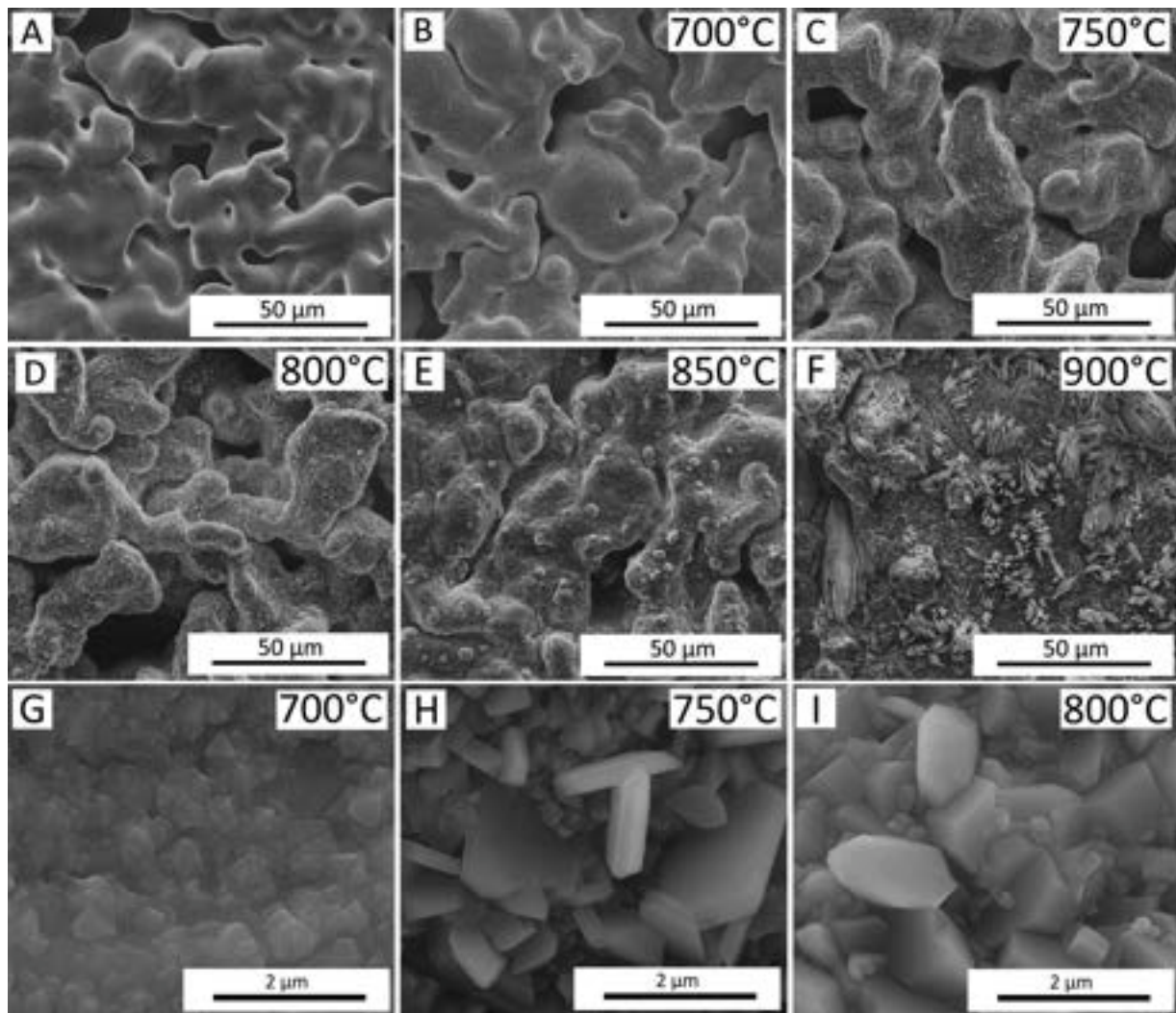
The calculated corrosion rate values were used to determine the activation energy of the oxidation process. The plot of  $k_p$  vs the inverse of the temperature is presented in Fig. 2D. The points follow a line with the activation energy of  $\sim 2.7$  eV. As cited by Palcut et al., the activation energy of Cr diffusion in Cr<sub>2</sub>O<sub>3</sub> is  $\sim 2.9$  eV (280 kJ mol<sup>-1</sup>) [42], therefore the obtained value corresponds well with the assumed Cr diffusion oxidation rate limitation.

For dense alloys, Palcut et al. has obtained an activation energy of  $\sim 2.5$  eV for Crofer 22 APU alloy [43], and for a similar Sanergy alloy, Skilbred et al. calculated an activation energy of 2.82 eV [39]. In general, the obtained value corresponds well with the expected one.

### 3.3. Post-mortem analysis of porous alloys

SEM images of the surfaces of the alloys oxidised for 100 h at 700 °C, 750 °C, 800 °C, 850 °C, and 900 °C are presented in Fig. 3A–I.

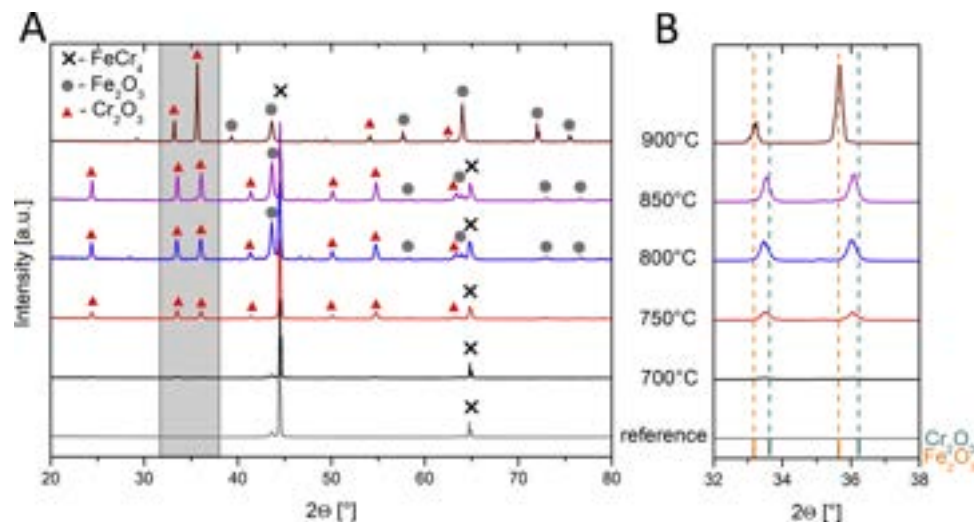




**Fig. 3.** SEM surface of samples A) non-oxidised; oxidised for 100 h at B, G) 700 °C, C, H) 750 °C, D, I) 800 °C, E) 850 °C and F) 900 °C.

The surface of the alloy oxidised at 700 °C shows, at low magnification, only slight changes in comparison to the not-oxidised alloy. The higher magnification shown in Fig. 3G reveals the formation of small (<1 μm), densely packed crystallites on the surface. The alloys oxidised at 750 °C

and 800 °C show a clear change of the surface, which becomes rougher, but still, no large changes of the alloy microstructure are observed, i.e. pores are clearly visible. Higher magnification images (Fig. 3H and I) show the growth of larger crystallites. Especially at 750 °C, the platelet



**Fig. 4.** XRD patterns of the reference and oxidised alloys: A) full range scan 20–80°, B) magnification of the 32–38° range.

shape of the larger crystals growing from a layer of smaller crystals is visible. At 800 °C, the crystallites grow further. Severe microstructure change occurred for the alloy oxidised at 850 °C and 900 °C. High temperature leads to a porosity decrease. In the case of the alloy oxidised at 900 °C, a dense surface is visible. The alloy was completely oxidised, with no features of the initial porous alloy remaining.

The oxidation temperature thus has an effect not only on the amount of the oxide (as determined by the weight gain) but also on the crystallite's morphology. Oxide scales with different crystallite sizes can have an effect on cation diffusion since the relative amount of grains and grain boundaries will be altered.

Surface morphological studies were followed by phase analysis using XRD. The measured diffraction patterns, for samples oxidised at 700 °C, 750 °C, 800 °C, 850 °C, and 900 °C for 100 h are presented in Fig. 4A–B. A reference pattern of the non-oxidised steel has also been included (CrFe4, ICDD PDF number 65-4664).

The alloy oxidised at 700 °C for 100 h shows only a minor peak at the position of the main peak of the Cr<sub>2</sub>O<sub>3</sub> phase (ICDD PDF number 38-1479), visible in Fig. 4B. For the alloy oxidised at 750 °C for 100 h,

new phases clearly formed, however the main alloy peak at ~45° is the most intense.

The oxide peaks can be matched well to the Cr<sub>2</sub>O<sub>3</sub> and possibly to Fe<sub>2</sub>O<sub>3</sub> (ICDD PDF number 33-664) phases, which have similar structures and diffractograms. Peaks are shifted, most likely due to iron doping of the oxide phase or due to experimental conditions (sample displacement). For the samples oxidised at 800 °C (and higher) shifting of the peaks towards the Fe<sub>2</sub>O<sub>3</sub> reference, the position could be observed. The sample oxidised at 900 °C shows only peaks from the oxide phase, whereby the metallic substrate is not detectable anymore.

The enlargement of the main oxide peak area, presented in Fig. 4B, shows good agreement of the oxide position with the Fe<sub>2</sub>O<sub>3</sub> peaks for the sample oxidised at 900 °C. For the other temperatures, there seems to be a mixed (Fe,Cr)<sub>2</sub>O<sub>3</sub> oxide.

Due to the small Mn content in the alloy (~0.2 wt.%), possibly also Mn,Cr spinel could form, but its presence was not detected in this study.

SEM images of cross-sections of samples oxidised at 700 °C, 750 °C, and 800 °C are presented in Fig. 5A–F. The low-magnification images (Fig. 5A, B, C) show a lack of changes in the overall microstructure. The

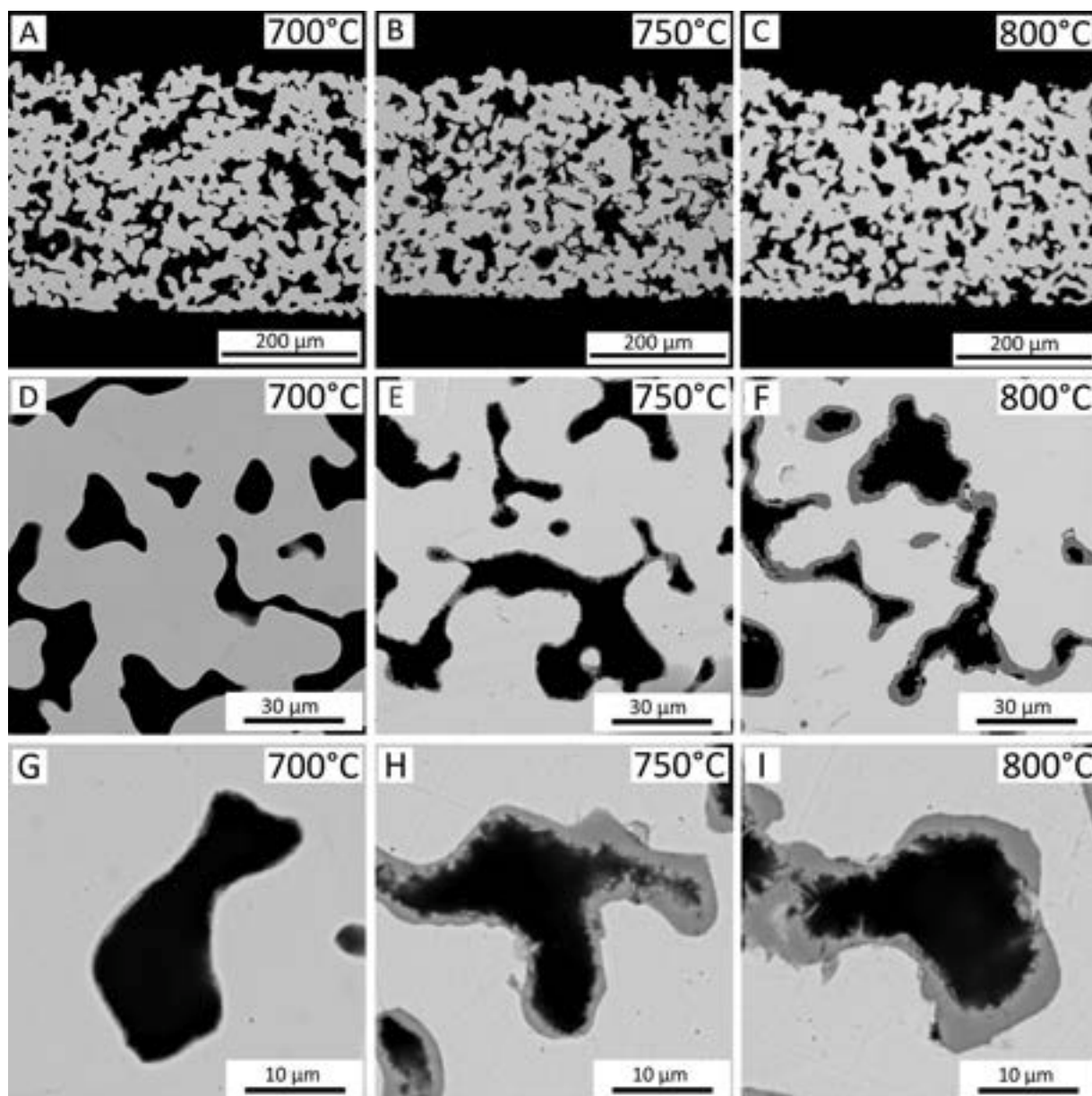
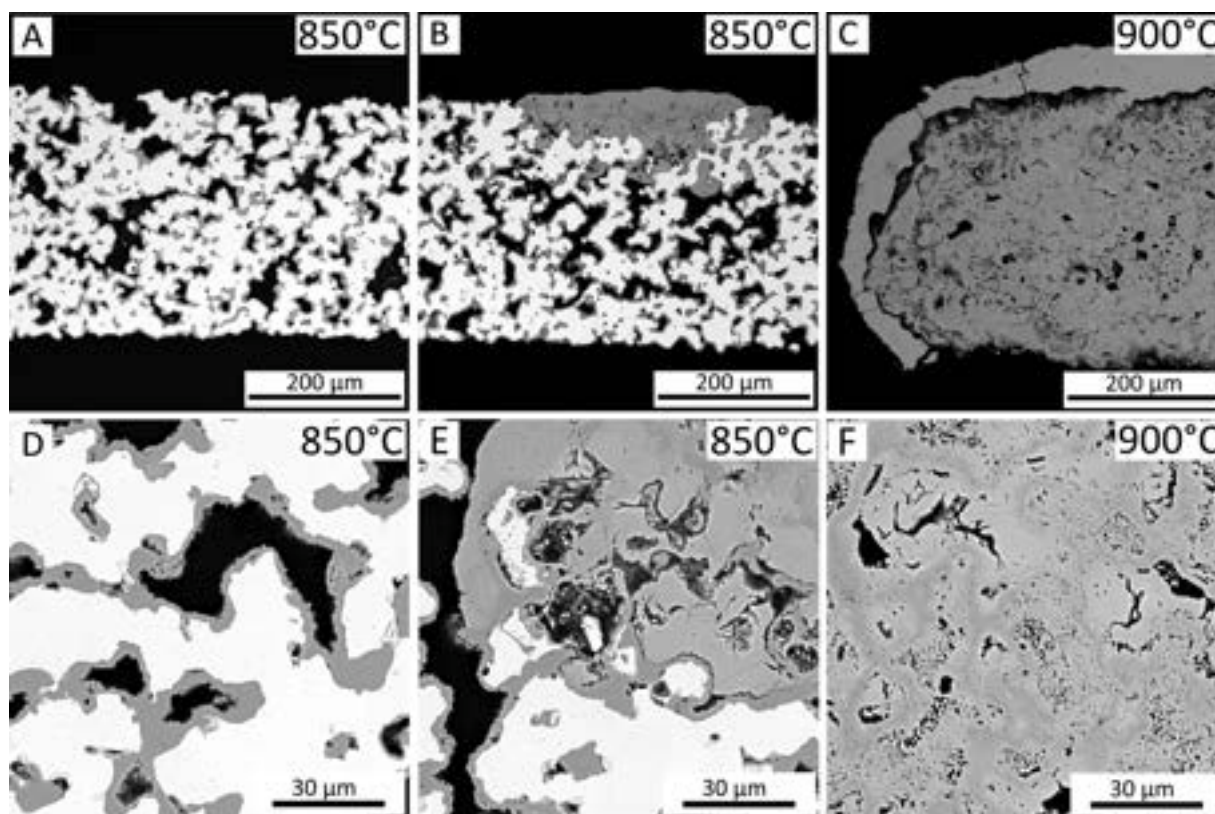


Fig. 5. SEM cross-section images of the alloy oxidised for 100 h at A,D,G) 700 °C, B,E,H) 750 °C, C,F,I) 800 °C.



**Fig. 6.** SEM cross-section images of the alloy oxidised for 100 h at A, D) 850 °C in place without breakaway corrosion, B, E) 850 °C for 100 h in a place with breakaway corrosion and C, F) 900 °C for 100 h.

sample oxidised at 700 °C for 100 h, with the relative weight gain of  $\sim 1\%$  ( $\sim 0.05 \text{ mg cm}^{-2}$ ), shows no visible change in comparison to the not-aged sample (Fig. 1). Even at higher magnification (Fig. 5D and G), the formation of the oxide scale is hardly visible. For a sample oxidised at 750 °C, with a weight gain of  $\sim 2.5\%$  ( $\sim 0.11 \text{ mg cm}^{-2}$ ), the thin layer of oxide is noticeable at lower magnifications (Fig. 5B and E). At higher magnification (Fig. 5H), a small amount of oxide is clearly visible, but it does not block the pores. The sample oxidised at 800 °C, with a weight gain of  $\sim 5\%$  ( $\sim 0.21 \text{ mg cm}^{-2}$ ), when observed at the lowest magnification (Fig. 5C) shows hardly visible oxide that formed within the pores, whereas when observed at higher magnifications (Fig. 5F and I), the oxide becomes easily visible on the surface of grains. A continuous oxide layer covers uniformly the whole surface, with a thickness of 2–3  $\mu\text{m}$ . The pores decrease in size due to oxide scale growth filling the available space.

The cross-section images of samples oxidised at 850 °C and 900 °C for 100 h are presented in Fig. 6A–F. Most of the sample oxidised at 850 °C (Fig. 6A), characterised by a  $\sim 7.5\%$  weight gain ( $\sim 0.35 \text{ mg cm}^{-2}$ ), did not show signs of breakaway oxidation. Excessive oxidation could be obtained, however, in at least one place along the studied cross-section (Fig. 6B). As seen in the higher magnification image (Fig. 6D), the oxidation at 850 °C leads to formation of the clearly visible oxide scale. The oxide fills the pores to a measurable extent and starts filling the small pores (necks) between the grains. The oxide scale covers the surface well, no scale detachment, delamination or cracking is visible. The breakaway spot is formed near the surface/edge of the sample. The heavily oxidised region extends  $\sim 200 \mu\text{m}$  in width and penetrates up to  $\sim 100 \mu\text{m}$  in depth. The rapid oxidation of Fe can explain the observed

linear weight gain curve (Fig. 2A), but due to the relatively small extent (very limited number of spots) of the breakaway corrosion, it did not dominate the overall weight gain trend.

The sample that was exposed to 900 °C for 100 h, with a weight gain of  $\sim 43\%$  ( $\sim 2 \text{ mg cm}^{-2}$ ), shows only the oxide phase, no metallic particles could be found in SEM images. The sample shows a relatively dense microstructure, with a very dense shell around the sample core.

To determine the chemical composition of the oxide scale and the breakaway region, the EDX analysis was performed for the cross-section of the sample oxidised at 850 °C for 100 h. Two regions were analyzed: one where no breakaway oxidation was found (Fig. 7A) and a second one, with a visible breakaway corrosion spot (Fig. 7B).

The oxide scale is composed of Cr and O, which supplemented by the XRD results suggest formation of a pure  $\text{Cr}_2\text{O}_3$  scale. Due to the presence of a minor amount of Mn in the alloy ( $\sim 0.2 \text{ wt.}\%$ ), the potential formation of an  $(\text{Mn,Cr})_3\text{O}_4$  spinel could be expected. However, even though a thorough analysis was performed, it did not show the formation of the spinel phase. As seen in Fig. 7A, the Mn signal (qualitative) is mostly concentrated inside the grains, so this seems to be an artefact coming from EDX fitting. Additional higher magnification analyses (not shown here) did not reveal any signs of Mn-rich oxide on top of chromia. The amount of Mn in the studied alloy is lower than in Crofer 22 APU (Mn  $\sim 0.4 \text{ wt.}\%$ ) which might be crucial in forming a continuous spinel scale.

The breakaway spot, presented in Fig. 7B, shows high iron, chromium, and oxygen content (Table 3). Region 1, representing the alloy composition after oxidation, shows a Cr content of  $\sim 10 \text{ at.}\%$  with the remaining Fe. The alloy core has been thus heavily depleted from the



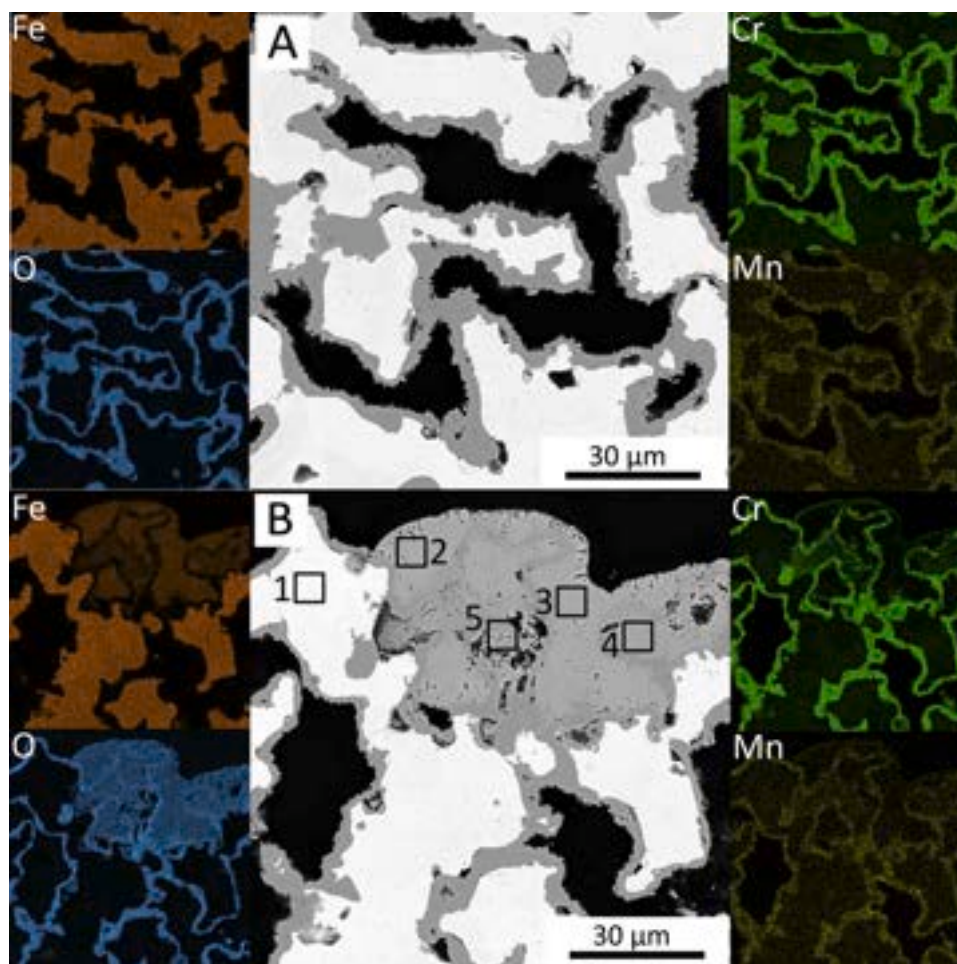


Fig. 7. EDX analysis(qualitative maps) of sample oxidised at 850 °C for 100 h. A) place without breakaway corrosion, B) place with breakaway corrosion.

**Table 3**

Chemical composition of regions marked in Fig. 7 B(obtained from EDX measurements).

Region	Fe at. %	Cr at. %	Mn at. %	O at. %
1	90.3	9.7	<0.1	–
2	34.5	1.7	<0.1	63.8
3	33.5	2.5	<0.1	63.9
4	28.0	7.1	–	64.9
5	20.7	13.9	0.2	65.2

initial ~21 wt.% of Cr content. Region 2, inside the breakaway zone, is mainly composed of iron (~34 at.%) with low Cr content (< 2at.%) with oxygen as balance. A similar composition is obtained for regions 3 and 4. Region 5 shows both high concentrations of iron, chromium, and oxygen. Analysing the breakaway region of the elemental map presented in Fig. 7B, it seems that Cr is mainly contained in a layer, that initially covered the steel grains. At some point, the Cr depleted grains started to oxidise, forming iron rich oxides. The chromia layer remained relatively stable and thus its structure is retained within the formed oxide.

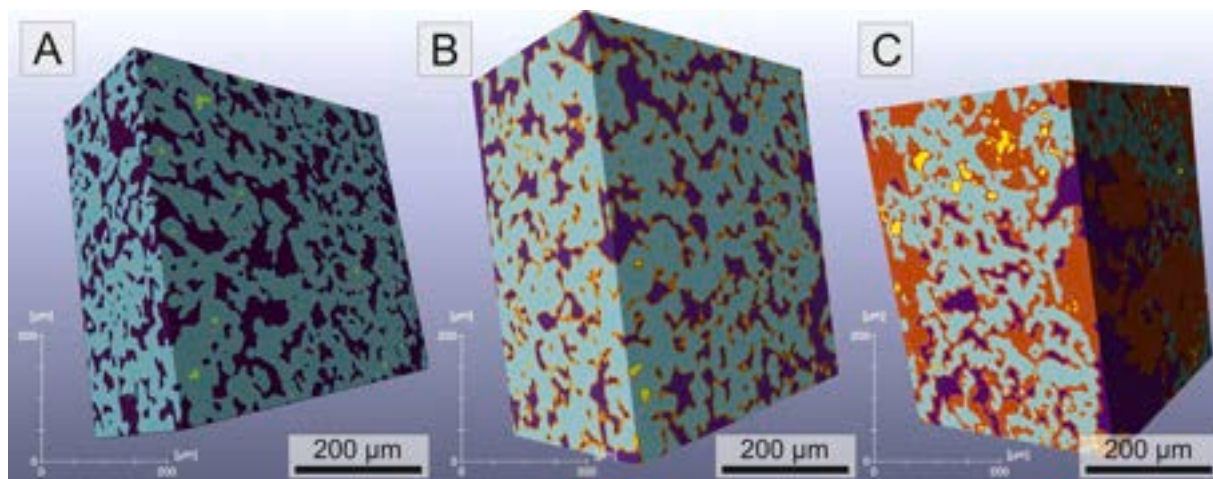
The breakaway corrosion originated near to the external surface of the porous alloy and only in a few spots. For the particles near the external surface of the alloy, the incoming flux of the Cr will be limited spatially, so the formation of breakaway corrosion closer to the surface than to the middle can be rationalised. Another considered possibility is Cr evaporation from the external surface, whereas in the internal surfaces the atmosphere would get saturated faster. Similarly, the differences in water and oxygen availability for places near the surface of the

alloy might also affect breakaway corrosion appearance in these regions.

In addition to SEM microscopy, tomographic studies of selected samples (not-oxidised, oxidised at 800 °C for 100 h and 900 °C for 30 h) were performed. Fig. 8 presents results of material segmentation of the reconstructed volumes showing the distribution of different phases. For the oxidised samples, it was possible to distinguish between the metallic core, the oxide, and the porosity phases. To the best of our knowledge, it is the first time such observations were made. Obtaining high contrast between the materials considered in this paper and high spatial resolution using X-rays with energy sufficient for penetration of this type of samples (about 1 mm steel) remains a challenge. The thin oxide layer can be resolved using synchrotron radiation, thanks to its high brilliance and partial coherence. Therefore, it was possible to obtain sufficient contrast between the oxide layer and the metallic phase as well as submicron spatial resolution. The differentiation of the phases can be used to quantitatively measure the extent of corrosion based on 3D microstructure, enhancing the information obtained by SEM.

For the sample oxidised at 800 °C for 100 h (weight gain of ~4.65 %), the oxide is observed uniformly covering the steel particles, no breakaway corrosion was found within the investigated volume, in-line with SEM observations. For the sample oxidised at 900 °C for 30 h (weight gain of ~7%), the oxide forms several breakaway spots. Based on the images, the volume of the three phases can be calculated. The data is presented in Table 4. Based on the results, it is visible that upon the oxidation, the metallic phase transforms into the oxide phase at the expense of porosity. For the sample oxidised at 800 °C for 100 h, the steel volume decreased from the initial ~68 % to 63 %, the open porosity decreased from the initial ~32 % to ~21 % and the oxide phase





**Fig. 8.** Phase segmentation based on synchrotron tomography of samples: A) before oxidation, B) oxidised for 100 h at 800 °C and C) oxidised for 30 h at 900 °C (turquoise – steel, orange-oxide, purple – open pores, green- closed pores).

**Table 4**

Summary of the phase composition of selected samples evaluated based on tomography data.

Temperature	Time	Figure	Steel vol%	Oxide vol%	Open porosity vol%	Closed porosity vol%
–	–	Fig. 8 A	67.7	–	32.2	0.1
800 °C	100 h	Fig. 8 B	62.8	16.6	20.5	0.1
900 °C	30 h	Fig. 8 C	46.3	41.0	11.3	1.4

contributes with  $\sim 17\%$  of the total volume. Based on the densities of the steel ( $7.7 \text{ g cm}^{-3}$ ) and the oxide (chromia density of  $5.22 \text{ g cm}^{-3}$ ), the measured decrease of the steel phase corresponds theoretically to  $\sim 16\%$  oxide volume, which agrees well with the value determined by the tomography.

For the sample oxidised at 900 °C for 30 h, the oxide phase constitutes 41 % of the total volume, with the remaining low porosity of  $\sim 11\%$ .

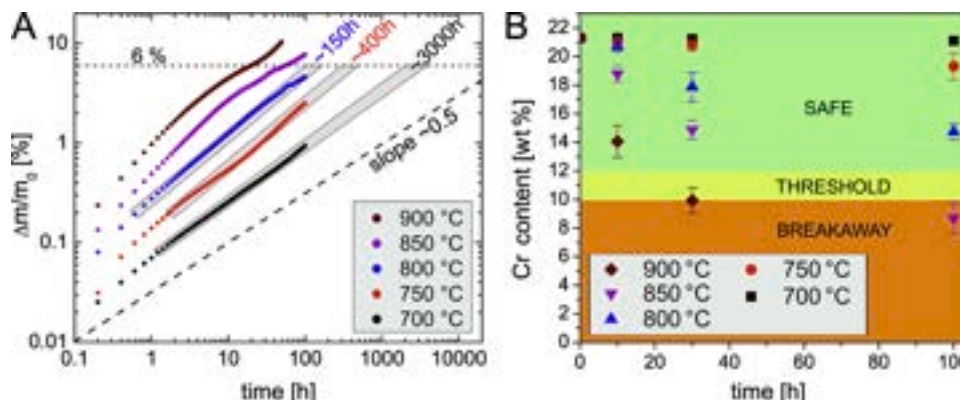
As seen in Figs. 7B and 8 C, the breakaway corrosion of porous alloys leads to large microstructural changes of the alloys and is limiting their applications. For the specific alloy used in this study, it occurs within times as short as  $\sim 100$  h at 850 °C and even shorter at higher temperatures. It would be beneficial to develop models, predicting the lifetime of porous alloys so that their use within the safe limits would be possible.

### 3.4. Lifetime prediction of porous alloys

Based on the obtained oxidation kinetics results, a rough lifetime prediction can be made. The prediction is relevant to the specific alloy (in terms of its microstructure and chemical composition), but the methodology can be used for other alloys as well. The advantage of the method is its relative simplicity, but on the other hand, it requires assuming some critical weight gain limit, at which the start of breakaway corrosion is supposed to.

The method presented here is only an approximation of complex oxidation phenomena and should be treated as a simplified methodology only. The prediction is based on the extrapolation of the weight gain data, presented in Fig. 2B. Based on the weight gain curves and microscopic/tomographic observations, it can be assumed that the breakaway oxidation starts at a weight gain of  $\sim 6\%$ . For the alloy oxidised at 800 °C the weight gain reached  $\sim 5\%$  after 100 h and no breakaway oxidation was found in the SEM post-mortem analyses. For the sample oxidised at 850 °C, the weight gain after 100 h reached 7.5 % and the breakaway corrosion already started. For the oxidation at 900 °C, a change of weight gain slope can be observed at  $\sim 6\%$ . Therefore this weight gain value has been selected as a potential start of the breakaway corrosion.

The log-log weight gain plot can be used to extrapolate the linear curves to reach the weight gain limit of  $\sim 6\%$ , which would be the lifetime limit – time before the breakaway oxidation can be expected (Fig. 9A). The data for 900 °C and 850 °C seems to fit within the proposed model. For the lower temperatures, the predicted lifetimes are  $136 \pm 20$  h for 800 °C,  $395 \pm 50$  h for 750 °C and  $2916 \pm 170$  h for 700 °C



**Fig. 9.** A) Log-log extrapolation of weight gain and B) chromium content in the alloy determined by EDX.

°C. The predicted lifetimes seem quite low. For high temperature fuel cells, the desired lifetimes of the stacks are within the 10000–40000 hours range (for mobile and stationary systems, respectively). Therefore it seems that the porous alloys with the presented chemical composition and microstructure should be operated at temperatures lower than 700 °C. Alternatively, specially tailored protective coatings could be developed.

The measured weight gain is due to oxygen pick up, which can be calculated into Cr consumption. A rough estimation yields a value of ~13 wt.% Cr consumed (corresponding to 9 wt.% Cr remaining in the bulk). This estimation is in good agreement with the EDX analysis of the oxidised alloy, which was 9.7 % (region 1 in Fig. 7B). The Cr content in the alloys after different stages of oxidation was analysed by EDX and the results are plotted in Fig. 9B. The figure has been color-coded into three regions – based on the obtained results the operation of the porous alloy is safe (green area) down to ~12 wt.% Cr content below which some smaller particles can be oxidised heavily. For a Cr content <10 wt.%, most of the alloy will be heavily oxidised (orange area).

The obtained lifetime predictions are roughly in-line with some of the literature reports. The discussion of the applicability of the proposed lifetime prediction based on the available literature data is hard due to differences in porous metal morphology and compositions. Moreover, there is yet not much data about oxidation of porous alloys.

Huczkowski et al. have studied the oxidation of flat Crofer 22 APU alloys with different thicknesses [18]. Based on the measured corrosion rates, the lifetime of Crofer 22 APU at 800 °C was ~8000 h for 100 µm sample thickness. Extrapolated to a thickness of 50 µm, the lifetime would be only ~3000 h. The planar, 2D geometry makes a large difference from the spherical grain geometry. Chyrkin et al. have studied the oxidation and lifetime of Inconel 625 (austenitic alloy) foams with different particle sizes. For the foams made with small particles (~10 µm), oxidation lifetimes as low as ~100 h at 900 °C were obtained experimentally and used to validate the model. By increasing the particle size to ~30 µm, the lifetime could be increased to 400–500 h. The model predicts that a temperature decrease to 700 °C can lead to a lifetime above 10000 h.

Shen et al. have performed long term durability tests of metal-supported solid oxide electrolysis cells. In their design, the cell has porous metal sheets on both sides (hydrogen/steam and air/oxygen). The employed steel is based on a 434 composition, which has 16–18 wt.% Cr. The authors performed ~1000 h long aging test. The authors did not observe breakaway oxidation within the studied period. The oxide scale thickness has been determined to be ~2 µm for the air side and ~1 µm for the hydrogen side. Brandner has reported in his PhD thesis, oxidation results of ~18 % porous Crofer 22 APU sheets [36]. The experiments were carried out in air at 800 °C. The surface specific weight gain after 1000 h was ~0.5 mg cm<sup>-2</sup>. Based on his observations, the lifetime of such alloy has been predicted to be between 200–500 h –relatively short for possible practical application. Schiller et al. have presented a ~2400 h long test for a porous metal-supported electrolysis cell carried out at 800 °C [44]. The porous metal substrate was based on Plansee ITM alloy (Fe based, ~26 wt.% Cr, with the addition of ~1 wt.% Y<sub>2</sub>O<sub>3</sub>). The porous metal support did not undergo breakaway oxidation within the test time, which seems to survive much longer than our simple prediction. Though the microstructure and composition of the alloy were quite similar to that studied here, the support was exposed to a reducing atmosphere (hydrogen/steam). Exposures in reducing atmospheres result in lower corrosion rates than in air, which seems especially visible in the case of porous alloys [25,45]. Also, the addition of even a small amount of Y<sub>2</sub>O<sub>3</sub> might play a major role in extending the alloy lifetime in harsh conditions [46].

Due to the complex geometry of the porous alloys and foams, their oxidation limited lifetime is much shorter than for dense alloys. To fully develop a reliable lifetime model for porous alloys, more long-term, controlled condition exposure studies are needed, also including samples with different microstructures.

Lifetime prediction is a complex problem, depending heavily on the potential failure mode, alloy composition, and microstructure. In the present work, results indicate that the lifetime was limited by Cr depletion. Failure due to oxide detachment due to reaching a critical oxide thickness and stress level cannot be excluded.

#### 4. Conclusions

This work has evaluated short term (~100 h) high temperature corrosion properties of a ~30 % porous Fe22Cr alloy in the temperature range 700 °C – 900 °C. To determine the specific surface area, synchrotron tomographic microscopy was applied. This technique allowed obtaining the surface value (~0.022 m<sup>2</sup> g<sup>-1</sup>) from a relatively small sample. The corrosion results demonstrate that the corrosion rate of porous alloys is similar to corrosion rates of dense alloys, i.e. the complex shape has no visible effect on the underlying corrosion phenomena. The corrosion kinetics is acceptable at 700 °C, whereas at higher temperatures the alloy microstructure changes considerably even after only 100 h of exposure. Oxidation of samples at 850 °C and 900 °C leads to breakaway corrosion and the alloy becomes fully oxidised after 100 h at 900 °C. The tomographic analysis was also performed on oxidised alloys and it allowed for a determination of the relative content of the steel/oxide/pore phases. Using tomography, it is possible to analyse 3D microstructures of the alloys quantitatively, which strongly supplements the weight gain and microscopic analyses. 3D visualization achieved from tomographic microscopy gives also a better insight into the amount distribution of breakaway spots as compared with 2D imaging.

Based on the obtained experimental results, a methodology for lifetime prediction has been proposed. Based on the experimentally derived critical oxidation level (weight gain of ~6%), a double logarithmic plot was used to extrapolate the data from lower temperatures. The predicted lifetime at 700 °C is ~3000 h, which is relatively short. The results show that there is a need for longer term studies, which will be the focus of our future work.

#### CRedit authorship contribution statement

**D. Koszelow:** Investigation, Methodology, Data curation, Visualization, Writing - original draft. **M. Makowska:** Writing - review & editing, Formal analysis, Validation. **F. Marone:** Writing - review & editing, Software, Validation. **J. Karczewski:** Validation, Data curation. **P. Jasiński:** Methodology, Resources, Supervision. **S. Molin:** Conceptualization, Methodology, Writing - original draft, Supervision, Funding acquisition.

#### Declaration of Competing Interest

The authors report no declarations of interest.

#### Acknowledgments

This project was supported by National Science Centre Poland (NCN) Sonata Bis 8 project number 2018/30/E/ST8/00821 “High-temperature corrosion studies and development of oxidation lifetime model of alloy powders and sintered porous alloys: effects of composition and microstructure”.

The authors would like to acknowledge Höganäs AB, Sweden for porous steel samples production and the Paul Scherrer Institut, Villigen, Switzerland for granting beamtime (proposal 20181598) at the TOMCAT beamline of the Swiss Light Source.

## References

- [1] D.J. Young, *High Temperature Oxidation and Corrosion of Metals*, Elsevier, 2008.
- [2] M.C. Tucker, Progress in metal-supported solid oxide fuel cells: a review, *J. Power Sources* 195 (2010) 4570–4582, <https://doi.org/10.1016/j.jpowsour.2010.02.035>.
- [3] S. Linderöth, Solid oxide cell R&D at Risø National Laboratory—and its transfer to technology, *J. Electroceram.* 22 (2009) 61–66, <https://doi.org/10.1007/s10832-008-9458-6>.
- [4] M.C. Tucker, G.Y. Lau, C.P. Jacobson, L.C. DeJonghe, S.J. Visco, Stability and robustness of metal-supported SOFCs, *J. Power Sources* 175 (2008) 447–451, <https://doi.org/10.1016/j.jpowsour.2007.09.032>.
- [5] M.C. Tucker, Durability of symmetric-structured metal-supported solid oxide fuel cells, *J. Power Sources* 369 (2017) 6–12, <https://doi.org/10.1016/j.jpowsour.2017.09.075>.
- [6] L. Niewolak, D.J. Young, H. Hattendorf, L. Singheiser, W.J. Quadakkers, Mechanisms of oxide scale formation on ferritic interconnect steel in simulated low and high pO<sub>2</sub> service environments of solid oxide fuel cells, *Oxid. Met.* 82 (2014) 123–143, <https://doi.org/10.1007/s11085-014-9481-8>.
- [7] T. Thublaor, S. Chandra-ambhorn, High temperature oxidation and chromium volatilisation of AISI 430 stainless steel coated by Mn-Co and Mn-Co-Cu oxides for SOFC interconnect application, *Corros. Sci.* 174 (2020), 108802, <https://doi.org/10.1016/j.corsci.2020.108802>.
- [8] L.-P. Wang, W. Yang, Z.-B. Ma, J.-H. Zhu, Y.-T. Li, First-principles study of chromium diffusion in the ferritic Fe-Cr alloy, *Comput. Mater. Sci.* 181 (2020), 109733, <https://doi.org/10.1016/j.commatsci.2020.109733>.
- [9] A. Holt, P. Kofstad, Electrical conductivity and defect structure of Cr<sub>2</sub>O<sub>3</sub>. II. Reduced temperatures (<~1000°C), *Solid State Ion.* 69 (1994) 137–143, [https://doi.org/10.1016/0167-2738\(94\)90402-2](https://doi.org/10.1016/0167-2738(94)90402-2).
- [10] R. Wang, Z. Sun, J.-P. Choi, S.N. Basu, J.W. Stevenson, M.C. Tucker, Ferritic stainless steel interconnects for protonic ceramic electrochemical cell stacks: oxidation behavior and protective coatings, *Int. J. Hydrogen Energy* 44 (2019) 25297–25309, <https://doi.org/10.1016/j.ijhydene.2019.08.041>.
- [11] M.A. Hassan, O. Bin Mamat, M. Mehdi, Review: Influence of alloy addition and spinel coatings on Cr-based metallic interconnects of solid oxide fuel cells, *Int. J. Hydrogen Energy* 45 (2020) 25191–25209, <https://doi.org/10.1016/j.ijhydene.2020.06.234>.
- [12] M.C. Tucker, Progress in metal-supported solid oxide electrolysis cells: a review, *Int. J. Hydrogen Energy* 45 (2020) 24203–24218, <https://doi.org/10.1016/j.ijhydene.2020.06.300>.
- [13] A. Persdotter, J. Eklund, J. Liske, T. Jonsson, Beyond breakaway corrosion – influence of chromium, nickel and aluminum on corrosion of iron-based alloys at 600 °C, *Corros. Sci.* 177 (2020), 108961, <https://doi.org/10.1016/j.corsci.2020.108961>.
- [14] B. Timurkutluk, S. Toros, S. Onbilgin, H.G. Korkmaz, Determination of formability characteristics of Crofer 22 APU sheets as interconnector for solid oxide fuel cells, *Int. J. Hydrogen Energy* 43 (2018) 14638–14647, <https://doi.org/10.1016/j.ijhydene.2018.04.243>.
- [15] N.J. Magdefrau, L. Chen, E.Y. Sun, M. Aindow, Effects of alloy heat treatment on oxidation kinetics and scale morphology for Crofer 22 APU, *J. Power Sources* 241 (2013) 756–767, <https://doi.org/10.1016/j.jpowsour.2013.03.181>.
- [16] P. Alnegren, M. Sattari, J. Froitzheim, J.E. Svensson, Degradation of ferritic stainless steels under conditions used for solid oxide fuel cells and electrolyzers at varying oxygen pressures, *Corros. Sci.* 110 (2016) 200–212, <https://doi.org/10.1016/j.corsci.2016.04.030>.
- [17] J.A. Glasscock, L. Mikkelsen, Å.H. Persson, G. Pećanac, J. Malzbender, P. Blennow, F. Bozza, P.V. Hendriksen, Porous Fe<sub>21</sub>Cr<sub>7</sub>Al<sub>1</sub>Mo<sub>0.5</sub>Y metal supports for oxygen transport membranes: thermo-mechanical properties, sintering and corrosion behaviour, *Solid State Ion.* 242 (2013) 33–44, <https://doi.org/10.1016/j.ssi.2013.04.006>.
- [18] P. Huczukowski, V. Shemet, J. Piron-Abellan, L. Singheiser, W.J. Quadakkers, N. Christiansen, Oxidation limited life times of chromia forming ferritic steels, *Mater. Corros.* 55 (2004) 825–830, <https://doi.org/10.1002/maco.200303798>.
- [19] P. Huczukowski, N. Christiansen, V. Shemet, J. Piron-Abellan, L. Singheiser, W. J. Quadakkers, Oxidation induced lifetime limits of chromia forming ferritic interconnector steels, *J. Fuel Cell Sci. Technol.* 1 (2004) 30, <https://doi.org/10.1115/1.1782925>.
- [20] J.A. Glasscock, V. Esposito, S.P.V. Foghmoes, T. Stegk, D. Matuschek, M.W.H. Ley, S. Ramousse, The effect of forming stresses on the sintering of ultra-fine Ce<sub>0.9</sub>Gd<sub>0.1</sub>O<sub>2-δ</sub> powders, *J. Eur. Ceram. Soc.* 33 (2013) 1289–1296, <https://doi.org/10.1016/j.jeurceramsoc.2012.12.015>.
- [21] Y. Matus, L. Dejonghe, C. Jacobson, S. Visco, Metal-supported solid oxide fuel cell membranes for rapid thermal cycling, *Solid State Ion.* 176 (2005) 443–449, <https://doi.org/10.1016/j.ssi.2004.09.056>.
- [22] D.N. Boccaccini, H.L. Frandsen, B.R. Sudireddy, P. Blennow, Å.H. Persson, K. Kwok, P. Vang Hendriksen, Creep behaviour of porous metal supports for solid oxide fuel cells, *Int. J. Hydrogen Energy* 39 (2014) 21569–21580, <https://doi.org/10.1016/j.ijhydene.2014.07.138>.
- [23] G. Reiss, H.L. Frandsen, W. Brandstätter, A. Weber, Numerical evaluation of microstructural parameters of porous supports in metal-supported solid oxide fuel cells, *J. Power Sources* 273 (2015) 1006–1015, <https://doi.org/10.1016/j.jpowsour.2014.09.185>.
- [24] M. Stange, C. Denonville, Y. Larring, A. Brevet, A. Montani, Improvement of corrosion properties of porous alloy supports for solid oxide fuel cells, *Int. J. Hydrogen Energy* 42 (2017) 12485–12495, <https://doi.org/10.1016/j.ijhydene.2017.03.170>.
- [25] E. Stefan, C. Denonville, Y. Larring, M. Stange, R. Haugsrud, Oxidation study of porous metal substrates for metal supported proton ceramic electrolyzer cells, *Corros. Sci.* 164 (2020), 108335, <https://doi.org/10.1016/j.corsci.2019.108335>.
- [26] M. Mokhtari, T. Wada, C. Le Boullet, J. Duchet-Rumeau, H. Kato, E. Maire, N. Mary, Corrosion resistance of porous ferritic stainless steel produced by liquid metal dealloying of Incoloy 800, *Corros. Sci.* 166 (2020), 108468, <https://doi.org/10.1016/j.corsci.2020.108468>.
- [27] C. Asensio-Jimenez, L. Niewolak, H. Hattendorf, B. Kuhn, P. Huczukowski, L. Singheiser, W.J. Quadakkers, Effect of Specimen Thickness on the Oxidation Rate of High Chromium Ferritic Steels: The Significance of Intrinsic Alloy Creep Strength, *Oxid. Met.* (n.d.) 1–14, <https://doi.org/10.1007/s11085-012-9323-5>.
- [28] D.J. Young, A. Chyrkin, W.J. Quadakkers, A simple expression for predicting the oxidation limited life of thin components manufactured from FCC high temperature alloys, *Oxid. Met.* 77 (2012) 253–264, <https://doi.org/10.1007/s11085-012-9283-9>.
- [29] G. Lovric, R. Mokso, C.M. Schlepütz, M. Stampanoni, A multi-purpose imaging endstation for high-resolution micrometer-scaled sub-second tomography, *Phys. Med.* 32 (2016) 1771–1778, <https://doi.org/10.1016/j.ejmp.2016.08.012>.
- [30] F. Marone, A. Studer, H. Billich, L. Sala, M. Stampanoni, Towards on-the-fly data post-processing for real-time tomographic imaging at TOMCAT, *Adv. Struct. Chem. Imaging* 3 (2017) 1–11, <https://doi.org/10.1186/s40679-016-0035-9>.
- [31] D. Paganin, S.C. Mayo, T.E. Gureyev, P.R. Miller, S.W. Wilkins, Simultaneous phase and amplitude extraction from a single defocused image of a homogeneous object, *J. Microsc.* 206 (2002) 33–40, <https://doi.org/10.1046/j.1365-2818.2002.01010.x>.
- [32] D Visualization & Analysis Software, (n.d.).
- [33] H. Gschiel, C. Gierl-Mayer, H. Danninger, P.-O. Larsson, H. Vidarsson, Manufacturing and microstructure of porous metal supports for a solid oxide fuel cell, *Powder Metall.* 58 (2015) 178–181, <https://doi.org/10.1179/0032589915Z.000000000237>.
- [34] R. Sachitanand, M. Sattari, J.E. Svensson, J. Froitzheim, Evaluation of the oxidation and Cr evaporation properties of selected FeCr alloys used as SOFC interconnects, *Int. J. Hydrogen Energy* 38 (2013) 15328–15334, <https://doi.org/10.1016/j.ijhydene.2013.09.044>.
- [35] M. Park, J.-S. Shin, S. Lee, H.-J. Kim, H. An, H. Ji, H. Kim, J.-W. Son, J.-H. Lee, B.-K. Kim, H.-W. Lee, K.J. Yoon, Thermal degradation mechanism of ferritic alloy (Crofer 22 APU), *Corros. Sci.* 134 (2018) 17–22, <https://doi.org/10.1016/j.corsci.2018.01.022>.
- [36] M. Brandner, *Verbundstruktur für Hochtemperatur- brennstoffzellen in mobilen Anwendungen*, 2006.
- [37] L. Rose, O. Kesler, C. Decès-Petit, T. Troczynski, R. Maric, Characterization of porous stainless steel 430 for low- and intermediate-temperature solid oxide fuel cell (SOFC) substrates, *Int. J. Green Energy* 6 (2009) 638–645, <https://doi.org/10.1080/15435070903372510>.
- [38] N.V. Gavrilov, V.V. Ivanov, A.S. Kamenetskikh, A.V. Nikonov, Investigations of Mn-Co-O and Mn-Co-Y-O coatings deposited by the magnetron sputtering on ferritic stainless steels, *Surf. Coat. Technol.* 206 (2011) 1252–1258, <https://doi.org/10.1016/j.surfcoat.2011.08.036>.
- [39] A.W.B. Skilbred, R. Haugsrud, Sandvik Sanergy HT - A potential interconnect material for LaNbO<sub>4</sub>-based proton ceramic fuel cells, *J. Power Sources* 206 (2012) 70–76, <https://doi.org/10.1016/j.jpowsour.2012.01.101>.
- [40] H. Falk-Windisch, J.E. Svensson, J. Froitzheim, The effect of temperature on chromium vaporization and oxide scale growth on interconnect steels for Solid Oxide Fuel Cells, *J. Power Sources* 287 (2015) 25–35, <https://doi.org/10.1016/j.jpowsour.2015.04.040>.
- [41] J.W. Fergus, Metallic interconnects for solid oxide fuel cells, *Mater. Sci. Eng. A* 397 (2005) 271–283, <https://doi.org/10.1016/j.msea.2005.02.047>.
- [42] M. Palcut, L. Mikkelsen, K. Neufeld, M. Chen, R. Knibbe, P.V. Hendriksen, Corrosion stability of ferritic stainless steels for solid oxide electrolyser cell interconnects, *Corros. Sci.* 52 (2010) 3309–3320, <https://doi.org/10.1016/j.corsci.2010.06.006>.
- [43] M. Palcut, L. Mikkelsen, K. Neufeld, M. Chen, R. Knibbe, P.V. Hendriksen, Corrosion stability of ferritic stainless steels for solid oxide electrolyser cell interconnects, *Corros. Sci.* 52 (2010) 3309–3320.
- [44] G. Schiller, A. Ansar, M. Lang, O. Patz, High temperature water electrolysis using metal supported solid oxide electrolyser cells (SOEC), *J. Appl. Electrochem.* 39 (2009) 293–301, <https://doi.org/10.1007/s10800-008-9672-6>.
- [45] S. Molin, B. Kusz, M. Gazda, P. Jasinski, Evaluation of porous 430L stainless steel for SOFC operation at intermediate temperatures, *J. Power Sources* 181 (2008) 31–37, <https://doi.org/10.1016/j.jpowsour.2007.10.009>.
- [46] S. Molin, M. Gazda, P. Jasinski, Coatings for improvement of high temperature corrosion resistance of porous alloys, *J. Eur. Ceram. Soc.* 31 (2011) 2707–2710, <https://doi.org/10.1016/j.jeurceramsoc.2011.02.007>.

## **5.2. Morphology changes in Fe-Cr porous alloys upon high-temperature oxidation quantified by X-ray tomographic microscopy**

While SEM imaging does enable the estimation of scale thickness, relying solely on two-dimensional cross-sections for this purpose can lead to deceptive conclusions. As an illustration, the separated oxidation centers appear as large, irregular features located a substantial distance from one another throughout the entire volume of the sample. Consequently, determining their dimensions based on the two-dimensional cross-section of a specimen is unfeasible, as the outcome would be highly location-dependent. In addition, if the cross-section is prepared in a non-representative place, the breakaway oxidation centers may be easily missed. In order to examine the alloy's intricate morphology comprehensively, synchrotron tomographic microscopy was employed.

Synchrotron tomographic microscopy provided insight into the complex three-dimensional structure of various phases of the samples. In this study, the tomographic microscopy was performed using a monochromatic X-ray beam allowing not only to analyze the morphology, but also to distinguishing and quantify particular phases: the metallic core, oxide scale, and porosity (as defined in the publication).

The analysis of the tomographic images revealed the increase of specific surface area of porous alloy from initial  $0.020 \text{ m}^2 \text{ g}^{-1}$  to  $0.030 \text{ m}^2 \text{ g}^{-1}$  after oxidation process performed at  $900^\circ\text{C}$  for 10 h. The average oxide scale thickness was determined as  $1.12 \text{ }\mu\text{m}$  for samples oxidized at  $850^\circ\text{C}$  for 10 h. On the other hand, for the samples oxidized at  $900^\circ\text{C}$  for 10 h the oxide scale thickness was  $2.45 \text{ }\mu\text{m}$  which is the same value as for sample oxidized at  $850^\circ\text{C}$  for 100 h. These experiments allowed to confirm that the oxidation process leads to decrease of porosity. The maximum detected change of pores' radius was from  $15.0 \text{ }\mu\text{m}$  to  $10.8 \text{ }\mu\text{m}$  for the sample oxidized at  $850^\circ\text{C}$  for 100 h, which amounts to a 28 % decrease.

The tomographic analysis provided data which can deepen our understanding of how the high-temperature oxidation process impacts the degradation of the porous alloys. Moreover, the data obtained from the experiments allowed to determine the specific surface area of porous alloys which is essential in the context of the lifespan prediction model.

My original contribution in this work was:

- Calculating the specific surface area of porous alloy before and after oxidation.
- Performing three-dimensional images analysis that revealed microstructural changes, such as average pore size in the alloy after oxidation at high-temperatures.
- Comparing two-dimensional SEM images with three-dimensional tomographic images and analyzing them.



Statement of the co-authors' contribution to the publication entitled 'Morphology changes in Fe-Cr porous alloys upon high-temperature oxidation quantified by X-ray tomographic microscopy':

<b>Name and surname</b>	<b>Contribution to the publication</b>	<b>Signature</b>
Damian Koszelow	Conceptualization, Methodology, Formal Analysis, Investigation, Writing – Original Draft	
Sebastian Molin	Conceptualization, Supervision, Project administration, Funding acquisition, Writing – Review & Editing	
Jakub Karczewski	Investigation – SEM imaging	
Federica Marone	Investigation – synchrotron tomography analysis, Writing – Review & Editing	
Małgorzata Makowska	Investigation – synchrotron tomography analysis, Writing – Review & Editing	



# Morphology changes in Fe-Cr porous alloys upon high-temperature oxidation quantified by X-ray tomographic microscopy



D. Koszelow<sup>a</sup>, S. Molin<sup>a</sup>, J. Karczewski<sup>b</sup>, F. Marone<sup>c</sup>, M. Makowska<sup>d,\*</sup>

<sup>a</sup> Faculty of Electronics, Telecommunications and Informatics, Gdańsk University of Technology, Poland

<sup>b</sup> Faculty of Applied Physics and Mathematics, Gdańsk University of Technology, Poland

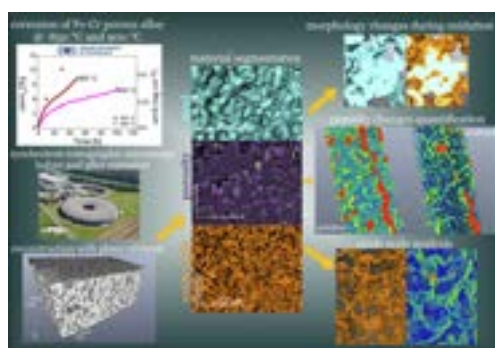
<sup>c</sup> Swiss Light Source, Paul Scherrer Institut, Villigen, Switzerland

<sup>d</sup> Laboratory for Nuclear Materials, Laboratory for Synchrotron Radiation and Femtochemistry, Paul Scherrer Institut, Villigen, Switzerland

## HIGHLIGHTS

- A high-temperature oxidation at 850 °C (10 h, 30 h, 100 h) and 900 °C (10 h) of porous ferritic stainless steel Fe22Cr was performed and investigated by synchrotron tomographic microscopy.
- Tomographic analysis of corresponding regions in porous steel before and after corrosion.
- Distinguish metallic core, oxide scale, open and closed porosity phases.
- Quantification of microstructural changes such as specific surface area of steel, grain size distribution.
- 3D mapping of oxide scale thickness and pore size distribution.

## GRAPHICAL ABSTRACT



## ARTICLE INFO

### Article history:

Received 19 January 2022

Revised 16 February 2022

Accepted 24 February 2022

Available online 03 March 2022

### Keywords:

Stainless steel

X-ray tomography

SEM

High-temperature corrosion

## ABSTRACT

The effect of high-temperature oxidation at 850 °C (10 h, 30 h, 100 h) and 900 °C (10 h) on porous (~30 % porosity) ferritic stainless steel (Fe22Cr) has been investigated using synchrotron tomographic microscopy, which allowed for visualisation, separation and quantitative analysis of the metallic core, closed pores, open pores and oxide scale phase. The same regions within the samples were investigated before and after oxidation performed at different conditions. Quantitative analysis of the tomographic data provided information on changes upon oxidation of the relative volume of the different phases, the specific surface area (SSA) of the metallic core, the thickness of the oxide scale and pore size distribution. The results were discussed in the context of thermogravimetric analysis of the samples and supported by SEM imaging. It was observed that oxidation leads to an increase of the SSA of steel and the largest increase (~50 %) was obtained for the sample processed for 100 h at 850 °C. It is demonstrated the open porosity forms a network of connected channels within the sample and it dominates in the volume. In addition, the 3D imaging revealed breakaway oxidation areas for samples, for which this phenomenon remained undetected using 2D SEM analysis.

© 2022 The Authors. Published by Elsevier Ltd. This is an open access article under the CC BY-NC-ND license (<http://creativecommons.org/licenses/by-nc-nd/4.0/>).

## 1. Introduction

Due to high corrosion resistance, high chromium content alloys are commonly used in certain types of nuclear reactors, turbines,

\* Corresponding author.

E-mail address: [malgorzata.makowska@psi.ch](mailto:malgorzata.makowska@psi.ch) (M. Makowska).

and engines [1–3]. The properties of dense chromia ( $\text{Cr}_2\text{O}_3$ ) forming alloys have been thoroughly studied in recent decades and they are well described in the literature [4–6]. Selected ferritic steel alloys, such as Crofer 22 APU or Crofer 22H were proposed as interconnect materials in solid oxide fuel cell (SOFC) and solid oxide electrolysis cell (SOEC) stacks [7–9]. The main superiority of these alloys for application in solid oxide cells (SOC i.e. SOFC and SOEC) is high electrical conductivity of the chromia scale at operating conditions of SOC ( $\sim 1 - 10 \text{ mS cm}^{-1}$  at  $600 - 800^\circ\text{C}$ ) [10].  $\text{SiO}_2$  or  $\text{Al}_2\text{O}_3$  forming alloys provide even higher corrosion resistance, but their much lower electrical conductivity disqualifies them for such applications in SOC. Typically, SOC interconnectors in commercial applications are produced from ceramic materials, however they are expensive and hard to manufacture in a specific shape. Thus, chromia forming alloys are considered a promising alternative for these components because of their electrical conductivity and ease of fabrication. Additionally, porous form of FeCr alloys can play a role of a support in metal-supported solid oxide cells (MS-SOC) because of decreasing the weight and cost of the whole device.

Porous steel alloys have been investigated intensively by many groups in the last years [11–13] because of their high application potential, for instance in gas membranes and sensor systems. The high amount of open porosity ensuring efficient gas transport is a prerequisite for the mentioned applications. On the other hand, open porosity results in orders of magnitude larger alloy-oxygen interface area, which may significantly accelerate the oxidation process. The oxide scale growth rate is a key factor for many potential applications of porous chromia forming alloys, since it leads to the limitation of the size of the pores or even closing the pore channels by filling them with chromia during oxidation. Deeper analysis of the oxidation mechanism of porous ferritic alloys, in particular the oxide thickness growth and corresponding morphology changes, closing porosity and the grain size distribution changes, is essential for enabling their usage in SOC and gas membranes as well as further broadening of their application field.

The mechanism of oxidation has been examined for dense ferritic alloys but the porous form of these alloys has not been evaluated in detail yet. Typically, the mechanism of oxidation is investigated based on mass gain measurements and SEM/EDX studies [5,14–17]. However, detailed information about oxide scale growth dynamics and grain distribution changes is still unknown. Up to now, there are only a few published works about the oxidation process of porous alloys [14,18–23].

Glasscock et al. [18] investigated the potential of using the porous Fe<sub>21</sub>Cr<sub>7</sub>Al<sub>1</sub>Mo<sub>0.5</sub>Y alloy as support for oxygen transport membranes. They showed that porosity  $\geq 30\%$  with pore sizes much larger than the maximum oxide thickness of  $3 \mu\text{m}$  is required to prevent pore-blockage by oxide scale growth and to ensure good gas transport throughout the lifetime of the device. The changes of the alloy porosity were determined using BET adsorption, mercury porosimetry, and image analysis of SEM micrographs. These methods allow for calculating the percentage of pore volume and estimation of the pore size distribution but information about changes of SSA and oxides scale morphology after oxidation is still missing.

The most common tool used for determining microstructural changes of the alloy due to oxidation is scanning electron microscopy (SEM) [14], which, however, allows only for analysing randomly selected cross-sections of the sample in 2D. The oxide scale thickness cannot be properly evaluated from 2D images, as the observed thickness depends on the orientation of the scale layer with respect to the cross-section plane. Moreover, this value can be inaccurate because of the irregular growth of the oxide scale [24]. Therefore, analysis of the scale thickness should be performed taking into account the 3-dimensional geometry of the material

and based on the imaging of a representative volume of samples, and not only a cross-section.

X-ray tomographic microscopy (also called micro computed tomography,  $\mu\text{CT}$ ) is a non-destructive method, which provides insight into the 3-dimensional morphology of different phases in a material and enables their relative volumetric quantification, if these phases are characterized by sufficient contrast [25]. This advanced method was used for the observation of microstructure changes, phase composition changes, and damage mechanisms of different alloys by several research groups [26–37]. Kapat et al. have investigated the influence of porosity and pore size distribution in a Ti6Al4V foam on its physicomaterial properties for medical implant applications [26]. The porosity was determined via 2D SEM image analysis, water displacement method and from synchrotron tomographic microscopy. The decrease of porosity was linked to the reduction of pore connectivity. Mokhtari et al. [31] analysed FeCr alloys with a  $30 - 70\%$  range of porosity created by a dealloying process. The authors used tomographic microscopy for calculation of the SSA and average pore size. Le et al. [30] investigated the effect of porosity on the fatigue behaviour of AlSi7Mg0.3 alloys obtained by the lost foam casting process. They showed that stress concentrations at the pores are increased and lead to local plasticity. Additionally, simulations of the influence of pore shape on fatigue strength were performed and indicated the real casting pores (more irregular) provide more significant sensitivity on fatigue strength compared with spherical pores. Thus, the examination of the real structure of porosity is essential for predicting the properties (and lifetime) of the alloys. Synchrotron tomography was also applied for studies of the porosity evolution in freeze-cast iron foams [38,39] using setup providing voxel size of  $2.45 \mu\text{m}$ . In several works, laboratory  $\mu\text{CT}$  with  $2.5 \mu\text{m}$  voxel size was performed to provide data on porosity, necessary to be used in modelling of mechanical properties of porous alloys [40,41]. In our recent work, we have demonstrated that synchrotron tomographic microscopy allows for the separation and quantification of porosity, metallic core, and oxide scale phases in porous ferritic steel [24].

X-ray tomographic microscopy provides insight into the 3-dimensional morphology, while SEM is limited to 2D images. Electron microscopy allows however resolving features of dimensions beyond the spatial resolution of the  $\mu\text{CT}$  technique, meaning that SEM images allow for recognising more details in the microstructure. For instance, nitride precipitate that can appear during oxidation of the high chromium ferritic alloys [6,42,43] with a size from submicron to a few microns are at the edge of the capabilities of  $\mu\text{CT}$ . Thus, it might be possible to detect them, but not to analyse their morphology. Achieving higher resolution with  $\mu\text{CT}$  is possible at the expense of a significant decrease of the field of view, nevertheless, the resolution achievable with SEM cannot be reached by  $\mu\text{CT}$ . In this work, it was important to investigate volume large enough to obtain representative statistics of the measured quantities keeping a possibly high spatial resolution of images. Therefore, we use both electron microscopy and synchrotron tomographic microscopy as complementary methods, as such approach allows for complex 3-dimensional analysis of the sample in a broad size scale range, providing a full picture of morphology changes in porous steel upon oxidation.

In this work, results of detailed studies of the 3-dimensional morphology the porous Fe<sub>22</sub>Cr alloy oxidised in air at  $850^\circ\text{C}$  and  $900^\circ\text{C}$  are presented. Specimens were investigated with SEM and synchrotron tomographic microscopy before and after ex-situ oxidation. For tomographic measurements before and after oxidation, exactly the same area of each sample was localised, analysed and the morphology before and after the process was compared. The results allowed for evaluation of changes upon oxidation of the SSA of the metallic core, oxide thickness and average grain size



of the alloy for different oxidation conditions (time, temperature). Moreover, breakaway oxidation centres were identified. To the best of our knowledge, this is the first work addressing the changes in microstructure, grains size, and oxide thickness of chromia forming porous alloys by three-dimensional analysis.

## 2. Experimental

### 2.1. Sample preparation

A porous alloy sheet  $\sim 100 \times 100 \text{ mm}^2$  with a thickness of 0.35 mm was obtained from Höganäs AB (experimental alloy MW2, Höganäs, Sweden). It was prepared by a tape-casting process from a steel powder slurry, followed by drying, debinding, and sintering in a reducing atmosphere (1250 °C, 30 min,  $\text{H}_2$ ). The porosity of the alloy determined by the producer is 30 %. Chemical composition of the alloy is presented in Table 1. Three series of samples were prepared from the 0.35 mm thick sheet, which was cut into smaller pieces of different sizes depending on the performed experiment. In the first series, for the thermogravimetric analysis,  $\sim 3 \times 3 \times 0.35 \text{ mm}^3$  pieces of the alloy were prepared. The second series was prepared for the ex-situ oxidation measurements, with dimensions of  $\sim 10 \times 10 \times 0.35 \text{ mm}^3$ , and for X-ray tomography, the third series consisted of elongated samples ( $\sim 6 \times 1 \times 0.35 \text{ mm}^3$ ). Before use, samples were cleaned in an ultrasonic bath in ethanol (99.9 %) followed by acetone (99.9 %).

### 2.2. Thermogravimetric analysis

The thermogravimetric analysis during oxidation of the alloy was performed using a Netzsch TG 209 F3 Tarsus thermobalance. The heating and cooling rates were  $3 \text{ }^\circ\text{C min}^{-1}$ . The experiment was carried out in air atmosphere with a flow rate of  $50 \text{ ml min}^{-1}$ . Samples were exposed to a corrosive environment for 100 h at 850 °C and for  $\sim 40 \text{ h}$  at 900 °C (due to instabilities of the thermobalance for long measurements at high temperature). The results were plotted as the relative mass change of the sample and mass gain per surface area of the sample (determined from the tomography measurements) over time.

### 2.3. Scanning electron microscopy

The second series of samples was oxidised ex-situ for 10 h, 30 h, and 100 h at 850 °C and 900 °C for evaluation of the alloy morphology changes. SEM imaging was performed using a Phenom XL electron microscope (Thermo Fisher Scientific, Netherlands) on polished cross-sections of the samples. All SEM images were recorded using backscatter electron detector (BSE). The microscope is equipped with an EDX detector (Thermo Fisher Scientific, 25 mm<sup>2</sup> Silicon Drift Detector), which was used for elemental analysis of the steel (EDX analyses performed at acceleration voltage of 15 kV).

### 2.4. Synchrotron tomographic microscopy

Samples for the tomography investigation were oxidised under the same conditions, as the samples for the SEM studies. X-ray tomographic microscopy characterization of samples was per-

formed at the TOMCAT beamline of the Swiss Light Source (SLS) at the Paul Scherrer Institute, Villigen, Switzerland. A parallel X-ray beam with an energy of 40 keV was used. The detector setup was composed of a scintillator converting X-rays into visible light, an objective lens and a sCMOS camera with settings resulting in a field of view (FOV) of approximately  $0.8 \text{ mm} \times 0.8 \text{ mm}$  and an image pixel size of  $0.325 \text{ }\mu\text{m}$ . A total of 1001 projections over  $180^\circ$  were recorded, each with 1600 ms exposure, resulting in scans lasting about 26 min. Each sample was investigated using exactly the same setup before and after exposure to corrosive conditions. During measurements after oxidation, the same region of the sample, which was scanned before oxidation, was localised and measured with identical parameters.

The reconstruction of the acquired tomograms was conducted using the in-house developed pipeline available at the beamline that provides complete tomographic volumes immediately after data acquisition, allowing for quick adjustment of measurement and reconstruction algorithm parameters. The acquired projections were tomographically reconstructed after dark- and flat-field correction and phase retrieval with the Paganin algorithm [44]. Phase retrieval was helpful in increasing the signal-to-noise and contrast-to-noise ratios. The achieved contrast in the images reconstructed with this approach allowed for a relatively straightforward material segmentation based only on intensity thresholding, which was performed using the commercial software Avizo 9.4. The intensity ranges that were assigned to steel, porosity and oxide scale, were selected based on the histogram minima defined for one of the samples with a high oxidation degree (here referred to as CT900.10). Then, exactly the same intensity ranges were applied to all the analysed samples for segmentation of the particular phases. The reconstruction provided 16-bit images with a dynamic range from 0 to 65535, and it was calculated, that an increase by 1% of the threshold value used for the steel phase, would result in higher fraction of this phase by 0.5%. Although the absolute values of calculated material fractions depend on the selected intensity thresholds, applying the same intensity ranges for all the samples allows for reasonable comparison of the oxidation-induced changes. It was observed that the oxide scale of thickness about  $1 \text{ }\mu\text{m}$  was possible to detect in the reconstructed volumes, thus,  $1 \text{ }\mu\text{m}$  was further considered as a spatial resolution of the analysed images.

Avizo software was also used to evaluate the oxide scale thickness distribution and to perform alloy grain separation for evaluation of the grain size distribution. Moreover, a comprehensive porosity analysis was performed, which allowed for estimating changes upon oxidation of the average pore channel cross-section as well as changes of the amount of open, closed and total porosity. Direct comparison and observation of microstructural alterations from the non-oxidised to oxidised state of the samples was possible, since exactly the same region in the measured volumes in both states was localised and analysed.

The role of porosity for applications of the allows as SOFC/SOEC interconnects or gas membranes is connected to the efficiency of gas transport. Thus, in this work, for the evaluation of the porosity changes upon oxidation, the pores are considered as a network of channels. The distribution of the pore channel thicknesses was evaluated using an algorithm that computes the local thickness of a selected material for each voxel in the binary volume. In this

**Table 1**  
Chemical composition of the alloy (provided by the producer).

		Analyzed chemical composition, %										
Target composition	Fe	Cr	Ni	Mo	Mn	Cu	Si	Nb	C	O	N	S
Fe22Cr	Bal.	22.0	0.03	0.01	0.23	0.02	0.08	0.02	0.04	0.58	0.07	0.01

particular case, the binary volume consisted of pore pixels labelled with “1” and other pixels (for any kind of material) labelled with “0” are assigned to all the other voxels. The local thickness is defined as the diameter of the largest possible ball containing this voxel and fully inscribed within the analysed material (in this case pores). This commonly used approach has been described in detail in [45] and is implemented in the Avizo software in the “Thickness Map” module. The same approach and algorithm were used for determining the oxide scale thickness.

### 3. Results and discussion

#### 3.1. Thermogravimetric analysis

Relative mass changes of the samples during exposure to air at temperatures of 850 °C and 900 °C are presented in Fig. 1. The thermogravimetric data were compared with separate ex-situ mass measurements. For samples oxidised at 850 °C, ex-situ (pink data points in Fig. 1) and isothermal mass gains (pink solid line) are comparable, but for alloys oxidised at 900 °C, significantly different values were obtained. However, in the case of the ex-situ oxidation, the samples spent a longer time at high temperatures due to the heating and cooling process. For such a high temperature as 900 °C, it can cause higher values of ex-situ measured mass gain but the oxidation rate is considerably slower at lower temperatures so, this effect is negligible for samples oxidised at 850 °C. A previous investigation [24] has shown that the oxidation process of porous Fe22Cr alloy follows a parabolic rate law thus, its kinetics is limited by diffusion of  $\text{Cr}^{3+}$  cations. The threshold level of mass gain for breakaway oxidation appearance was established as about 6 wt%.

#### 3.2. SEM analysis of samples before and after oxidation

EDX analysis on polished cross-sections was used to evaluate the alloy's chemical composition. The final results were 21.3 wt% Cr and 0.26 wt% Mn, with iron as a balance. Taking into consideration the relatively high inaccuracy of the EDX method, the chemical composition was in agreement with the producer data. The morphology of the surface and polished cross-section of the alloy is presented in Fig. 2. The particles are well connected and necks between the grains are well visible (Fig. 2D). Also from cross-section images, the interfaces between grains are noticeable (Fig. 2B).

Fig. 3 shows the SEM images of oxidised samples. The sample oxidised at 850 °C for 10 h is presented in the first column

(Fig. 3 A, E, I). Images taken at higher magnification revealed the presence of a thin layer of an oxide scale varying in thickness in the range of 1–2  $\mu\text{m}$ . The oxide scale observed for a sample oxidised at 850 °C for 30 h (Fig. 3 B, F, J) appears locally thicker (1–4  $\mu\text{m}$ ) than it is for a sample that has been oxidised for 10 h. Further oxidation of the alloy up to 100 h (at 850 °C) leads to breakaway oxidation (Fig. 3 C) which, in this case, appeared at the surface of the sample. The sample was penetrated up to 150  $\mu\text{m}$  by the breakaway oxidation area. Even at lower magnifications, the oxide scale around the grains is visible on the whole cross-section. The oxide thickness observed in these images (Fig. 3C, G and K) does not significantly differ from the sample oxidised at 850 °C for 30 h (Fig. 3 B, F, J) and can be estimated to 1 – 5  $\mu\text{m}$ . For the alloy oxidised at 900 °C for 10 h (Fig. 3 D, H, L) breakaway oxidation was not observed in the prepared cross-section and the oxide thickness was approximately 2–5  $\mu\text{m}$ , which is comparable with both, the sample oxidised at 850 °C for 100 h, and the sample oxidised at 850 °C for 30 h. However, the tomographic microscopy experiment has revealed that the breakaway oxidation region occurred also for the sample oxidised at 850 °C for 30 h (CT850.30) and for the sample oxidised at 900 °C for 10 h (CT900.10) but this aspect will be elaborated in the next section. In our previous work, a change in the slope of the thermogravimetric curve after 10 h of oxidation at 900 °C was observed. It corresponds to 6% mass gain which was determined as the breakaway oxidation appearance threshold value for Fe22Cr alloy [24]. This confirms that analysis of SEM images is not sufficient to determine changes in alloy morphology and 3-dimensional analysis is necessary for accurate breakaway oxidation region detection.

#### 3.3. Synchrotron tomographic microscopy

##### 3.3.1. Oxide scale thickness and morphology

Although SEM imaging allows for estimation of the scale thickness, as discussed in the introduction, its evaluation from 2D cross-sections can be misleading. Moreover, there might be some variations in the whole volume. For instance, the breakaway oxidation centres appear as large, irregular features in locations remote from each other. Therefore, their size cannot be evaluated from the 2D cross-section of a sample, as the result strongly depends on the location of the cross section. Moreover, the breakaway oxidation centres can be easily overlooked if the cross-section is prepared in a wrong location. Thus, for a detailed analysis of the complex morphology of the alloy, synchrotron tomographic microscopy was performed. Detailed information about mass changes for the samples used in the tomography experiment was gathered in Table 2. The applied sample name relates to the series of the sample after tomography measurement in order to distinguish results from tomography from the other techniques.

Fig. 4 presents a visualisation of sample CT850.100 before (Fig. 4 A) and after (Fig. 4 B) oxidation obtained by volume rendering of the reconstructed data with reconstructed slices (Fig. 4 C and D) corresponding to the clipping planes visible in the 3D images Fig. 4 A and B (the front planes). The necks between the grains are clearly visible and in the case of the oxidised samples, it is apparent that the contrast between different phases allows to distinguish the oxide phase from the metallic core. Consequently, material segmentation was performed for each sample, and its material statistics (summarized in Table 3) evaluated.

Oxide growth, caused by diffusion of either cations or anions, is a temperature activated process. Our previous research [24] has shown, that indeed, temperature plays a key role in oxidation kinetics of porous alloys. Thus, this study is focused on the comparison of the oxidation process for samples oxidised at different temperatures, but with the same holding time. Fig. 5 and Fig. 6 present results of material segmentation before and after exposure for

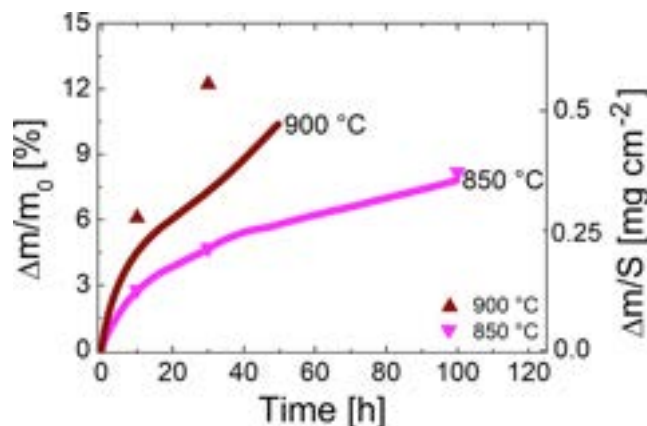
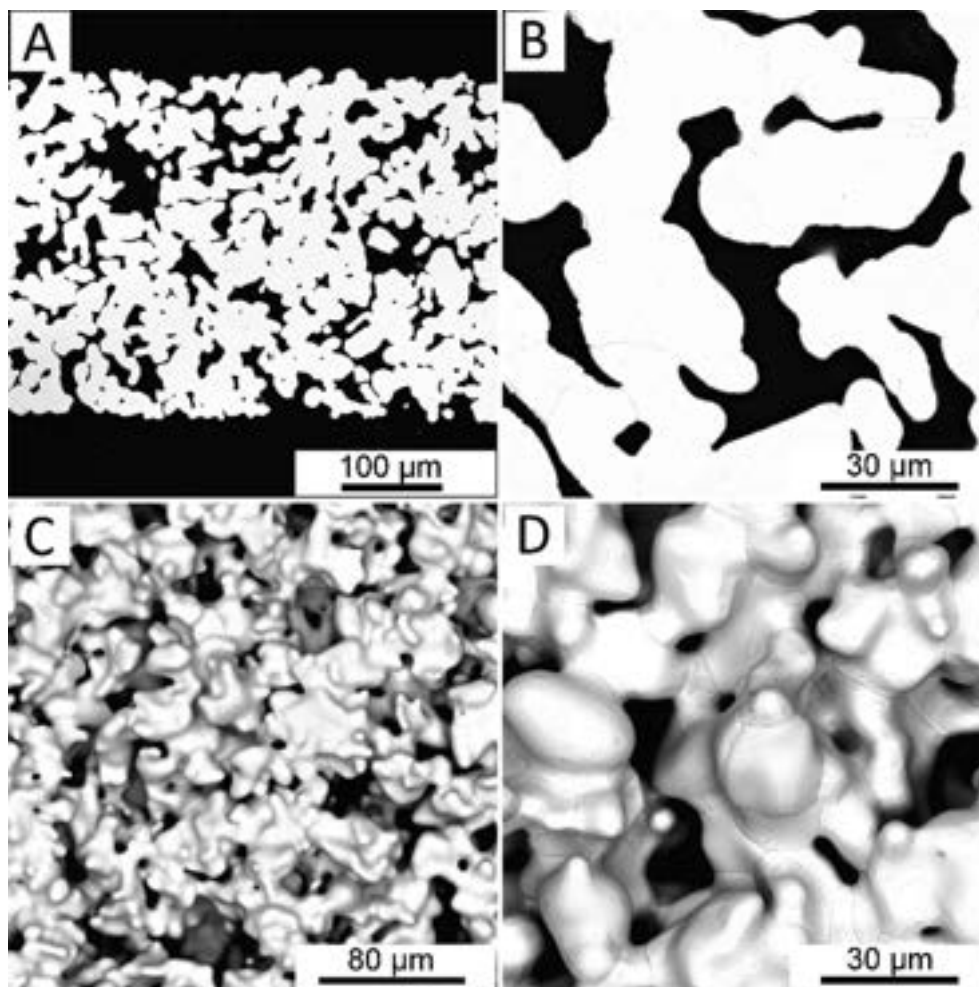


Fig. 1. Isothermal (solid line) and ex-situ (markers) mass gain of samples oxidised at 850 °C and 900 °C.



**Fig. 2.** SEM images of A, B) cross-section; C, D) surface of as-received MW2 alloy.

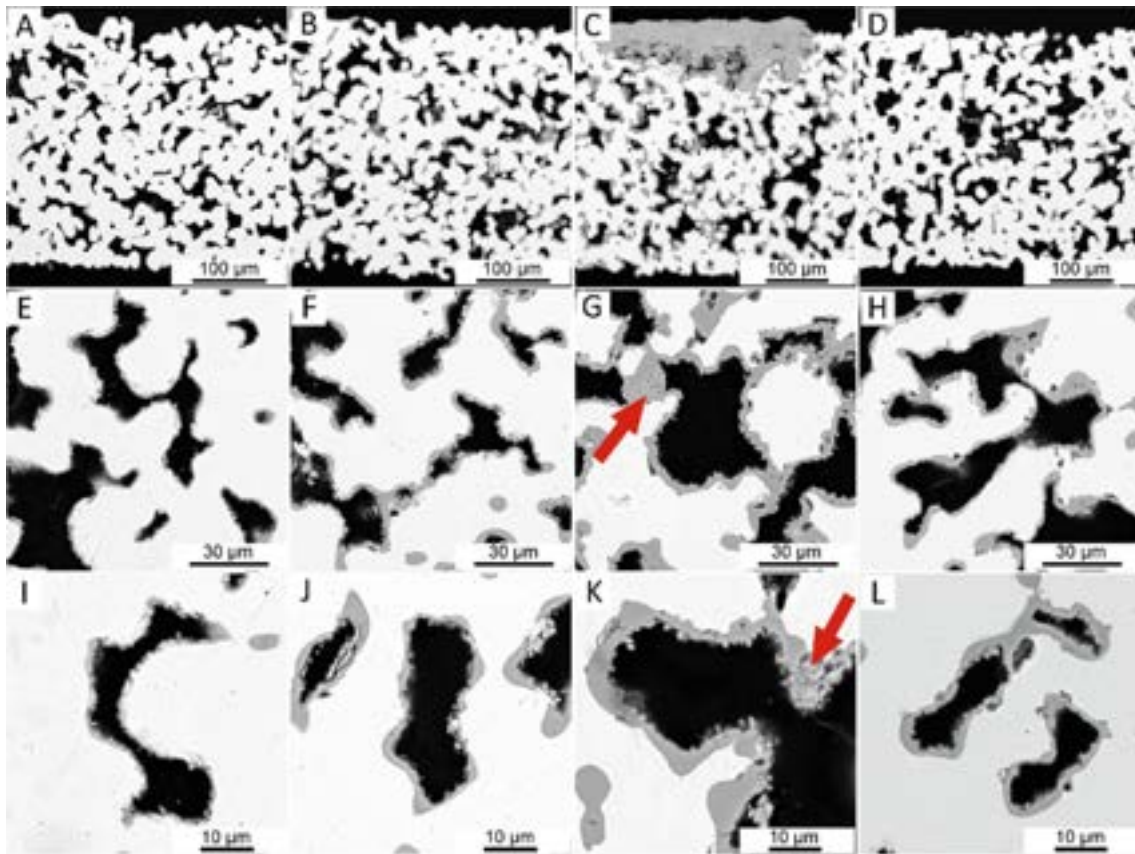
CT850.10 and CT900.10 samples, respectively. For both samples, the same region before (Fig. 5 A, Fig. 6 A) and after (Fig. 5 B, Fig. 6 B) oxidation is presented. As seen in both Fig. 5 and Fig. 6, the oxide scale has grown on the surface of the alloy's grains. In the case of sample CT850.10 (Fig. 5), the oxide scale is relatively smooth and covers tightly the grains surface. In the SEM images there is a small oxide roughness visible (Fig. 3I) for this sample, but it cannot be resolved in tomographic images. The roughness of the oxide scale in CT900.10, appears significantly larger (Fig. 6) as compared to CT850.10 (Fig. 5). Additionally, some porosity within the oxide scale is present, which was also observed in SEM images of a sample oxidised under the same conditions (Fig. 3H).

Based on the obtained segmentation results, the oxide scale thickness was evaluated using the "Thickness Map" module for each voxel of the oxide phase, which allowed for visualisation of the oxide thickness distribution. Examples of such visualisation are illustrated in Fig. 7 A, C for sample CT850.30 and in Fig. 7 D for sample CT900.10, which show 3-dimensional maps of the oxide thickness. Fig. 7 B illustrates volume rendering of the oxide phase in the corresponding region of sample CT850.30, based on which the thickness map in Fig. 7 A was evaluated. The colour scale assigned to voxels in Fig. 7A reflects the thickness of the oxide layer evaluated for the corresponding voxels. As seen in Fig. 7A, the breakaway oxidation area could be clearly identified for the CT850.30 sample. Taking into consideration the whole investigated volume of this sample, even more regions with breakaway oxida-

tion were found, supporting the higher mass gain measured for the CT850.30 sample compared to sample CT900.10 (Table 2). In contrast, the average thickness of the oxide scale is larger for CT900.10 (Table 4) because as seen in Fig. 7 C and Fig. 7 D, the colour scale for the CT900.10 sample is shifted towards the red colour in comparison to the sample CT850.30 colour scale for the whole presented volume. For a deeper understanding of the places of breakaway oxidation origin, in situ experiments are necessary. Based on such thickness maps generated for each of the investigated samples, the corresponding histograms were evaluated, which are shown in Fig. 8.

In the histograms in Fig. 8, there is a clear maximum visible for each investigated sample, except for CT850.10, which had the lowest oxidation degree. The lack of a peak in the CT850.10 oxide thickness histogram is related to the spatial resolution, which in this case is about 1 µm. Objects beyond this resolution, for instance oxide layers thinner than 1 µm, cannot be assessed based on these data. Thus, the sample CT850.10 is at the edge of the capabilities of tomographic microscopy performed with parameters selected for this work and therefore, this method could not be applied to samples with a lower degree of oxidation than CT850.10. Based on the oxide thickness histograms, the mean oxide thickness values were calculated and summarized in Table 4. For the CT850.10 sample it was 1.12 µm, for the CT850.30 sample oxidised the oxide scale thickness was 2.11 µm and it increased to 2.45 µm for samples CT850.100 and CT900.10. These values are lower than in the case of SEM images analysis of the oxide scale thickness. However,





**Fig. 3.** SEM cross-section images of the alloy oxidised A, E, I) for 10 h at 850 °C; B, F, J) for 30 h at 850 °C; C, G, K) for 100 h at 850 °C; D, H, L) for 10 h at 900 °C. The red arrows indicate the porosity and roughness of the oxide scale. (For interpretation of the references to colour in this figure legend, the reader is referred to the web version of this article.)

**Table 2**

List of samples with mass changes.

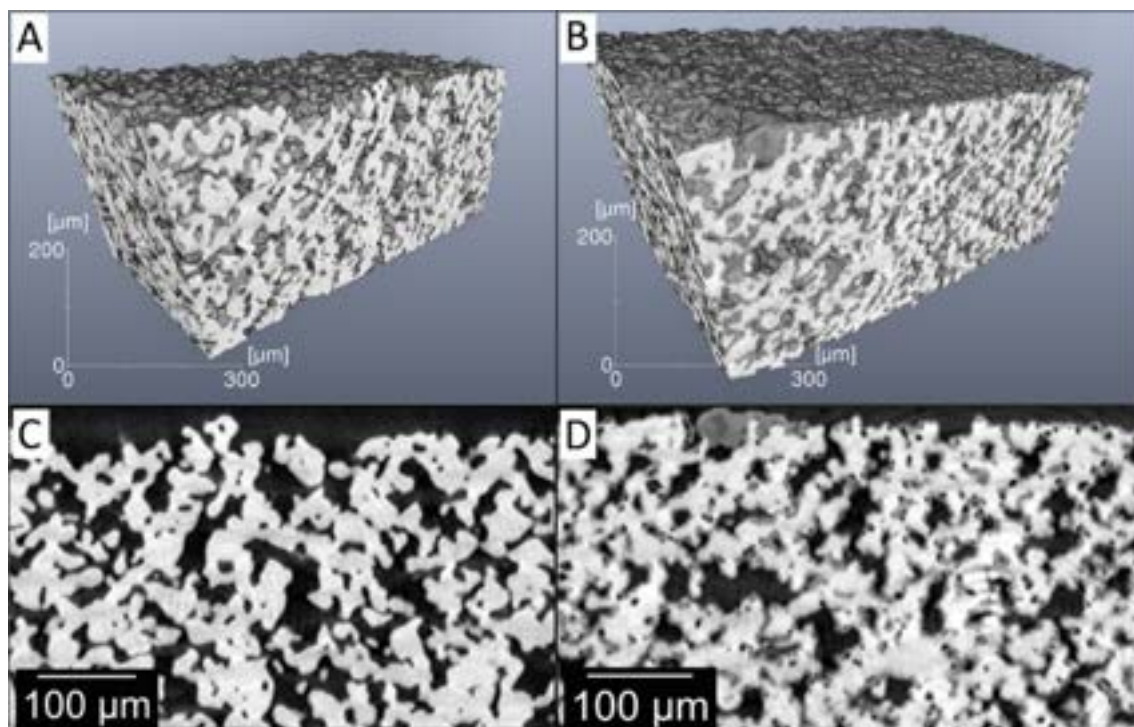
Sample name	Oxidation conditions	Initial weight [mg]	Final weight [mg]	$\Delta m/m_0$ [%]
CT850.10	850 °C, 10 h	18.13	18.61	2.65
CT850.30	850 °C, 30 h	7.35	7.77	5.71
CT850.100	850 °C, 100 h	13.75	14.90	8.36
CT900.10	900 °C, 10 h	12.84	13.53	5.37

SEM images show only a specified slice, which does not represent the whole sample volume, so the results of the tomography-based calculations are more comprehensive.

Material segmentation allows for calculation of the amount of different phases (alloy – oxide – pore), which is directly linked to the oxidation degree. In sample CT850.10, the oxide scale occupies 18.8 % of the sample's volume (volume occupied by a material, excluding porosity), which is calculated from the material segmentation results (Table 3), as a fraction of the volume of the oxide divided by the sum of alloy and oxide scale' volumes. The volume of the oxide scale contribution calculated for this sample from the measured mass gain (Table 2), is 11.6 %. Such difference is caused by several factors. Small porosity and roughness of the oxide scale visible in SEM images (examples are marked with the arrows in Fig. 3G and K) cannot be resolved in the tomograms. Therefore, the volume assigned to the oxide scale evaluated from the tomographic data, includes also these features and thus, it is significantly larger than the value obtained from the mass gain measurements that consider only fully dense material. Possible other reason might be a changing volume of the alloy phase, based on a decreasing diameter of alloy particles, altering oxide growth

from a typical outward diffusion driven to a complex one, where formation of internal porosity/voids can be expected. In other words, porosity and roughness beyond the resolution were labelled as the oxide material and thus, the oxide phase assigned via material segmentation has a lower density than theoretical  $\text{Cr}_2\text{O}_3$  density.

In case of sample CT900.10, the fraction of the oxide phase based on material segmentation results (Table 3) was 34.9 % of the sample's volume, again assuming that the total sample volume is a sum of oxide scale and alloy contributions (Table 3). Based on mass gain data of the same sample (Table 2), the determined oxide scale fraction is 22.2 %, which is a significantly lower value as compared to tomography-based calculations. The roughness and porosity of the oxide scale in CT900.10, which partially are not resolvable in tomography, as well as the microstructural changes, are significantly larger (Fig. 6) compared with CT850.10 (Fig. 5), so the difference of the oxide scale contribution calculated based on tomographic microscopy and mass gain data is even more significant in case of CT900.10. As mentioned above, these calculations of phase fraction do not take into account the porosity and roughness of the oxide scale, which is beyond the tomographic

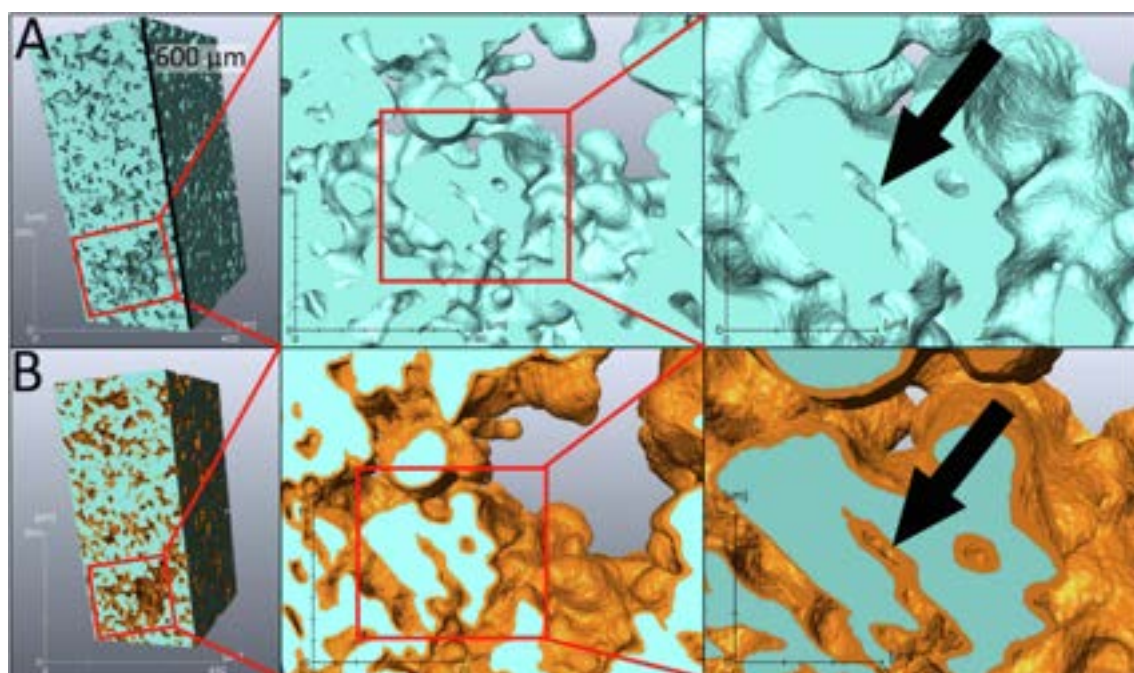


**Fig. 4.** Volume rendering of the reconstructed tomographic volume of sample CT850.100 a) before and b) after oxidation with reconstructed slices corresponding to the clipping planes (front planes) in the 3D images.

**Table 3**

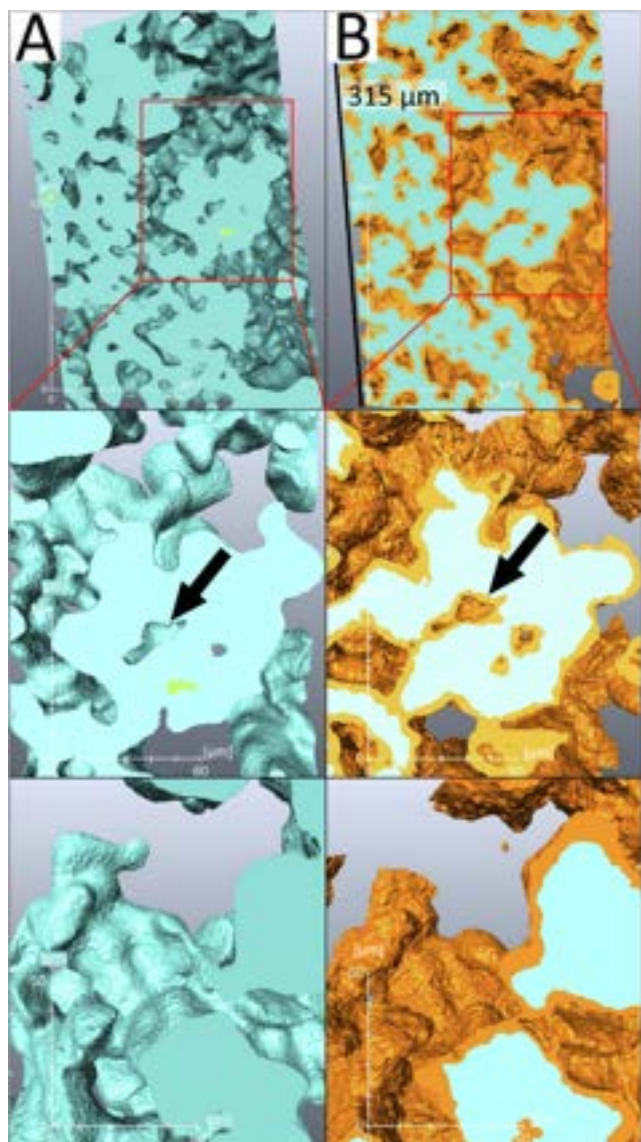
Material statistics before and after oxidation (vol %).

Sample	Oxidation conditions	Steel		Oxide		Open pores		Closed pores		Oxide / (Oxide + Steel)
		Before	After	Before	After	Before	After	Before	After	
CT850.10	850 °C, 10 h	67.85	62.46	–	14.42	32.04	22.97	0.10	0.14	18.76
CT850.30	850 °C, 30 h	67.57	57.40	–	20.50	32.35	22.00	0.07	0.10	26.32
CT850.100	850 °C, 100 h	67.40	52.70	–	26.80	32.51	20.40	0.09	0.10	33.71
CT900.10	900 °C, 10 h	61.41	46.50	–	24.90	38.52	28.50	0.07	0.10	34.87



**Fig. 5.** Visualisation of the metallic core (turquoise) and oxide scale (orange) based on volume rendering of the results of material segmentation for sample CT850.10 A) before oxidation, B) after oxidation at 850 °C for 10 h. Black arrows show exemplary regions where pore channels are blocked by the oxidation process. (For interpretation of the references to colour in this figure legend, the reader is referred to the web version of this article.)





**Fig. 6.** Visualisation of the metallic core (turquoise), the oxide scale (orange) and the closed porosity (green) based on volume rendering of the results of material segmentation for sample CT900.10 A) before oxidation, B) after oxidation at 900 °C for 10 h. Black arrows show exemplary regions where pore channels are blocked by the oxidation process. (For interpretation of the references to colour in this figure legend, the reader is referred to the web version of this article.)

microscopy resolution (around  $1 \mu\text{m}^3$ ), though still visible in SEM images.

Detailed statistics of phase composition for each sample were gathered in Table 3. For each of the investigated samples, the consumption of the steel phase is clearly visible. The longer the oxidation time, the more advanced the transition of the alloy into the oxide scale is observed like in the case of CT850.100 and CT900.10. The contribution of the oxide scale for the CT900.10 sample is similar to the CT850.100 sample, which demonstrates the strong temperature effect on the oxide scale growth.

Higher oxidation degrees lead to the breakaway oxidation observed as large oxide agglomerates in certain locations. Understanding their formation process is crucial for the usage of the alloy because it determines the lifetime and possible applications of the alloy. In Fig. 7, presenting a map of the oxide scale thickness with corresponding oxide scale morphology of the same region, the breakaway oxidation centre is clearly observed as the red colour

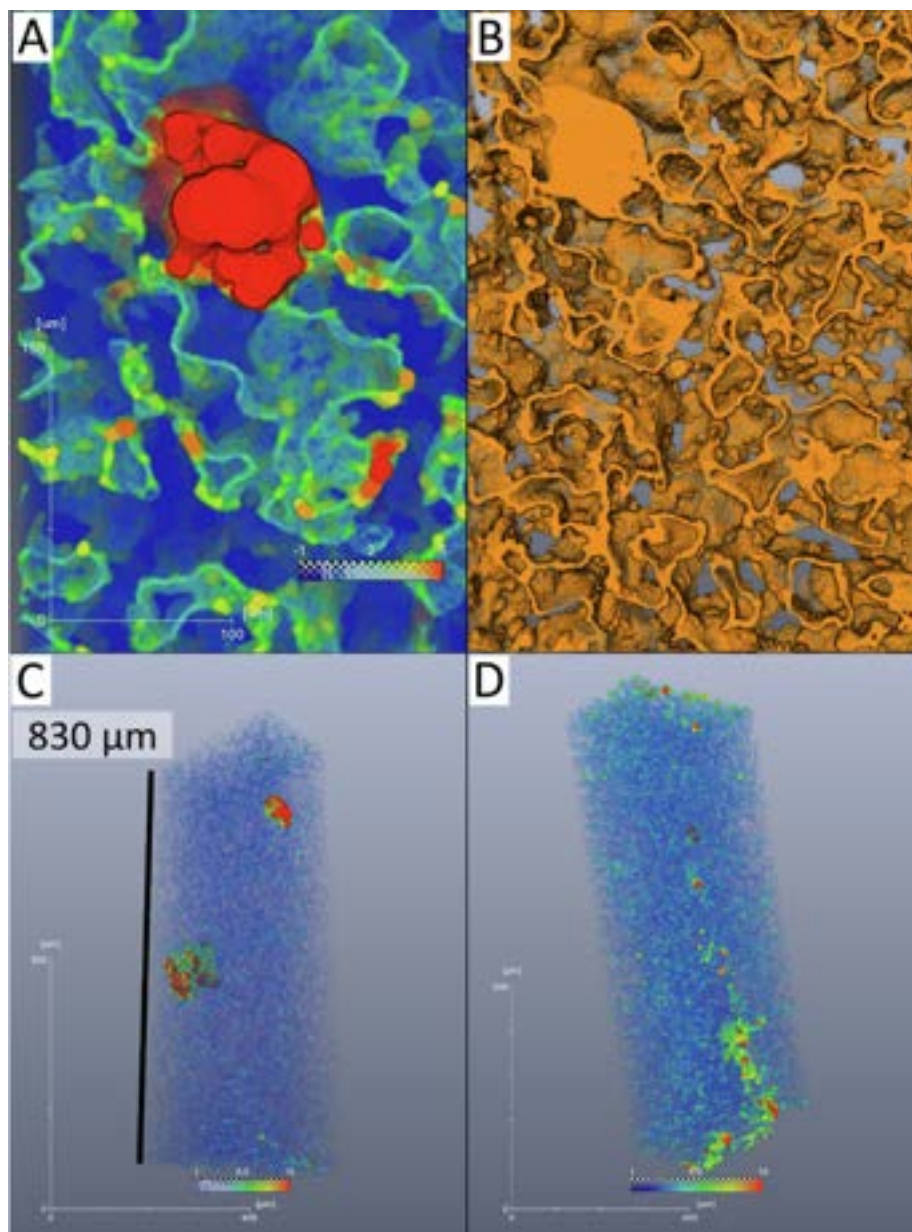
area. Similar features were detected also in the measured volumes of CT850.100 and CT900.10 samples (not shown here). The average oxide scale thickness for the CT850.30 sample is  $2.11 \mu\text{m}$  (Table 4) but locally it reaches significantly higher values in the breakaway oxidation region. According to the SEM analysis, the breakaway region appears only for the sample oxidised at 850 °C for 100 h but the tomographic experiments revealed that it has occurred also for the CT850.30 and CT900.10, demonstrating the necessity of the 3D analysis for detailed oxidation process research. The results of tomography studies presented here, indicate that the previously established threshold for breakaway oxidation appearance of  $\sim 6 \text{ wt\%}$  mass gain was slightly overestimated, since breakaway oxidation also occurs for lower mass gain values, as in case of samples CT850.30 (5.71 wt%) and CT900.10 (5.37 wt%).

### 3.3.2. Specific surface area and particle size

Material segmentation of the reconstructed volumes allows for generating a surface of each selected material, and consequently to evaluate its SSA, as a ratio of the surface area and weight. The SSA of the non-oxidised alloy was  $0.020 \text{ m}^2\text{g}^{-1}$  and it was observed that it changes after the oxidation process depending on the time of oxidation and on the temperature. The obtained values (Table 4) show a 10 % growth of SSA after 10 h of oxidation at 850 °C (CT850.10), while after 100 h at the same temperature (CT850.100), SSA grew by >50%. A similar increase ( $\sim 50 \%$ ) was observed for the CT900.10 sample. During oxidation, the oxide scale growth is irregular (as showed in Fig. 6), so the surface of the remaining alloy becomes more irregular as well, which explains the increase in its surface. It should be noted that due to the resolution limitation, in case of the more oxidized samples SSA might underestimated, however in the SEM images we observe that the fine roughness and porosity, which is not resolved in tomography is significant rather for the oxide scale, and less significant for the steel, for which SSA is evaluated.

Additionally, the total weight of the alloy fraction becomes smaller, which was also evaluated based on the obtained material statistics. Thus, the SSA of the alloy increases during the oxidation process. This results in an increased oxygen-alloy contact area, which in turn, facilitates further oxidation. On the other hand, oxide scale growth provides a diffusion barrier for chromium cations, which slows down the oxidation process. In the case of the investigated samples, this effect seems to counterbalance the effect of SSA growth.

Another important factor in the oxidation process is the grain size distribution of the porous alloys, as it is strongly related to the SSA. Moreover, oxidation processes of porous Fe22Cr alloy are determined by the diffusion of  $\text{Cr}^{3+}$  cations from the bulk to the surface, so for smaller particles, the diffusion path is shorter, which in turn accelerates the oxide scale growth. Tomographic microscopy is a well-suited tool for analysis of the particle size in porous alloys. For this purpose, particle separation was performed for the binary volume of the metallic core separated from other phases, which allowed for evaluation of statistics of steel particle size. Table 4 provides detailed information on particle size for each investigated sample. Average particle size before oxidation was very similar for each sample and it decreased during the oxidation. Surprisingly, the largest change was observed not for the sample CT850.100, which reached highest mass gain, but for the sample CT900.10, which was oxidised at highest temperature. The measured particle size was not related to the oxide morphology, so the observed effect may be linked to the more advanced breakaway oxidation in sample CT850.100. However, due to the change of particles morphologies, it is often not possible to justify if the particle separation was performed correctly for samples after oxidation. Therefore, such analysis should be performed via in-situ experiments. Further details, how the particle size distribution



**Fig. 7.** A, C) Oxide scale thickness map for the CT850.30 sample with B) corresponding morphology of the same sample region and comparison with D) the oxide scale thickness map for the CT900.10 sample.

analysis was performed are presented in the [supplementary material](#).

### 3.3.3. Effect of oxidation on porosity

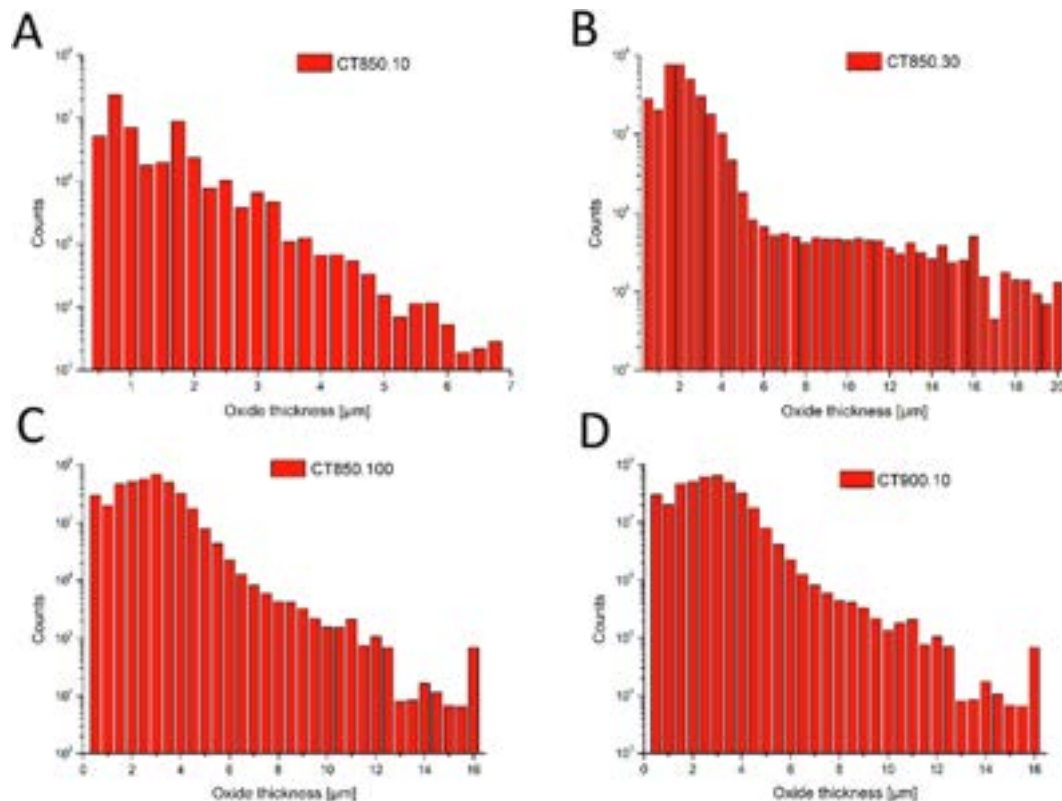
Analysis of the tomographic measurements clearly demonstrate that the open porosity dominates for the investigated alloy and creates a system of connected channels, which is crucial for applications requiring efficient gas transport through the material, as it is required for instance in membrane systems. Oxidation leads to the growth of the oxide scale resulting in formation of closed porosity and blocking of some pore channels, as it is visible for instance in [Figs. 5 and 6](#) in the locations marked by black arrows. However, the obtained material statistics ([Table 3](#)) shows that even after oxidation of the sample CT850.100, for which the most advanced oxidation degree was reached, the initial character of porosity was maintained, since the closed porosity was only  $\sim 0.1$  vol% of whole sample volume.

More importantly, during oxidation the overall porosity volume fraction and the size of the pore channels decrease because of the oxide scale growth. The porosity of the raw alloy calculated from the tomographic data varied between 32.0% and 32.5% for samples CT850.10, CT850.30 and CT850.100, which is in agreement with a value obtained with Archimedes method of 31% ( $\pm 2\%$ ). The sample CT900.10 had a significantly larger initial porosity of 38.2%. After oxidation, the porosity of samples has decreased to  $\sim 23\%$ , 22%, 20.4% and 28.5% ([Table 3](#)) for samples CT850.10, CT850.30, CT850.100 and CT900.10, respectively. These results, especially for sample CT900.10, show the importance of comparing the porosity before and after oxidation for the same volume, as the initial values may vary.

The size of the pore channels was evaluated as the “pore thickness”, which was calculated for each voxel using the same Thickness Map module, as for the oxide thickness evaluation. For the calculation of the average pore thickness, pores with a diameter

**Table 4**  
Evaluation of morphology changes.

Sample name	Specific surface area (SSA) [m <sup>2</sup> /g]		Average particle size [μm] (>6 μm) ( <b>average gauss fit</b> )		Average pore thickness > 1 μm) ( <b>lognormal fit &gt; 1 μm</b> )		Oxide thickness	
	Before	After	Before	After	Before	After	Before	After
CT850.10	0.020	0.022	32.5	31.5	13.6	12.6	–	1.12
			<b>32.7</b>	<b>32.0</b>	<b>14.0</b>	<b>12.4</b>		
CT850.30	0.020	0.027	31.3	27.6	13.0	10.1	–	2.11
			<b>30.4</b>	<b>27.8</b>	<b>15.0</b>	<b>10.8</b>		
CT850.100	0.020	0.031	30.5	26.7	12.5	10.3	–	2.45
			<b>30.2</b>	<b>27.0</b>	<b>14.5</b>	<b>11.0</b>		
CT900.10	0.020	0.030	31.0	26.7	16.5	14.8	–	2.45
			<b>31.4</b>	<b>27.1</b>	<b>17.9</b>	<b>15.4</b>		



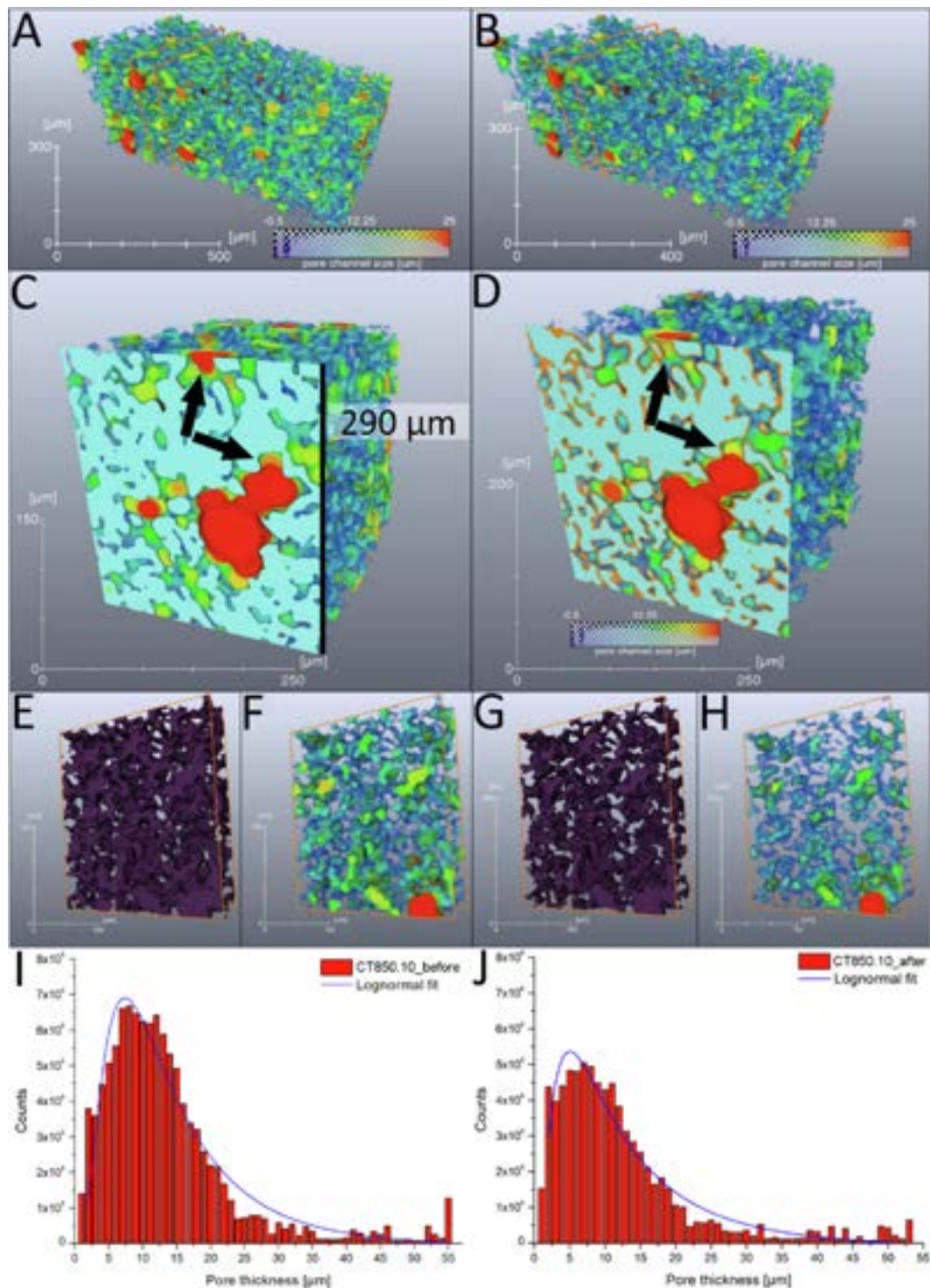
**Fig. 8.** Oxide scale thickness distribution for A) CT850.10, B) CT850.30, C) CT850.100, D) CT900.10.

below 1 μm were excluded from the statistics. As mentioned in the previous sections, there are cracks within the oxide scale, which are visible in SEM images (Fig. 3 K). In the case of tomography measurements, they are not detected but they appear as a small change in the grey scale. Moreover, such small objects do not significantly change the total porosity, as their fraction in the whole porosity is negligible.

The morphology and size distribution of porosity of samples CT850.10 and CT900.10 is illustrated in the 3-dimensional maps in Figs. 9 and 10, respectively. The colour scale corresponds to

the pore size value (blue is assigned to the smallest pores and red to the biggest ones). Fig. 9A and 10A represent the porosity thickness before oxidation and Fig. 9B and 10B after oxidation for CT850.10 and CT900.10, respectively. In both cases, the colour scales are shifted towards the blue colour after oxidation, this being more apparent for CT900.10. The pore size shrinkage is also clearly observed in clipping planes (Fig. 9C and Fig. 9D), which illustrate pore channel thickness maps before and after oxidation with exemplary regions of reduced pore size after oxidation marked by arrows.

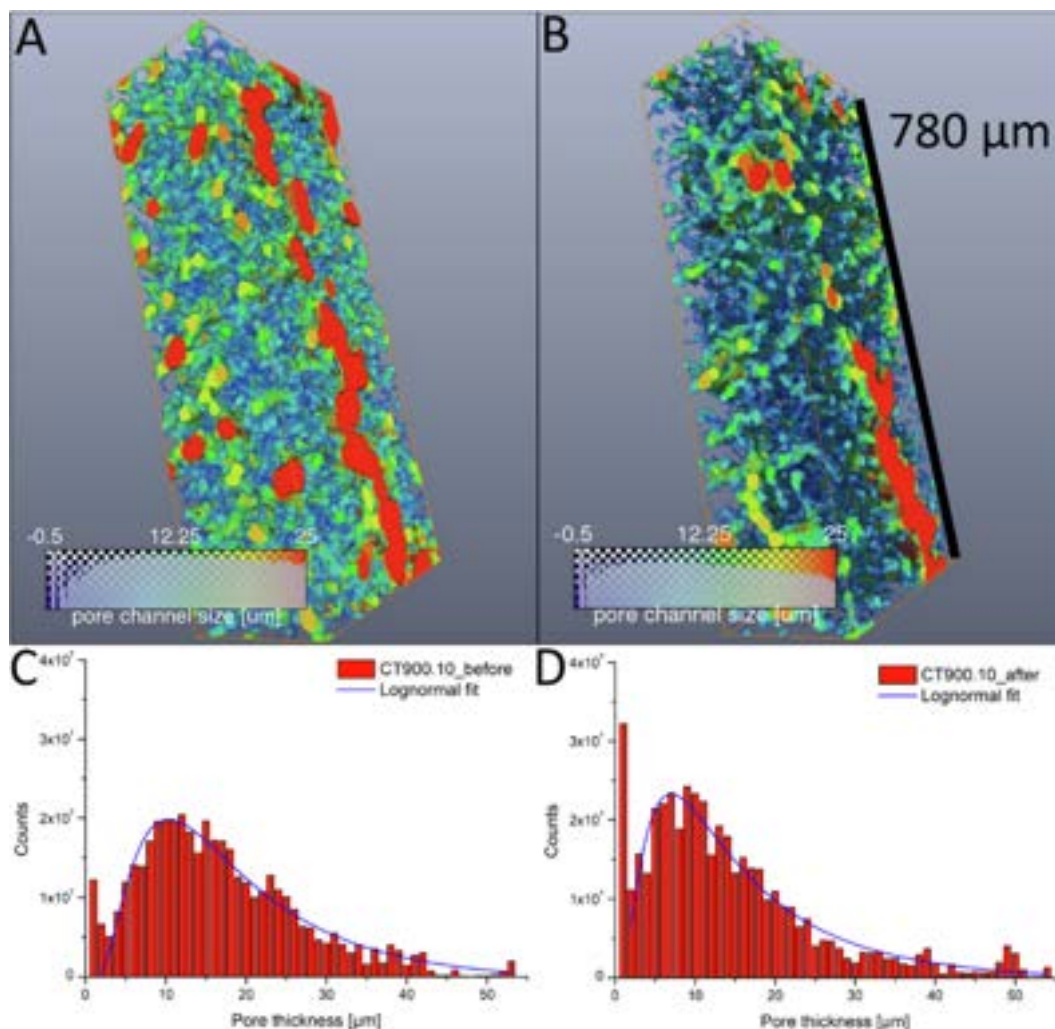




**Fig. 9.** A) Visualisation of pore channels thickness size for the CT850.10 sample before and B) after oxidation with exemplary clipping plane C) before and D) after oxidation. Morphology of the pore channels for the CT850.10 sample E) before and G) after oxidation with corresponding pore size distribution (F, G) and histograms of pore channels size thickness (I, J). Black arrows indicate exemplary corresponding regions of pore thickness map before (C) and after (D) oxidation.

The channel structure and changes of pore morphology before and after oxidation (purple colour), are illustrated in Fig. 9 E, G, respectively, which show volume rendering of the porosity phase obtained from material segmentation. These images show volume elements marked in Fig. 9 A and B with orange frames. The corresponding pores size distribution visualisation of the same volume fractions are presented in Fig. 9 F and Fig. 9 H. Decreasing of poros-

ity is clearly visible not only from comparison of colour scale in the pore channels thickness 3D maps, but also from decreasing of pores volume after oxidation which is observed as reduction of purple colour phase in Fig. 9 G as compared to Fig. 9 E. In the histograms of the pore thickness maps (Fig. 9 I, J), a decrease of the average pore size is also visible, as a shift of the fitted lognormal function peak and a smaller amount of pore voxels' counts for



**Fig. 10.** Visualisation of pore channels thickness size for CT900.10 A) before B) after oxidation with C, D) corresponding histograms of pore channel size thickness.

the oxidised sample compared with the non-oxidised one. Results of evaluation of changes in pore morphology, SSA, and oxide thickness are summarized in Table 4.

#### 4. Conclusions

A detailed study of the effect of high-temperature oxidation on the morphology changes in porous Fe22Cr stainless steel in the temperature range of 850 – 900 °C was performed using two complementary imaging techniques. Synchrotron tomographic microscopy provided insight into the complex 3-dimensional structure of various phases of the samples, while scanning electron microscopy allowed for resolving features beyond the spatial resolution of the tomographic measurements.

Tomographic microscopy was performed using a monochromatic X-ray beam, which together with the optimization of the reconstruction algorithm parameters, allowed not only for analysis of the morphology, but also for distinguishing and quantification of particular phases: the metallic core, oxide scale and porosity. Image analysis performed for the reconstructed volumes was used to analyse porosity and steel morphology changes, as well as the oxide scale growth occurring during the oxidation process. Each investigated sample was scanned before and after oxidation and in both cases, exactly the same regions were localised and analysed. Additionally, SEM images showed the microporosity and

cracks of the oxide scale that were not visible in tomograms, which was essential for understanding the results of material segmentation of tomographic data.

Analysis of the oxide scale has shown that for porous alloys the 3D analysis is necessary to evaluate the thickness of the oxide scale because the measurement of oxide scale thickness performed from 2D SEM images strongly depends on the polishing plane and the angle of polishing selection. The 3D analysis proved that for longer oxidation (time effect), as well as for higher oxidation temperature (temperature effect), the oxide scale thickness increases, which is connected with the SSA growth of the alloy. After oxidation for 10 h at 900 °C (CT900.10 sample) the SSA has increased by 50 % thus, the possible oxygen-alloy contact area has also become significantly larger. However, the oxide scale is also a diffusion barrier for  $\text{Cr}^{3+}$  cations and this effect seems to counterbalance the effect of SSA growth on the oxidation process because no change of slope is observed in mass gain measurements. The increase of SSA was also confirmed by particle size analysis. For each investigated sample the average particle size decreased after oxidation which is connected with the SSA growth and similarly to this effect, the greatest fall of average particle size was observed for the most oxidised samples.

Although the SEM analysis revealed breakaway region only for the CT850.100 sample, the tomography experiment proved its occurrence also for the CT850.30 and CT900.10 samples. This

shows that the 3D analysis is necessary for oxidation research of porous ferritic alloys. Nevertheless, SEM imaging, due to its higher spatial resolution, is a complementary method that is necessary for correct interpretation and full understanding of the tomographic results. These studies show the breakaway oxidation regions after oxidation in specific conditions but the origin of these regions remains unknown. Moreover, for the CT850.30 sample a few regions of breakaway oxidation have been identified thus, the mass gain of this sample was even bigger than in the case of CT900.10 but for the sample oxidised at the same temperature for 100 h (CT850.100) only one bigger place of breakaway oxidation was detected. For establishing preferable areas for breakaway oxidation appearance and their origin, in situ tomography studies are necessary, which will be the scope of our further research.

The porosity analysis showed that it has a form of connected channels and the open porosity dominates in the investigated alloy. Although, closed porosity was also detected and its fraction has increased during the oxidation, its amount was still so low that it should have no significant effect on the alloy properties, at least in the investigated range of oxidation degree. A more important effect appeared to be the significant decrease of the size of the open pores, caused by the growth of the oxide scale in the volume of pores. For the sample with the highest degree of oxidation (for the CT850.100 sample), the average pore channel size was decreased by 24 % (taking into consideration fitted lognormal function), showing that the studied alloy cannot be efficiently used as a gas membrane at so high temperatures.

The presented study provides a new characterization method of porous ferritic alloys by quantitative analysis of distinguished oxide, alloy and pore phases. The presented tomographic analysis provided data, which can improve the understanding of porous alloys failure caused by oxidation, modelling of the porous alloys' oxidation process and allow for prediction of the porous alloy lifetime.

### Declaration of Competing Interest

The authors declare that they have no known competing financial interests or personal relationships that could have appeared to influence the work reported in this paper.

### Acknowledgements

This project was supported by National Science Centre Poland (NCN) Sonata Bis 8 project number 2018/30/E/ST8/00821 "High-temperature corrosion studies and development of oxidation lifetime model of alloy powders and sintered porous alloys: effects of composition and microstructure".

The authors would like to acknowledge Höganäs AB, Sweden for porous steel samples production and the Paul Scherrer Institut, Villigen, Switzerland for provision of synchrotron radiation beamtime (proposal 20181598) at the TOMCAT beamline of the Swiss Light Source.

### Data availability

The raw/processed data required to reproduce these findings cannot be shared at this time as the data also forms part of an ongoing study.

### Appendix A. Supplementary material

Supplementary data to this article can be found online at <https://doi.org/10.1016/j.matdes.2022.110492>.

### References

- [1] D.J. Young, *High temperature oxidation and corrosion of metals*, Elsevier, 2008.
- [2] M.J. Pomeroy, Coatings for gas turbine materials and long term stability issues, *Mater. Des.* 26 (3) (2005) 223–231, <https://doi.org/10.1016/j.matdes.2004.02.005>.
- [3] H.J.C. Voorwald, R.C. Coisse, M.O.H. Cioffi, Fatigue strength of X45CrSi93 stainless steel applied as internal combustion engine valves, *Procedia Eng.* 10 (2011) 1256–1261, <https://doi.org/10.1016/j.proeng.2011.04.209>.
- [4] M. Park, J.-S. Shin, S. Lee, H.-J. Kim, H. An, H.-i. Ji, H. Kim, J.-W. Son, J.-H. Lee, B.-K. Kim, H.-W. Lee, K.J. Yoon, Thermal degradation mechanism of ferritic alloy (Crofer 22 APU), *Corros. Sci.* 134 (2018) 17–22, <https://doi.org/10.1016/j.corsci.2018.01.022>.
- [5] B. Talic, S. Molin, P.V. Hendriksen, H.L. Lein, Effect of pre-oxidation on the oxidation resistance of Crofer 22 APU, *Corros. Sci.* 138 (2018) 189–199, <https://doi.org/10.1016/j.corsci.2018.04.016>.
- [6] M. Bianco, S. Poitel, J.E. Hong, S. Yang, Z.J. Wang, M. Willinger, R. Steinberger-Wilckens, J. Van herle, Corrosion behaviour of nitrided ferritic stainless steels for use in solid oxide fuel cell devices, *Corros. Sci.* 165 (2020), <https://doi.org/10.1016/j.corsci.2019.108414>.
- [7] B. Öztürk, A. Topcu, S. Öztürk, Ö.N. Cora, Oxidation, electrical and mechanical properties of Crofer®22 solid oxide fuel cell metallic interconnects manufactured through powder metallurgy, *Int. J. Hydrogen Energy.* 43 (23) (2018) 10822–10833, <https://doi.org/10.1016/j.ijhydene.2018.01.078>.
- [8] A. Topcu, B. Öztürk, Ö.N. Cora, Performance evaluation of machined and powder metallurgically fabricated Crofer®22 APU interconnects for SOFC applications, *Int. J. Hydrogen Energy.* 47 (5) (2022) 3437–3448, <https://doi.org/10.1016/j.ijhydene.2021.06.036>.
- [9] J. Cao, M. Zheng, Z. Wang, X. Si, C. Li, X. Wang, Z. He, J. Qi, A low-temperature sealing method for metal-supported oxide fuel cell applications: Ni–Sn transient liquid phase bonding, *Vacuum* 187 (2021) 110048, <https://doi.org/10.1016/j.vacuum.2021.110048>.
- [10] A. Holt, P. Kofstad, Electrical conductivity and defect structure of Cr<sub>2</sub>O<sub>3</sub>. II. Reduced temperatures (<~1000°C), *Solid State Ionics* 69 (1994) 137–143, [https://doi.org/10.1016/0167-2738\(94\)90402-2](https://doi.org/10.1016/0167-2738(94)90402-2).
- [11] Y.H. Xiang, L.Z. Liu, J.C. Shao, H.J. Jin, A universal scaling relationship between the strength and Young's modulus of dealloyed porous Fe<sub>0.80</sub>Cr<sub>0.20</sub>, *Acta Mater.* 186 (2020) 105–115, <https://doi.org/10.1016/j.actamat.2019.12.046>.
- [12] C. Witherspoon, P. Zheng, M. Chmielus, D.C. Dunand, P. Müllner, Effect of porosity on the magneto-mechanical behavior of polycrystalline magnetic shape-memory Ni–Mn–Ga foams, *Acta Mater.* 92 (2015) 64–71, <https://doi.org/10.1016/j.actamat.2015.03.038>.
- [13] L. Zhao, S. Ha, K.W. Sharp, A.B. Geltmacher, R.W. Fonda, A.H. Kinsey, Y. Zhang, S.M. Ryan, D. Erdeniz, D.C. Dunand, K.J. Hemker, J.K. Guest, T.P. Weihs, Permeability measurements and modeling of topology-optimized metallic 3-D woven lattices, *Acta Mater.* 81 (2014) 326–336, <https://doi.org/10.1016/j.actamat.2014.08.037>.
- [14] E. Stefan, C. Denonville, Y. Larring, M. Stange, R. Haugsrud, Oxidation study of porous metal substrates for metal supported proton ceramic electrolyzer cells, *Corros. Sci.* 164 (2020) 108335, <https://doi.org/10.1016/j.corsci.2019.108335>.
- [15] M. Palcut, L. Mikkelsen, K. Neufeld, M. Chen, R. Knibbe, P.V. Hendriksen, Corrosion stability of ferritic stainless steels for solid oxide electrolyser cell interconnects, *Corros. Sci.* 52 (10) (2010) 3309–3320, <https://doi.org/10.1016/j.corsci.2010.06.006>.
- [16] R. Wang, Z. Sun, J.-P. Choi, S.N. Basu, J.W. Stevenson, M.C. Tucker, Ferritic stainless steel interconnects for protonic ceramic electrochemical cell stacks: Oxidation behavior and protective coatings, *Int. J. Hydrogen Energy.* 44 (2019) 25297–25309, <https://doi.org/10.1016/j.ijhydene.2019.08.041>.
- [17] A.W.B. Skilbred, R. Haugsrud, Sandvik Sanergy HT - A potential interconnect material for LaNbO<sub>4</sub>-based proton ceramic fuel cells, *J. Power Sources.* 206 (2012) 70–76, <https://doi.org/10.1016/j.jpowsour.2012.01.101>.
- [18] J.A. Glasscock, L. Mikkelsen, A.H. Persson, G. Pecanac, J. Malzbender, P. Blennow, F. Bozza, P.V. Hendriksen, Porous Fe<sub>21</sub>Cr<sub>7</sub>Al<sub>1</sub>Mo<sub>0.5</sub>Y metal supports for oxygen transport membranes: Thermo-mechanical properties, sintering and corrosion behaviour, *Solid State Ionics* 242 (2013) 33–44, <https://doi.org/10.1016/j.ssi.2013.04.006>.
- [19] D.N. Boccaccini, H.L. Frandsen, B.R. Sudireddy, P. Blennow, A.H. Persson, K. Kwok, P. Vang Hendriksen, Creep behaviour of porous metal supports for solid oxide fuel cells, *Int. J. Hydrogen Energy.* 39 (2014) 21569–21580, <https://doi.org/10.1016/j.ijhydene.2014.07.138>.
- [20] Y. Matus, L. Dejonghe, C. Jacobson, S. Visco, Metal-supported solid oxide fuel cell membranes for rapid thermal cycling, *Solid State Ionics* 176 (5–6) (2005) 443–449, <https://doi.org/10.1016/j.ssi.2004.09.056>.
- [21] G. Reiss, H.L. Frandsen, W. Brandstätter, A. Weber, Numerical evaluation of micro-structural parameters of porous supports in metal-supported solid oxide fuel cells, *J. Power Sources.* 273 (2015) 1006–1015, <https://doi.org/10.1016/j.jpowsour.2014.09.185>.
- [22] M. Stange, C. Denonville, Y. Larring, A. Brevet, A. Montani, O. Sicardy, J. Mougín, P.O. Larsson, Improvement of corrosion properties of porous alloy supports for solid oxide fuel cells, *Int. J. Hydrogen Energy.* 42 (17) (2017) 12485–12495, <https://doi.org/10.1016/j.ijhydene.2017.03.170>.
- [23] M. Mokhtari, T. Wada, C. Le Boulrot, J. Duchet-Rumeau, H. Kato, E. Maire, N. Mary, Corrosion resistance of porous ferritic stainless steel produced by liquid metal dealloying of Incoloy 800, *Corros. Sci.* 166 (2020) 108468, <https://doi.org/10.1016/j.corsci.2020.108468>.



- [24] D. Koszelow, M. Makowska, F. Marone, J. Karczewski, P. Jasiński, S. Molin, High Temperature Corrosion Evaluation and Lifetime Prediction of Porous Fe22Cr Stainless Steel in Air in Temperature Range 700–900°C, *Corros. Sci.* 189 (2021) 109589, <https://doi.org/10.1016/j.corsci.2021.109589>.
- [25] P.J. Withers, C. Bouman, S. Carmignato, V. Cnudde, D. Grimaldi, C.K. Hagen, E. Maire, M. Manley, A. Du Plessis, S.R. Stock, X-ray computed tomography, *Nat. Rev. Methods Prim.* 1 (1) (2021), <https://doi.org/10.1038/s43586-021-00015-4>.
- [26] K. Kapat, P.K. Srivas, A.P. Rameshbabu, P.P. Maity, S. Jana, J. Dutta, P. Majumdar, D. Chakrabarti, S. Dhara, Influence of Porosity and Pore-Size Distribution in Ti6Al4 v Foam on Physicomechanical Properties, Osteogenesis, and Quantitative Validation of Bone Ingrowth by Micro-Computed Tomography, *ACS Appl. Mater. Interfaces.* 9 (45) (2017) 39235–39248, <https://doi.org/10.1021/acsami.7b13960>.
- [27] H.J. Simon, G. Cibir, C. Reinhard, Y. Liu, E. Schofield, I.C. Freestone, Influence of microstructure on the corrosion of archaeological iron observed using 3D synchrotron micro-tomography, *Corros. Sci.* 159 (2019) 31–34, <https://doi.org/10.1016/j.corsci.2019.108132>.
- [28] S.S. Singh, C. Schwartzstein, J.J. Williams, X. Xiao, F. De Carlo, N. Chawla, 3D microstructural characterization and mechanical properties of constituent particles in Al 7075 alloys using X-ray synchrotron tomography and nanoindentation, *J. Alloys Compd.* 602 (2014) 163–174, <https://doi.org/10.1016/j.jallcom.2014.03.010>.
- [29] J.C. Hastie, M.E. Kartal, L.N. Carter, M.M. Attallah, D.M. Mulvihill, Classifying shape of internal pores within AlSi10Mg alloy manufactured by laser powder bed fusion using 3D X-ray micro computed tomography: Influence of processing parameters and heat treatment, *Mater. Charact.* 163 (2020) 110225, <https://doi.org/10.1016/j.matchar.2020.110225>.
- [30] V.D. Le, N. Saintier, F. Morel, D. Bellett, P. Osmond, Investigation of the effect of porosity on the high cycle fatigue behaviour of cast Al-Si alloy by X-ray micro-tomography, *Int. J. Fatigue.* 106 (2018) 24–37, <https://doi.org/10.1016/j.ijfatigue.2017.09.012>.
- [31] M. Mokhtari, C. Le Bourlot, J. Adrien, A. Bonnin, T. Wada, J. Duchet-Rumeau, H. Kato, E. Maire, Microstructure characterization by X-ray tomography and EBSD of porous FeCr produced by liquid metal dealloying, *Mater. Charact.* 144 (2018) 166–172, <https://doi.org/10.1016/j.matchar.2018.06.032>.
- [32] S. Dezecot, J.Y. Buffiere, A. Koster, V. Maurel, F. Szmytka, E. Charkaluk, N. Dahdah, A. El Bartali, N. Limodin, J.F. Witz, In situ 3D characterization of high temperature fatigue damage mechanisms in a cast aluminum alloy using synchrotron X-ray tomography, *Scr. Mater.* 113 (2016) 254–258, <https://doi.org/10.1016/j.scriptamat.2015.11.017>.
- [33] A. Idhil, C.N. Borca, A.-C. Uldry, M. Victoria, M. Samaras, Investigating the structure of iron-chromium alloys using synchrotron based X-ray microanalysis, *J. Nucl. Mater.* 416 (1–2) (2011) 65–69, <https://doi.org/10.1016/j.jnucmat.2010.11.097>.
- [34] Z. Wang, S. Wu, G. Kang, H. Li, Z. Wu, Y. Fu, P.J. Withers, In-situ synchrotron X-ray tomography investigation of damage mechanism of an extruded magnesium alloy in uniaxial low-cycle fatigue with ratchetting, *Acta Mater.* 211 (2021) 116881, <https://doi.org/10.1016/j.actamat.2021.116881>.
- [35] A.E. Paz y Puente, D. Erdeniz, J.L. Fife, D.C. Dunand, In situ X-ray tomographic microscopy of Kirkendall pore formation and evolution during homogenization of pack-aluminized Ni-Cr wires, *Acta Mater.* 103 (2016) 534–546, <https://doi.org/10.1016/j.actamat.2015.10.013>.
- [36] J. Stef, A. Poulon-Quintin, A. Redjaimia, J. Ghanbaja, O. Ferry, M. De Sousa, M. Gouné, Mechanism of porosity formation and influence on mechanical properties in selective laser melting of Ti-6Al-4V parts, *Mater. Des.* 156 (2018) 480–493, <https://doi.org/10.1016/j.matdes.2018.06.049>.
- [37] N. Ali, L. Zhang, H. Zhou, A. Zhao, C. Zhang, Y. Gao, Elucidation of void defects by soft reduction in medium carbon steel via EBSD and X-ray computed tomography, *Mater. Des.* 209 (2021) 109978, <https://doi.org/10.1016/j.matdes.2021.109978>.
- [38] S.K. Wilke, D.C. Dunand, Structural evolution of directionally freeze-cast iron foams during oxidation/reduction cycles, *Acta Mater.* 162 (2019) 90–102, <https://doi.org/10.1016/j.actamat.2018.09.054>.
- [39] T. Um, S.K. Wilke, H. Choe, D.C. Dunand, Effects of pore morphology on the cyclical oxidation/reduction of iron foams created via camphene-based freeze casting, *J. Alloys Compd.* 845 (2020) 156278, <https://doi.org/10.1016/j.jallcom.2020.156278>.
- [40] K. Kwok, D. Boccaccini, Å.H. Persson, H.L. Frandsen, Homogenization of steady-state creep of porous metals using three-dimensional microstructural reconstructions, *Int. J. Solids Struct.* 78–79 (2016) 38–46, <https://doi.org/10.1016/j.ijsolstr.2015.09.020>.
- [41] K. Zhuravleva, R. Müller, L. Schultz, J. Eckert, A. Gebert, M. Bobeth, G. Cuniberti, Determination of the Young's modulus of porous  $\beta$ -type Ti-40Nb by finite element analysis, *Mater. Des.* 64 (2014) 1–8, <https://doi.org/10.1016/j.matdes.2014.07.027>.
- [42] B. Mortimer, P. Gieveson, K.H. Jack, Precipitation of nitrides in ferritic iron alloys containing chromium, *Scand. J. Metall.* 1 (1972) 203–209.
- [43] G. Miyamoto, A. Yonemoto, Y. Tanaka, T. Furuhashi, T. Maki, Microstructure in a plasma-nitrided Fe-18 mass% Cr alloy, *Acta Mater.* 54 (18) (2006) 4771–4779, <https://doi.org/10.1016/j.actamat.2006.06.006>.
- [44] D. Paganin, S.C. Mayo, T.E. Gureyev, P.R. Miller, S.W. Wilkins, Simultaneous phase and amplitude extraction from a single defocused image of a homogeneous object, *J. Microsc.* 206 (1) (2002) 33–40, <https://doi.org/10.1046/j.1365-2818.2002.01010.x>.
- [45] T. Hildebrand, P. Rüeggsegger, A new method for the model-independent assessment of thickness in three-dimensional images, *J. Microsc.* 185 (1997) 67–75, <https://doi.org/10.1046/j.1365-2818.1997.1340694.x>.

## Particle size distribution analysis

In addition to the morphology and porosity of alloys, grain distribution might also be a key factor in the corrosion process, as it is strongly related to the specific surface area. The mass gain measurements (Figure 2) revealed that for porous Fe22Cr alloy the diffusion of  $\text{Cr}^{3+}$  cations determines the corrosion process, so for smaller particles, the diffusion path is shorter, which in turn accelerates the oxide scale growth. In addition to that, a decrease in particle size is connected with SSA increase (Table 4) which also leads to higher oxidation rate, as it was discussed in the 3.3.2 section.

Tomographic microscopy is a perfect tool for analysis of particle size and their connectivity in porous alloys. For this purpose, particle separation was performed for the binary volume of metallic core separated from other phases, which allowed for evaluation of statistics of steel particle size. In Figure S1 A-B, the particle size distribution of the non-oxidised sample is presented with corresponding histograms. The particle boundaries are clearly observed in narrow necks areas, so the obtained distribution seems to correspond well with the real structure of the alloy. The histograms for a non-oxidised sample and samples CT850.10, CT850.30, CT850.100, CT900.10 after oxidation are presented in order to show changes in particle size distribution and the Figure S.1C-J. The average value of particle size calculated from the fitted Gauss function is consistent with 'raw' data analysis (Table 4) thus, the contribution of particle size seems to be described as gaussian dependence. Analysis of histograms of particle size before and after oxidation for all investigated samples demonstrates that even after strong oxidation (like in the case of CT900.10 sample) the shape of the histogram is preserved, so the Gauss fitting can be still applied. The count peak values on 'y' axis before and after oxidation does not change significantly after oxidation but the fraction of the smallest particle remarkably increases.

Table 4 provides detailed information on particle size for each investigated sample. The smallest particles with volume below  $100 \mu\text{m}^3$  (which corresponds with  $\sim 6 \mu\text{m}$  equivalent diameter) were excluded from average calculations because of limited spatial resolution of the tomographic measurements. Even taking into consideration this assumption, the mean particle size decreased during corrosion exposure from  $32.5 \mu\text{m}$  to  $31.5 \mu\text{m}$  for the CT850.10 sample which was the least oxidised sample while for the CT900.10 sample this parameter decreased from  $31.0 \mu\text{m}$  to  $26.7 \mu\text{m}$ . These values correspond with a higher observed SSA increase for the CT900.10 sample than for CT850.10 and is in agreement with the noticeable shift of average particle size on the histograms.

Up to now, there is still a lack of systematic study about particle size effect on the corrosion process for ferritic alloys. Abe et al. [32] examined alloy grain size effect on corrosion resistance of dense Inconel 600 in  $850^\circ\text{C}$  steam. The average grain sizes used in this work were  $90 \mu\text{m}$ ,  $110 \mu\text{m}$ ,  $180 \mu\text{m}$  and  $320 \mu\text{m}$  and the corrosion process for each investigated fraction fulfilled the parabolic rate law. Until the breakaway corrosion occurred the largest grain alloy revealed the slowest corrosion rate, and for the smallest grain fraction the corrosion rate was the highest which is the same result as in our study for porous Fe22Cr alloy. However, the comparison between dense and porous alloys could not be accurate because one particle within porous alloy consists of many grains. The information about the diffusion character of the corrosion process allows for supposing that for smaller particle size alloy the corrosion rate is faster but more detailed research is still necessary.

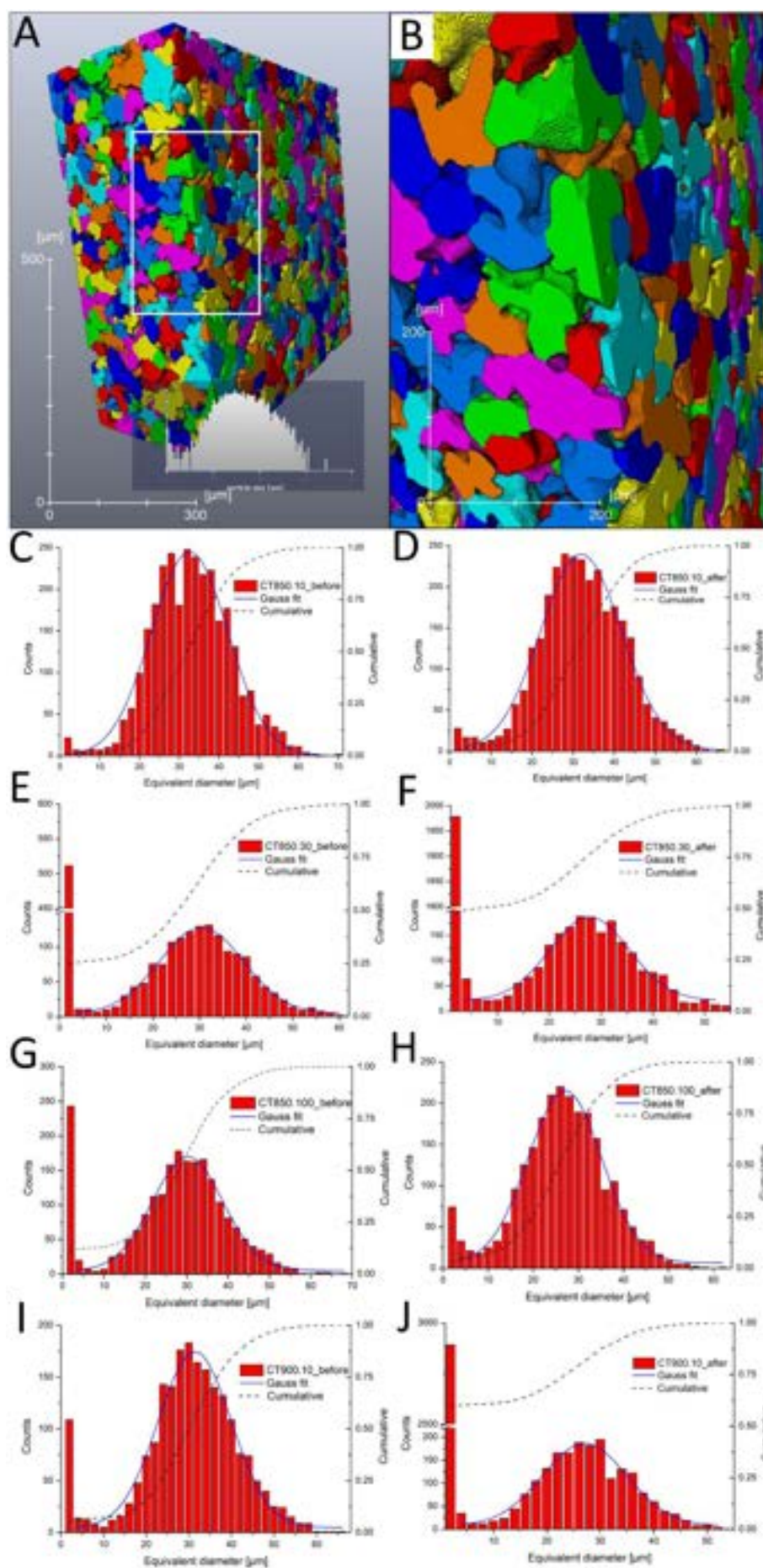


Figure S1. Grain distribution of non-oxidised sample with corresponding histograms of equivalent diameter of 'raw' sample compared with histogram of equivalent diameter after exposure for C,D) CT850.10 E,F) CT850.30 G,H) CT850.100 I,J) CT900.10.

### Oxide scale thickness analysis

For a better understanding of the oxide scale growth, the additional histograms of the percent contribution of oxide thickness are shown in Figure S2 for each examined sample. The dash lines divide histograms into regions where cumulative counts for the oxide scale thickness are ~99 % and ~1 % of all counts. Locally, the oxide scale that grew on two (or more) particles could be counted as one, but this representation of the oxide thickness data demonstrates a small contribution of the highest values in histograms, so the chosen calculation algorithm seems to be accurate.

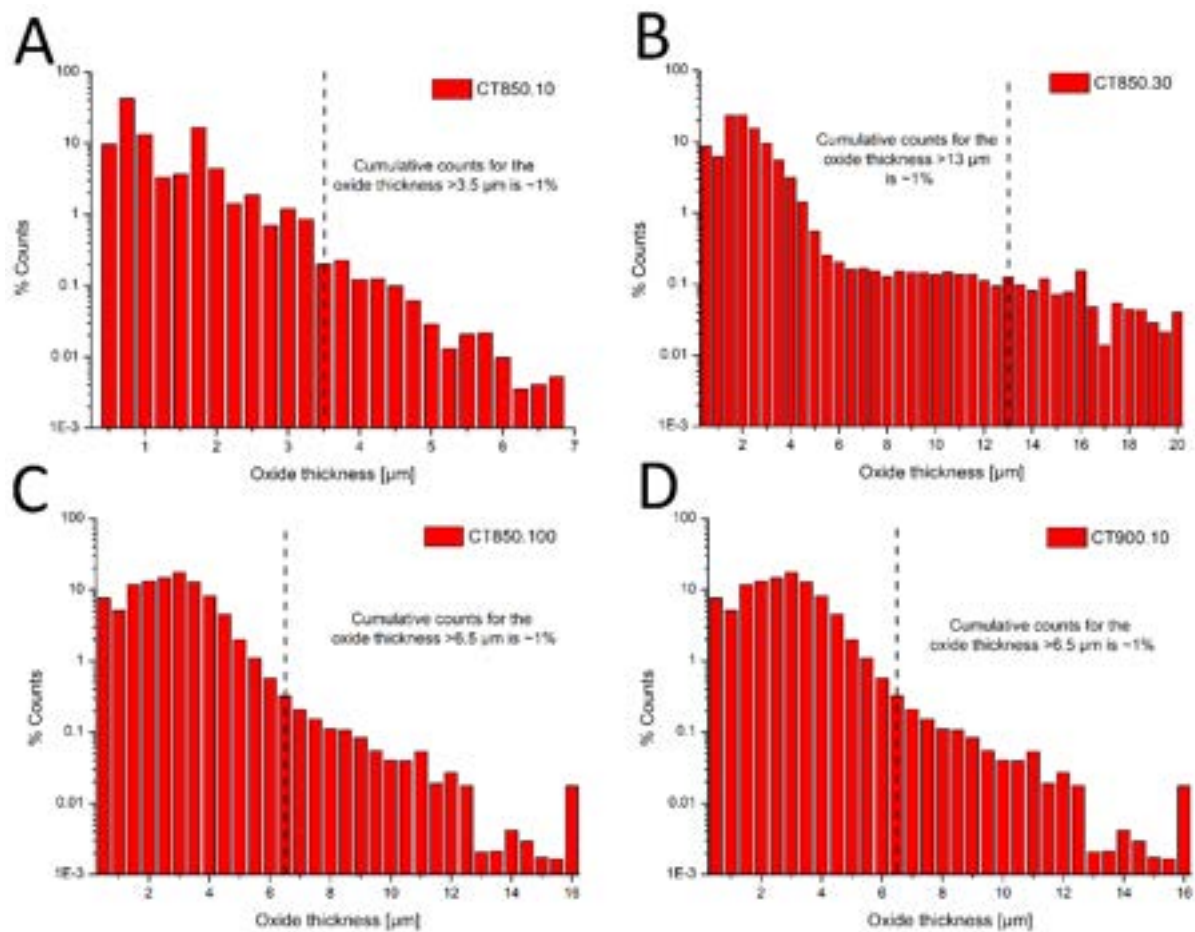


Figure S2. Percent contribution of the oxide thickness calculated for A) CT850.10, B) CT850.30, C) CT850.100 and D) CT900.10.

### **5.3. High-temperature corrosion of ~ 30 Pct porous FeCr stainless steels in air: long-term evaluation up to breakaway**

The model that was proposed in the publication presented in Section 5.1. relied on short-term oxidation tests. In this work, a validation of the proposed model based on long-term oxidation experiments was performed at temperature ranging from 600°C to 900°C for three different alloy compositions: Fe20Cr, Fe22Cr, and Fe27Cr.

It was confirmed that the corrosion process for porous ferritic chromia-forming alloys is limited by the diffusion process, and that the alloy lifespan depends on its chemical composition. The alloys with higher initial chromium content proved to have a longer lifespan at all considered temperatures.

The extrapolated weight gain curves of the Fe20Cr and Fe22Cr were in line with the experimentally measured mass gains obtained by cyclic oxidation tests. The experimentally determined times when breakaway corrosion appears were < 1750 and 2750 hours for the Fe20Cr and Fe22Cr alloys oxidized at 700°C, respectively. On the other hand, the lifespan that was calculated using the model (at the same temperature) was 1250 h  $\pm$  535 h and 1460 h  $\pm$  640 h for Fe20Cr and Fe22Cr, respectively. The model seems to underestimate the lifetime of the alloys.


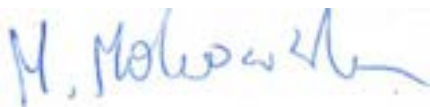




Interestingly, the long-term exposure of porous alloys to the temperature of 600°C revealed that even 6000 h of oxidation did not significantly change the Cr content within the alloys. Moreover, the porosity of the samples was barely impacted. The weight gain curve for these samples revealed ~ 1 wt. % of change for Fe22Cr and Fe27Cr alloys and ~2 wt. % for Fe20Cr alloy. It indicates that porous ferritic alloys are promising material for application in devices operating at ~600°C.

My original contribution in this work was:

- Improving the high-temperature corrosion model for porous alloys by taking into consideration different chemical compositions
- Validating the lifespan prediction model proposed in [DK1] based on long-term oxidation experiments



Statement of the co-authors' contribution to the publication entitled 'High-temperature corrosion of ~ 30 Pct porous FeCr stainless steels in air: long-term evaluation up to breakaway':

Name and surname	Contribution to the publication	Signature
Damian Koszelow	Conceptualization, Methodology, Formal Analysis, Investigation, Writing – Original Draft	
Małgorzata Makowska	Supervision, Formal Analysis, Writing – Review & Editing	
Agnieszka Drewniak	Validation, Writing – Review & Editing	
Grzegorz Cempura	Investigation – SEM/TEM imaging	
Piotr Jasiński	Supervision, Resources	
Sebastian Molin	Conceptualization, Supervision, Project administration, Funding acquisition, Writing – Review & Editing	



# High-temperature Corrosion of ~ 30 Pct Porous FeCr Stainless Steels in Air: Long-Term Evaluation Up to Breakaway

D. KOSZELOW, M. MAKOWSKA, A. DREWNIAK, G. CEMPURA, P. JASIŃSKI, and S. MOLIN

In this work, a long-term (up to 6000 hours) corrosion evaluation of three porous (~ 30 pct of initial porosity) ferritic iron-chromium alloys with different Cr contents (20, 22, and 27 wt pct of Cr) was carried out at 600 °C, 700 °C, 800 °C, and 900 °C in air. Mass gain measurements and SEM analyses revealed that at temperatures above 600 °C, all alloys exhibit breakaway corrosion, whereas at 600 °C, none of the alloys were heavily oxidized even after 6000 hours. Based on the results, the diffusion character of the corrosion of porous chromia-forming alloys was identified. The microstructure changes at high temperatures in porous alloys containing 22 wt pct of Cr were determined in detail by transmission electron microscopy. The proposed prediction model indicated that the lifetimes of the Fe20Cr and Fe22Cr alloys were determined as 1250 hours ( $\pm$  535 hours) and 1460 hours ( $\pm$  640 hours), respectively. It is in agreement with the long-term oxidation experiment. For the Fe27Cr alloy, the deviation between predicted and observed lifetimes occurs. The proposed model allows for qualitative estimation of the porous alloys' lifetime with experimentally validated accuracy.

<https://doi.org/10.1007/s11661-023-07005-z>

© The Author(s) 2023

## I. INTRODUCTION

THE porous form of ferritic alloys (characterized by code centered cubic crystallographic structure—BCC) was proposed as a support component in solid oxide cells (SOCs).<sup>[1–3]</sup> The advantages of using porous alloys in such devices are their lower price, which allows for decreasing a cost of the whole device when compared with the SOC components that used advanced ceramic components, as well as the manufacturability of complex shapes.<sup>[4]</sup> Other possible applications of porous alloys include their use as components of gas membranes<sup>[5]</sup> and sensor systems.<sup>[6]</sup> However, use of porous iron-chromium

alloys (as well as other porous alloys) at high temperatures is hindered by the limited knowledge of their oxidation properties under operating conditions.

Porous alloys have significantly larger specific surface areas than their dense forms, so the interface between the air (oxygen source) and alloy is also greater. As indicated in our previous work, the specific surface area of a porous alloy is up to 28 times larger than that of its dense form,<sup>[7]</sup> which is expected to have a tremendous impact on the corrosion kinetics. For the long-term corrosion resistance of the ferritic FeCr alloys, the most important factor is the chromium reservoir. During the high-temperature exposure, the chromium oxidizes into chromia up to the moment that there is large loss of chromium in the alloy and oxidation of Fe starts. The uncontrolled oxidation of Fe is called breakaway corrosion process. Due to the increased interface area between air and the alloy, for porous alloys, the appearance of a breakaway corrosion is expected to be faster than for the dense alloys. Nevertheless, the influence of the alloys' porosity on their corrosion resistance has not been well described yet, and there are still only a few papers on the corrosion of porous alloys.<sup>[8–14]</sup>

Stefan *et al.* demonstrated that the corrosion process of porous FeCr alloys follows the parabolic rate law, which confirms the diffusion character of the corrosion process for porous ferritic alloys (similarly to the case of

D. KOSZELOW, A. DREWNIAK, P. JASIŃSKI, and S. MOLIN are with the Advanced Materials Centre, Faculty of Electronics, Telecommunications and Informatics, Gdańsk University of Technology, 80-233 Gdańsk, Poland. Contact e-mail: damian.koszelow@pg.edu.pl M. MAKOWSKA is with the Laboratory for Nuclear Materials, Laboratory for Synchrotron Radiation and Femtochemistry, Paul Scherrer Institut, 5232 Villigen, Switzerland. G. CEMPURA is with the AGH University of Science and Technology, Faculty of Metal Engineering and Industrial Computer Science, International Centre of Electron Microscopy for Materials Science, al. Mickiewicza 30, 30-059 Krakow, Poland.

Manuscript submitted November 7, 2022; accepted February 4, 2023.

Article published online February 27, 2023

dense alloys).<sup>[11]</sup> Boccaccini *et al.* indicated the similarity of the creep mechanism between porous and dense alloys at 650 °C to 800 °C, which is important for metal-supported solid oxide fuel cell applications.<sup>[9]</sup> High creep resistance protects against electrolyte bending during operation.

To ensure a sufficient (> 10,000 hours) lifespan of devices containing components consisting of porous ferritic alloys, specific requirements, such as gas permeation and high conductivity under operating conditions, have to be fulfilled. High chromium content (usually > 16 wt pct) alloys seem to be the only good choice because of their high corrosion resistance in air and hydrogen atmospheres. Many research groups have demonstrated the use of dense forms of these alloys (such as Crofer 22 APU and Crofer 22 H by Sanergy, which contain 20 to 24 wt pct Cr) in SOC systems.<sup>[15–20]</sup> During the exposure, a slow diffusion of  $\text{Cr}^{3+}$  cations leads to the formation of a continuous passive layer of  $\text{Cr}_2\text{O}_3$  on the alloy surface that protects the alloy from further oxidation.<sup>[21–23]</sup> The same mechanism of the corrosion process is observed for porous FeCr alloys. Although there are metal oxides with better corrosion protective properties than  $\text{Cr}_2\text{O}_3$  (*i.e.*,  $\text{Al}_2\text{O}_3$  and  $\text{SiO}_2$ ),<sup>[24–26]</sup> they cannot be used for the discussed application due to their poor electrical conductivity at high temperatures ( $10^{-8}$  to  $5 \times 10^{-3} \text{ mS cm}^{-1}$  at 500 °C to 1000 °C for  $\text{Al}_2\text{O}_3$  and  $10^{-5}$  to  $2 \times 10^{-3} \text{ mS cm}^{-1}$  at 500 °C to 1000 °C for  $\text{SiO}_2$ ).<sup>[27]</sup> In contrast, chromia ( $\text{Cr}_2\text{O}_3$ ) has an electrical conductivity of 1 to 10  $\text{mS cm}^{-1}$  at 600 °C to 800 °C.<sup>[28]</sup>

Several approaches have been developed to estimate the lifespan of alloys in recent years. For instance, Huczowski *et al.* connected the thickness of an alloy sheet with its lifespan.<sup>[29]</sup> They observed that for chromia-forming alloys, the time to the appearance of breakaway corrosion increases with the specimen's thickness. For example, the lifespan of Crofer 22 APU increases by almost 2 orders of magnitude when the thickness of the oxidized sample increases from 0.1 to 1 mm. Asensio-Jimenez *et al.* also confirmed a similar dependence.<sup>[30]</sup> On the other hand, Tucker *et al.* proposed a 3  $\mu\text{m}$  thickness of oxide scale as a threshold value for estimating the lifespan of the alloy.<sup>[31]</sup> Huczowski *et al.* showed that there is a threshold value of chromium content which provides a protective feature (~ 12 wt pct of Cr in FeCr systems).<sup>[29,32]</sup> In our previous work, a similar model for estimating the lifespan of porous Fe22Cr was proposed, and it assumed a 10 to 12 pct chromium content threshold band to reach a breakaway corrosion formation point.<sup>[7]</sup> This model took into consideration only short-term oxidation data, so it should still be verified by long-term experiments.

The porous form of high chromium FeCr alloys is considered a potential support material in SOCs. The chemical composition provides sufficient electrical conductivity for efficient current collection. The open porosity of the investigated alloy allows for gas transport through the material, which is an important feature for reactant supply to SOCs electrodes. The growing oxide consumes Cr and also decreases gas transport

through the porous alloy, shortening its lifespan. To the best of our knowledge, this is the first work addressing the lifespan evaluation of the porous FeCr alloys based on long-term oxidation tests. Defining the lifespan of the porous ferritic FeCr alloys allows for the determination of the lifespan of metal-supported SOCs and gas membranes. Thus, long-term oxidation research is necessary for the creation of the lifespan prediction model of porous FeCr alloys.

This study describes an evaluation of the long-term (up to 6000 hours) corrosion process for porous FeCr alloys with different Cr contents (20 to 27 wt pct Cr) in the 600 °C to 900 °C temperature range. The obtained results were compared with the available dense alloy data. Then, the lifespan of the alloys was estimated based on information from post-mortem analyses such as mass gains and changes in the chromium level during exposure for each alloy composition.

## II. EXPERIMENTAL

### A. Sample Preparation

Porous metal sheets were sourced from Höganäs AB (experimental alloys Fe20Cr, Fe22Cr and Fe27Cr, Höganäs, Sweden). These alloys were produced from powders with a particle size fraction < 53  $\mu\text{m}$  by a tape-casting process and were sintered in hydrogen (1250 °C for 30 minutes). The sintered sheets had dimensions of ~ 10 × 10  $\text{cm}^2$  and a thickness of ~ 0.35 mm. The composition of each investigated alloy reported by the producer is presented in Table S.1. These data were confirmed by the Inductively Coupled Plasma (ICP) spectroscopy and energy-dispersive X-ray (EDX) methods.

The initial porosity of the samples reported by the producer is 30 pct. This value was confirmed using two approaches: the Archimedes method—liquid displacement (using kerosene), and an electron microscopy image analysis using the commercial Phenom PoroMetric Software (Thermo Fisher). The porosity was determined by analyzing 20 pictures taken at a magnification of 2500× for each analyzed specimen. The error bars were calculated as a standard deviation of the mean value. The porosity was also determined *via* the image analysis method after selected time intervals for each oxidation temperature.

For the long-term oxidation experiments, the alloy sheet was cut into 1 × 1  $\text{cm}$  squares. For the short-term thermogravimetric experiments, samples with dimensions of 1 × 2  $\text{cm}$  were used. After cutting, the samples were cleaned in an ultrasonic bath sequentially in acetone and ethanol.

### B. Long-Term Oxidation Tests

Long-term cyclic high-temperature oxidation was performed in a chamber furnace in an air atmosphere at 600 °C, 700 °C, 800 °C, and 900 °C. For each temperature, at least 10 specimens of each alloy were used for statistics/reproducibility. The oxidation cycles

at 600 °C, 700 °C, and 800 °C had a duration of 100 and 150 hours initially (total 250 hours) followed by cycles of 250 hours up to breakaway. For 900 °C, the cycles were 10, 20, and 70 hours, totalling 100 hours. The heating and cooling rates were 180 °C h<sup>-1</sup>. The samples were periodically removed from the furnace and weighed on a microbalance (Radwag XA 5Y.M, accuracy of 1 µg, Poland). The mass gain was calculated as the relative mass change (pct) with respect to the initial sample mass. The mass gain was also recalculated to the surface specific mass gain (mg cm<sup>-2</sup>), using the surface area information from our previous work (0.022 cm<sup>2</sup> g<sup>-1</sup>, calculated from a tomographic experiment<sup>[7]</sup>).

### C. Thermogravimetric Analysis

Short-term thermogravimetric experiments were performed using a CI Precision MK5-2 (United Kingdom) thermobalance. The oxidation time at a holding temperature of 700 °C was 300 hours and a heating rate of 180 °C h<sup>-1</sup>. Measurements were carried out with an airflow rate of 30 mL min<sup>-1</sup>.

The lifetimes of the porous alloys were predicted based on short-term isothermal thermogravimetric data and the methodology developed in Reference 7. For Fe20Cr and Fe27Cr, the threshold mass gain values for the appearance of breakaway corrosion were calculated as 5.1 and 8.3 pct, respectively (determined at 900 °C). Short-term mass gain curves, presented in log-log plots, were extrapolated using the linear regression method. The confidence interval was determined by the prediction band method, assuming a 95 pct confidence level. The predicted lifetime was the intersection of the fitting and the threshold mass gain values. These data were compared with the cyclic oxidation mass gains and scanning electron microscopy (SEM) micrographs of the alloys.

### D. Microscopy Analysis

The microstructure of the samples was analyzed using scanning (SEM) and transmission (TEM) electron microscopy. A Phenom XL SEM microscope (Thermo Fisher Scientific, Netherlands) was used to observe changes on the surface and polished cross-section microstructure of the alloys. A backscatter electron detector (BSE) was used. Changes in the chemical compositions were determined by energy-dispersive X-ray spectroscopy (EDX) using an integrated analyzer (Thermo Fisher Scientific, 25 mm<sup>2</sup> Silicon Drift Detector).

The Cr content of the as-produced and differently oxidized alloys was calculated as the average of 15 EDX measurements carried out in different regions of the samples. The error bars were determined as the standard deviation.

The samples for the TEM investigations were prepared as lamellae. They were prepared by sputtering the sample surface with Ga<sup>+</sup> ions emitted from a liquid metal ion source (FIB). A thin Pt layer was deposited on the region of interest to minimize the curtain effect while

thinning the sample with the ion beam. The lamellae were finished with thinning down to a level of several dozen nanometers after being mounted in a TEM-dedicated copper grid.

The TEM/STEM analyses were performed using a Cs probe-corrected Titan Cubed G2 60-300 microscope (FEI) equipped with the ChemiSTEM™ system. High-resolution STEM (HRSTEM) images were acquired using a high-angle annular dark-field (HAADF) detector.

## III. RESULTS AND DISCUSSION

### A. Characterization of the Raw Porous Alloys

The Fe20Cr, Fe22Cr, and Fe27Cr alloys have a ferritic crystallographic structure and their chemical compositions, as measured by the ICP and EDX methods, which are presented in Table I. The alloys differ mainly in the Cr and Mn content. A good correlation between the values obtained by the ICP and EDX methods was obtained. The results of both techniques are also consistent with the alloy composition provided by the manufacturer (Table S.1).

The surface and cross-section SEM images of the Fe22Cr alloy are presented in Figure 1. The surfaces of the Fe20Cr and Fe27Cr alloys were similar and are presented in Figure S.1. Figure 1(b) shows well-connected steel particles with grain boundaries. The porosity of the alloy is clearly visible. The results of the porosity measurements were similar for all alloys. Using the Archimedes method, the porosity was 30 ± 2 pct, while the porosity was determined as 29 ± 5 pct for each investigated alloy by the image analysis of the polished cross sections. Based on the image analysis, the average pore size (equivalent diameter) was ~ 11 µm, with a median pore size of ~ 7 µm (results summarized in Table S.2). No significant differences in the morphology or porosity of the alloys were observed, which justifies also using the experimentally determined specific surface area of the Fe22Cr sample for Fe20Cr and Fe27Cr alloys.

### B. Long-Term Corrosion Exposures of Porous Alloys

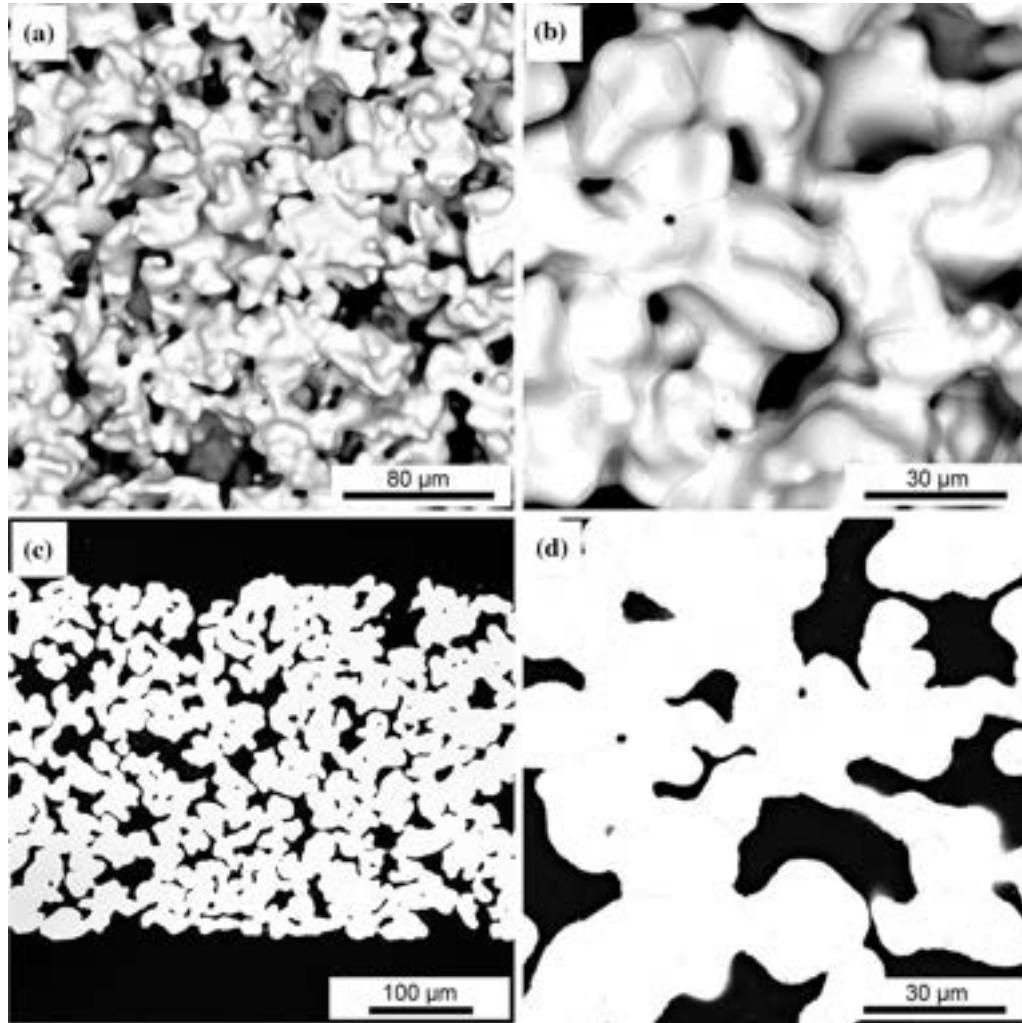
The alloys were oxidized at high temperatures (600 °C, 700 °C, 800 °C, and 900 °C) in an air atmosphere to determine the properties of the corrosion kinetics. The results of the mass changes are presented in Figures 2(a) through (d).

At 600 °C, even though the oxidation time was quite substantial (6000 hours, 24 thermal cycles), the overall mass gain was low, *i.e.*, < 2 pct. A noticeable difference can be observed between the Fe20Cr and the Fe22Cr/Fe27Cr alloys. For the Fe20Cr, the first oxidation cycle (0 to 100 hours) caused a rapid ~ 1 pct mass gain, which later on developed similarly to the Fe22Cr/Fe27Cr (further ~ 1 wt pct increase). The cause for the initial mass gain is the formation of iron oxide in this initial oxidation time, as will be substantiated later.



**Table I. Chemical Composition of the Alloys Obtained from the ICP and EDX Measurements**

Target Composition	Fe	Analyzed Chemical Composition, Wt F					[Information from the ICP Measurement]				EDX, Wt Pct	
		Cr	Mn	Ni	Si		Ti	Co	Ca	Na	Cr	Mn
Fe20Cr	bal	20.86	0.03	0.05	0.08		0.01	0.02	0.00	0.02	20.2	0.0
Fe22Cr	bal	21.87	0.25	0.02	0.08		0.01	0.01	0.00	0.00	21.3	0.1
Fe27Cr	bal	26.77	0.33	0.01	0.08		0.01	0.01	0.04	0.00	27.6	0.2

**Fig. 1—SEM (backscatter electron detector) images of (a, b) surface, (c, d) cross section of the as-produced Fe22Cr alloy.**

At 700 °C, the mass gain of the different alloys was similar until ~ 2000 hours, where a deviation for the Fe20Cr alloy was observed (at ~ 12 wt pct), due to the start of breakaway oxidation. At ~ 2750 hours (~ 9 pct), the Fe22Cr alloy started to increase its mass. For the Fe27Cr, with the highest Cr content, the mass gain increased steadily until ~ 4750 hours, when breakaway could be observed *via* increased mass change.

At 800 °C and 900 °C, the mass gains were much faster. At 800 °C, breakaway oxidation occurred in less than 500 hours. At 900 °C, the time to breakaway for all

the alloys was < 100 hours. The mass gain data show the strong dependence on the temperature, and a dependence on the alloy Cr content.

The appearance of breakaway corrosion could be easily detected from Figures 2(b) and (c) as a change of the curve's slope. A deviation from linear dependence was clearly visible for the Fe20Cr alloy after 2000 hours of oxidation at 700 °C and after 500 hours of oxidation at 800 °C. The same behavior was observed for the Fe22Cr alloy after 3000 hours of oxidation at 700 °C and 500 hours of oxidation at 800 °C. For the Fe27Cr

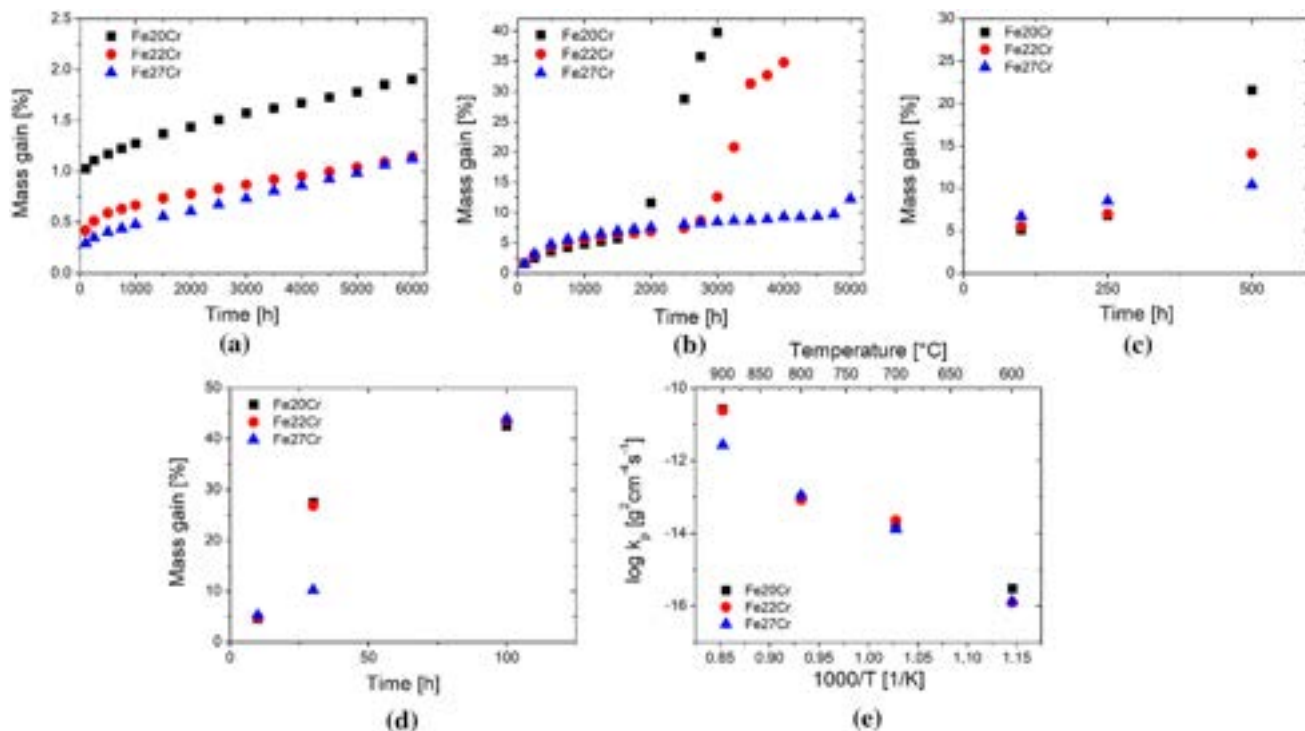


Fig. 2—Percentage mass change of oxidized Fe20Cr, Fe22Cr, and Fe27Cr alloys at (a) 600 °C, (b) 700 °C, (c) 800 °C, and (d) 900 °C. (e) The Arrhenius plot for Fe20Cr, Fe22Cr, and Fe27Cr alloys.

alloy, linear dependence was observed for each temperature and the first signs of breakaway corrosion appeared after 4750 hours of oxidation at 700 °C, but no trace of this was detected at 800 °C. The times that breakaway corrosion were determined to occur are based on macroscopically determined mass gain data. As studied by tomography,<sup>[33]</sup> the breakaway can occur locally in separated regions within the sample, which does not cause a large, measurable mass gain. Rough estimation of the mass gain for a totally oxidized (~ 43 wt pct mass gain) single particle of 20  $\mu\text{m}$  diameter is only ~ 10 ng, so, well below the balance accuracy (~ 1  $\mu\text{g}$ ). Therefore, the macroscopically determined start point of the breakaway oxidation is observed with some delay and the local breakaway oxidation starts earlier. Figures S.2 and S.3 present the mass gains of the individual samples measured in each series. The scatter, which corresponds to the breakaway corrosion starting point, is noticeable. Therefore, the average breakaway oxidation start time for the set of samples has to be treated as a generalized, statistical process.

At 900 °C, the oxidation process is extremely fast. After 100 hours of oxidation, full oxidation (~ 43 wt pct mass gain) was observed for each investigated alloy. For the Fe20Cr and Fe22Cr samples, the observed mass gain was already significantly higher than for the Fe27Cr after 30 hours of oxidation, which might indicate the formation of breakaway corrosion regions for these alloys.

To determine the possible oxidation mechanism, the mass gain data were plotted in a log-log graph (Figure S.4). The mass gains follow linear curves, with a slope approaching  $n \sim 0.5$ , which indicates a diffusion-limited oxidation process. Typically, outward cation diffusion ( $\text{Cr}^{3+}$ ) is the rate-limiting step in FeCr alloys. This mechanism can be described by the parabolic rate law using the equation:

$$\left(\frac{\Delta m}{S}\right)^2 = k_p \times t, \quad [1]$$

where  $S$  is the surface of the alloy,  $\Delta m$  is a change of the alloy's mass,  $k_p$  is the parabolic rate constant, and  $t$  is the time of exposure to high-temperature conditions. Typically, the  $k_p$  values are dependent on the temperature according to the Arrhenius equation:

$$k_p = A \times \exp\left(-\frac{E_A}{RT}\right), \quad [2]$$

which can be used to calculate the activation energy ( $E_A$ ).

Based on the assumption of the parabolic kinetic law, corrosion rate constants ( $k_p$ ) and activation energies ( $E_A$ ) were fitted to Eqs. [1] and [2] and are summarized in Table II and presented in Figure 2(e).

The corrosion rates calculated from the parabolic rate law were similar for each alloy composition at 600 °C ( $1.2 \times 10^{-16}$  to  $3.1 \times 10^{-16} \text{ g}^2\text{cm}^{-4} \text{ s}^{-1}$ ) and at 700 °C

Table II. Corrosion Parameters After Oxidation at Different Temperatures of Fe20Cr, Fe22Cr, and Fe27Cr Alloys

Alloy	Temperature (°C)	Mass Gain @ 100 h		Mass Gain @ 1000 h (500 h for 800 °C)		Mass Gain @ 3000 h		Corrosion Rate— $k_p$ ( $\text{g}^2 \text{cm}^{-4} \text{s}^{-1}$ )	$k_p \text{ temp}/k_p 600^\circ\text{C}$	Activation Energy (eV)
		Pct	$\text{mg cm}^{-2}$	Pct	$\text{mg cm}^{-2}$	Pct	$\text{mg cm}^{-2}$			
Fe20Cr	600	0.9	$4.5 \times 10^{-2}$	1.2	$6.0 \times 10^{-2}$	1.6	$7.9 \times 10^{-2}$	$3.1 \times 10^{-16}$	1	3.12
	700	1.6	$7.9 \times 10^{-2}$	4.8	0.1	39.8	2.0	$1.7 \times 10^{-14}$	55	
	800	5.1	0.3	21.6	1.1	—	—	$9.3 \times 10^{-14}$	294	
Fe22Cr	900	42.5	2.1	—	—	—	—	$2.7 \times 10^{-11}$	87,097	
	600	0.4	$2.2 \times 10^{-2}$	0.7	$3.4 \times 10^{-2}$	0.9	$4.4 \times 10^{-2}$	$1.3 \times 10^{-16}$	1	3.31
	700	1.7	$8.3 \times 10^{-2}$	5.6	0.3	12.6	0.6	$2.3 \times 10^{-14}$	177	
Fe27Cr	800	5.6	0.3	14.1	0.7	—	—	$8.3 \times 10^{-14}$	638	
	900	43.6	2.2	—	—	—	—	$2.4 \times 10^{-11}$	184,615	
	600	0.3	$1.5 \times 10^{-2}$	0.5	$2.4 \times 10^{-2}$	0.7	$3.7 \times 10^{-2}$	$1.3 \times 10^{-16}$	1	2.83
	700	1.5	$7.5 \times 10^{-2}$	6.1	0.3	8.5	0.4	$1.3 \times 10^{-14}$	100	
	800	8.5	0.3	10.4	0.5	—	—	$1.1 \times 10^{-13}$	846	
	900	43.9	2.2	—	—	—	—	$2.7 \times 10^{-12}$	20,769	

Table III. Chemical Composition of Regions Marked in Fig. 5 (Obtained from EDX Measurements)

Region	Cr (At. Pct)	O (At. Pct)	N (At. Pct)
1	35.7	64.3	—
2	34.7	65.3	—
3	35.8	64.2	—
4	88.0	—	12.0
5	87.9	—	11.9
6	89.4	—	10.6

( $1.3 \times 10^{-14}$  to  $2.3 \times 10^{-14} \text{ g}^2 \text{cm}^{-4} \text{s}^{-1}$ ). Differences were clearly visible for higher temperatures, namely for 800 °C and 900 °C (data collected in Tables II and III). The data obtained at 800 °C correspond well to the corrosion rates obtained for dense alloys with a similar chemical composition, e.g., Crofer 22 APU. Magdefrau *et al.* calculated the corrosion rate for Crofer 22 APU as  $4.8 \times 10^{-14} \text{ g}^2 \text{cm}^{-4} \text{s}^{-1}$  at 800 °C.<sup>[16]</sup> Skilbred *et al.* determined this parameter as  $5.4 \times 10^{-14} \text{ g}^2 \text{cm}^{-4} \text{s}^{-1}$  at 800 °C for Sandvik Sanergy HT.<sup>[34]</sup> These data are in line with the results obtained for the Fe22Cr alloy. Small changes of this parameter could be caused by compositional differences such as the Cr content or the presence of other minor alloying elements.<sup>[35]</sup>

The oxidation process before the occurrence of breakaway corrosion can be considered similar to the oxidation of dense alloys, even with more complex geometry. The complex geometry is accounted for in the limited Cr reservoir (due to the high surface-to-volume ratio), but the underlying phenomena remain the same.

As presented in Figure 2(e), the values of activation energies were similar ( $\sim 3 \text{ eV}$ ) for each alloy. The chemical composition, e.g., the different Cr contents and addition of Mn, had no visible effects on the dynamics of oxidation. The activation energy is consistent with the values reported for ferritic chromia formers. Wang *et al.* calculated the activation energy of chromium diffusion in  $\text{Cr}_2\text{O}_3$  as 240 to 280  $\text{kJ mol}^{-1}$  ( $\sim 2.5$  to  $2.9 \text{ eV}$ ).<sup>[36]</sup> Talic *et al.* calculated the activation energy of the corrosion process for Crofer 22 APU as 310  $\text{kJ mol}^{-1}$  ( $\sim 3.2 \text{ eV}$ ).<sup>[37]</sup> Palcut *et al.* determined the activation energy of the same alloy as 2.6 eV.<sup>[38]</sup>

### C. Post-mortem Analysis of Porous Alloys

#### 1. Scanning electron microscopy study

SEM images of the cross sections of the heavily oxidized alloys at 800 °C and slightly oxidized at 600 °C are shown in Figure 3, whereas the images of the alloys oxidized at 700 °C, which show an intermediate oxidation stage, are presented in more detail in Figure 4. Additionally, SEM images of the surfaces of Fe20Cr, Fe22Cr, and Fe27Cr alloys after oxidation at 700 °C for 3000 hours are presented in Figure S.6 (Supplementary Material).

In the first row (Figures 3(a) through (c)), images of the Fe20Cr, Fe22Cr, and Fe27Cr alloys oxidized at 800 °C for 100 hours are presented. All samples show well-defined and distinguishable oxide scale, which was detected *via* X-Ray diffraction measurement as  $\text{Cr}_2\text{O}_3$ .<sup>[7]</sup> The XRD patterns of unoxidized Fe22Cr alloy, as well as after

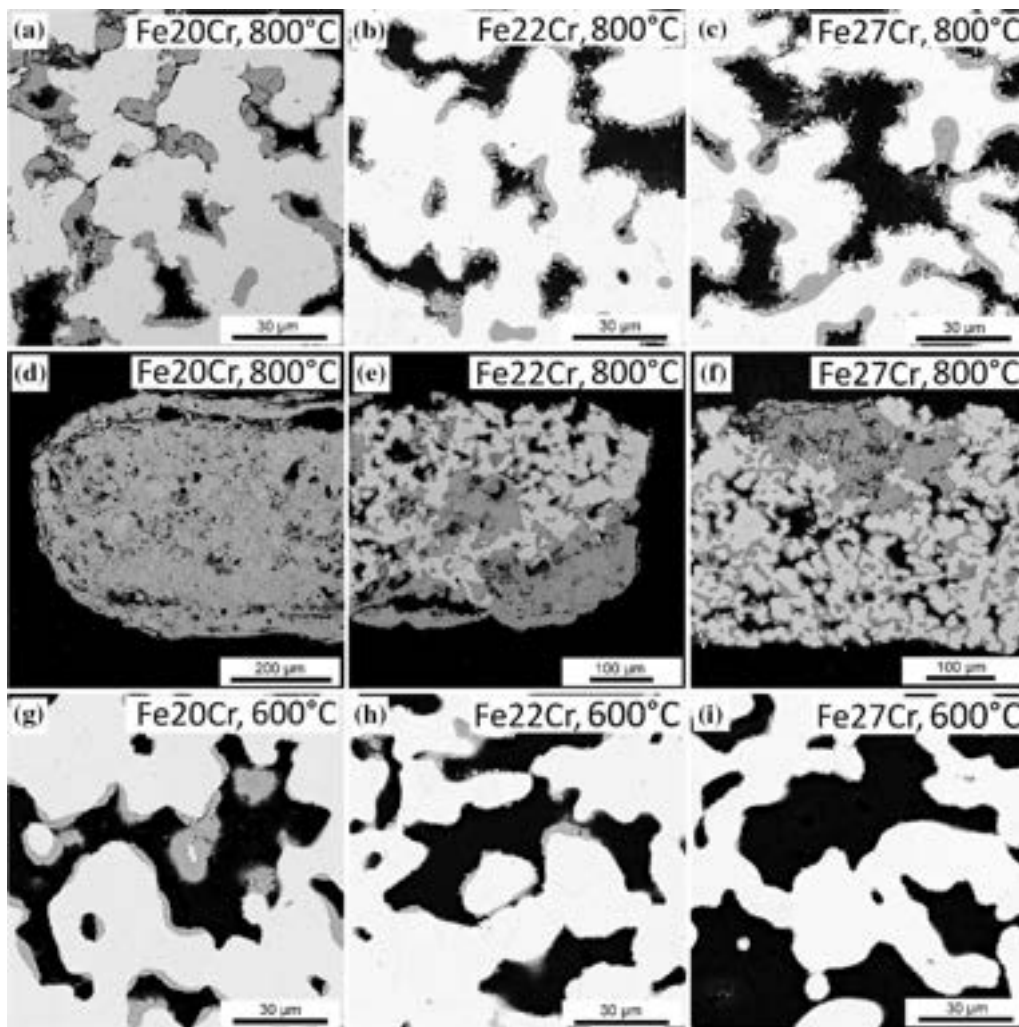


Fig. 3—SEM images of Fe20Cr (a, d, g), Fe22Cr (b, e, h), and Fe27Cr (c, f, i) alloys oxidized at 800 °C for 100 h (a, b, c), 500 h (d, e, f) and oxidized at 600 °C for 6000 h (g, h, i).

different steps of oxidation are also presented in Figure S.7 (Supplementary material). The Fe20Cr alloy shows the highest amount of the oxide formed, with some pores entirely filled and, therefore, exhibiting significantly reduced porosity. The oxide is severely cracked, indicating its brittleness and poor mechanical properties.

For the Fe22Cr and Fe27Cr alloys, the cross sections after 100 hours at 800 °C show similar a microstructure—a thinner layer (below 5 µm) of  $\text{Cr}_2\text{O}_3$ , when compared with the Fe20Cr alloy, was observed.

The second row of Figure 3 shows microstructures of the Fe20Cr, Fe22Cr, and Fe27Cr alloys after 500 hours of oxidation at 800 °C. The Fe20Cr alloy (Figure 3(d)) presents a fully oxidized sample with no recognizable initial morphology and porosity. The mass gain of the sample was ~ 43 pct, which confirms full oxidation of the available chromium and iron.<sup>[7]</sup> For both the Fe22Cr and Fe27Cr alloys (Figures 3(e) and (f)), the microstructures show the remaining metallic core and also some heavily oxidized regions where breakaway oxidation appeared. Most of the samples still show a retained initial porosity reduced by the formed oxide.

In contrast to oxidation at 800 °C, where breakaway oxidation for all the alloys had already occurred by 500 hours, oxidation at 600 °C had a less severe effect. Even after 6000 hours of oxidation, the oxide scale was only easily visible on the Fe20Cr sample (Figure 3(g)), whereas on the higher Cr-content alloys, it was slightly visible (Figures 3(h) and (i)). Breakaway oxidation was not observed for any of these samples. The SEM micrographs correspond well with the mass gain of the samples. For the Fe20Cr sample, the mass gain was ~ 1.8 pct whereas for both the Fe22Cr and Fe27Cr, the mass gains were ~ 1 pct. To justify the higher mass gain of the Fe20Cr, an additional EDX analysis was performed for this alloy oxidized at 600 °C for 6000 hours. The obtained chemical element maps are presented in Figure S.5 (Supplementary material). A two-phase structure consisting of iron oxide (inner layer) and chromium oxide (outer layer) can be observed in the regions around the pores. The formation of such structures could be caused by the iron oxidizing only slightly slower than the chromium at 600 °C. At higher temperatures, the chromium oxidizes significantly faster



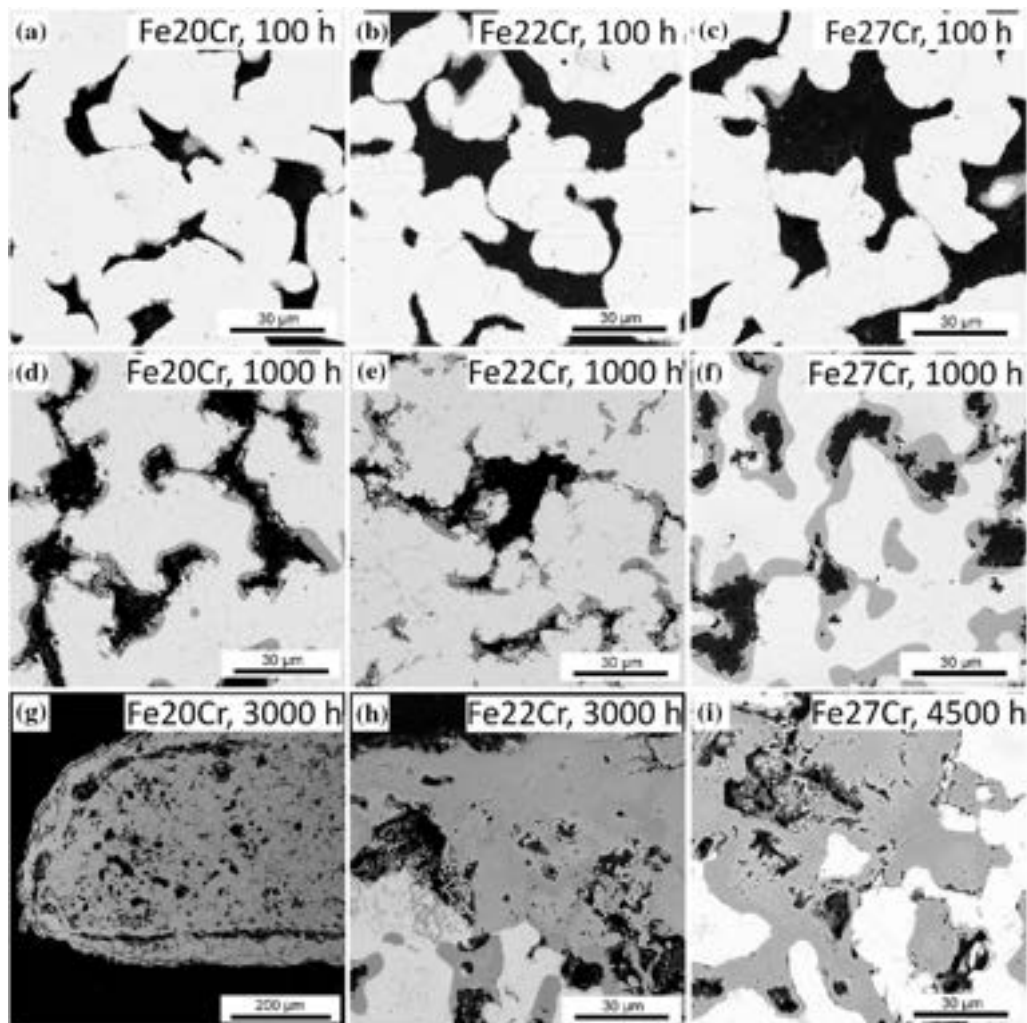


Fig. 4—SEM images of Fe20Cr (a, d, g), Fe22Cr (b, e, h) and Fe27Cr (c, f, i) alloys oxidized at 700 °C for 100 h (a, b, c), 1000 h (d, e, f), 3000 h (g, h), and 4500 h (i).

than the iron, so the two-phase structure is not observed in that case.

Further analysis was focused on samples oxidized at 700 °C, which seems to be the upper limit temperature for possible long-term operation of FeCr porous alloys. SEM images of the cross section of the alloys oxidized at 700 °C for different times are presented in Figure 4.

In the first row (Figures 4(a) through (c)), images of the Fe20Cr, Fe22Cr, and Fe27Cr alloys oxidized for 100 hours are shown. For each chemical composition, the oxide scale is barely visible at the surface of the particles. These micrographs correspond to an ~ 1.5 pct mass gain for each investigated sample.

The second row of Figure 4 reveals microstructures of Fe20Cr, Fe22Cr, and Fe27Cr alloys after 1000 hours of oxidation at 700 °C. For each presented sample, the oxide scale is distinguishable and limits the initial porosity (discussed later in detail), but no breakaway corrosion region was detected. The mass gain for the Fe20Cr samples after 1000 hours at 700 °C is 4.8 pct,

whereas for the Fe22Cr and Fe27Cr oxidized under the same conditions, the mass gains are 5.6 and 6.1 pct, respectively.

Images of the Fe20Cr and Fe22Cr samples after 3000 hours of oxidation at 700 °C are presented in Figures 4(g) and (h), respectively. The Fe20Cr alloy (Figure 4(g)) is fully oxidized with no sign of metallic core and initial porosity, which corresponds with the ~ 40 pct mass gain. For the Fe22Cr alloy (Figure 4(h)), breakaway corrosion regions were detected but the metallic core is still visible. This result is in agreement with the mass gain plot (Figure 2(b)) that shows a deviation from the linear dependence of the mass growth after 3000 hours of oxidation at 700 °C.

In contrast to the Fe20Cr and Fe22Cr alloys, no breakaway corrosion region was identified for the Fe27Cr samples after 3000 hours of oxidation at 700 °C. After 3000 hours of oxidation at 700 °C, the mass gain for the Fe27Cr samples was ~ 8.5 pct, while for the Fe20Cr and Fe22Cr samples, it was 40 and 12.5

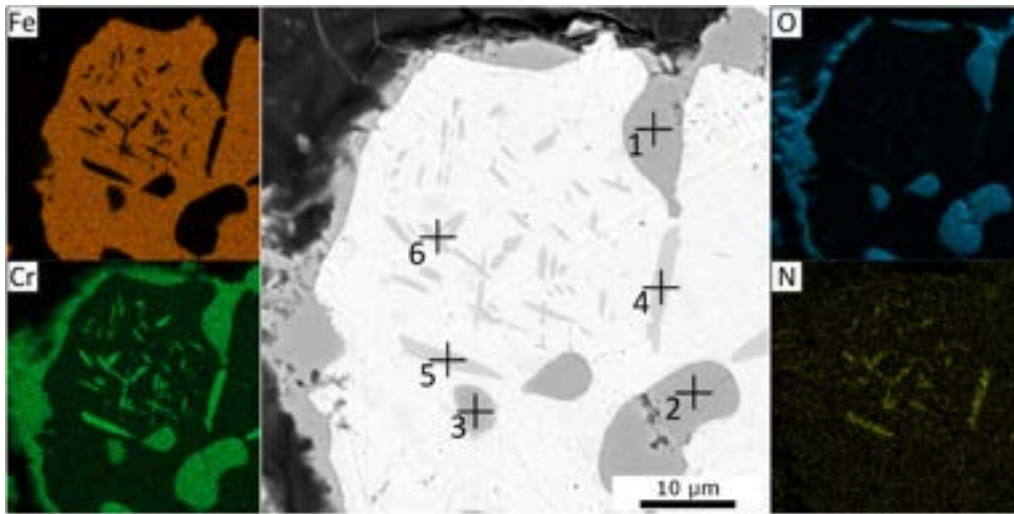


Fig. 5—EDX analysis (qualitative maps) of sample oxidized at 700 °C for 4500 h.

pct, respectively. The mass gain measurements (Figure 2(b)) for the Fe27Cr alloy also did not show a rapid increase in the mass change.

After 4500 hours of oxidation at 700 °C, breakaway corrosion appeared for Fe27Cr alloy (Figure 4(i)), which corresponds to a 9.4 pct mass gain of the samples. It seems to be the start of the sample's accelerated oxidation, which might be caused by the appearance of breakaway corrosion only in one region of the whole sample, and thus, no rapid mass change, as observed in Figure 2(b).

## 2. Internal precipitations

Detailed analysis of the SEM images indicated the presence of internal precipitates (e.g., Figure 5) in some of the particles of the Fe22Cr and Fe27Cr alloys oxidized at  $\geq 700$  °C. For oxidation at 600 °C, no precipitates were observed.

For the Fe20Cr alloy, which has the lowest Cr content, no formation of the precipitates was detected among the studied samples, but their formation cannot be unambiguously ruled out.

For the Fe22Cr, the precipitates were observed after oxidation at 700 °C for 3000 hours, whereas they were not visible after 1000 hours of oxidation. For oxidation at 800 °C, the precipitates were already visible after 100 hours.

For the Fe27Cr alloy, the precipitates were observed after 1000 and 100 hours for oxidation temperatures of 700 °C and 800 °C, respectively.

A typical microstructure and chemical composition of the precipitates are presented in Figure 5 based on the Fe27Cr alloy oxidized at 700 °C for 4500 hours. The darker regions inside the particles exhibit increased signal from the nitrogen and chromium elements (based on EDX). The specific elemental compositions obtained for the point measurements indicated in Figure 5 are summarized in Table III. Points 1 to 3 correspond to oxide scale—Cr<sub>2</sub>O<sub>3</sub>—whereas an analysis of points 4 to 6 revealed the presence of nitrogen and chromium, with no

apparent oxygen signal, indicating the formation of a Cr–N phase. Due to the low concentration of N in the raw alloy, the nitrogen is believed to have diffused from the atmosphere (air) to inside the grains.

Cr<sub>2</sub>N is a stable phase for ferritic alloys which contain less than 20 wt pct of Cr in a nitriding atmosphere in a temperature range of 500 °C to 1000 °C. Cr<sub>2</sub>N also appears for alloys with more than 20 wt pct of Cr.<sup>[39]</sup>

Miyamoto *et al.* investigated the Fe18Cr system in a nitriding atmosphere in a temperature range of 470 °C to 670 °C. They recognized disk- and rod-shaped CrN structures and rod-shaped Cr<sub>2</sub>N structures in the cross sections of the samples. A Cr<sub>2</sub>N phase probably transformed into CrN during nitriding at 670 °C.<sup>[40]</sup> A mostly rod-shaped precipitated phase was observed for the samples investigated in this study.

For the samples oxidized at 700 °C and 800 °C, mixed structures of CrN and Cr<sub>2</sub>N probably appeared. Interestingly, Bianco *et al.* indicated that purposeful controlled nitriding of the dense ferritic alloys could improve their performance when used as interconnectors in solid oxide fuel cells.<sup>[41]</sup> In our case, the samples were not prenitrided before further experiments, but spontaneous nitridation was observed during the long-term oxidation study.

Based on the limited number of analyzed samples, it seems that a higher temperature ( $\geq 700$  °C) and higher Cr content in the alloys lead to formation of the CrN<sub>x</sub> precipitates. The large surface area (and surface-to-volume ratio) of the porous alloys possibly also helps ensure a possible high flux of N, as similar nitridation has not been reported in the case of dense alloys with a similar chemical composition and exposed to similar conditions (e.g., Crofer 22 APU oxidized up to 900 °C).

The binding of Cr by N can cause an increase in chromium consumption within the alloy, not connected to the formation of oxide scale, which can decrease the lifetime of porous ferritic alloys.

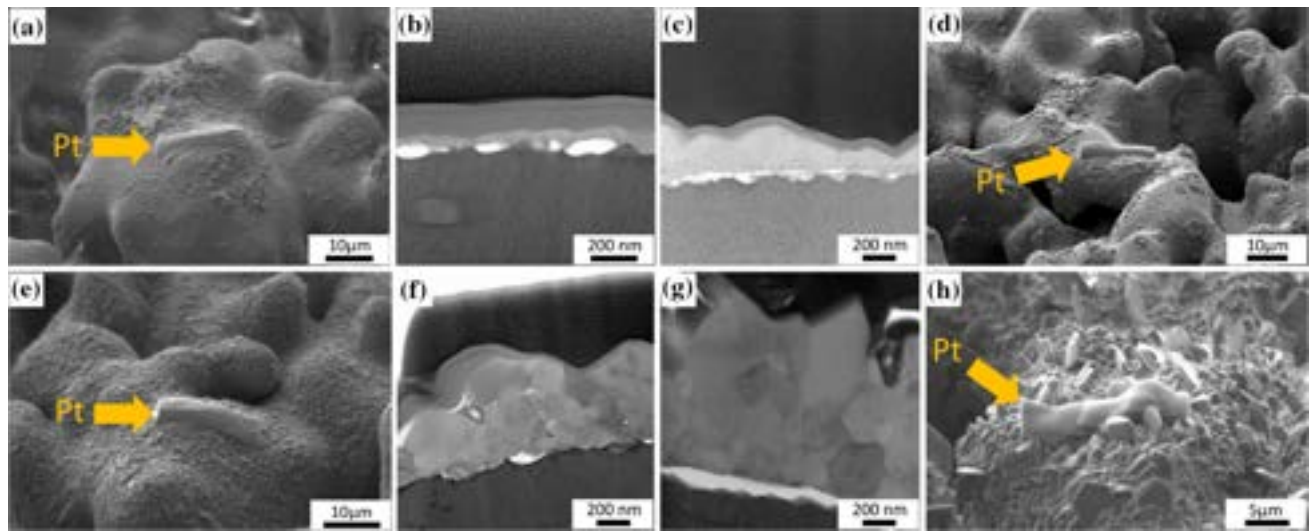


Fig. 6—SEM (surface) and STEM (FIB-lamellae cut) images of Fe22Cr alloy oxidized at (a, b) 600 °C for 3000 h; (c, d) 600 °C for 6000 h; (e, f) 700 °C for 100 h; (g, h) 700 °C for 3000 h.

### 3. Transmission electron microscopy study

Detailed characterization of the alloy-oxide was carried out on the FIB-cut lamellae by STEM. The analysis of the samples included the Fe22Cr after 3000 and 6000 hours at 600 °C and after 100 and 3000 hours at 700 °C. SEM images from the FIB-cutting process are also included. The lamellae were cut from the top parts of the particles, where the Pt cap layers are visible. The STEM images show the microstructure differences between differently oxidized samples (Figure 6).

In Figure 6(b), an alloy-oxide interface of the alloy oxidized for 3000 hours at 600 °C is presented. A thin, continuous (~ 20 to 40 nm) layer of oxide phase is visible but between the oxide and alloy phases, some voids were detected (white color). The voids in the alloy-oxide interface did not appear continuously and their widths were ~ 30 to 50 nm. After 6000 hours of oxidation at 600 °C, voids were also observed on the alloy-oxide interface (Figure 6(c)). The chromium oxide in the region close to the alloy had a fine grain structure and the further away from the alloy, the larger the oxide grains. The thickness of the discontinuous layer of voids was still about 30 to 50 nm, but the thickness of the continuous oxide scale increased to approximately 100 to 200 nm.

The changed chromium oxide grain size within the oxide scale layer was observed after 100 hours of oxidation at 700 °C (Figure 6(f)). The smallest grains were located near the alloy (about 10 to 50 nm in diameter) and the bigger grains were further away from the alloy with diameters of approximately 50 to 250 nm. The total thickness of the oxide scale was about 0.7 to 1.5 μm, which was in agreement with the analysis of the SEM images. The diameter of the voids was about 30 to 50 nm, so no changes of their size were identified in comparison with the samples oxidized at 600 °C.

After 3000 hours of oxidation at 700 °C, all grains had a similar diameter of ~ 200 to 300 μm (Figure 6(g)).

There were also cracks within the oxide scale which also confirm destructive impact of the oxidation process.

The chemical composition of the lamellae was analyzed by EDX for the Fe22Cr samples oxidized at 600 °C for 6000 hours (Figure 7(a)) and at 700 °C for 3000 hours (Figure 7(b)). The results indicate that the oxide scale is composed of chromia scale. A small addition of Mn to the alloy did not result in the formation of a continuous Mn-Cr spinel layer, probably because the amount of Mn was too small (0.23 wt pct).<sup>[7]</sup> A trace of silicon (probably as a silica phase) can also be observed at the steel-chromia interface on the sample oxidized at 700 °C at 3000 hours.

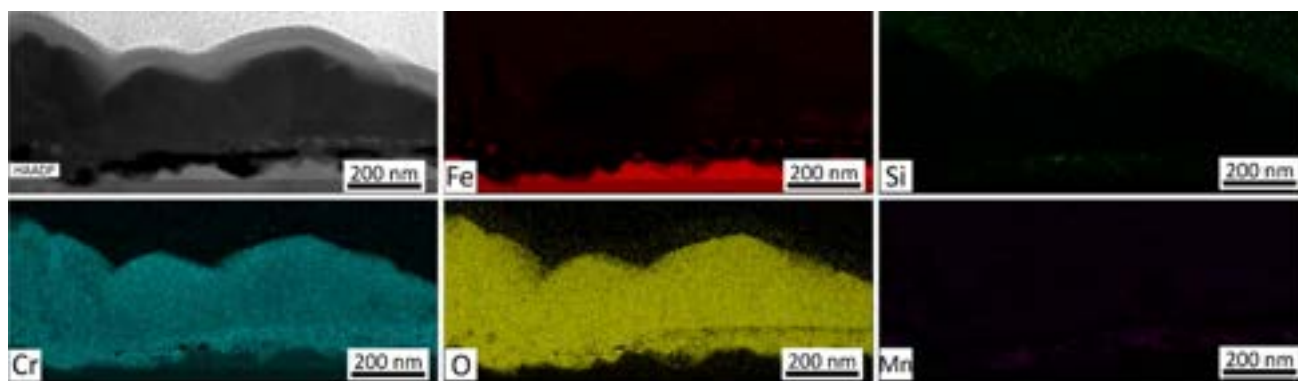
### 4. Chromium reservoir

The formation of a protective chromia scale depends on the available chromium content in the bulk. Above a certain threshold value, the formation of a continuous chromia scale can be sustained, whereas below the threshold value, the oxidation of iron starts taking place, *i.e.*, as an occurrence of breakaway oxidation. Determining the threshold value of the chromium content is important for predicting the lifetime, as it defines the conditions of breakaway oxidation formation.

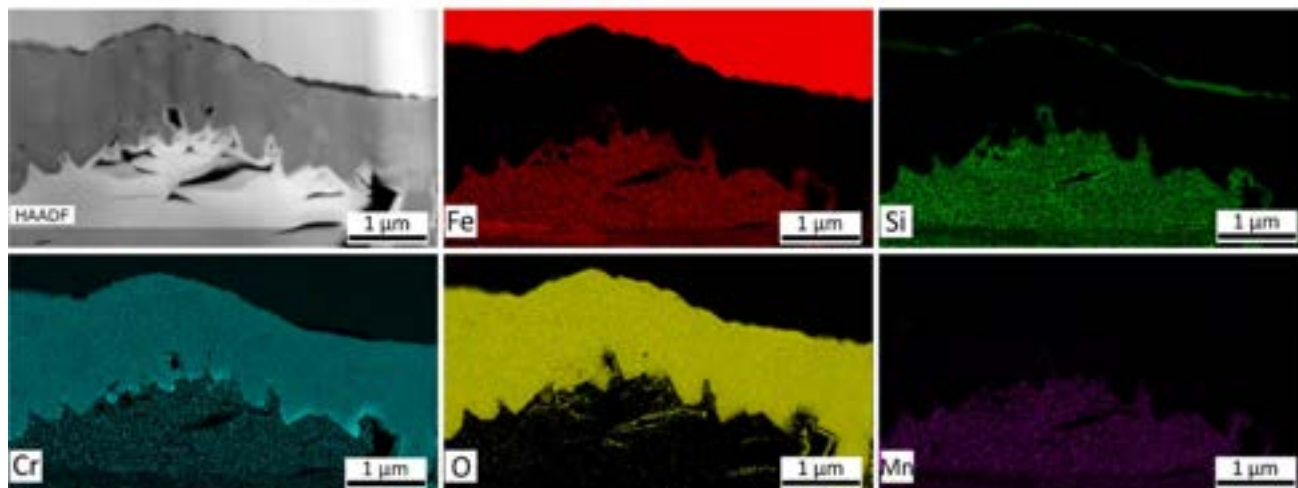
Huczowski *et al.* established a threshold value of chromium content (10 wt pct) which determines the occurrence of breakaway oxidation. Our previous research<sup>[24]</sup> confirmed that this threshold value is in the range of 10 to 12 wt pct of Cr for short-term (up to 100 hours) oxidation experiments. The changes in the chromium content based on long-term oxidation research are presented in Figure 8.

For oxidation at 600 °C, even after 6000 hours, negligible changes in the chromium content were noted for all the alloys (Figure 8(a)). Barely visible microstructure changes were observed *via* SEM for samples oxidized at 600 °C, while the mass gains of these samples did not exceed 2 pct.





(a)



(b)

Fig. 7—EDX analysis based on TEM images for samples (a) oxidized at 600 °C for 6000 h, and (b) oxidized at 700 °C for 3000 h.

In the case of oxidation at 700 °C, changes in the chromium content were measurable (Figure 8(b)). For the Fe20Cr alloy, the level of the chromium content decreased from the initial 22 wt pct to ~ 14 pct after 1000 hours of oxidation, which is only 2 pct above the threshold band, and then after 2000 hours of oxidation, the samples were fully oxidized. For the Fe22Cr alloy, the Cr content after 3000 hours of oxidation was calculated as 12.7 pct ( $\pm 0.9$  pct), which could be in the threshold band. The SEM analysis of this sample showed the formation of breakaway corrosion, but only in a few regions at the edges of the samples. For the Fe27Cr alloy, breakaway corrosion was not visible in the SEM images, and the chromium content after 3000 hours of oxidation at 700 °C was determined as 19.3 wt pct, which is definitely in the safe band.

In comparison to lower temperatures, the chromium content in the samples oxidized at 800 °C decreased faster (Figure 8(c)). Exposure for only 250 hours was sufficient for breakaway corrosion to occur in the Fe20Cr and Fe22Cr alloys. The chromium content of these alloys was 8.5 and 8.4 pct, respectively. This is consistent with the assumption that breakaway corrosion starts at ~ 12 wt pct remaining Cr in the alloy.

The Fe27Cr alloy had the highest remaining chromium content after 250 hours of oxidation at 800 °C (15.5 wt pct), which was still significantly above 12 wt pct; therefore, no breakaway corrosion was expected in this case. However, after 500 hours of oxidation at 850 °C, the remaining chromium in the Fe27Cr alloy was ~ 8.5 wt pct, which is below the threshold band and breakaway corrosion was expected to form. This is supported by the SEM analysis (Figure 3(f)) and mass gain data (Figure 2(c)), where breakaway oxidation was indeed detected.

### 5. Porosity changes

Experimentally determined porosity changes caused by the oxidation are shown in Figures 8(d) through (f) for samples oxidized at 600 °C, 700 °C, and 800 °C, respectively. A loss of porosity can lead to the functional failure of the porous element.

For the samples oxidized at 600 °C, the porosity did not change even after 6000 hours of exposure, which is consistent with the small mass gain (Figure 2(a)) and no visible microstructural changes (Figures 3(g) through (i)).

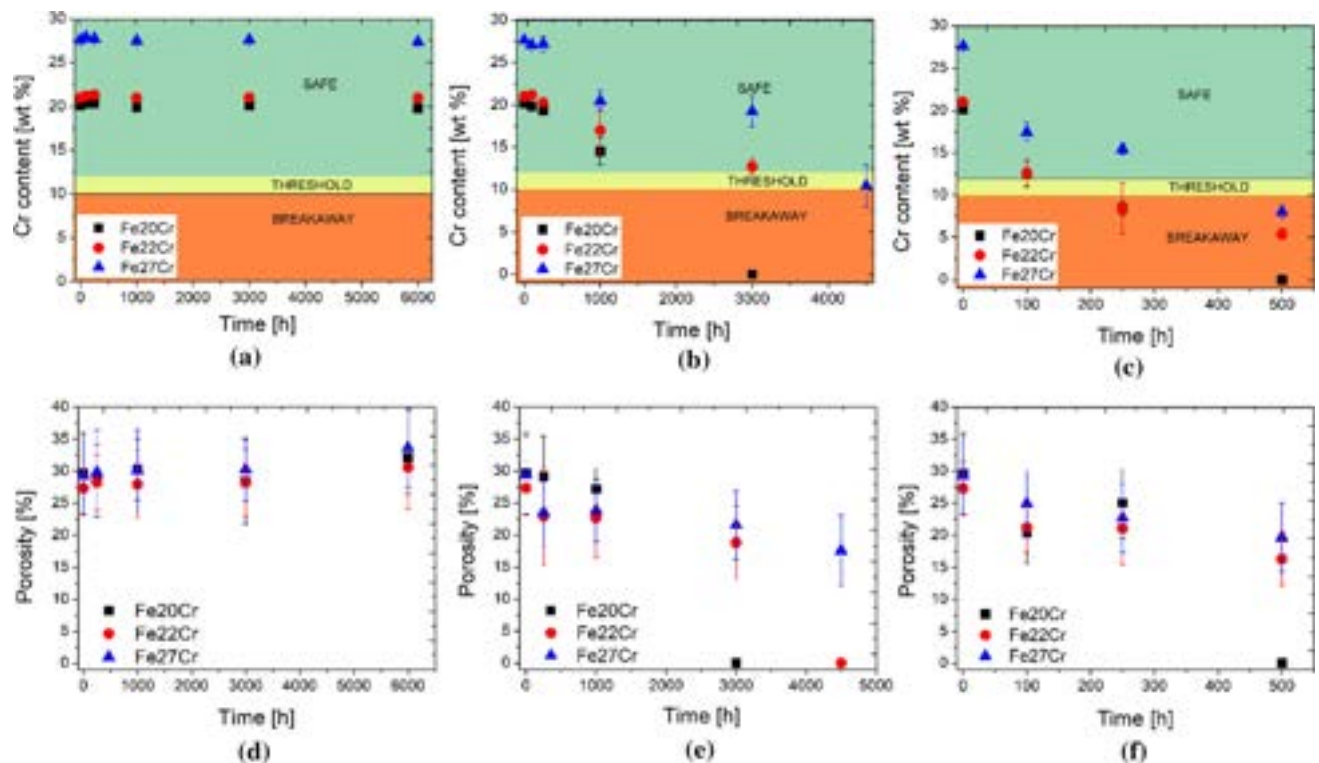


Fig. 8—Cr content in the alloy determined by EDX for Fe20Cr, Fe22Cr, and Fe27Cr alloys oxidized at (a) 600 °C, (b) 700 °C, and (c) 800 °C. Porosity of the samples oxidized at (d) 600 °C, (e) 700 °C, and (f) 800 °C.

Noticeable changes in porosity were observed for samples oxidized at 700 °C. For the Fe20Cr alloy, a small decrease in the porosity was observed during the first 1000 hours of the experiment and then a fast decrease in porosity followed. A similar, two-stage type of decrease in porosity was also observed for the Fe22Cr. Rapid porosity loss occurred after 3000 hours, which is consistent with the mass gain data and the occurrence of breakaway oxidation, as observed by SEM (Figure 4(h)). For the Fe27Cr samples, a monotonic decrease in porosity was observed up to 4500 hours.

For the samples oxidized at 800 °C, the porosity loss was more pronounced than at lower temperatures. The Fe20Cr alloy was fully oxidized after 500 hours of oxidation. For the Fe22Cr and Fe27Cr samples, a monotonic porosity loss was also observed. After 500 hours of exposure, the first indications of breakaway corrosion were observed for these samples (Figures 3(e) and (f)), which is consistent with the high mass changes—14.1 and 10.4 pct for the Fe22Cr and Fe27Cr, respectively.

#### D. Lifetime Prediction of Porous Alloys

Based on the determined threshold chromium content and oxidation kinetics data, a lifetime prediction can be established.

In our previous work, we used only short-term oxidation data for the long-term prediction. This study supplements the short-term isothermal oxidation data

with a long-term cyclic oxidation validation. Moreover, in this study, changes in the chromium content were studied in a wider range of temperatures and for three alloys with different initial Cr contents, which are presented in Figures 8(a) through (c).

Isothermal (700 °C) thermogravimetric mass gain data for the alloys are presented in Figure 9. For each alloy, a threshold value of the mass gain, when breakaway corrosion should have appeared, was recalculated based on the experimentally determined value for the Fe22Cr alloy (6 wt pct).<sup>[7]</sup> Assuming that breakaway corrosion starts when the Cr content in the alloys decreases to ~12 wt pct (top of the threshold range, 10 to 12 wt pct), the critical Cr consumption (equivalent to a specific mass gain) can be calculated for each of the alloys. For the Fe20Cr and Fe27Cr alloys, the critical mass gain was 5.1 and 8.3 wt pct, respectively.

For the Fe20Cr and Fe22Cr alloys, the cyclic and isothermal mass gains show good agreement. The prediction model indicated that the lifetimes of the Fe20Cr and Fe22Cr alloys were determined as 1250 hours ( $\pm 535$  hours) and 1460 hours ( $\pm 640$  hours), respectively. Even though the relative error of the predicted alloy's lifetime seems to be relatively high, an assumed prediction band is determined for the log-log scale plot, resulting in artificially high values of the relative error. The extrapolated curves for the Fe20Cr and Fe22Cr are in line with the experimentally measured mass gains, as presented in Figures 9(a) and (b).

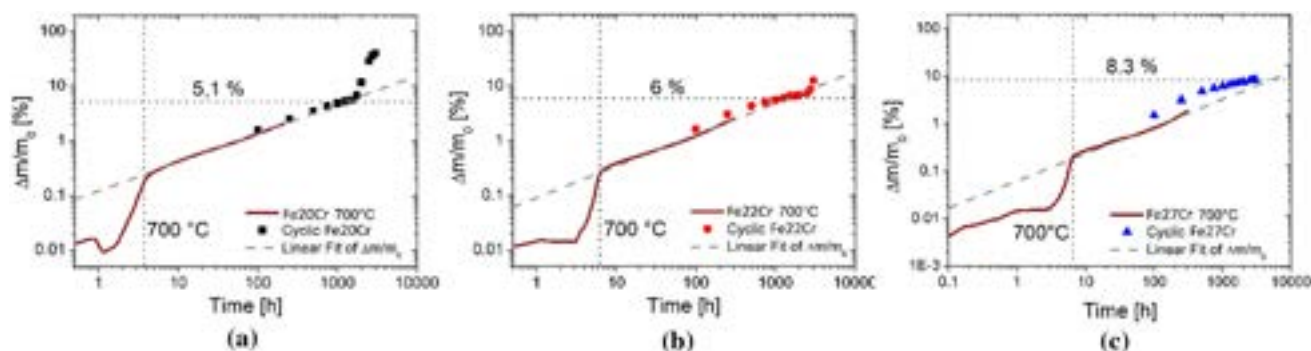


Fig. 9—Linear extrapolation of thermogravimetric data for (a) Fe20Cr alloy, (b) Fe22Cr alloy, and (c) Fe27Cr alloy. For each chemical composition, a threshold level of chromium content and cyclic weight measurements were also plotted.

The experimentally determined times when breakaway corrosion appears are  $< 1750$  and  $2750$  hours for the Fe20Cr and Fe22Cr alloys, respectively. The model seems to underestimate the lifetime of the alloys.

The breakaway oxidation time observed as a change of the slope for the mass gain data could be misleading, as proved by a comparison of the thermogravimetric plot for the Fe27Cr oxidized at  $700\text{ }^{\circ}\text{C}$  (Figure 2(b)) and a SEM image (Figure 4(i)). The mass gain measurements reveal the occurrence of breakaway corrosion with a delay of a few hundred hours. The lifetime prediction obtained from the proposed model seems to be more accurate and better reflects the real lifetime of porous alloys. Such difference in the estimated lifetime based on the mass gain measurements and real lifetime was also proven by the SEM and tomography studies.<sup>[33]</sup>

For the Fe27Cr alloy, the cyclic and isothermal mass gain data show a visible difference. The cyclic measurements provide an 8.3 wt pct mass gain after 3000 hours, but the predicted lifetime of the alloy is about 5070 hours ( $\pm 2740$  hours).

For the Fe27Cr alloy, breakaway corrosion did not appear after 3000 hours of oxidation at  $700\text{ }^{\circ}\text{C}$ . It was observed after 4500 hours of oxidation at  $700\text{ }^{\circ}\text{C}$ . The shorter lifetimes provided by the prediction model could be caused by the log-log scale effect. The relative distance between 1000 and 2000 hours in the log-log plot was small, so the calculated lifetimes could be disturbed.

The main goal of the applied prediction model was a rough estimation of lifetimes of the alloys. Additionally, the best way to predict the lifetime of a porous alloy was to consider the chromium content data, mass gains, and microscopy analysis.

#### IV. CONCLUSIONS

In this work, the lifetime of porous FeCr alloys was predicted based on a long-term (up to 6000 hours) corrosion evaluation in a wide temperature range ( $600\text{ }^{\circ}\text{C}$  to  $900\text{ }^{\circ}\text{C}$ ). Alloys with a similar microstructure, but different chemical compositions (Fe20Cr, Fe22Cr,

Fe27Cr) were studied. The main difference was the chromium content, which is a key factor in determining the lifetimes of the alloys.

Oxidation at  $600\text{ }^{\circ}\text{C}$  did not cause severe degradation of any of the alloys. The oxide growth rate was low ( $\sim 10^{-16}\text{ g}^2\text{ cm}^{-4}\text{ s}^{-1}$ ) and did not change the chemical composition due to Cr consumption, nor modifies the porous structure of the alloy by filling of pores by oxidation products. Oxidation at  $700\text{ }^{\circ}\text{C}$  was characterized by an increased oxide growth rate ( $\sim 10^{-14}\text{ g}^2\text{ cm}^{-4}\text{ s}^{-1}$ ), which caused a visible alteration of the properties of the samples. For the oxidation at  $800\text{ }^{\circ}\text{C}$ , rapid growth of oxide scale was observed ( $\sim 10^{-13}\text{ g}^2\text{ cm}^{-4}\text{ s}^{-1}$ ).

The initial porosity of the samples decreased from the initial 30 pct during exposure, except for the samples oxidized at  $600\text{ }^{\circ}\text{C}$ . These results are consistent with the Cr consumption analysis. The Cr level for the samples oxidized at  $700\text{ }^{\circ}\text{C}$  and  $800\text{ }^{\circ}\text{C}$  decreased, but was constant for the samples oxidized at  $600\text{ }^{\circ}\text{C}$ . The long-term results confirmed that, for the samples consisting of 12 wt pct of Cr (or below), the formation of breakaway corrosion was detected *via* SEM imaging.

A comparison of the mass gain data with SEM micrographs indicated that determining the formation of breakaway corrosion based on a change in the slope of the thermogravimetric data can be misleading. The SEM images of the Fe27Cr alloy oxidized at  $700\text{ }^{\circ}\text{C}$  for 4500 hours revealed the occurrence of breakaway corrosion (Figure 4(i)), but no changes in the slope in the mass gain plot (Figure 2(b)) were observed. The time of the formation of breakaway corrosion estimated based on the mass gain plot should be decreased by a few hundred hours.

An analysis of the mass gains, SEM and TEM images, and thermogravimetric data in the context of predicting the lifetime of a porous alloy confirmed that an assumed 9 wt pct of chromium content in the alloy was the limit value that determined the appearance of breakaway corrosion (independently of the alloy's chemical composition). The applied prediction model made it possible to roughly estimate each alloy's lifetime and confirmed the diffusion character of the corrosion process for porous alloys. The lifetime prediction was compared with the long-term experimental oxidation results. The



convergence of these data proved the concept of estimating the lifetime of porous alloys based only on short-term results. The model seems to accurately predict the lifetime of the alloys, more precisely than can be evaluated based on the average mass gain data.

To sum up, the corrosion process for porous alloys was revealed to be limited by a diffusion process (slope of the mass gain plots). The alloy's lifetime depended on its chemical composition—the more chromium in the 'raw' alloy, the longer the lifespan. Such porous alloys can be considered promising materials for high-temperature applications, especially at 600 °C, where a long lifetime can be achieved.

## ACKNOWLEDGMENTS

This project was supported by the National Science Centre Poland (NCN) Sonata Bis 8 project number 2018/30/E/ST8/00821, "High-temperature corrosion studies and development of oxidation lifetime model of alloy powders and sintered porous alloys: effects of composition and microstructure."

## FUNDING

This project has received funding from the European Union's Horizon 2020 research and innovation programme under Grant Agreement No 823717 – ESTEEM3.

## CONFLICT OF INTEREST

On behalf of all authors, the corresponding author states that there is no conflict of interest.

## OPEN ACCESS

This article is licensed under a Creative Commons Attribution 4.0 International License, which permits use, sharing, adaptation, distribution and reproduction in any medium or format, as long as you give appropriate credit to the original author(s) and the source, provide a link to the Creative Commons licence, and indicate if changes were made. The images or other third party material in this article are included in the article's Creative Commons licence, unless indicated otherwise in a credit line to the material. If material is not included in the article's Creative Commons licence and your intended use is not permitted by statutory regulation or exceeds the permitted use, you will need

to obtain permission directly from the copyright holder. To view a copy of this licence, visit <http://creativecommons.org/licenses/by/4.0/>.

## SUPPLEMENTARY INFORMATION

The online version contains supplementary material available at <https://doi.org/10.1007/s11661-023-07005-z>.

## REFERENCES

1. J.C.W. Mah, A. Muchtar, M.R. Somalu, and M.J. Ghazali: *Int. J. Hydrogen Energy*, 2017, vol. 42, pp. 9219–29.
2. R. Wang, Z. Sun, J.-P. Choi, S.N. Basu, J.W. Stevenson, and M.C. Tucker: *Int. J. Hydrogen Energy*, 2019, vol. 44, pp. 25297–25309.
3. M.A. Hassan, O. Bin Mamat, and M. Mehdi: *Int. J. Hydrogen Energy*, 2020, vol. 45, pp. 25191–25209.
4. Z. Yang: *Int. Mater. Rev.*, 2008, vol. 53, pp. 39–52.
5. J.A. Glasscock, L. Mikkelsen, Å.H. Persson, G. Pećanac, J. Malzbender, P. Blennow, F. Bozza, and P.V. Hendriksen: *Solid State Ionics*, 2013, vol. 242, pp. 33–44.
6. Y.H. Xiang, L.Z. Liu, J.C. Shao, and H.J. Jin: *Acta Mater.*, 2020, vol. 186, pp. 105–15.
7. D. Koszelow, M. Makowska, F. Marone, J. Karczewski, P. Jasinski, and S. Molin: *Corros. Sci.*, 2021, vol. 189, 109589.
8. Y. Matus, L. Dejonghe, C. Jacobson, and S. Visco: *Solid State Ionics*, 2005, vol. 176, pp. 443–49.
9. D.N. Boccaccini, H.L. Frandsen, B.R. Sudireddy, P. Blennow, Å.H. Persson, K. Kwok, and P. Vang Hendriksen: *Int. J. Hydrogen Energy*, 2014, vol. 39, pp. 21569–80.
10. G. Reiss, H.L. Frandsen, W. Brandstätter, and A. Weber: *J. Power Sources*, 2015, vol. 273, pp. 1006–15.
11. E. Stefan, C. Denonville, Y. Larring, M. Stange, and R. Haugsrud: *Corros. Sci.*, 2020, vol. 164, 108335.
12. M. Mokhtari, T. Wada, C. Le Bourlot, J. Duchet-Rumeau, H. Kato, E. Maire, and N. Mary: *Corros. Sci.*, 2020, vol. 166, 108468.
13. S. Molin, B. Kusz, M. Gazda, and P. Jasinski: *J. Power Sources*, 2008, vol. 181, pp. 31–37.
14. X. Cai, Y. Liu, X. Wang, X. Jiao, J. Wang, F. Akhtar, and P. Feng: *Metall. Mater. Trans. A Phys. Metall. Mater. Sci.*, 2018, vol. 49, pp. 3683–91.
15. B. Öztürk, A. Topcu, S. Öztürk, and Ö.N. Cora: *Int. J. Hydrogen Energy*, 2018, vol. 43, pp. 10822–33.
16. N.J. Magdefrau, L. Chen, E.Y. Sun, and M. Aindow: *J. Power Sources*, 2013, vol. 241, pp. 756–67.
17. P. Alnegren, M. Sattari, J. Froitzheim, and J.E. Svensson: *Corros. Sci.*, 2016, vol. 110, pp. 200–12.
18. H. Shahbaznejad and H. Ebrahimifar: *J. Mater. Sci. Mater. Electron.*, 2021, vol. 32, pp. 7550–66.
19. W.N. Liu, X. Sun, E. Stephens, and M.A. Khaleel: *J. Power Sources*, 2009, vol. 189, pp. 1044–50.
20. B. Timurkutluk, S. Toros, S. Onbilgin, and H.G. Korkmaz: *Int. J. Hydrogen Energy*, 2018, vol. 43, pp. 14638–47.
21. A. Meharwal, M. Kumar, S.K. Karak, J.D. Majumdar, and I. Manna: *Metall. Mater. Trans. A Phys. Metall. Mater. Sci.*, 2020, vol. 51, pp. 5257–67.
22. B.V. Mahesh, R.K. Singh Raman, and C.C. Koch: *Metall. Mater. Trans. A Phys. Metall. Mater. Sci.*, 2015, vol. 46, pp. 1814–24.
23. V.G. Efremenko, Y.G. Chabak, A. Lekatou, A.E. Karantzalis, and A.V. Efremenko: *Metall. Mater. Trans. A Phys. Metall. Mater. Sci.*, 2016, vol. 47, pp. 1529–43.
24. J. Masalski, J. Gluszek, J. Zabrzski, K. Nitsch, and P. Gluszek: *Thin Solid Films*, 1999, vol. 349, pp. 186–90.

25. A.M. Lazar, W.P. Yespica, S. Marcelin, N. Pébère, D. Samélor, C. Tendero, and C. Vahlas: *Corros. Sci.*, 2014, vol. 81, pp. 125–31.
26. G. Ruhi, O.P. Modi, A.S.K. Sinha, and I.B. Singh: *Corros. Sci.*, 2008, vol. 50, pp. 639–49.
27. P. Pavlasek, J. Rybař, S. Ďuriš, and J. Palenčar: *Meas. Sci. Rev.*, 2019, vol. 19, pp. 209–12.
28. A. Holt and P. Kofstad: *Solid State Ionics*, 1994, vol. 69, pp. 137–43.
29. P. Huczowski, V. Shemet, J. Piron-Abellan, L. Singheiser, W.J. Quadakkers, and N. Christiansen: *Mater. Corros.*, 2004, vol. 55, pp. 825–30.
30. C. Asensio-Jimenez, L. Niewolak, H. Hattendorf, B. Kuhn, P. Huczowski, L. Singheiser, and W.J. Quadakkers: *Oxid. Met.*, 2013, vol. 79, pp. 1–4.
31. M.C. Tucker: *Int. J. Hydrogen Energy*, 2020, vol. 45, pp. 24203–18.
32. P. Huczowski, N. Christiansen, V. Shemet, J. Piron-Abellan, L. Singheiser, and W.J. Quadakkers: *J. Fuel Cell Sci. Technol.*, 2004, vol. 1, pp. 30–34.
33. D. Koszelow, S. Molin, J. Karczewski, F. Marone, and M. Makowska: *Mater. Des.*, 2022, vol. 215, 110492.
34. A.W.B. Skilbred and R. Haugsrud: *J. Power Sources*, 2012, vol. 206, pp. 70–76.
35. J.W. Fergus: *Mater. Sci. Eng. A*, 2005, vol. 397, pp. 271–83.
36. Y. Wang, Y. Liu, H. Tang, W. Li, and C. Han: *Trans. Nonferrous Met. Soc. China (English Ed.)*, 2017, vol. 27, pp. 1558–68.
37. B. Talic, S. Molin, P.V. Hendriksen, and H.L. Lein: *Corros. Sci.*, 2018, vol. 138, pp. 189–99.
38. M. Palcut, L. Mikkelsen, K. Neufeld, M. Chen, R. Knibbe, and P.V. Hendriksen: *Corros. Sci.*, 2010, vol. 52, pp. 3309–20.
39. B. Mortimer, P. Grieveson, and K.H. Jack: *Scand. J. Metall.*, 1972, vol. 1, pp. 203–09.
40. G. Miyamoto, A. Yonemoto, Y. Tanaka, T. Furuhashi, and T. Maki: *Acta Mater.*, 2006, vol. 54, pp. 4771–79.
41. M. Bianco, S. Poitel, J.E. Hong, S. Yang, Z.J. Wang, M. Willinger, R. Steinberger-Wilckens, and J. Van Herle: *Corros. Sci.*, 2020, vol. 165, 108414.

**Publisher's Note** Springer Nature remains neutral with regard to jurisdictional claims in published maps and institutional affiliations.



# **Supplementary material for:** **High-temperature Corrosion of ~30% Porous FeCr Stainless Steels in Air: Long-term Evaluation up to Breakaway**

D. Koszelow<sup>a</sup>, M. Makowska<sup>b</sup>, A. Drewniak<sup>a</sup>, G. Cempura<sup>c</sup>, P. Jasiński<sup>a</sup>, S. Molin<sup>a</sup>

<sup>a</sup> Advanced Materials Centre, Faculty of Electronics, Telecommunications and Informatics, Gdańsk University of Technology, 80-233 Gdańsk, Poland

<sup>b</sup> Laboratory for Nuclear Materials, Laboratory for Synchrotron Radiation and Femtochemistry, Paul Scherrer Institut, Villigen, Switzerland

<sup>c</sup> AGH University of Science and Technology, Faculty of Metal Engineering and Industrial Computer Science, International Centre of Electron Microscopy for Materials Science, al. Mickiewicza 30, 30-059 Krakow, Poland

Table S.1. Chemical composition of the alloys given by the producer

Target composition	Fe	Analyzed chemical composition, % [information from the producer]									
		Cr	Mn	Mo	Ni	Cu	Si	Nb	C	O	N
Fe20Cr	Bal.	20.0	0.03	0.02	0.07	0.03	0.08	0.02	0.01	0.03	0.01
Fe22Cr	Bal.	22.0	0.23	0.01	0.03	0.02	0.08	0.02	0.04	0.58	0.07
Fe27Cr	Bal.	27.0	0.30	0.04	0.01	0.00	0.08	0.02	0.01	0.03	0.02

Table S.2. Pores statistic obtained from SEM images analysis

Alloy (magnification)	Range of equivalent diameter [μm]	Average equivalent diameter [μm]	Median equivalent diameter [μm]	Porosity [%]
Fe20Cr (1500x)	1.76 – 70.1	12.4	7.47	29.40
Fe20Cr (2500x)	1.06 – 71.2	11.2	6.09	29.58
Fe22Cr (1500x)	1.76 – 74.4	11.2	6.84	27.68
Fe22Cr (2500x)	1.11 – 58.6	10.9	6.82	27.33
Fe27Cr (1500x)	1.76 – 77.4	10.2	5.90	26.64
Fe27Cr (2500x)	1.08 – 65.2	11.5	7.45	29.37

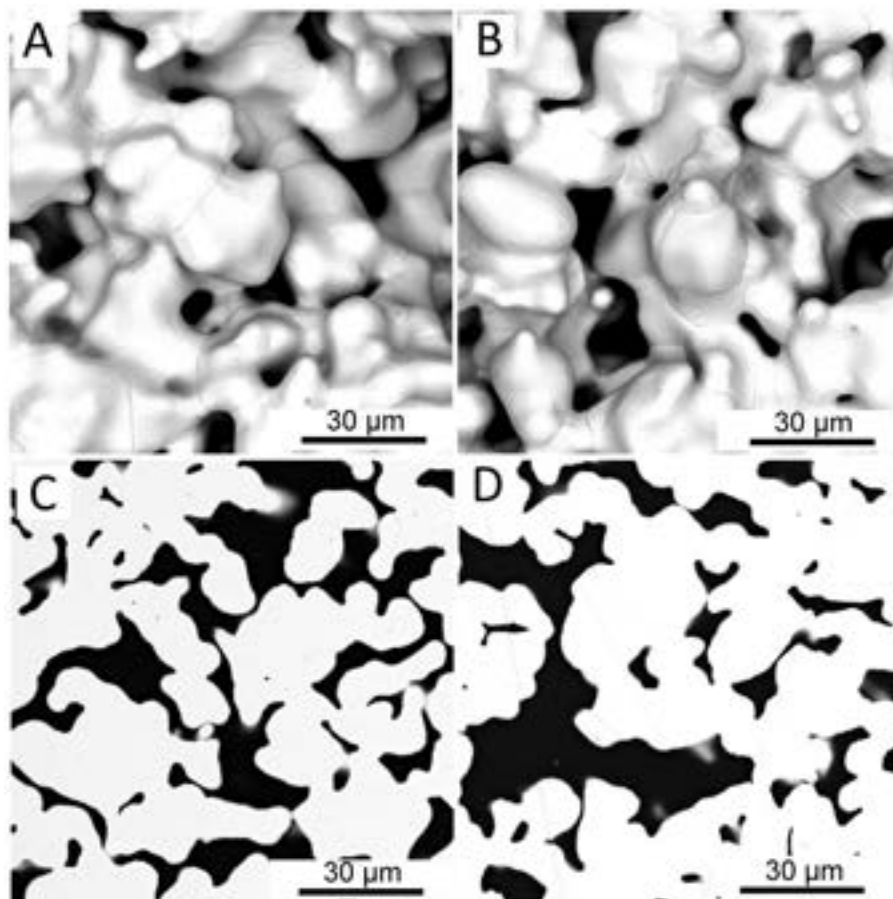


Figure S.1. SEM images of non-oxidised A) surface, C) cross-section of Fe20Cr alloy and B) surface, D) cross-section of Fe27Cr alloy.

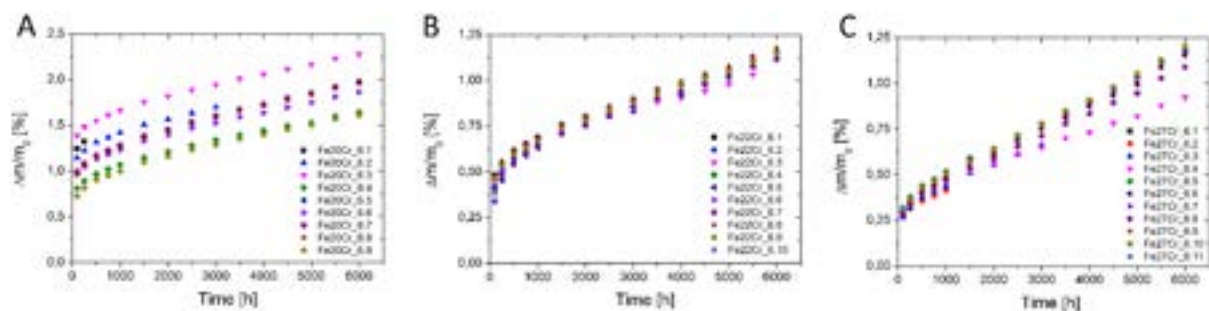


Figure S.2. The mass gain of the individual A) Fe20Cr B) Fe22Cr and C) Fe27Cr specimens oxidised at 600°C.

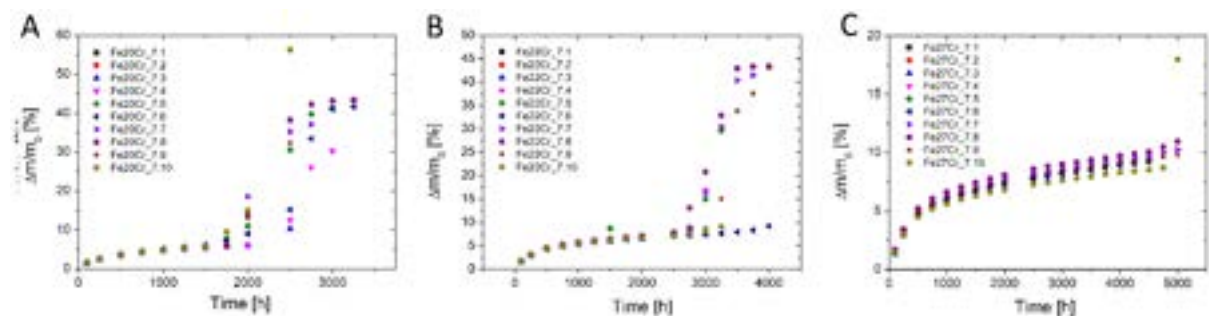


Figure S.3. The mass gain of the individual A) Fe20Cr B) Fe22Cr and C) Fe27Cr specimens oxidised at 700°C.

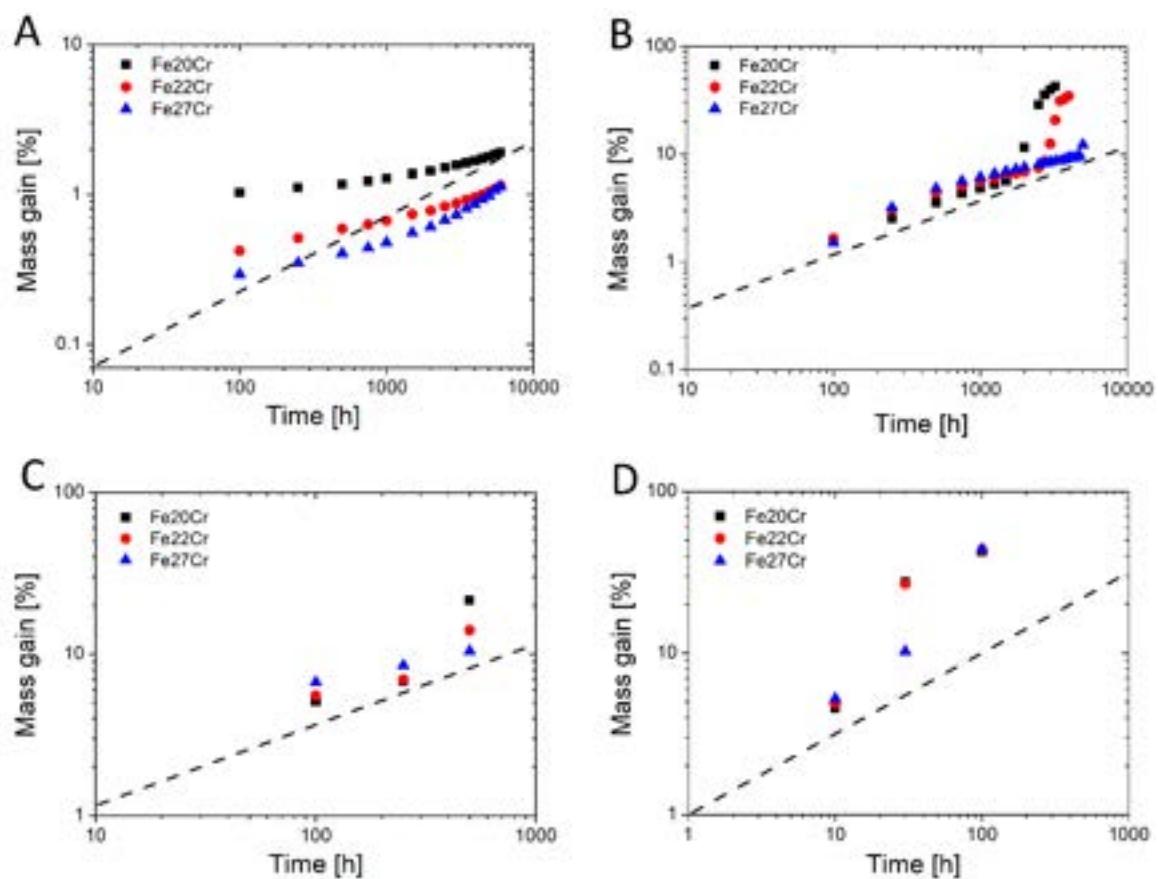


Figure S.4. The log-log plot of mass gain data for Fe20Cr, Fe22Cr and Fe27Cr oxidised at A) 600°C, B) 700°C, C) 800°C and D) 900°C. The dash lines represent 0.5 slope lines.

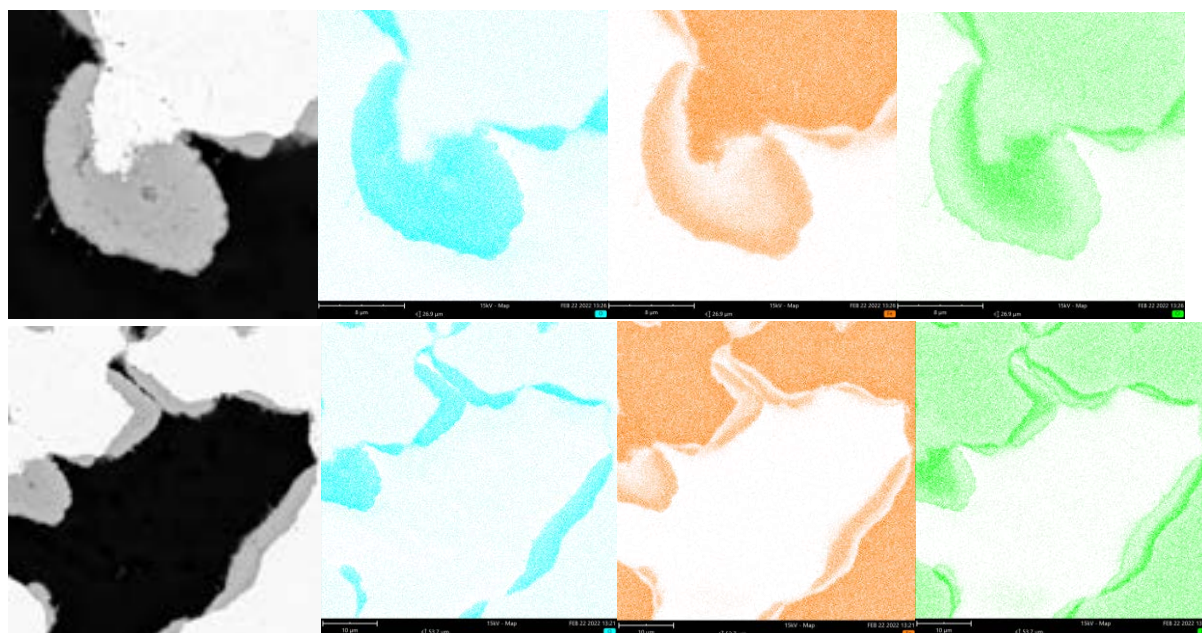


Figure S.5. EDX analysis of Fe20Cr alloy after 6000 h oxidation at 600°C.

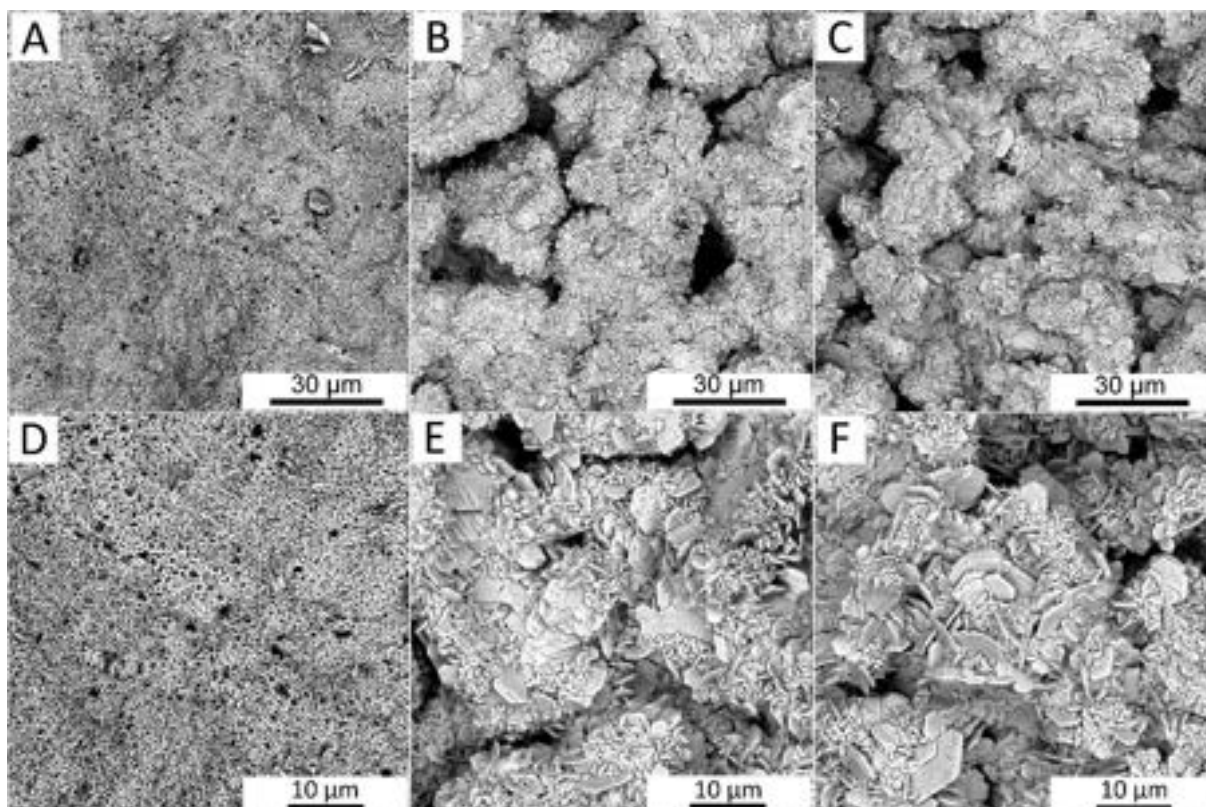


Figure S.6. SEM images of A, C) Fe20Cr, B, E) Fe22Cr and C, F) Fe27Cr alloy surface after oxidation at 700°C for 3000 h.

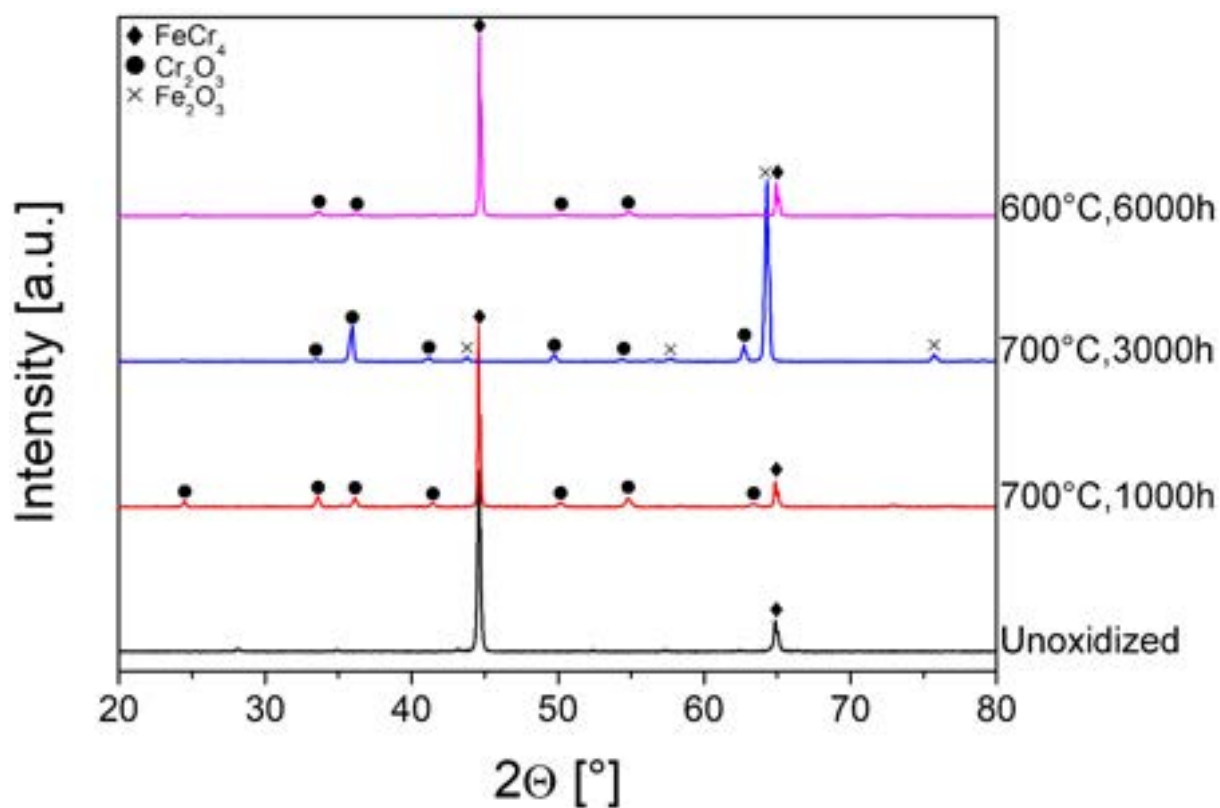


Figure S.7. XRD patterns of the reference Fe22Cr alloy and after different steps of oxidation.



#### **5.4. Pre-oxidation of porous ferritic Fe22Cr alloys for lifespan extension at high temperature**

In order to extend the lifespan of the porous ferritic alloys, the pre-oxidation process performed at 850°C and 900°C was proposed. The idea of pre-oxidation relies on the increase of Cr<sub>2</sub>O<sub>3</sub> grain size (for chromia-forming alloys) as well as a decrease in the relative number of grain boundaries at high temperatures. It leads to altering the grain and grain boundary diffusion fluxes in the oxide scale formed at high temperatures. In consequence, the total diffusion flux of Cr cations decreases, slowing down the oxidation rate at high temperatures which are below the pre-oxidation temperature.

In this work, the positive effect of the pre-oxidation process on the porous ferritic Fe22Cr alloy's lifespan was investigated. It was revealed that the most significant parameter for the lifespan extension is the temperature of the pre-oxidation process. The longest lifespan was achieved for samples pre-oxidized at 900°C for 40 min. At these conditions, a relative weight gain was ~5 times lower than for reference samples. Therefore, the pre-oxidized porous ferritic alloys can be considered as the replacement of the ceramic's components in IT-SOCs.

My original contribution in this work was:

- Performing synchrotron tomography experiments at TOMCAT beamline at Paul Scherrer Institute in Switzerland and data analyzing thus obtained data
- Determining the lifespan extension of porous alloy achieved via pre-oxidation process

Statement of the co-authors' contribution to the publication entitled 'Pre-Oxidation of Porous Ferritic Fe22cr Alloys for Lifespan Extension at High Temperature':

Name and surname	Contribution to the publication	Signature
Damian Koszelow	Conceptualization, Methodology, Formal Analysis, Investigation, Writing – Original Draft	
Małgorzata Makowska	Supervision, Formal Analysis, Writing – Review & Editing	
Federica Marone	Investigation – synchrotron tomography analysis, Writing – Review & Editing	
Grzegorz Cempura	Investigation – SEM/TEM imaging	
Matthieu Tomas	Investigation – chromium evaporation measurements, Writing – Review & Editing,	
Jan Froitzheim	Supervision, Writing – Review & Editing,	
Sebastian Molin	Conceptualization, Supervision, Project administration, Funding acquisition, Writing – Review & Editing	



# Pre-oxidation of porous ferritic Fe22Cr alloys for lifespan extension at high-temperature

D. Koszelow<sup>a,\*</sup>, M. Makowska<sup>b</sup>, F. Marone<sup>c</sup>, G. Cempura<sup>d</sup>, M. Tomas<sup>e</sup>, J. Froitzheim<sup>e</sup>, S. Molin<sup>a</sup>

<sup>a</sup> Advanced Materials Centre, Faculty of Electronics, Telecommunications and Informatics, Gdańsk University of Technology, Gdańsk 80-233, Poland

<sup>b</sup> Laboratory of Nuclear Materials, Laboratory of Synchrotron Radiation and Femtochemistry, Paul Scherrer Institut, Villigen 5232, Switzerland

<sup>c</sup> Swiss Light Source, Paul Scherrer Institut, Villigen, Switzerland

<sup>d</sup> Centre of Electron Microscopy for Materials Science, Faculty of Metal Engineering and Industrial Computer Science, AGH University of Krakow, Al. Mickiewicza 30, Krakow 30-059, Poland

<sup>e</sup> Energy and Materials, Chalmers University of Technology, Kemivägen 10, Gothenburg 41296, Sweden

## ARTICLE INFO

### Keywords:

Porous alloy  
Corrosion  
Lifespan prediction  
Fuel cells  
Tomographic microscopy

## ABSTRACT

Pre-oxidation of porous ferritic Fe22Cr alloys was extensively studied in this paper. Weight gain measurements and SEM analysis revealed that pre-oxidation performed at 900°C for 40 min increased the lifespan of the alloy. A Cr evaporation study did not disclose any significant influence of the pre-oxidation process on the Cr content in the alloy. For a more detailed assessment, TEM imaging and X-ray tomography measurements of pre-oxidized samples were performed. These analyses showed that alteration in the grain and grain boundary diffusion fluxes might be the key for explaining the corrosion prevention role of pre-oxidation.

## 1. Introduction

Advanced alloys are essential for high-temperature devices, including gas turbines, engines, and heat exchangers [1–3]. In recent years, ferritic high-chromium alloys have been considered as support materials for solid oxide cells (SOCs) [4–9]. Advanced ceramic components, which are widely used in SOCs, are expensive and difficult to manufacture [10]. Thus, the application of alloys allows for decreasing the cost of the device and provides shape flexibility.

The typical operating temperature of SOCs exceeds 600°C [11], thus the basic hindrance to using metallic components is the corrosion process [12]. The oxide scale, which is the result of the corrosion process, limits the lifespan of the whole device by decreasing the electrical conductivity of the metallic support. Alloys protection from high-temperature corrosion relies upon the formation of a passivating, protective layer on their surface that limits further oxide growth. [13–15].

One of the elements that forms the passivating layer of oxide scale on the alloy surface in typical SOC operating conditions is chromium. Chromia (Cr<sub>2</sub>O<sub>3</sub>) has a reasonably high conductivity (~1–10 mS cm<sup>-1</sup> at 600 °C–800 °C [16]) combined with low oxide scale growth. Cr-based

ferritic alloys like Crofer 22 APU or Crofer 22 H are considered a support material in solid oxide cells [17]. [18–21]. For alloys that contain more than 26 wt% of Cr, the brittle sigma phase occurs at high temperatures, which is not desirable in the context of solid oxide cell application [22].

The corrosion process has been described in detail throughout the last decades for dense alloys [23–25]. Nevertheless, there are only a limited number of publications about the corrosion of porous ferritic alloys, especially in the context of their lifetime in solid oxide cell operating conditions [26–32]. Koszelow et al. showed that for the same chemical composition and thickness of the alloy sheet, the specific surface area of a porous alloy (~30% porosity) can be 28 times higher than that of a dense form [30]. It indicates a higher contact area between the alloy surface and air, which is a key factor in defining the oxide scale growth rate process.

There are several approaches to evaluate the threshold value of the alloy's lifespan. Tucker et al. defined a threshold value for the oxide scale thickness (~3 μm), which determines the lifespan of the porous alloy [33]. This assumption allowed to settle the possible temperatures and times of oxidation for a Fe22Cr porous alloy in a 9:1 H<sub>2</sub>O:H<sub>2</sub> environment. Nevertheless, in their work, a limited reservoir of Cr inside the alloy particles was not taken into consideration. In this study, the

\* Correspondence to: Gdańsk University of Technology, Poland.

E-mail address: [damian.koszelow@pg.edu.pl](mailto:damian.koszelow@pg.edu.pl) (D. Koszelow).



lifespan is defined as the time for the occurrence of breakaway oxidation, which is a Fe-rich oxide scale formed in the case of depletion of the scale-forming element in the alloy. The same definition of alloy lifespan was applied by Stefan et al., who determined the formation of the breakaway corrosion region for Fe22Cr alloy oxidized at 800°C for ~200 h in air environment [34]. Oxidation tests performed in 2.5% H<sub>2</sub>O and 5% H<sub>2</sub>/Ar revealed the priority of (Fe,Cr)<sub>3</sub>O<sub>4</sub> spinel formation, and no breakaway corrosion region was detected.

Koszelow et al. studied the corrosion process of a porous Fe22Cr alloy in the context of its lifespan. They investigated the kinetics of the corrosion process based on the isothermal weight gain obtained at temperatures ranging from 700 °C to 900 °C. Moreover, the chromium content in the alloy was determined after selected time intervals of oxidation [30]. It allowed for the creation of a simple lifespan prediction model for porous alloys based on the data of only 100 hours of oxidation. According to this model, the lifespan of the alloy depends on the chromium reservoir in the alloy. In the earlier work by Huczowski et al., the authors determined the threshold amount of Cr in the Crofer 22 APU alloy to be 16 wt% [35,36].

Following the parabolic law of oxidation by the Fe22Cr alloy was confirmed in our previous study [26,29]. For chromia forming ferritic alloys, outward Cr-cation diffusion is often cited as the prevalent oxidation mechanism, though with the incorporation of reactive elements, the oxidation mechanism can be modified to be driven by anion inward diffusion [37,38].

The idea of pre-oxidation for chromia-forming alloys means an oxidation at a temperature higher than the intended operation temperature to create a well-defined oxide scale, increase the size of Cr<sub>2</sub>O<sub>3</sub> grains and decrease the grain boundaries of the oxide scale. Assuming that the migration of Cr cations is faster in the grain boundaries than within the chromia grains, the effective diffusion flux of Cr cations decreases, a slowdown of the corrosion rate during oxidation at lower temperatures can thus be observed.

Talic et al. investigated the effect of pre-oxidation on the oxidation resistance of dense 0.8 mm – 0.9 mm Crofer 22 APU sheets [39]. They performed pre-oxidation at 900°C for 2 h and at 1100°C for 5 h, followed by oxidation exposures at 800°C. It was confirmed that the oxidation of Crofer 22 APU follows the parabolic rate law. The authors emphasized that the positive impact of pre-oxidation is likely associated with alterations in the Cr species transport characteristics within the thermally formed Cr<sub>2</sub>O<sub>3</sub> layer, resulting from a modification of the grain size and/or the defect structure.

Hong et al. investigated the pre-oxidation effect of ferritic T92 stainless steel [40]. They confirmed that the weight gain is 3 times lower for pre-oxidized samples when compared with samples without the pre-oxidation step. There are only a few publications regarding the pre-oxidation process effect on porous ferritic alloys.

Tucker et al. performed pre-oxidation tests of porous P434L (16.66 wt% of Cr, 0.94 wt% of Mo, 0.85 wt% of Si, Fe-balanced) alloy [41]. They revealed ~5 times lower relative weight gain for pre-oxidized (at 850°C for 10 h) samples when compared with the weight gain of as-sintered samples at 700°C in air as well as in a hydrogen/steam environment. The same effect was observed for a LSCF-coated porous P434L alloy in an air and oxygen environment.

Even though the positive effect of the pre-oxidation process was confirmed for dense and porous ferritic alloys, there is still a lack of knowledge about the limitations of this process, including the effect of temperature on pre-oxidation, which can be used to improve the corrosion properties, and the pre-oxidation time. Information about the possible lifespan extension of porous pre-oxidized alloys is missing.

In this study, the pre-oxidation process for porous Fe22Cr alloy was investigated in the context of its possible application at high temperatures, e.g., as SOC support on the air side. The pre-oxidation temperatures were selected based on our previous studies, which revealed experimentally that the lifespan of the porous alloy is >2 000 h at 700°C [30,42]. However, at 900°C the determined lifespan was only ~10 h.

Therefore, for operating at 700°C, the pre-oxidation process was investigated at 850°C and 900°C to provide sufficient oxide scale grain growth and prevent quick breakaway corrosion formation. The X-ray tomography experiments and weight gain measurements allowed us to settle the parameters (temperature and time) of the pre-oxidation process for porous Fe22Cr, which were tested at 700°C and 750°C. These conditions were established based on a correlation between the oxide scale growth expressed by weight gain and 3D microstructure changes observed at different steps of high-temperature oxidation at 850°C. Based on oxidation tests, the selected pre-oxidation conditions were validated.

## 2. Experimental

### 2.1. Sample preparation

The sheets of porous Fe22Cr alloy were provided by Höganäs AB. The alloy was produced by a tape-casting method from powder (<53 µm), and the as-received sheet was debinded and sintered in hydrogen (1250°C for 30 min). The composition of the alloy given by the producer is presented in Table 1. This information was confirmed by Inductively Coupled Plasma (ICP) spectroscopy and energy-dispersive X-ray (EDX) measurements. The producer reported the porosity of the alloy as 30%, which was confirmed by the Archimedes method (using kerosene as a medium) as well as by the analysis of scanning electron microscope (SEM) images using dedicated PoroMetric Software (Thermo Fisher). The porosity was evaluated based on the SEM images, as a mean value of results obtained from 20 images taken at 2500x magnification. The measurement uncertainty was calculated as a standard deviation of the mean value obtained from image analysis.

For the oxidation tests, the samples with a size of 10 × 10 mm<sup>2</sup> were cut from a 0.4-mm-thick porous alloy sheet of Fe22Cr. For the X-ray tomographic study, elongated samples with dimensions of 6 × 1 mm<sup>2</sup> were prepared. Then the samples were cleaned in acetone, followed by ethanol, for 10 min in an ultrasonic bath.

### 2.2. Oxidation tests

For the pre-oxidation tests, four series of samples were prepared. Two of them were pre-oxidized at 850°C for 4 h and the remaining two series were pre-oxidized at 900°C for 40 min. One set of samples consisting of a series of samples pre-oxidized at 850°C for 4 h and 900 °C for 40 min, and reference samples (without the pre-oxidation step) were oxidized at 700°C. The second set (the same as the first one) was exposed to 750°C. All oxidation tests were performed in a chamber furnace (Kittec Squadro) in a lab ambient air atmosphere (relative humidity ~30%). For each pre-oxidation process and for the reference samples, 7 samples were used. Detailed information about the oxidation conditions of the investigated samples is presented in Table 2.

The time and temperature of the pre-oxidation were chosen based on our previous study of porous alloys' oxidation in order to obtain ~1% of weight gain after pre-oxidation. The reference samples were investigated to confirm the lifespan extension effect of the pre-oxidized porous alloy. The heating and cooling rates were 180 °C h<sup>-1</sup> and the full time of oxidation was calculated without these processes. The oxidized samples were removed from the furnace after 250 h intervals in order to weigh them using a microbalance Radwag XA 5Y.M. with an accuracy of 1 µg.

The weight gain of the samples was calculated as a relative (percentage) mass change with respect to the initial sample mass. In the weight gain plots, the points represent the average mass change for the set of samples. The weight changes were also recalculated taking into consideration the specific surface area information, which is 0.022 cm<sup>2</sup> g<sup>-1</sup> (obtained from the tomographic study presented in our previous work [29]). The oxidation tests were terminated for selected samples in order to perform post-mortem analysis.

**Table 1**

A composition of the porous Fe22Cr alloy given by the producer.

Element	Fe	Cr	Mn	Mo	Cu	Si	Ni	C	Nb
wt%	Bal.	22	0.23	0.01	0.02	0.08	0.03	0.01	0.02

**Table 2**

Oxidation conditions of the investigated porous Fe22Cr alloys.

Set no.	Preoxidation temperature [°C]	Preoxidation time [min]	Oxidation temperature [°C]
1	900	40	700
2	850	240	700
3	900	40	750
4	850	240	750

### 2.3. Chromium evaporation

Cr(VI) evaporation measurements were carried out in horizontal tube furnaces using an airflow of 6000 sl•min<sup>-1</sup> for up to 500 h. Cr(VI) vaporization is a significant issue in terms of the longevity of the fuel cell stack. Therefore, it is necessary to quantify the rate of Cr(VI) evaporation during the exposure. Cr(VI) vaporization was measured for all samples using the denuder technique, which allows in situ determinations of Cr(VI) evaporation. A detailed description of the Cr(VI) evaporation measurement procedure can be found elsewhere [43]. At least two sets of three samples were exposed, and Cr(VI) evaporation measurements were performed at regular intervals.

### 2.4. Synchrotron tomographic microscopy

In order to validate the positive effect of the chosen pre-oxidation conditions (~1 wt% weight gain), the X-ray tomographic study was performed at the TOMCAT beamline of the Swiss Light Source (SLS) at the Paul Scherrer Institute, Villigen, Switzerland. The cut and cleaned rectangle-shaped sample was stuck to the metallic holder using wax to prevent any horizontal or vertical motion during the experiment. A parallel X-ray beam with an energy of 40 keV was used. The detector configuration comprised a scintillator that turned X-rays into visible light, an objective lens, and a sCMOS camera that generated an image characterized by a pixel size of 0.325 µm and a field of view of around 0.8 mm × 0.7 mm. With a total of 1001 projections across 180° recorded, each with a 1600 ms exposure, scans took roughly 26 minutes to complete. The scans were performed for the sample after selected time intervals of oxidation in air at 850 °C using a heat blower. A thermocouple indicated that the temperature fluctuation was ~5 °C. The tomograms were generated for the sample after 3 h, 5.5 h, 7.5 h, 10 h, 12.5 h, 15 h, 17.5 h, 20 h, 22.5 h, 25 h, 27.5 h, and 30 h of oxidation.

The collected tomograms were reconstructed utilizing the in-house developed pipeline accessible at the beamline, which gives entire tomographic volumes immediately after the data acquisition and enables the rapid modification of the measurement and reconstruction algorithm parameters. The obtained projections were tomographically reconstructed after dark- and flat-field correction and phase retrieval (according to the Paganin method [44]). Signal-to-noise and contrast-to-noise ratios were improved with the use of phase retrieval. The achieved contrast in the images reconstructed with this approach allowed for a relatively straightforward material segmentation based only on intensity thresholding, which was performed using the commercial software Thermo Scientific Avizo 9.4. The intensity ranges assigned to the steel, porosity, and oxide scales were determined based on the histogram minima for one of the samples with a significant degree of oxidation. For phase segmentation, the same intensity ranges were then applied to the measured tomograms. Although the absolute values of estimated material percentages are dependent on the intensity thresholds chosen, applying the same intensity ranges to all samples

enables a realistic comparison of oxidation-induced changes. It was noted that for these tomographic measurements, it is possible to distinguish objects of ~1.5 µm in the reconstructed volumes; hence, 1.5 µm was regarded as the resolution of the analyzed images.

### 2.5. Scanning electron microscopy analysis

In order to evaluate the morphology changes of pre-oxidized samples after further oxidation at lower temperatures, scanning electron microscopy was employed. The images of porous alloys oxidized without a pre-oxidation step were taken as references. SEM imaging was performed using a Phenom XL electron microscope (Thermo Fisher Scientific, Netherlands) on polished cross-sections of the samples. All SEM images were recorded using a backscatter electron detector (BSE). The microscope was equipped with an EDX detector (Thermo Fisher Scientific, 25 mm<sup>2</sup> Silicon Drift Detector), which was used for elemental analysis of steel (EDX analyses performed at an acceleration voltage of 15 kV).

The morphology changes of porous alloys that are caused by the oxidation process are crucial for determining the effect of pre-oxidation. Thus, in this work, morphology changes as well as phase composition are evaluated in detail for the first hours of oxidation.

### 2.6. Transmission electron microscopy analysis

The samples for TEM imaging were prepared as lamellae. They were prepared by sputtering the sample surface with Ga<sup>+</sup> ions emitted from a liquid metal ion source (FIB). The lamellae were finished with thinning down to a level of several dozen nanometers after being mounted in a TEM-dedicated copper grid.

The TEM/STEM analyses were performed using a Cs probe-corrected Titan Cubed G2 60–300 microscope (FEI) equipped with the ChemiSTEM™ system. High-resolution STEM (HRSTEM) images were acquired using a high-angle annular dark-field (HAADF) detector.

## 3. Results and discussion

### 3.1. Non-oxidized alloy analysis

The surface morphology and cross-sectional microstructure of the unoxidized porous Fe22Cr alloy are presented in Fig. 1. The necks between particles are clearly visible for both surface (Fig. 1 D) and cross-sectional (Fig. 1 B) images. The porosity of the alloy is easily recognizable, even for low magnification images (Fig. 1 A, C). Using the Archimedes method, the porosity was calculated as (30 ± 2) %. The SEM image analysis method revealed (29 ± 5) % porosity, which is in agreement with both the Archimedes method and the value given by the producer (~30%) data.

The composition of the investigated alloy, determined by the producer, is shown in Table 1. For confirmation of this data, Inductively Coupled Plasma Spectroscopy (ICP) and EDX measurements were performed. The obtained compositions are presented in Table 3. The ICP data corresponds with the composition provided by the producer. The EDX measurement revealed some small differences in the Cr and Mn levels. However, taking into consideration limitations in the accuracy of this technique, the resultant composition of the investigated alloy corresponds well with the producer data.

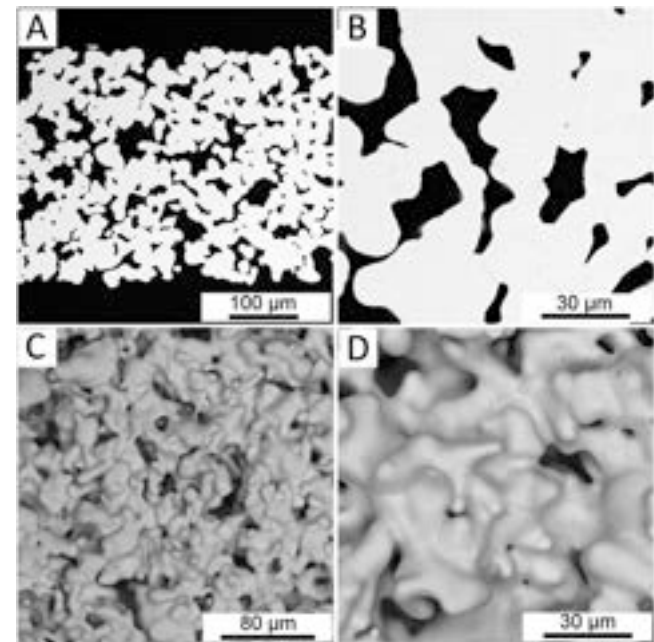


Fig. 1. SEM images of A, B) cross-section; C, D) surface of as-received Fe22Cr alloy.

3.2. Pre-oxidized samples morphology

The impact of the pre-oxidation process on the longevity of porous alloys is determined by modifications in the fluxes of grain and grain boundary diffusion. For the evaluation of this effect, a detailed

morphology analysis is necessary. In Fig. 2, SEM images of a porous alloy surface are presented. In the first row (Fig. 2 A – C), images of the Fe22Cr alloy pre-oxidized at 850°C are shown. The second-row images illustrate the porous Fe22Cr alloy pre-oxidized at 900°C for 40 min.

The images of the samples after the pre-oxidation taken at 2000 x magnification (Fig. 2 A and D) reveal well-connected particles with easily observed necks between them. The oxide scale phase is noticeable on the particle surface for both considered samples. At this low magnification, no significant morphological difference between the porous alloy pre-oxidized at 850°C for 4 h and pre-oxidized at 900°C for 40 min is visible.

For the alloys' images taken at 5000 x magnification (Fig. 2 B and E for the Fe22Cr alloy pre-oxidized at 850°C for 4 h and pre-oxidized at 900°C for 40 min, respectively), the oxide scale is easily detectable on the particle surface. A difference in chromia crystal size is observed between the considered samples. Based on the images taken at 5000 x magnification, it seems that bigger chromia crystals could be detected for the sample pre-oxidized at 850°C for 4 h than for the sample pre-oxidized at 900°C for 40 min.

Images taken at 10 000 x magnification for the alloy pre-oxidized at 850°C for 4 h and pre-oxidized at 900°C for 40 min are shown in Fig. 2 C and F, respectively. Microstructural differences are easily observed when comparing the oxide scale crystals size. Chromia crystals are larger for the sample pre-oxidized at 850°C for 4 h – their width reaches up to 5 μm. On the other hand, chromia crystals observed on the surface of the porous alloy pre-oxidized at 900°C for 40 min are ~ 1 – 2 μm in width.

In Fig. 3 SEM images of the cross-section of the porous Fe22Cr alloy pre-oxidized at 900°C for 40 min are presented. The images were obtained by Focus Ion Beam preparation of the sample for TEM imaging. The analysis of the pre-oxidized sample image (Fig. 3A) reveals the slightly visible oxide scale on the alloy surface. Nevertheless, the thickness of the oxide scale is <0.5 μm, therefore the morphology of the

Table 3  
Chemical composition of the alloys obtained from ICP and EDX measurements.

Target composition	Fe	Analysed chemical composition, wt% [information from the ICP measurement]								EDX, wt%	
		Cr	Mn	Ni	Si	Ti	Co	Ca	Na	Cr	Mn
Fe22Cr	Bal.	21.87	0.25	0.02	0.08	0.01	0.01	0.00	0.00	21.3	0.1

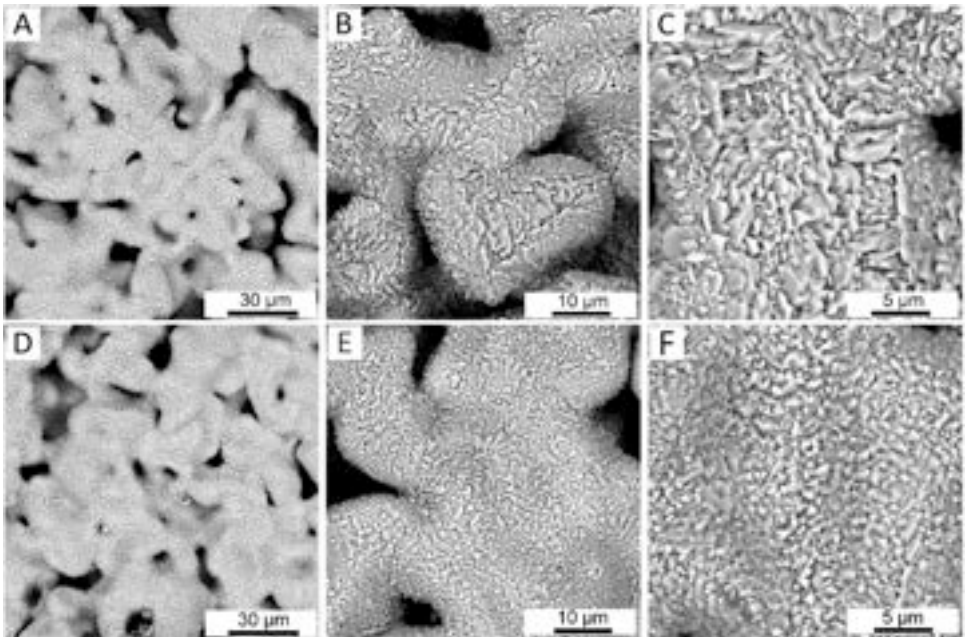
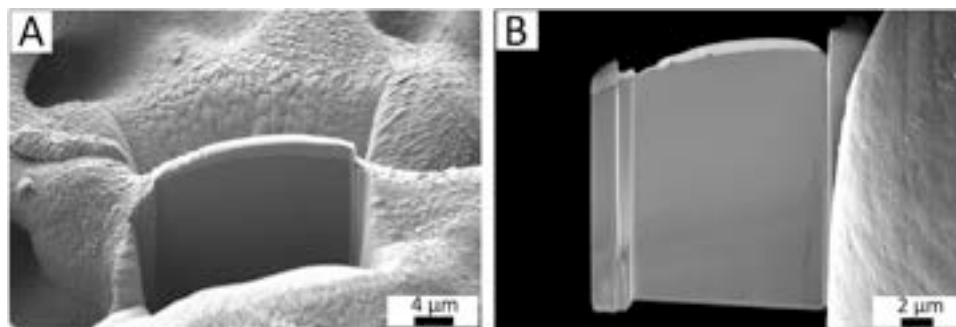


Fig. 2. SEM images of the alloy surface after (a-c) pre oxidation at 850°C for 4 h, (d-f) pre-oxidation at 900°C for 40 min.





**Fig. 3.** SEM images of the porous Fe22Cr cross-section after pre-oxidation at 900°C for 40 min taken at A) 2000 x, and B) 4000 x magnification.

pre-oxidized samples is macroscopically similar to the raw samples presented in Fig. 1A - B. For the images taken at 4000 x magnification (Fig. 3B) the continuous oxide scale layer can be recognized on the surface of alloy particles. The thickness of the oxide scale is below 0.5 µm.

### 3.3. Pre-oxidation conditions validation via 3D microstructure analysis

In spite of the fact that SEM imaging is a technique that allows for the evaluation of the oxide scale thickness for different samples, it can also be misleading. A specific polished cross-section might not be representative for determining the microstructure of the sample, especially for porous samples, which consist of many different-size particles that form a high-specific surface area structure. In order to observe the microstructural changes of porous metallic alloys, a 3D analysis is necessary. Thus, synchrotron tomography was employed to analyze the selected samples.

The visualization of the sample oxidized at 850 °C for 5.5 h obtained by volume rendering of the reconstructed slices is presented in Fig. 4A. The necks between the alloy particles are easily observed, as well as the porosity of the sample. Phase contrast allows for distinguishing the metallic core, oxide scale, and porosity phases. Thus, material segmentation was performed based on the different gray scales of each phase. An exemplary slice of the selected piece of the reconstructed volume that was used for detailed analysis is presented in Fig. 4B. The segmentation of the selected volume is illustrated in Fig. 4C, where orange is assigned to the oxide scale, and the metallic core is represented by turquoise.

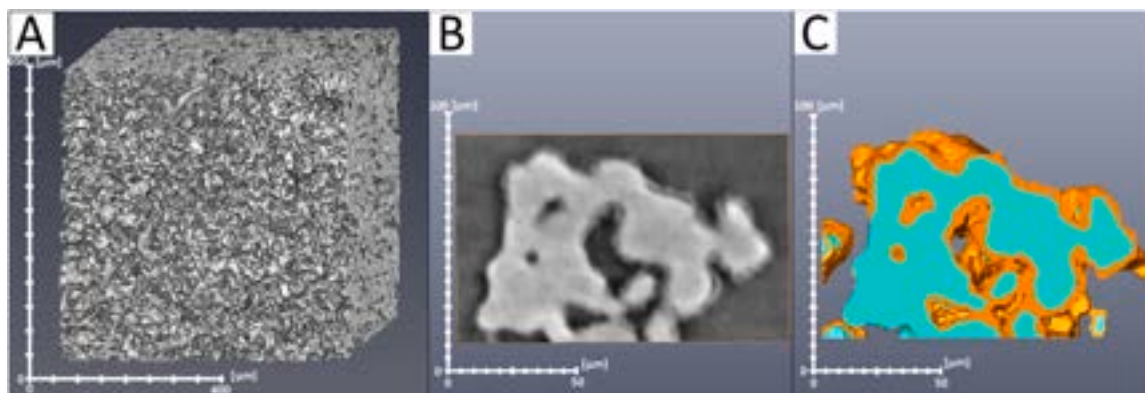
The investigated time intervals of the tomographic analyses (3 h and 5.5 h) are not exactly the same as the pre-oxidation process performed at 850°C (4 h). It means that the observed microstructural changes cannot be directly compared with the microscopic data obtained with SEM analysis. Nevertheless, tomographic measurements enable the observation of microstructural changes both before and after the chosen pre-

oxidation time. Therefore, the analysis of the tomographic data conclusively allows for the validation of the required pre-oxidation time to achieve a positive impact on the alloy lifespan.

In Fig. 5, the results of material segmentation for the Fe22Cr alloy before (Fig. 5A) and after different times of pre-oxidation (3 h, 5.5 h, and 30 h for Fig. 5B-D, respectively) performed at 850 °C are presented. The different colors are assigned to the particular phase: the oxide scale is represented by orange, and the metallic core is represented by turquoise. For each of these images, the same region of sample was selected in order to observe the microstructural changes during the oxidation process. For the unoxidized sample (Fig. 5A) the necks between particles are clearly visible, as are the pores within the whole sample's volume. The surface of the metallic core is smooth, and no signs of oxide scale were detected.

After 3 h of oxidation (Fig. 5B) the oxide scale is apparent, but there are still regions without visible chromia on the alloy's surface (marked by the black arrow). However, the resolution of the tomographic measurements is ~1.5 µm. Therefore, it seems likely that the oxide scale thickness does not exceed 1.5 µm and it cannot be recognized via microtomographic techniques. For the sample oxidized for 5.5 h at 850°C (Fig. 5C), the regions of the uncovered alloy's surface are still observed (marked by the black arrows). However, the first signs of oxide scale can be recognized in the place that corresponds with the region marked by the black arrow in Fig. 5B. In Table 4a relative volume for each detected phase is summarized. A small difference in the oxide scale amount between the sample oxidized for 3 h and 5.5 h (from 23.9 vol% to 24.6 vol%) indicates that even longer pre-oxidation time than assumed 4 h, that cause ~1 wt% weight gain, can be applied to achieve a positive effect from the pre-oxidation process.

After 30 h of oxidation at 850 °C, the oxide scale was detected not only on the whole alloy surface but also inside the alloy's particles (Fig. 5D). Moreover, in some regions, the extension of the oxide scale regions occurred. This observation is consistent with the tomographic



**Fig. 4.** A) Visualisation of the sample oxidized at 850 °C for 5.5 h obtained by volume rendering of the reconstructed slices, B) exemplary slice of the sample region selected to the detailed analysis, C) material segmentation of the chosen reconstructed volume.

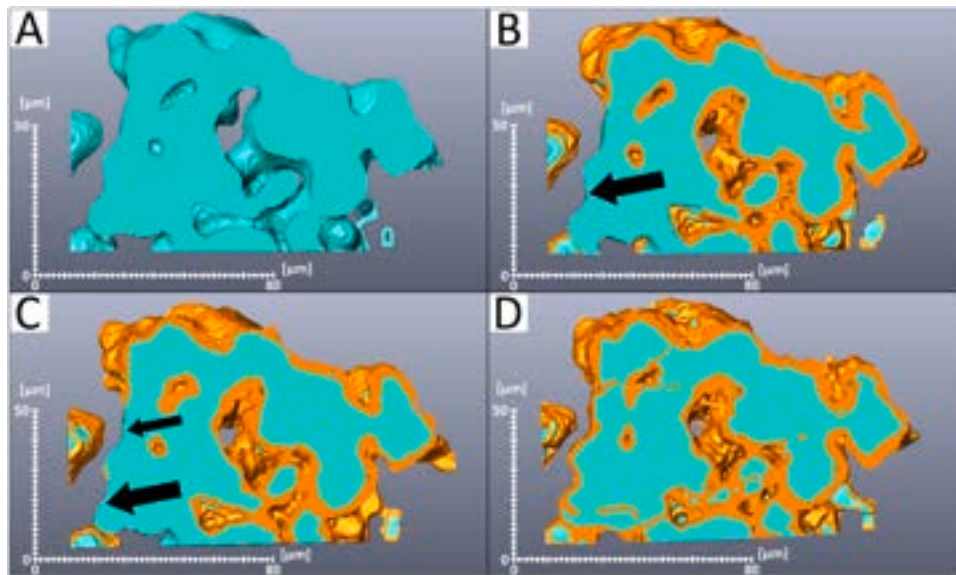


Fig. 5. Material segmentation for the Fe22Cr alloy (a) before and (b-d) after 3 h, 5.5 h and 30 h of oxidation performed at 850°C, respectively.

Table 4

Material statistics after oxidation at 850°C.

Time of oxidation [h]	Alloy [vol%]	Oxide scale [vol%]
3	76.1	23.9
5.5	75.4	24.6
30	68.9	31.1

analysis of the Fe22Cr alloy performed in our previous study [42]. The relative oxide scale volume increased from 24.6% after 5.5 h of oxidation to 31.1% after 30 h at the same temperature. The oxidation at 850°C (and higher) leads to fast formation of breakaway corrosion when 6 wt% of relative weight gain is reached (based on our previous study). On the other hand, oxidation at high temperatures can be applied for a shorter time for the pre-oxidation process.

### 3.4. Oxide scale growth kinetics at 700°C

The relative weight gain for all investigated porous Fe22Cr samples is presented in Fig. 6. The first set of samples was pre-oxidized at 900 °C for 40 min, and the second one was pre-oxidized at 850 °C for 4 h. The weight gain after the pre-oxidation steps was 1.05% and 1.12%, respectively. Then, further exposure of the samples was performed at 700 °C (Fig. 6A and C). The relative weight gain for the pre-oxidized

samples is significantly lower when compared with the reference samples (oxidized at 700°C without the pre-oxidation step). For the reference samples, a threshold value of 6 wt% in relative weight gain was reached after 1500 h of oxidation at 700°C.

The samples pre-oxidized at 900°C for 40 min reveal lower relative weight gain than samples pre-oxidized at 850°C for 4 h. Our previous study of porous alloys' long-term performance disclosed that ~ 6 wt% is a threshold value of relative weight gain for breakaway corrosion appearance in Fe22Cr alloys. The same relative weight gain data as in Fig. 6A is also presented in a log-log scale, as shown in Fig. 6C. The cross point between the linear extrapolation of the relative weight gain data and the dashed line, which represents the threshold value of 6 wt% indicates the predicted lifespan of the alloy. The lifespan of the alloy pre-oxidized at 900°C for 40 min was calculated as  $(3765 \pm 450)$  h, and for the alloy pre-oxidized at 850°C for 4 h, the lifespan was  $(2220 \pm 310)$  h. The measurement uncertainty for the lifespan estimation was calculated taking into consideration the 95% prediction band. The uncertainty of the weight gain measurements was counted as the standard deviation of the mean. Then, the weight gain of the samples pre-oxidized at 850°C for 4 h and further 2000 h oxidation at 700°C was  $(5.41 \pm 0.73)$  %. This weight gain range reached the threshold limit of 6 wt%, thus the obtained result indicates breakaway corrosion region appearance in this case. For the samples pre-oxidized at 900 °C, the measured weight gain after 2000 h of oxidation at 700°C was much lower: 3.91 wt%.

The weight gain measurements allow for the determination of the

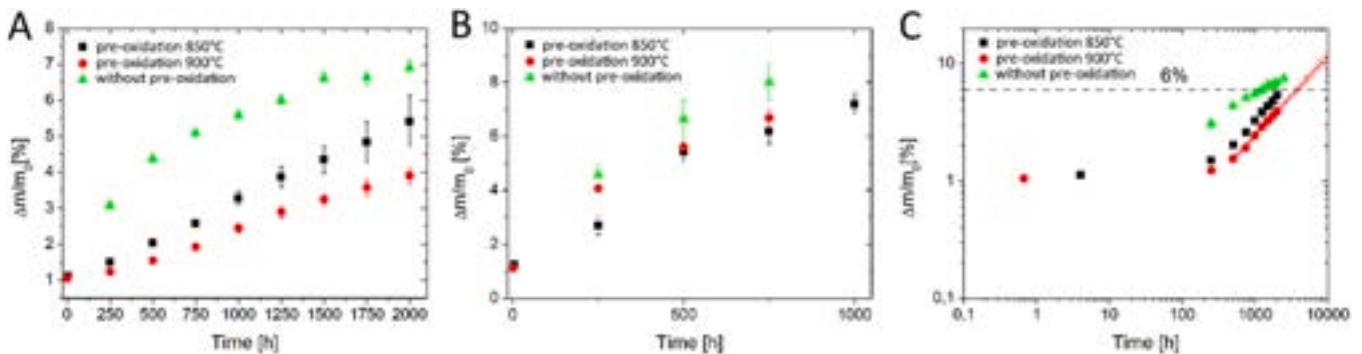


Fig. 6. Percentage mass change of raw, pre-oxidized at 850°C for 4 h and pre-oxidized at 900°C for 40 min alloys oxidized at (a) 700°C for 2000 h and (b) 750°C for 1000 h. (c) Log-log plot the data presented in (a) with the lifespan prediction lines. The 6 wt% dash line represents the assumed threshold level for the breakaway corrosion appearance.

oxidation kinetics for the investigated alloy. Based on the weight gain data illustrated in the log-log scale (Fig. 6 C), the slope of the curves was calculated using linear regression. For the pre-oxidized samples, two of the first points were excluded from the analysis. For the reference samples, the calculated slope was 0.42, and for both series of pre-oxidized samples it was 0.69. This change of slope indicates that another mechanism started to determine the oxidation kinetics of the investigated alloy after the pre-oxidation step. This is analyzed in detail in Section 3.9.

The available literature data as well as our previous study reveal that Cr-based ferritic alloys follow a parabolic law of corrosion expressed by equation  $\left(\frac{\Delta m}{S}\right)^2 = k_p t$ , where  $\Delta m$  [g] is the weight gain of the sample,  $S$  is the surface area of the alloy [ $\text{cm}^2$ ],  $t$  is time of oxidation [s], and  $k_p$  is the parabolic rate constant [ $\text{g}^2 \text{cm}^{-4} \text{s}^{-1}$ ]. Based on the available surface area data for the Fe22Cr alloy determined in our previous work ( $220 \text{ cm}^2 \text{ g}^{-1}$ ), weight gain data has been recalculated per surface area, which allowed to calculate corrosion rate parameters for comparison with data from bulk alloys (Figure S.3.). The parabolic rate constant of the corrosion process found in this study is  $1.2 \times 10^{-14} \text{ g}^2 \text{cm}^{-4} \text{s}^{-1}$  for raw samples,  $9.7 \times 10^{-15} \text{ g}^2 \text{cm}^{-4} \text{s}^{-1}$  for samples pre-oxidized at  $850^\circ\text{C}$ , and  $5.1 \times 10^{-15} \text{ g}^2 \text{cm}^{-4} \text{s}^{-1}$  for samples pre-oxidized at  $900^\circ\text{C}$ . In our previous study, the  $k_p$  value was determined for the same porous Fe22Cr alloy as  $4.5 \times 10^{-15} \text{ g}^2 \text{cm}^{-4} \text{s}^{-1}$  for oxidation at  $700^\circ\text{C}$  (without the pre-oxidation step). The difference between these results is due to the character of the oxidation experiments: in our former work we carried out short term isothermal exposures, whereas in the present work, we carry out long term cyclic exposures. The value obtained for raw alloys agrees with the literature data for similar alloys (Crofer 22 APU/H). Falk-Windisch et al. calculated the  $k_p$  value for Crofer 22 H as  $4.5 \times 10^{-16}$ ,  $1.1 \times 10^{-14}$  and  $3.3 \times 10^{-13} \text{ g}^2 \text{cm}^{-4} \text{s}^{-1}$  for 650, 750, and  $850^\circ\text{C}$ , respectively [45]. Stefan et al. obtained the  $k_p$  values of  $8 \times 10^{-15} \text{ g}^2 \text{cm}^{-4} \text{s}^{-1}$  and  $1 \times 10^{-12} \text{ g}^2 \text{cm}^{-4} \text{s}^{-1}$  from the oxidation tests performed for porous Fe20Cr alloy at  $700^\circ\text{C}$  and  $800^\circ\text{C}$ , respectively [46].

### 3.5. Oxide scale growth kinetics at $750^\circ\text{C}$

Fig. 6 B shows the relative weight gain of samples that were pre-oxidized at  $900^\circ\text{C}$  for 40 minutes and  $850^\circ\text{C}$  for 4 hours, during oxidation at  $750^\circ\text{C}$  (sets no. 3 and 4 in Table 2). The weight gains were 1.26% and 1.12%, respectively. Like the samples that were oxidized at  $700^\circ\text{C}$ , the reference alloy, that was oxidized at  $750^\circ\text{C}$  without the pre-oxidation step, showed the highest relative weight gain when compared to the samples that had already been pre-oxidized. The difference in weight gain between the alloys pre-oxidized at  $850^\circ\text{C}$  for 4 h and the alloys pre-oxidized at  $900^\circ\text{C}$  for 40 min is negligible after 500 h of oxidation. After 750 h of oxidation at  $750^\circ\text{C}$ , the higher increase in weight gain for samples pre-oxidized at  $900^\circ\text{C}$  for 40 min is noticeable. In contrast to the samples pre-oxidized at  $850^\circ\text{C}$  for 4 h, for samples pre-oxidized at  $900^\circ\text{C}$  for 40 min, breakaway corrosion regions were detected (Figure S.2. in supplementary materials).

### 3.6. Cr evaporation

In addition to oxidation kinetics, Cr evaporation from porous alloys has been determined. The results of Cr evaporation for raw samples, pre-oxidized alloys at  $850^\circ\text{C}$  for 4 h, and pre-oxidized alloys at  $900^\circ\text{C}$  for 40 min are presented in Fig. 7 A-C, respectively. The cumulative Cr evaporation curves reveal only slight changes between raw alloy oxidation and the oxidation of pre-oxidized alloys. The highest total Cr evaporation is observed for the alloy pre-oxidized at  $900^\circ\text{C}$  for 40 min, which is  $2.32 \times 10^{-4} \text{ mg cm}^{-2}$  after 500 h and the lowest one is  $1.57 \times 10^{-4} \text{ mg cm}^{-2}$  for the alloy pre-oxidized at  $850^\circ\text{C}$  for 4 h. The Cr evaporation rate is also comparable for all investigated samples, and varies from  $\sim 2 \times 10^{-7} \text{ mg cm}^{-2} \text{ h}^{-1}$  to  $8 \times 10^{-7} \text{ mg cm}^{-2} \text{ h}^{-1}$ . No significant difference between the Cr evaporation of raw alloys and pre-oxidized alloys is visible. It seems that the pre-oxidation process does not significantly change the rate of Cr evaporation from the alloy.

The chromia present on the alloy surface undergoes evaporation, due to the formation of volatile hexavalent Cr species. These compounds constitute the reason for the deterioration of the oxygen electrode in SOC systems [14,45]. Therefore, the influence of Cr evaporation for the ferritic Cr-based ferritic alloys was investigated, especially in the context of potential interconnector material in SOCs [47–50].

Falk-Windisch et al. studied the effect of temperature on chromium vaporization and oxide scale growth for Crofer 22 H and Sanergy HT alloys [45]. They performed Cr evaporation measurements at  $650^\circ\text{C}$ ,  $750^\circ\text{C}$ , and  $850^\circ\text{C}$  for 500 h, revealing that both steels showed rather similar oxidation and vaporization behavior. Furthermore, they demonstrated that a decrease in temperature of  $100^\circ\text{C}$  results in a fivefold reduction in overall weight gain, but the vaporization of Cr decreases by a factor of 2–3.

Reisert et al. investigated Cr evaporation for a 434 L porous alloy pre-oxidized at  $850^\circ\text{C}$  for 10 h in air with 3% of  $\text{H}_2\text{O}$  [51]. The specific surface area of the studied alloy was  $0.025 \text{ m}^2 \text{ g}^{-1}$ . The obtained Cr evaporation rate was  $6.3 \times 10^{-6} \text{ mg cm}^{-2} \text{ h}^{-1}$ . The higher value compared with this work is due to the lower temperature and humidity in the present experiments.

However, the Cr evaporation rate curves for the porous Fe22Cr alloy (Fig. 7) do not reveal the same tendency as it was indicated by other studies for bulk alloys with similar chemical composition [47,52,53]. It may be connected with a higher specific surface area for the porous alloy, so the larger possible area for the evaporation process. Moreover, the level of Mn within the alloy particles is possibly insufficient to form a Mn-rich spinel layer on their surface, thus the linear trend of the evaporated Cr is observed for the investigated alloy.

Koszelow et al. proved that based on the changes in Cr content inside the alloy particles, it is possible to estimate the possible lifespan of the porous Cr-based alloy [29]. Since there isn't a clear difference between reference and pre-oxidized alloys in terms of Cr evaporation, it may indicate that the pre-oxidation process doesn't have a significant effect on the oxide scale growth and thus, it does not influence the alloy's lifespan. The Cr evaporation rate for the raw alloy is noticeably higher than for the pre-oxidized samples for the first hundred hours of the

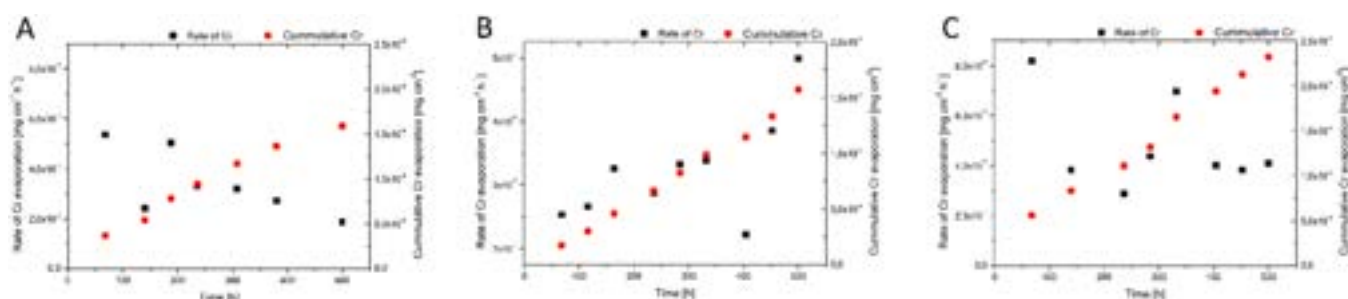


Fig. 7. The results of Cr evaporation for (a) raw samples (b) alloy pre-oxidized at  $850^\circ\text{C}$  for 4 h, (c) alloy pre-oxidized at  $900^\circ\text{C}$  for 40 min.



exposure. It corresponds with the weight gain results that revealed a significantly higher weight increase for raw samples when compared with the pre-oxidized samples (see Fig. 6 A). This shift in weight gain is also visible in the log-log plot (see Fig. 6 C).

### 3.7. Morphological SEM analysis after aging

According to the oxidation model, breakaway corrosion regions should be apparent for the sample pre-oxidized at 850°C for 4 h and further oxidized at 700°C for 2000 h. To validate the lifespan prediction model, SEM was employed for the pre-oxidized and aged samples. In Fig. 8, SEM images of the pre-oxidized and aged samples for 2000 h at 700°C are shown.

In the first row (Fig. 8A - C) the porous pre-oxidized at 850°C for 4 h and further oxidized at 700°C for 2000 h Fe22Cr alloy was shown. The image taken at 700 x magnification (Fig. 8A) reveals the breakaway corrosion region. It is in agreement with the oxidation exposure measurements (Fig. 6A), which show that the threshold weight gain limit (6 wt%) was reached for the porous alloy pre-oxidized at 850°C and further sintered at 700°C for 2000 h. However, a large region without breakaway corrosion is observed for this sample. It means that the alloy is at the beginning of breakaway corrosion formation.

The images taken at 2000 x and 5000 x magnification (Fig. 8B and C, respectively) allow for determining the chromia thickness, which is  $\sim 3 \mu\text{m}$ . The oxide scale is apparent on the whole alloy surface, and it tightly covers all particles. Moreover, the oxide scale seems to occupy the pore regions observed before oxidation. The phenomenon of replacing the pore volume by the formation of the oxide scale was confirmed in our previous work [42].

The second-row images (Fig. 8D - F) show the porous Fe22Cr alloy pre-oxidized at 900°C for 40 min and further oxidized at 700°C for 2000 h. At lower magnification (Fig. 8D), the oxide scale is easily detectable on the particle surface. However, no signs of breakaway corrosion regions are observed. It corresponds to the weight gain measurements (3.91% of weight gain after 2000 h of oxidation at 700°C) and

the lifespan prediction model, which indicate that breakaway corrosion might be apparent only after  $3800 \text{ h} \pm 400 \text{ h}$ .

Higher magnification images of the porous Fe22Cr alloy pre-oxidized at 900°C for 40 min and further oxidized at 700°C for 2000 h are presented in Fig. 8 E and Fig. 8 F (taken at 2000 x and 5000 x, respectively). The chromia layer seems to be smooth and tightly covers the whole alloy surface. The thickness of the oxide scale is  $\sim 2 \mu\text{m}$ .

### 3.8. Grain size changes (TEM analysis)

Detailed characterization of the alloy-oxide was carried out on the FIB-cut lamellae by STEM. The analysis of the sample pre-oxidized at 900°C for 40 min was performed to determine the microstructural changes of the oxide scale, especially in the context of chromia grain size (Fig. 9). The analysis of the alloy pre-oxidized at 900°C for 40 min after further oxidation at 700°C for 2000 h was performed to observe the microstructural changes in detail (Fig. 10).

In Fig. 9A, the structure of the oxide scale layer is presented. A continuous layer of chromia is visible on the top of the alloy surface. The thickness of the oxide scale layer is in the range of 100 nm to 350 nm. Nevertheless, the voids between alloy and oxide scale are also detected, which is consistent with our previous study of long-term oxidized Fe22Cr alloy [26]. For the Fe22Cr alloy pre-oxidized at 900°C for 40 min and further oxidized at 700°C for 2000 h the oxide scale thickness is in the range from  $3 \mu\text{m}$  to  $4 \mu\text{m}$  (Fig. 10A). The voids between alloy and chromia are also visible.

In Fig. 9B, a higher magnification image of the alloy-oxide scale interface is presented. The voids are clearly observed, and their width ranges from  $\sim 70 \text{ nm}$  to  $\sim 150 \text{ nm}$ . Moreover, the differences in the oxide scale thickness are also visible, as shown in Fig. 9A. On the other hand, the higher magnification image of the pre-oxidized sample after further 2000 h oxidation reveals the elongated shape of the chromia grains, which form near the oxide scale-air interface. The width of these chromia grains is in the range from  $0.5 \mu\text{m}$  to  $1.5 \mu\text{m}$ . However, the oxide scale grains placed near the alloy particles are undistinguishable.

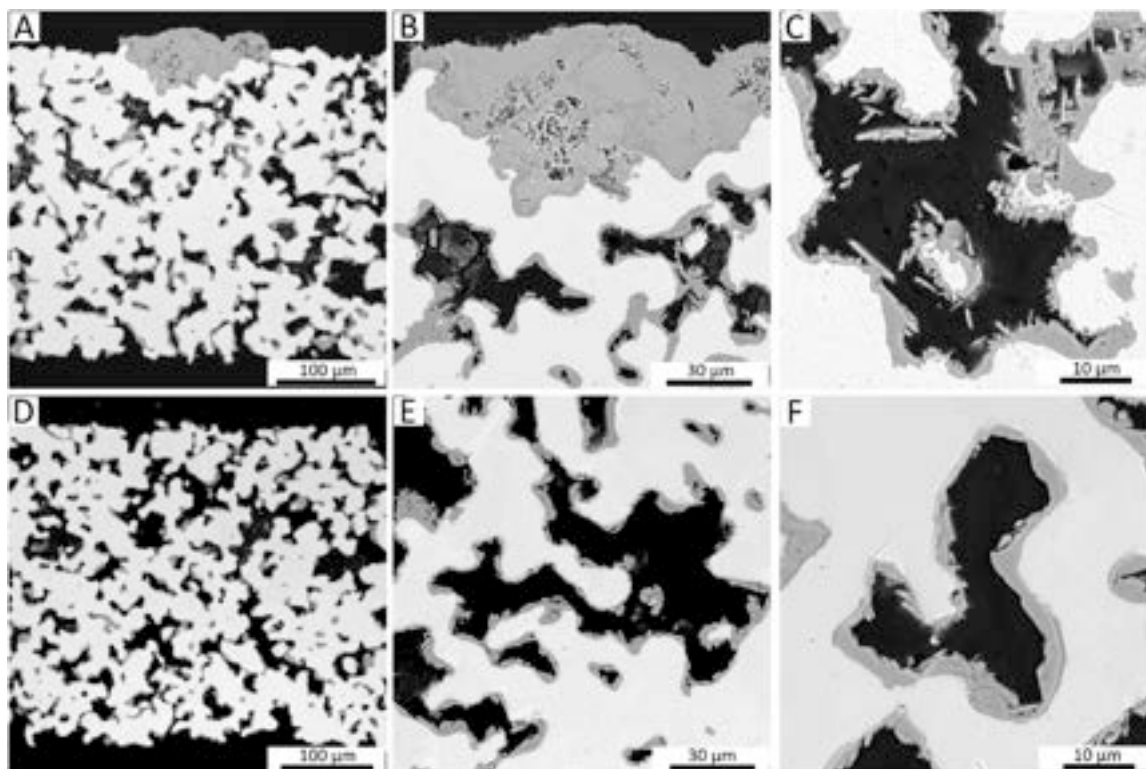


Fig. 8. SEM images of the pre-oxidized at A-C) 850°C for 4 h, and D-F) 900°C for 40 min Fe22Cr alloy after further 2000 h of oxidation at 700°C.



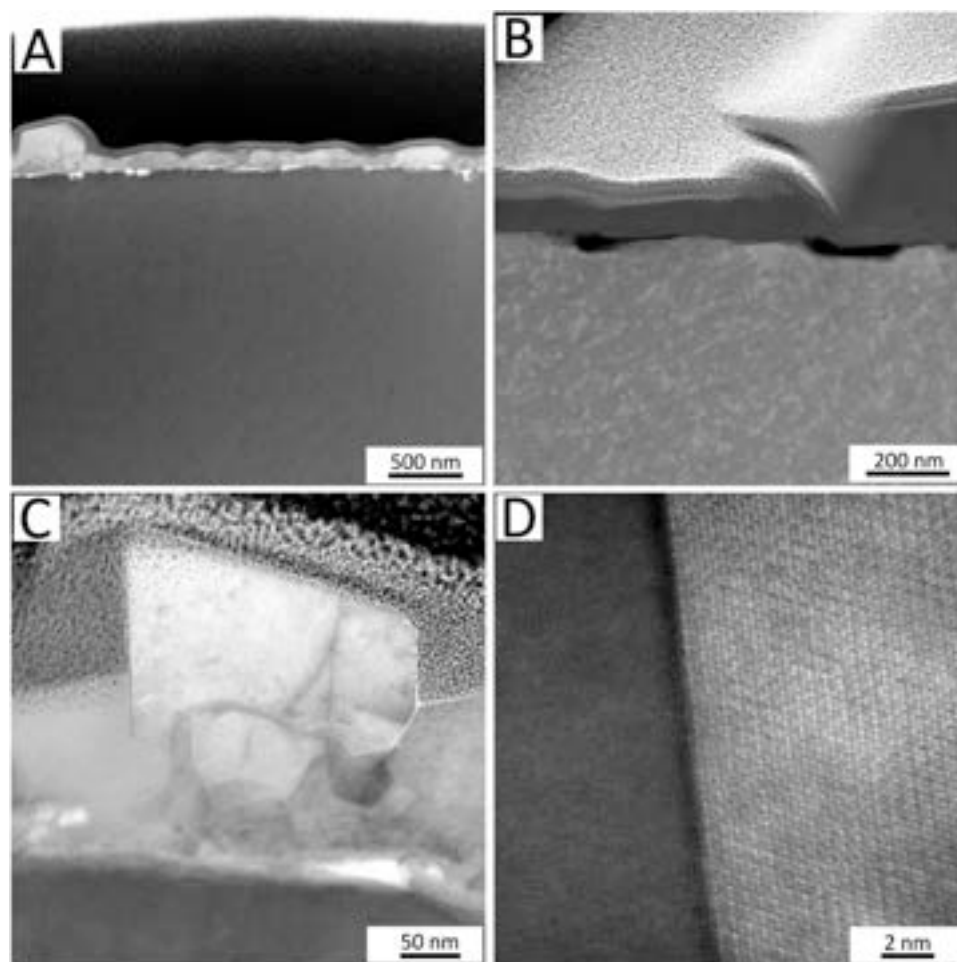


Fig. 9. TEM images of the porous Fe22Cr alloy pre-oxidized at 900°C for 40 min.

A detailed microstructure analysis of the oxide scale grains is presented in Fig. 9C. The grain size in the oxide scale layer differs between the alloy-oxide scale and oxide scale-air interfaces, similar to the sample aged at 700°C for 2000 h. The grains of the chromia at the alloy-oxide scale interface are undistinguishable. On the other hand, the oxide scale grains, which are located near the air, have a size range of ~50 nm to 150 nm. The grain boundary between these huge grains is presented in Fig. 9D. It is revealed that the grain boundary is incoherent, so the neighboring crystals are oriented in different directions. Thus, the diffusion of Cr species is probably determined by the grain boundary diffusion coefficient.

In Fig. 10C-D the alloy-oxide scale interface is presented at higher magnifications. The size of some oxide scale grains can be estimated as to be in the range of 25 nm to 50 nm. Nevertheless, some of the oxide scale grains do not reveal clear grain boundaries, so their size cannot be easily determined. In addition to that, the darker regions within the oxide scale layer might indicate different phases.

The EDX analysis of the oxide scale layer formed after pre-oxidation at 900°C and further oxidation at 700°C for 2000 h is presented in Figure S.5 and Figure S.6 in the supplementary part of this work. The analysis revealed the presence of elements such as Cr, O, and Fe in the examined alloy. Notably, the absence of detectable manganese can be attributed to its low concentration in the alloy (0.2 wt%). The significant presence of iron-rich regions within the oxide scale may indicate the onset of breakaway corrosion formation for the investigated alloy. This conjecture is reinforced by the detected quantity of Cr in the steel, which amounts to ~14 wt%. However, there is also a possibility that the presence of an iron-rich phase near the alloy – oxide scale interface is

possible due to Fe diffusion from the alloy to the oxide scale. Sabioni et al. investigated the diffusivities of Fe and Cr within the chromia formed on Fe15Cr alloy [54]. They revealed that the effective diffusion of Fe is greater than the diffusion of Cr at 750°C. On the other hand, the chromia formed on a Fe15Cr alloy was called as ‘thermodynamic barrier’ for iron diffusion because of the very low oxygen pressure at the alloy – oxide scale interface.

### 3.9. Discussion of a grain boundary diffusion mechanism

The pre-oxidation process influences the number of grain boundaries of Cr species in chromia via an induced increase of chromia grain size [55–62]. The outward  $\text{Cr}^{3+}$  cation diffusion is directly connected with the microstructure of the oxide scale for Cr-based ferritic alloys. The presence of structural defects like dislocations or grain boundaries leads to an increase in the effective diffusion coefficient. Moreover, it was proved that there is a direct connection between the parabolic weight gain and the diffusion mechanism because the transport of reactants (cations or anions) through an oxide scale is a diffusion-limited process for ferritic alloys [57].

The slope of the curves obtained from the linear regression of the weight gain data (Fig. 6C) changes from 0.42 (for raw alloys) to 0.69 (for both pre-oxidized sets of samples). From the slope change analysis, the two first points were excluded for the pre-oxidized samples. Despite the higher value of the slope of the weight gain data for the pre-oxidized samples, which could indicate shortening the lifespan of the alloy, the lifespan extension for these samples is observed in comparison to the raw alloy.

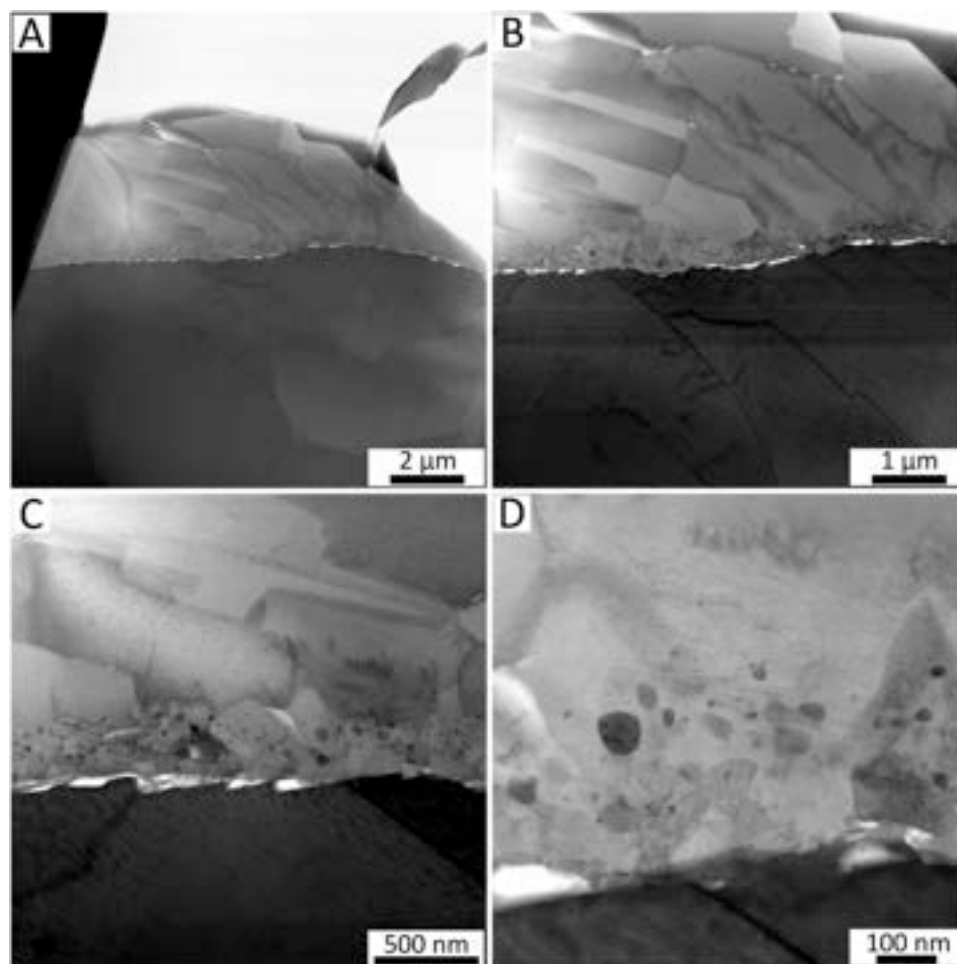


Fig. 10. TEM images of the porous Fe22Cr alloy pre-oxidized at 900°C for 40 min and aged at 700°C for 2000 h.

It was mentioned in Section 3.4. that the corrosion kinetics for the investigated Fe22Cr alloy follow the parabolic rate law [26,30]. It is also in agreement with the literature data collected for compositionally similar alloys, like Crofer 22 H or Crofer 22 APU [21,63,64]. These studies stated that following the parabolic rate law by the investigated alloys means that the outward Cr cation diffusion from the alloy particles to the oxide scale surface determines the corrosion phenomenon. Nevertheless, altering the grain and grain boundary diffusion fluxes by the pre-oxidation process seems to change the dominant character of the corrosion phenomenon, causing a slope change of the weight gain curve (Fig. 6C).

The increase of the slope to 0.69 for the pre-oxidized samples means that another competitive process influences the corrosion process. As the microstructural changes caused by the pre-oxidation, slow down the outward Cr cation diffusion process, the inward oxygen anion diffusion may play a relevant role for the corrosion phenomenon. However, the inward oxygen anion diffusion is described by the parabolic law of corrosion, as well as the outward chromium diffusion, so it cannot determine the increase of the weight gain curve's slope. On the other hand, Sabioni et al. investigated the relation between the oxidation growth rate of chromia scales and self-diffusion in  $\text{Cr}_2\text{O}_3$  [59]. They revealed that the oxygen diffusion is faster than the chromium diffusion in chromia, both in the bulk and in the grain boundaries. Nevertheless, they confirmed that the calculations clearly indicate that neither bulk nor grain-boundary diffusion of oxygen can be responsible for the observed growth rate. To adequately elucidate the observed alteration in oxidation kinetics for the pre-oxidized porous alloy, further investigation is required.

The most crucial factor for lifespan prediction for porous alloys is the Cr reservoir inside the alloy's particles. The lack of Cr in the alloy leads to breakaway corrosion formation. At SOC's operating temperatures, the Cr level decrease is caused by two processes: Cr consumption for oxide scale ( $\text{Cr}_2\text{O}_3$ ) formation and Cr evaporation [45]. Kim et al. investigated Cr volatilization of small ( $\sim 25 \mu\text{m}$ ) and large grain ( $\sim 250 \mu\text{m}$ ) Crofer 22 APU at 800°C for 700 h [50]. They revealed that the Cr evaporation rate for both samples is initially decreasing, but appears to stabilize at 400 h. The same behavior was observed by Stanislawski et al. for Crofer 22 APU [52,53]. However, the pre-oxidation process does not significantly impact the Cr evaporation rate for the porous Fe22Cr alloy, probably due to a lack of Mn, which precludes the formation of a protective spinel phase (see Fig. 7).

Based on the weight gain data (Fig. 6) it seems that the extension of the porous alloys' lifespan is possible for the pre-oxidized samples when compared with the raw porous alloys. Moreover, the pre-oxidation process performed at 900°C for 40 min leads to a reduction of the relative weight gain by  $\sim 5$  times (Figure S.3) when compared with the reference samples. The same result was achieved by Tucker et al. for the P434L ferritic porous alloy pre-oxidized at 850°C for 10 h and further oxidized at 700°C for 500 h [41]. Hong et al. obtained  $\sim 3$  times lower weight gain for pre-oxidized bulk T92 alloy at 700°C for 1 h at 21%  $\text{N}_2$  and 79%  $\text{O}_2$  atmosphere when compared with reference samples oxidized at 650°C [40].

An enhanced understanding of the pre-oxidation process's influence on the corrosion phenomenon is a complex issue. Taking into consideration the obtained results, it seems that a mix of parabolic and linear processes causes an increase of the weight gain curve slope. It was

confirmed that high temperature conditions do not only lead to oxide scale grain growth but also change the microstructure of the alloy, as was postulated in our previous work [42]. Therefore, for a detailed explanation of the pre-oxidation effect on the corrosion phenomenon in ferritic Cr-based alloys, further studies including 3D analysis of the pre-oxidized and oxidized samples are necessary. Based on the results presented in this work, the tomographic measurements of the porous alloy should be performed when the change of slope starts, for example as a part of synchrotron operando studies. In addition, the study of Cr and O diffusion coefficients in an oxide scale formed for pre-oxidized ferritic alloys should be performed by secondary ion mass spectrometry (SIMS) with the  $O^{18}$  isotope to determine the nature of the weight gain curve slope change that was observed in this study.

#### 4. Conclusions

In this work, the impact of the pre-oxidation process on the corrosion properties of the porous ferritic Fe22Cr alloy was investigated. Based on possible applications of porous alloys as supports and interconnect elements in solid oxide cells, the aging temperature for this study was chosen to be 700°C and 750°C. For the pre-oxidation process, temperatures of 850°C and 900°C were chosen based on our previous study. The role pre-oxidation was evaluated by combining thermogravimetry, Cr evaporation measurements as well as SEM, TEM and synchrotron-based X-ray tomography analyses.

Weight gain measurements lasted up to 2000 h (plus the pre-oxidation process time) for the samples oxidized at 700°C. Although the values of weight gain after the pre-oxidation process were close between samples pre-oxidized at 850 °C (1.12%) and samples pre-oxidized at 900°C (1.05%), the achieved alloy's lifespan was different. After 2000 h, the alloy pre-oxidized at 850°C reached the threshold level for breakaway corrosion appearance, which is 6 wt%. For the samples pre-oxidized at 900 °C, the measured weight gain after 2000 h of oxidation at 700°C was significantly lower (3.91 wt%).

The conclusions from the SEM images were consistent with the weight gain data. For the samples pre-oxidized at 900°C and further oxidized at 700°C for 2000 h, there was no evidence for breakaway corrosion appearance. Regions of fully oxidized alloy were instead detected in samples pre-oxidized at 850°C and further oxidized at 700°C for 2000 h. Nevertheless, the SEM technique did not allow for evaluation of morphological changes after the pre-oxidation process.

For the detailed analysis of morphological and compositional changes in pre-oxidized porous alloys, X-ray tomography measurements were performed. The X-ray tomography study revealed that the oxide scale growth is not regular in the alloy's volume. After 5.5 h of oxidation at 850 °C, there were regions with only limited chromia growth. The difference between samples oxidized at 850°C for 3 h and oxidized at 850°C for 5.5 h was not significant in the context of oxide scale thickness or the oxidized regions. Nevertheless, after 30 h of oxidation at 850 °C, the oxide scale covered the alloy surface tightly. Moreover, oxide scale "paths," which connected some oxidized regions, were detected. It is in agreement with our previous study concerning the lifespan prediction of porous Fe22Cr at higher temperatures, like 850°C and 900°C.

The detailed analysis of the oxide scale grain size was achieved by TEM imaging. TEM images revealed that after the pre-oxidation step at 900°C for 40 min, the grain size of chromia cannot be easily determined for the oxide scale close to the alloy particle, while the size of chromia grains close to the air interface was 50 nm – 170 nm. On the other hand, the chromia grain size for the sample pre-oxidized at 900°C for 40 min and aged at 700°C for 2000 h was determined to be in range from 25 µm to 75 µm for chromia grains close to the alloy particle.

Cr evaporation measurements were performed for raw and pre-oxidized samples to observe if the process influenced the oxide scale growth rate. The analysis performed at 700°C for 500 h did not show any particular changes between raw and pre-oxidized samples. Thus, the pre-oxidation process might slow down the  $Cr^{3+}$  cation diffusion by

altering the grain and grain boundary diffusion fluxes, but it did not significantly influence Cr evaporation from the alloy particles.

Taking into consideration all analyses performed, the pre-oxidation process could extend the possible lifespan of the porous Fe22Cr alloy. The most important factor for this extension is the temperature of the process. The longest lifespan was achieved for samples pre-oxidized at 900°C for 40 min. The proficient use of the pre-oxidation process could extend the lifespan of the metallic component in the MS-SOCs and allow for more efficient operation of these devices at intermediate temperatures.

#### CRedit authorship contribution statement

**Jan Froitzheim:** Writing – review & editing, Resources, Investigation, Formal analysis. **Matthieu Tomas:** Writing – review & editing, Resources, Investigation. **Grzegorz Cempura:** Writing – review & editing, Validation, Investigation, Data curation. **Federica Marone:** Writing – review & editing, Software, Methodology. **Małgorzata Makowska:** Writing – original draft, Supervision, Formal analysis. **Damian Koszelow:** Writing – review & editing, Writing – original draft, Validation, Methodology, Investigation, Data curation, Conceptualization. **Sebastian Molin:** Writing – review & editing, Validation, Supervision, Resources, Conceptualization

#### Declaration of Competing Interest

The authors declare the following financial interests/personal relationships which may be considered as potential competing interests: Sebastian Molin reports financial support was provided by National Science Centre Poland. If there are other authors, they declare that they have no known competing financial interests or personal relationships that could have appeared to influence the work reported in this paper.

#### Data availability

Data will be made available on request.

#### Acknowledgments

This project was supported by National Science Centre Poland (NCN) Sonata Bis 8 project number 2018/30/E/ST8/00821, "High-temperature corrosion studies and development of oxidation lifetime model of alloy powders and sintered porous alloys: effects of composition and microstructure".

The authors would like to acknowledge Höganäs AB, Sweden for porous steel samples production and the Paul Scherrer Institut, Villigen, Switzerland for granting beamtime (proposal 20211872) at the TOMCAT beamline of the Swiss Light Source.

#### Appendix A. Supporting information

Supplementary data associated with this article can be found in the online version at doi:10.1016/j.corsci.2024.112129.

#### References

- [1] D.J. Young, *High temperature oxidation and corrosion of metals*, Elsevier, 2008.
- [2] M.J. Pomeroy, Coatings for gas turbine materials and long term stability issues, *Mater. Des.* 26 (2005) 223–231, <https://doi.org/10.1016/j.matdes.2004.02.005>.
- [3] H.J.C. Voorwald, R.C. Coisse, M.O.H. Cioffi, Fatigue strength of X45CrSi93 stainless steel applied as internal combustion engine valves, *Procedia Eng.* 10 (2011) 1256–1261, <https://doi.org/10.1016/j.proeng.2011.04.209>.
- [4] B. Öztürk, A. Topcu, S. Öztürk, Ö.N. Cora, Oxidation, electrical and mechanical properties of Crofer®22 solid oxide fuel cell metallic interconnects manufactured through powder metallurgy, *Int. J. Hydrog. Energy* 43 (2018) 10822–10833, <https://doi.org/10.1016/j.ijhydene.2018.01.078>.
- [5] A. Topcu, B. Öztürk, Ö.N. Cora, Performance evaluation of machined and powder metallurgically fabricated Crofer®22 APU interconnects for SOFC applications, *Int.*



- J. Hydrog. Energy 47 (2022) 3437–3448, <https://doi.org/10.1016/j.ijhydene.2021.06.036>.
- [6] J. Cao, M. Zheng, Z. Wang, X. Si, C. Li, X. Wang, Z. He, J. Qi, A low-temperature sealing method for metal-supported oxide fuel cell applications: Ni–Sn transient liquid phase bonding, *Vacuum* 187 (2021) 110048, <https://doi.org/10.1016/j.vacuum.2021.110048>.
  - [7] E. Zanchi, J. Ignaczak, B. Kamecki, P. Jasiński, S. Molin, A.R. Boccaccini, F. Smeacetto, Manganese–cobalt based spinel coatings processed by electrophoretic deposition method: the influence of sintering on degradation issues of solid oxide cell oxygen electrodes at 750 °C, *Mater. (Basel)* 14 (2021), <https://doi.org/10.3390/ma14143836>.
  - [8] F. D'Isanto, M. Salvo, S. Molin, D. Koszelow, H. Javed, S. Akram, A. Chrysanthou, F. Smeacetto, Glass-ceramic joining of Fe22Cr porous alloy to Crofer22APU: interfacial issues and mechanical properties, *Ceram. Int.* 48 (2022) 28519–28527, <https://doi.org/10.1016/j.ceramint.2022.06.166>.
  - [9] F. Smeacetto, M. Salvo, M. Ferraris, J. Cho, A.R. Boccaccini, Glass-ceramic seal to join Crofer 22 APU alloy to YSZ ceramic in planar SOFCs, *J. Eur. Ceram. Soc.* 28 (2008) 61–68, <https://doi.org/10.1016/j.jeurceramsoc.2007.05.006>.
  - [10] Z. Yang, Recent advances in metallic interconnects for solid oxide fuel cells, *Int. Mater. Rev.* 53 (2008) 39–52, <https://doi.org/10.1179/174328007x212526>.
  - [11] A.J. Abd Aziz, N.A. Baharuddin, M.R. Somalu, A. Muchtar, Review of composite cathodes for intermediate-temperature solid oxide fuel cell applications, *Ceram. Int.* 46 (2020) 23314–23325, <https://doi.org/10.1016/j.ceramint.2020.06.176>.
  - [12] M.C. Tucker, Progress in metal-supported solid oxide fuel cells: a review, *J. Power Sources* 195 (2010) 4570–4582, <https://doi.org/10.1016/j.jpowsour.2010.02.035>.
  - [13] B. Lemieszek, J. Ignaczak, B. Kamecki, J. Karczewski, M.B. Mogensen, S. Molin, P. Jasiński, Electrolytic deposition of reactive element thin films on Crofer 22 APU and evaluation of the resulting high-temperature corrosion protection properties at 700 °C–900 °C, *Int. J. Hydrog. Energy* (2022), <https://doi.org/10.1016/j.ijhydene.2022.07.220>.
  - [14] E. Zanchi, J. Ignaczak, S. Molin, G. Cempura, A.R. Boccaccini, F. Smeacetto, Electrophoretic co-deposition of Mn<sub>1.5</sub>Co<sub>1.5</sub>O<sub>4</sub>, Fe<sub>2</sub>O<sub>3</sub> and CuO: unravelling the effect of simultaneous addition of Cu and Fe on the microstructural, thermo-mechanical and corrosion properties of in-situ modified spinel coatings for solid oxide cell intercon, *J. Eur. Ceram. Soc.* 42 (2022) 3271–3281, <https://doi.org/10.1016/j.jeurceramsoc.2022.02.008>.
  - [15] M. Palcut, L. Mikkelsen, K. Neufeld, M. Chen, R. Knibbe, P.V. Hendriksen, Corrosion stability of ferritic stainless steels for solid oxide electrolyser cell interconnects, *Corros. Sci.* 52 (2010) 3309–3320, <https://doi.org/10.1016/j.corsci.2010.06.006>.
  - [16] A. Holt, P. Kofstad, Electrical conductivity and defect structure of Cr<sub>2</sub>O<sub>3</sub>. II. Reduced temperatures (<~1000 °C), *Solid State Ionics*. 69 (1994) 137–143. [https://doi.org/10.1016/0167-2738\(94\)90402-2](https://doi.org/10.1016/0167-2738(94)90402-2).
  - [17] P. Pavlasek, J. Rybář, S. Duriš, J. Palenčár, Effects of quartz glass insulation on platinum gold thermocouples, *Meas. Sci. Rev.* 19 (2019) 209–212, <https://doi.org/10.2478/msr-2019-0027>.
  - [18] H. Shahbaznejad, H. Ebrahimi, A study on the oxidation and electrical behavior of crofer 22 APU solid oxide fuel cell interconnects with Ni–Co–CeO<sub>2</sub> composite coating, *J. Mater. Sci. Mater. Electron.* 32 (2021) 7550–7566, <https://doi.org/10.1007/s10854-021-05470-z>.
  - [19] W.N. Liu, X. Sun, E. Stephens, M.A. Khaleel, Life prediction of coated and uncoated metallic interconnect for solid oxide fuel cell applications, *J. Power Sources* 189 (2009) 1044–1050, <https://doi.org/10.1016/j.jpowsour.2008.12.143>.
  - [20] B. Timurkutluk, S. Toros, S. Onbilgin, H.G. Korkmaz, Determination of formability characteristics of Crofer 22 APU sheets as interconnector for solid oxide fuel cells, *Int. J. Hydrog. Energy* 43 (2018) 14638–14647, <https://doi.org/10.1016/j.ijhydene.2018.04.243>.
  - [21] N.J. Magdefrau, L. Chen, E.Y. Sun, M. Aindow, Effects of alloy heat treatment on oxidation kinetics and scale morphology for Crofer 22 APU, *J. Power Sources* 241 (2013) 756–767, <https://doi.org/10.1016/j.jpowsour.2013.03.181>.
  - [22] R.N. Hajra, H. Tripathy, C. Sudha, N. Vijayashanthi, S. Raju, S. Saroja, Effect of sigma phase on thermophysical properties of Fe5Cr45 alloy, *Intermetallics* 112 (2019) 106552, <https://doi.org/10.1016/j.intermet.2019.106552>.
  - [23] K. Popova, T. Prošek, Corrosion monitoring in atmospheric conditions: a review, *Met. (Basel)* 12 (2022), <https://doi.org/10.3390/met12020171>.
  - [24] H. Simillion, O. Dolgikh, H. Terryn, J. Deconinck, Atmospheric corrosion modeling, *Corros. Rev.* 32 (2014) 73–100, <https://doi.org/10.1515/corrrev-2014-0023>.
  - [25] Y. Cai, Y. Xu, Y. Zhao, X. Ma, Atmospheric corrosion prediction: a review, *Corros. Rev.* 38 (2020) 299–321, <https://doi.org/10.1515/corrrev-2019-0100>.
  - [26] D. Koszelow, M. Makowska, A. Drewniak, G. Cempura, P. Jasiński, S. Molin, High-temperature Corrosion of ~ 30 Pct Porous FeCr stainless steels in air: long-term evaluation up to breakaway, *Metall. Mater. Trans. A Phys. Metall. Mater. Sci.* (2023), <https://doi.org/10.1007/s11661-023-07005-z>.
  - [27] E. Sarasketa-Zabala, L. Otaegi, L.M. Rodriguez-Martinez, M.A. Alvarez, N. Burgos, F. Castro, I. Villarreal, High temperature stability of porous metal substrates under highly humidified hydrogen conditions for metal supported Solid Oxide Fuel Cells, *Solid State Ion.* 222–223 (2012) 16–22, <https://doi.org/10.1016/j.ssi.2012.06.014>.
  - [28] J.A. Glasscock, L. Mikkelsen, Å.H. Persson, G. Pećanac, J. Malzbender, P. Blennow, F. Bozza, P.V. Hendriksen, Porous Fe<sub>21</sub>Cr<sub>7</sub>Al<sub>10</sub>Mo<sub>0.5</sub>Y metal supports for oxygen transport membranes: thermo-mechanical properties, sintering and corrosion behaviour, *Solid State Ion.* 242 (2013) 33–44, <https://doi.org/10.1016/j.ssi.2013.04.006>.
  - [29] D. Koszelow, M. Makowska, F. Marone, J. Karczewski, P. Jasiński, S. Molin, High temperature corrosion evaluation and lifetime prediction of porous Fe22Cr stainless steel in air in temperature range 700–900 °C, *Corros. Sci.* 189 (2021), <https://doi.org/10.1016/j.corsci.2021.109589>.
  - [30] D. Koszelow, M. Makowska, F. Marone, J. Karczewski, P. Jasiński, S. Molin, High Temperature Corrosion Evaluation and Lifetime Prediction of Porous Fe22Cr Stainless Steel in Air in Temperature Range 700–900 °C, *Corros. Sci.* 189 (2021) 109589, <https://doi.org/10.1016/j.corsci.2021.109589>.
  - [31] J. Karczewski, K.J. Dunst, P. Jasiński, S. Molin, High temperature corrosion and corrosion protection of porous Ni22Cr alloys, *Surf. Coat. Technol.* 261 (2015) 385–390, <https://doi.org/10.1016/j.surfcoat.2014.10.051>.
  - [32] S. Molin, B. Kusz, M. Gazda, P. Jasiński, Evaluation of porous 430L stainless steel for SOFC operation at intermediate temperatures, *J. Power Sources* 181 (2008) 31–37, <https://doi.org/10.1016/j.jpowsour.2007.10.009>.
  - [33] M.C. Tucker, Progress in metal-supported solid oxide electrolysis cells: a review, *Int. J. Hydrog. Energy* 45 (2020) 24203–24218, <https://doi.org/10.1016/j.ijhydene.2020.06.300>.
  - [34] E. Stefan, C. Denonville, Y. Larring, M. Stange, R. Haugsrud, Oxidation study of porous metal substrates for metal supported proton ceramic electrolyzer cells, *Corros. Sci.* 164 (2020) 108335, <https://doi.org/10.1016/j.corsci.2019.108335>.
  - [35] P. Huczukowski, N. Christiansen, V. Shemet, J. Piron-Abellan, L. Singheiser, W. J. Quadackers, Oxidation induced lifetime limits of chromia forming ferritic interconnector steels, *J. Fuel Cell Sci. Technol.* 1 (2004) 30, <https://doi.org/10.1115/1.1782925>.
  - [36] P. Huczukowski, V. Shemet, J. Piron-Abellan, L. Singheiser, W.J. Quadackers, N. Christiansen, Oxidation limited life times of chromia forming ferritic steels, *Mater. Corros.* 55 (2004) 825–830, <https://doi.org/10.1002/maco.200303798>.
  - [37] M. Palcut, L. Mikkelsen, K. Neufeld, M. Chen, R. Knibbe, P.V. Hendriksen, Improved oxidation resistance of ferritic steels with LSM coating for high temperature electrochemical applications, *Int. J. Hydrog. Energy* 37 (2012) 8087–8094, <https://doi.org/10.1016/j.ijhydene.2011.11.138>.
  - [38] M. Palcut, L. Mikkelsen, K. Neufeld, M. Chen, R. Knibbe, P.V. Hendriksen, Corrosion stability of ferritic stainless steels for solid oxide electrolyser cell interconnects, *Corros. Sci.* 52 (2010) 3309–3320.
  - [39] B. Talic, S. Molin, P.V. Hendriksen, H.L. Lein, Effect of pre-oxidation on the oxidation resistance of Crofer 22 APU, *Corros. Sci.* 138 (2018) 189–199, <https://doi.org/10.1016/j.corsci.2018.04.016>.
  - [40] H. Xu, Z. Liang, J. Ding, Q. Zhao, S. Guan, Effect of pre-oxidation on the steam oxidation of heat-resistant steel T92, *High. Temp. Mater. Process.* 37 (2018) 733–739, <https://doi.org/10.1515/hmt-2017-0037>.
  - [41] F. Shen, M.M. Welandar, M.C. Tucker, Oxidation of porous stainless steel supports for metal-supported solid oxide electrolysis cells, *Int. J. Hydrog. Energy* 48 (2023) 12168–12175, <https://doi.org/10.1016/j.ijhydene.2022.11.235>.
  - [42] D. Koszelow, S. Molin, J. Karczewski, F. Marone, M. Makowska, Morphology changes in Fe–Cr porous alloys upon high-temperature oxidation quantified by X-ray tomographic microscopy, *Mater. Des.* 215 (2022) 110492, <https://doi.org/10.1016/j.matdes.2022.110492>.
  - [43] J. Froitzheim, H. Ravash, E. Larsson, L.G. Johansson, J.E. Svensson, Investigation of Chromium Volatilization from FeCr Interconnects by a Denuder Technique, *J. Electrochem. Soc.* 157 (2010) B1295, <https://doi.org/10.1149/1.3462987>.
  - [44] D. Paganin, S.C. Mayo, T.E. Gureyev, P.R. Miller, S.W. Wilkins, Simultaneous phase and amplitude extraction from a single defocused image of a homogeneous object, *J. Microsc.* 206 (2002) 33–40, <https://doi.org/10.1046/j.1365-2818.2002.01010.x>.
  - [45] H. Falk-Windisch, J.E. Svensson, J. Froitzheim, The effect of temperature on chromium vaporization and oxide scale growth on interconnect steels for Solid Oxide Fuel Cells, *J. Power Sources* 287 (2015) 25–35, <https://doi.org/10.1016/j.jpowsour.2015.04.040>.
  - [46] E. Stefan, C. Denonville, Y. Larring, M. Stange, R. Haugsrud, Oxidation study of porous metal substrates for metal supported proton ceramic electrolyzer cells, *Corros. Sci.* 164 (2020) 108335, <https://doi.org/10.1016/j.corsci.2019.108335>.
  - [47] H. Falk-Windisch, J.E. Svensson, J. Froitzheim, The effect of temperature on chromium vaporization and oxide scale growth on interconnect steels for Solid Oxide Fuel Cells, *J. Power Sources* 287 (2015) 25–35, <https://doi.org/10.1016/j.jpowsour.2015.04.040>.
  - [48] C. Goebel, R. Berger, C. Bernuy-Lopez, J. Westlinder, J.E. Svensson, J. Froitzheim, Long-term (4 year) degradation behavior of coated stainless steel 441 used for solid oxide fuel cell interconnect applications, *J. Power Sources* 449 (2020), <https://doi.org/10.1016/j.jpowsour.2019.227480>.
  - [49] R. Sachitanand, M. Sattari, J.E. Svensson, J. Froitzheim, Evaluation of the oxidation and Cr evaporation properties of selected FeCr alloys used as SOFC interconnects, *Int. J. Hydrog. Energy* 38 (2013) 15328–15334, <https://doi.org/10.1016/j.ijhydene.2013.09.044>.
  - [50] B.K. Kim, Y.S. Ko, I.H. Jung, H.N. Han, K.W. Yi, D.I. Kim, Role of the alloy grain boundaries in the high-temperature oxidation and Cr volatilization of 22wt% Cr ferritic stainless steel for SOFC applications, *Corros. Sci.* 213 (2023) 110940, <https://doi.org/10.1016/j.corsci.2022.110940>.
  - [51] M. Reisert, V. Berova, A. Aphale, P. Singh, M.C. Tucker, Oxidation of porous stainless steel supports for metal-supported solid oxide fuel cells, *Int. J. Hydrog. Energy* 45 (2020) 30882–30897, <https://doi.org/10.1016/j.ijhydene.2020.08.015>.
  - [52] M. Stanislawski, E. Wessel, K. Hilpert, T. Markus, L. Singheiser, Chromium Vaporization from High-Temperature Alloys, *J. Electrochem. Soc.* 154 (2007) A295, <https://doi.org/10.1149/1.2434690>.
  - [53] M. Stanislawski, J. Froitzheim, L. Niewolak, W.J. Quadackers, K. Hilpert, T. Markus, L. Singheiser, Reduction of chromium vaporization from SOFC interconnectors by highly effective coatings, *J. Power Sources* 164 (2007) 578–589, <https://doi.org/10.1016/j.jpowsour.2006.08.013>.

- [54] A.C.S. Sabioni, J.N.V. Souza, V. Ji, F. Jomard, V.B. Trindade, J.F. Carneiro, Study of ion diffusion in oxidation films grown on a model Fe-15%Cr alloy, *Solid State Ion.* 276 (2015) 1–8, <https://doi.org/10.1016/j.ssi.2015.03.027>.
- [55] P. Kofstad, K.P. Lillerud, Chromium transport through Cr<sub>2</sub>O<sub>3</sub> scales I. On lattice diffusion of chromium, *Oxid. Met.* 17 (1982) 177–194, <https://doi.org/10.1007/BF00738381>.
- [56] P. Kofstad, Defects and transport properties of metal oxides, *Oxid. Met.* 44 (1995) 3–27, <https://doi.org/10.1007/BF01046721>.
- [57] R.E. Lobnig, H.P. Schmidt, K. Hennesen, H.J. Grabke, Diffusion of cations in chromia layers grown on iron-base alloys, *Oxid. Met.* 37 (1992) 81–93, <https://doi.org/10.1007/BF00665632>.
- [58] A.C.S. Sabioni, B. Lesage, A.M. Huntz, J.C. Pivin, C. Monty, Self-diffusion in Cr<sub>2</sub>O<sub>3</sub> I. Chromium diffusion in single crystals, *Philos. Mag. A Phys. Condens. Matter, Struct. Defects Mech. Prop.* 66 (1992) 333–350, <https://doi.org/10.1080/01418619208201560>.
- [59] A.C.S. Sabioni, A.M. Huntz, J. Philibert, B. Lesage, C. Monty, Relation between the oxidation growth rate of chromia scales and self-diffusion in Cr<sub>2</sub>O<sub>3</sub>, *J. Mater. Sci.* 27 (1992) 4782–4790, <https://doi.org/10.1007/BF01166020>.
- [60] R.K. Gupta, R.K.S. Raman, C.C. Koch, B.S. Murty, Effect of nanocrystalline structure on the corrosion of a Fe<sub>20</sub>Cr alloy, *Int. J. Electrochem. Sci.* 8 (2013) 6791–6806, [https://doi.org/10.1016/s1452-3981\(23\)14806-1](https://doi.org/10.1016/s1452-3981(23)14806-1).
- [61] T. Suzuoka, Lattice and Grain Boundary in Polycrystals, *Trans. JIM.* 2 (1961).
- [62] S.C. Tsai, A.M. Huntz, C. Dolin, Growth mechanism of Cr<sub>2</sub>O<sub>3</sub> scales: oxygen and chromium diffusion, oxidation kinetics and effect of yttrium, *Mater. Sci. Eng. A.* 212 (1996) 6–13, [https://doi.org/10.1016/0921-5093\(96\)10173-8](https://doi.org/10.1016/0921-5093(96)10173-8).
- [63] A.W.B. Skilbred, R. Haugsrud, Sandvik Sanergy HT - A potential interconnect material for LaNbO<sub>4</sub>-based proton ceramic fuel cells, *J. Power Sources* 206 (2012) 70–76, <https://doi.org/10.1016/j.jpowsour.2012.01.101>.
- [64] B. Talic, S. Molin, P.V. Hendriksen, H.L. Lein, Effect of pre-oxidation on the oxidation resistance of Crofer 22 APU, *Corros. Sci.* 138 (2018) 189–199, <https://doi.org/10.1016/j.corsci.2018.04.016>.

## SUPPLEMENTARY MATERIALS

### Pre-oxidation of porous ferritic Fe22Cr alloy for lifespan extension at high-temperature

D. Koszelow<sup>a\*</sup>, M. Makowska<sup>b</sup>, F. Marone<sup>c</sup>, G. Cempura<sup>d</sup>, Matthieu Tomas<sup>e</sup>, Jan Froitzheim<sup>e</sup>, S. Molin<sup>a</sup>

<sup>a</sup> Advanced Materials Centre, Faculty of Electronics, Telecommunications and Informatics, Gdańsk University of Technology, 80-233 Gdańsk, Poland

<sup>b</sup> Laboratory of Nuclear Materials, Laboratory of Synchrotron Radiation and Femtochemistry, Paul Scherrer Institut, 5232 Villigen, Switzerland

<sup>c</sup> Swiss Light Source, Paul Scherrer Institut, Villigen, Switzerland

<sup>d</sup> Centre of Electron Microscopy for Materials Science, Faculty of Metal Engineering and Industrial Computer Science, AGH University of Krakow, Al. Mickiewicza 30, 30-059, Krakow, Poland

<sup>e</sup> Energy and Materials, Chalmers University of Technology Kemivägen 10, 41296 Gothenburg, Sweden

\*Corresponding author: Damian Koszelow, Gdańsk University of Technology, e-mail: damian.koszelow@pg.edu.pl

To determine the morphology changes of the porous Fe22Cr alloy under oxidation conditions (850°C), a larger representative region was chosen for the analysis, as presented in Figure. In these images, the visualisation of the volume rendering obtained from the reconstructed data was shown for unoxidized sample (Figure1 A) and for samples oxidised for 3 h, 5.5 h and 30 h at 850 °C (Figure1 B-D, respectively). For each presented volume the front slice was segmented to distinguish the metallic core and oxide scale phases. The turquoise colour represents alloy and orange colour represents oxide scale. For the samples oxidized for 3 h (Figure S.1 B), the oxide scale is visible. However, there are also regions without oxide scale. After additional 2.5 h of oxidation at 850 °C, 5.5 h in total (Figure1 C) most of the alloy surface is covered by the oxide scale. Nevertheless, there are still regions where the oxide scale has not been detected. For the sample oxidised for 30 h at 850 °C (Figure1 D) the oxide scale seems to cover entire alloy surface. Moreover, the oxide scale grows inside the alloy's particles.



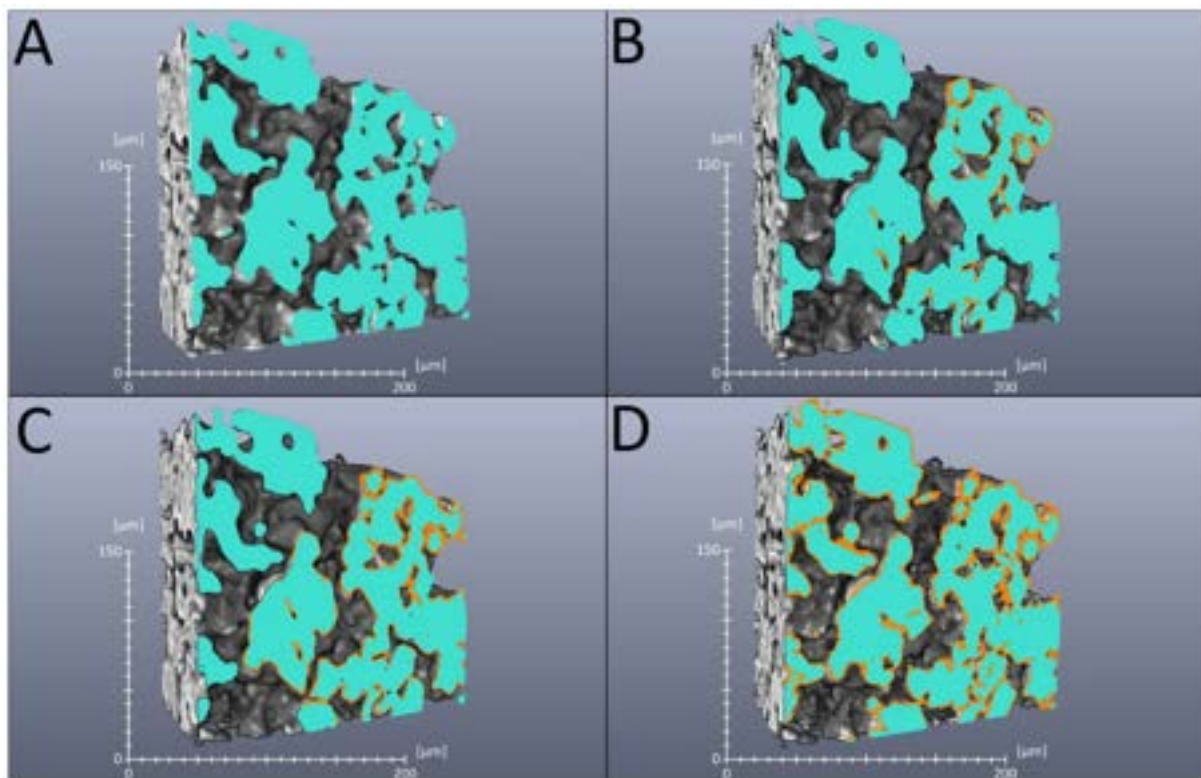


Figure S.1. The visualisation of the volume rendering obtained from the reconstructed data, with one slice after the segmentation process for (a) unoxidized sample (b-d) after 3 h, 5.5 h and 30 h of oxidation performed at 850 °C, respectively.

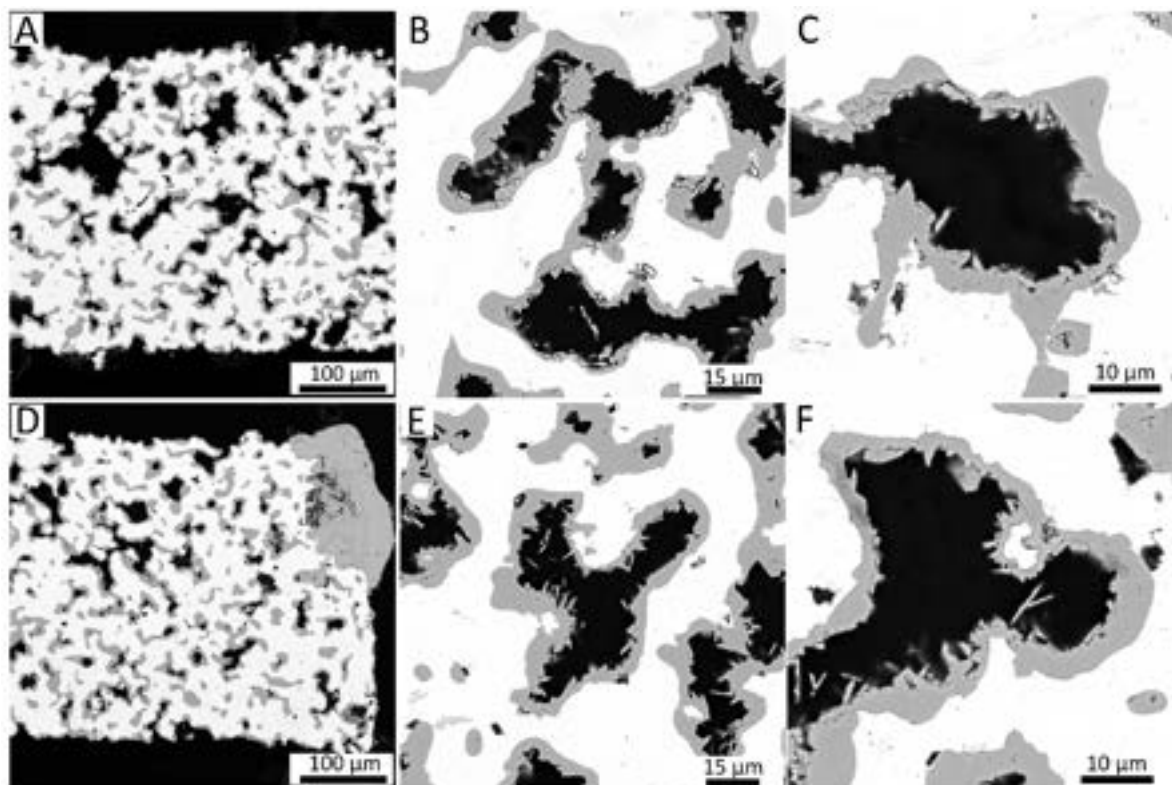


Figure S.2. SEM images of the porous Fe22Cr alloy pre-oxidized at A-C) 850°C for 4 h, D-F) 900°C for 40 min and further oxidized at 750°C for 750 h.

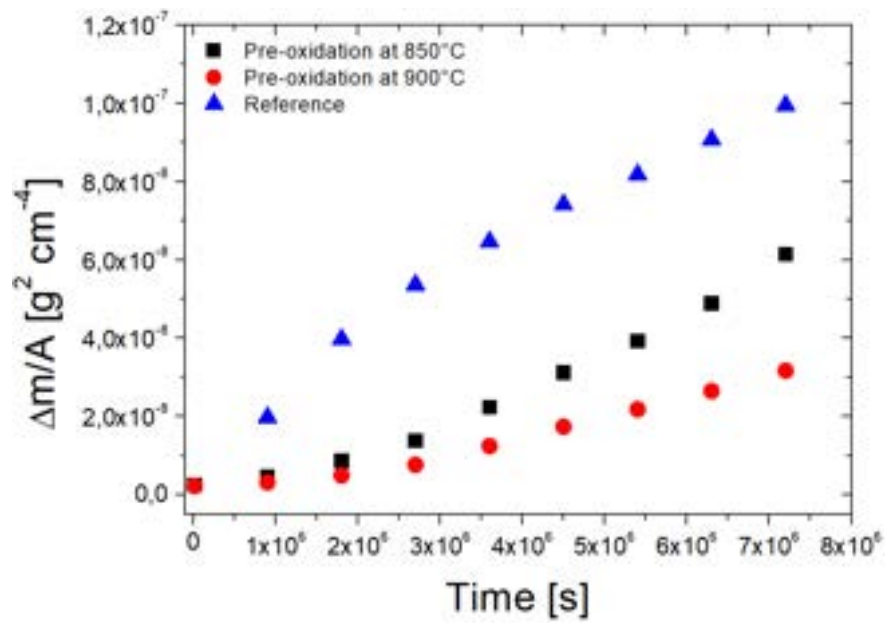


Figure S.3. Square weight change with respect to the initial surface area for the porous Fe22Cr alloy.

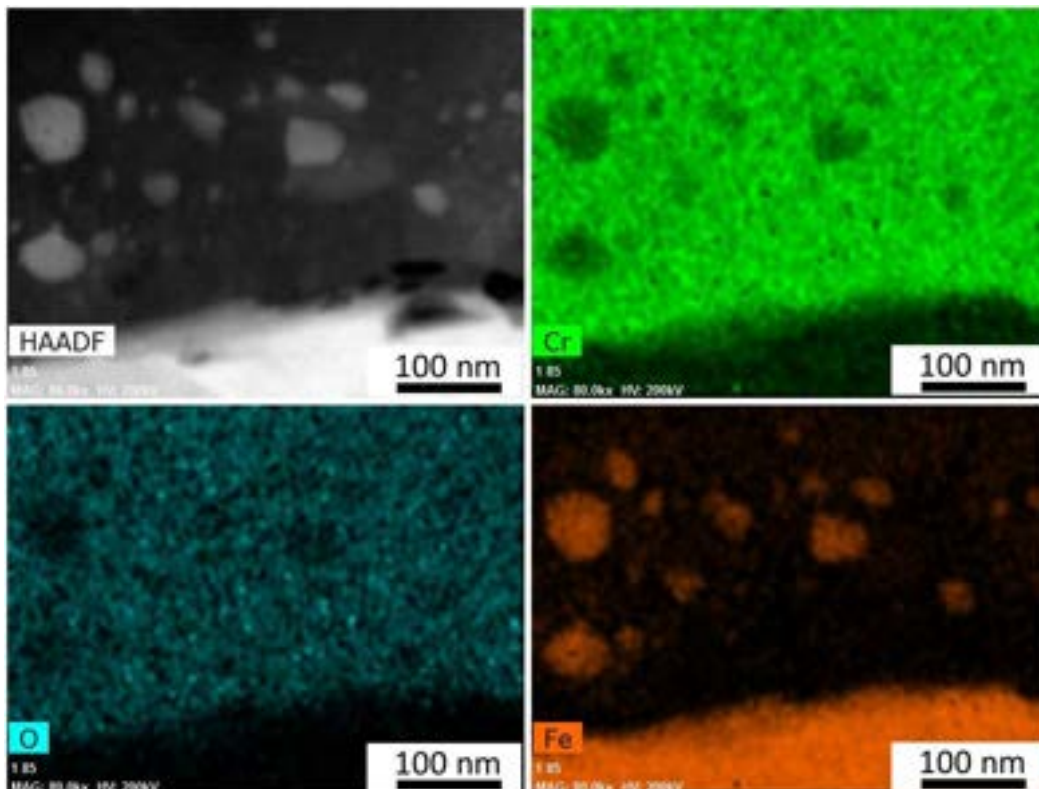


Figure S.5. TEM-EDX elemental maps for oxide scale of the sample pre-oxidized at 900°C for 40 min and further oxidized at 700°C for 2000 h.

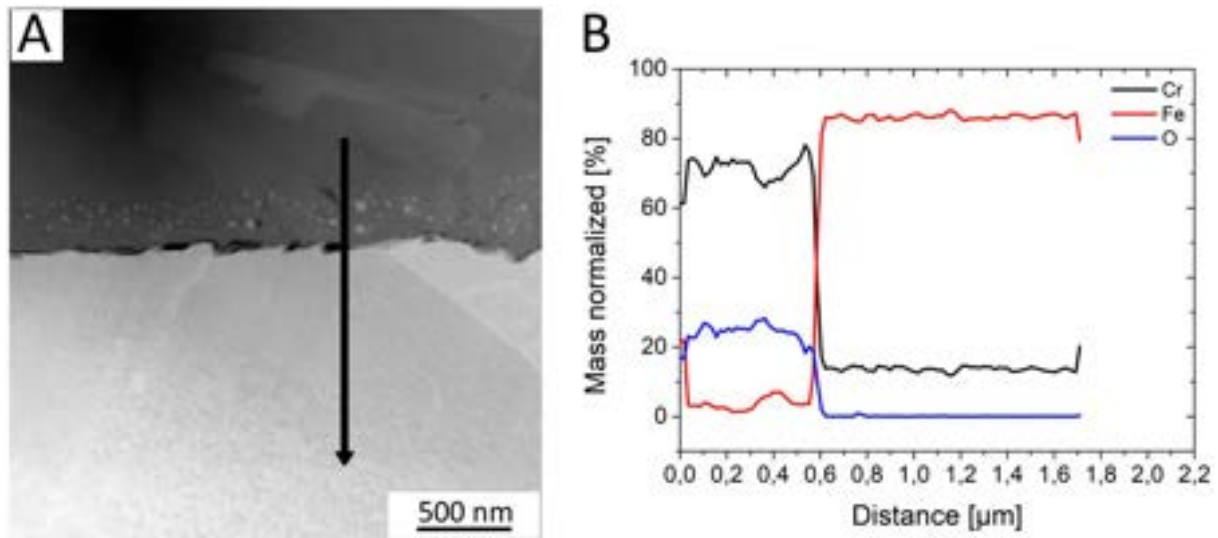


Figure S.6. TEM-EDX elemental line scan for the sample pre-oxidized at 900°C for 40 min and further oxidized at 700°C for 2000 h.

The detected elements are Cr, Fe, and O. The distribution of iron and oxygen indicates that the oxide scale layer is not uniform in chemical composition. The regions within the oxide scale layer that is close to the air are enriched in Fe. The TEM-EDX linear analysis confirms that there is depletion of Cr in the alloy particles close to the oxide scale from 22 wt % (initial amount of Cr in the alloy) to ~14 wt %. These TEM-EDX analyses might indicate that due to the lack of Cr reservoir, the Fe-rich oxides formation started. On the other hand, the weight gain data (Figure 6 C) indicates that there is above 1500 h of possible oxidation time up to breakaway corrosion formation. Moreover, based on the lifetime prediction model that was described in our previous work [30], the Cr level in the alloy obtained from TEM-EDX analysis is above the threshold level (10 wt % – 12 wt % of Cr) for the breakaway corrosion formation.

## **5.5. Glass-ceramic joining of Fe22Cr porous alloy to Crofer22APU: interfacial issues and mechanical properties**

In order to confirm that the beneficial effect of the pre-oxidation process of porous alloy can be applied in the MS-SOC systems, glass-ceramic joints consisting of porous Fe22Cr alloy were fabricated. Glass-ceramics are widely used to seal the gaps between solid oxide cell and interconnector. These materials are relatively easy to obtain and it is easy to adjust their chemical composition and mechanical properties. As MS-SOC components, glass-ceramics have to provide thermo-mechanical stability. Moreover, they have CTE that matches other components.

In this study, the joints of porous Fe22Cr alloy to a dense Crofer 22 APU were fabricated using silica-based, Ba-containing glass-ceramic. The research revealed that there are no defects and cracks at the porous alloy/glass ceramic interface of as-obtained joints. Moreover, the oxidation tests performed at 700°C for 500 h did not cause any undesirable changes either.


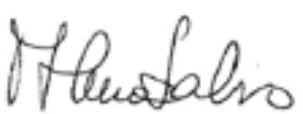




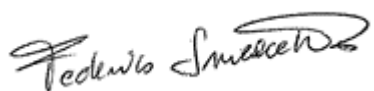
SEM imaging revealed oxide scale at the surface of the porous alloy and its interface with glass-ceramic. Nevertheless, the mechanical strength of the samples did not change after oxidation tests: before thermal exposure an average tensile strength was 7.4 MPa  $\pm$  0.5 MPa; after this process it was 7.7 MPa  $\pm$  2.9 MPa.

This study proved that pre-oxidized porous alloys offer advantageous engineering features, such as structure-wide gas permeability. In addition, the development of a dense-to-porous joint has an important role in producing dependable, effective, and sustainable MS-SOCs.

My original contribution in this work was:

- Determining the boundary conditions of the aging tests based on previous results presented in [DK1] and [DK3]
- Analyzing the corrosion experiments' results in the context of joint stability in SOC operating conditions

Statement of the co-authors' contribution to the publication entitled 'Glass-ceramic joining of Fe22Cr porous alloy to Crofer22APU: interfacial issues and mechanical properties':

Name and surname	Contribution to the publication	Signature
Fabiana D'Isanto	Conceptualization, Methodology, Formal Analysis, Investigation, Writing – Original Draft	
Milena Salvo	Supervision, Formal Analysis, Writing – Review & Editing	
Sebastian Molin	Validation, Writing – Review & Editing	
Damian Koszelow	Validation, Writing – Review & Editing, Resources	
Hassan Javed	Writing – Review & Editing	
Sufyan Akram	Methodology, Investigation	Sufyan Akram
Andreas Chrysanthou	Validation, Writing – Review & Editing	
Federico Smeacetto	Conceptualization, Supervision, Project administration, Funding acquisition Writing – Review & Editing	





# Glass-ceramic joining of Fe22Cr porous alloy to Crofer22APU: interfacial issues and mechanical properties

Fabiana D'Isanto<sup>a,\*</sup>, Milena Salvo<sup>a</sup>, Sebastian Molin<sup>b</sup>, Damian Koszelow<sup>b</sup>, Hassan Javed<sup>c</sup>, Sufyan Akram<sup>d</sup>, Andreas Chrysanthou<sup>d</sup>, Federico Smeacetto<sup>a</sup>

<sup>a</sup> Department of Applied Science and Technology, Politecnico di Torino, Corso Duca degli Abruzzi 24, 10129, Turin, Italy

<sup>b</sup> Advanced Materials Centre, Faculty of Electronics, Telecommunications and Informatics, Gdańsk University of Technology, ul. G. Narutowicza 11/12, 80-233, Gdańsk, Poland

<sup>c</sup> Sunfire GmbH, Gasanstaltstraße 2, 01237, Dresden, Germany

<sup>d</sup> School of Physics, Engineering and Computer Science, University of Hertfordshire, College Lane, Hatfield, Herts AL10 9AB, UK

## ARTICLE INFO

### Keywords:

Glass-ceramics

Joining

Porous alloys

Metal-supported SOC

## ABSTRACT

This work deals with the joining of porous Fe22Cr ferritic stainless steel to a dense Crofer22APU plate by using a silica-based, Ba-containing glass-ceramic. The chemical and interfacial stability and the mechanical properties of the joints were evaluated before and after thermal ageing at 700 °C for 500hrs. The sintering behaviour of the glass was assessed by using heating stage microscopy (HSM) to study the influence of a porous metal substrate on the shrinkage of the joining material. Scanning electron microscopy revealed that there were no defects or cracks at the porous alloy/glass-ceramic interface for both the as-joined samples and the samples after thermal ageing at 700 °C for 500 h. However, at this exposure temperature, the porous alloy started to form an oxide scale at the interface with the glass-ceramic and the internal surface of the porous alloy. Finally, the evaluation of the mechanical properties by tensile testing showed that the properties were not affected by thermal ageing at 700 °C.

## 1. Introduction

The porous metallic alloys sector is a major area of interest within the field of high-temperature engineering materials. The functional role of the porosity can be exploited in catalytic reactors (thanks to the high surface area for reactions), filters and metal-supported solid oxide cells (MS-SOCs).

Previous studies have evaluated the oxidation resistance of these alloys in the dense form [1–4] and they have been used for many decades as MS-SOCs [5], but recent studies on high-temperature corrosion of porous metal alloys [6–9] led to increasing interest due to important engineering features such as open porosity which allows gas transport and therefore these materials can be used for gas permeation membranes. Therefore, porous ferritic stainless steels (FSSs) constitute suitable candidate materials for use as metallic interconnects with high-temperature ceramic fuel cells [9,10] and gas separation membranes [11–13].

Solid oxide cell (SOC) technology has been developed due to its higher efficiency compared to combustion engines, silent operation and

fast charging. Improvements in materials, cell design and manufacturing processing have led to a very high level of technical refinement. More recently, due to the tendency of the cell to fail and assembling issues associated with the use of complex ceramic parts, there has been interest in alternative MS-SOC which can be exploited in the temperature range of 650–800 °C [14] thanks to their low cost, flexibility, robustness and manufacturability benefits. MS-SOCs allow for a lower cost balance of plant components (BoP) and higher redox stability.

To choose the most suitable material to produce interconnects, it is desirable to match the coefficient of thermal expansion (CTE) of the metal to that of the electrolyte [15]. Most manufacturers prefer Fe and Cr-based materials as ferritic stainless steels (e.g. 430 alloy), which are commonly used for automotive exhaust manifolds and mufflers thanks to their inexpensive and high-temperature resistance. This is the reason why FSSs have substituted the more expensive and difficult to manufacture ceramic interconnects in SOC design [16,17].

One of the major challenges in the design of solid oxide cell stacks is the selection of joining materials for sealing the metallic interconnect. The sealant role is fundamental to assure high durability and long-term

\* Corresponding author.

E-mail address: [fabiana.disanto@polito.it](mailto:fabiana.disanto@polito.it) (F. D'Isanto).

<https://doi.org/10.1016/j.ceramint.2022.06.166>

Received 20 April 2022; Received in revised form 8 June 2022; Accepted 15 June 2022

Available online 16 June 2022

0272-8842/© 2022 Elsevier Ltd and Techna Group S.r.l. All rights reserved.



performance. The most common sealing materials are glass-ceramics due to the simplicity of the sinter-crystallization process and the possibility to tailor their composition and thermo-mechanical properties. Moreover, several studies have reported that they can exhibit higher gas tightness than other typical sealants (i.e. brazing alloys) and superior stability in extreme working conditions [18–20]. Another advantage of using glass-ceramics is linked to the presence of a residual glassy phase after the sinter-crystallization process, which can minimize thermal stresses and provide self-healing properties that are very useful in thermal cycling conditions [21]. Furthermore, the formation of crystalline phases within the glass phase improves mechanical properties and drives the choice of the composition in terms of thermo-mechanical compatibility involving the coefficient of thermal expansion (CTE) matching with the SOC components [22].

The selected sealant inevitably influences the stability and the chemical compatibility at the interface between the sealant material and the SOC components. Some studies have shown that undesirable interfacial reactions are possible between Cr-based stainless steels and glass-ceramic sealants. For example, the  $\text{BaCrO}_4$  phase that has a high CTE ( $\sim 21\text{--}23 \times 10^{-6} \text{ K}^{-1}$ ) can form at the interface between Ba-containing glass-ceramics and Cr-containing metal interconnects [20,23].

Despite this, many research groups have studied and demonstrated the affinity and the effectiveness of glass-based sealants in solid oxide cells [24–27] and many suitable  $\text{BaO-SiO}_2\text{-Al}_2\text{O}_3$ -based systems have been successfully developed for SOC applications [25,28], but the current state of the art associated to the joining of porous to bulk alloys in SOC components by glass-based materials is very limited [29].

Previous studies [30] carried out oxidation tests of mixed glass-ceramics with FSS powders and revealed decreased oxidation rate compared with raw steel powder and suggested that the resulting oxide scale can enhance the sealant properties.

However, very few studies have dealt with the oxidation processes of porous ferritic stainless steels and there has been no detailed investigation of the joining and integration issues of these materials. A systematic understanding of how the stainless-steel porosity and the consequent corrosion reactions affect the interfacial behaviour with glass-based materials is still lacking.

This study describes the joining of porous Fe22Cr alloy to a dense Crofer 22APU plate with a silica barium-based glass-ceramic. The interfacial behaviour between the silica barium-based glass-ceramic and both dense and porous alloy interconnects will be discussed with particular focus on the morphological and chemical characterisation at the interface before and after thermal ageing at 700 °C for 500 h in air. Finally, tensile tests were performed on joined samples, comparing the tensile strength and the fracture surface between as-joined and aged specimens.

## 2. Materials and methods

The Fe22Cr porous alloy substrate (of composition Cr = 22 wt%; Mn = 0.23 wt%; Si = 0.08 wt%; Ni, Cu, Mo < 0.03 wt%, with Fe representing the balance), was produced by Höganäs AB (Höganäs, Sweden) and characterised for its resistance against high temperature oxidation in a study by Koszelow et al. [9]. The  $\sim 0.4$  mm thick porous sheet was manufactured by tape-casting of a steel particle slurry, followed by drying, debinding and sintering at 1250 °C in a pure  $\text{H}_2$  atmosphere for 30 min. Dense steel coupons were cut from a 0.3-mm-thick plate of Crofer22APU (Cr = 23 wt%, Mn = 0.45 wt%, La = 0.1 wt%, Ti = 0.06 wt %, Si and Al < 0.05 wt% with Fe representing the balance) provided by VDM Metals (Verdohl, Germany). Both porous and dense substrates were cleaned in acetone and ethanol for 10 min each in an ultrasonic bath. The joining material was a Ba-based glass-ceramic, referred to as GC2 [31]. The original glass was produced using conventional melting and casting from the following high-purity grade raw materials:  $\text{SiO}_2$  (Sigma Aldrich, 99.5% purity) with 55 mol%,  $\text{B}_2\text{O}_3$  (precursor  $\text{H}_3\text{BO}_3$ , Sigma Aldrich, 99% purity) with 8 mol%,  $\text{Al}_2\text{O}_3$  (Alfa Aesar, 99.9%

purity) with 4 mol%, CaO (precursor  $\text{CaCO}_3$  Sigma Aldrich, 99% purity) with 7 mol % and BaO (precursor  $\text{Ba}_2\text{CO}_3$  Thermoscientific, 99.8% purity) with 26 mol%. All the raw material powders were mixed for 24 h and melted in a Pt–Rh crucible in an electric furnace (LHT418PN2, Nabertherm GmbH, Lilienthal/Bremen, Germany) in air at 1500 °C for 1 h (the first 30 min a lid covered the crucible). The melt was cast onto a metal plate and the glass was subsequently ball-milled and sieved (particle size < 38  $\mu\text{m}$ ). The sintering behaviour of the glass powders on the porous substrate, as well as on  $\text{Al}_2\text{O}_3$  inert substrate was investigated using heating stage microscopy (HSM; Hesse Heating Microscope, Germany), with a heating rate of 5 °C/min, from room temperature up to the melting point identified by the instrument.

A small quantity of a slurry paste composed of ethanol (70 wt%) and glass powder (30 wt%) was manually deposited with a spatula between the two metal alloys (squared specimens  $\sim 11 \text{ mm} \times \sim 11 \text{ mm}$ ) to be joined. Preliminary tests carried out with different configurations led to the most effective joint with pre-oxidised (900 °C, 2h as dwelling time, at a 5 °C/min as heating/cooling rate) dense Crofer22APU placed on the top. The joining process was carried out in air at 950 °C for 1h (5 °C/min as heating/cooling rate) in a muffle furnace (L5/13/P330, Nabertherm GmbH, Lilienthal/Bremen, Germany). During the heat treatment, a stainless-steel weight was placed on top of the sandwich structure to apply a pressure of around 1.5 kPa. A Computed Tomography (CT) scan (Fraunhofer IKTS, Hermsdorf, Germany) was used to obtain morphological and qualitative density information of the joined sample under the following parameters: 9.25  $\mu\text{m}$  as resolution, 280 kV as acceleration voltage and 1s the exposure time for each projection. The reconstruction of the joint consists of creating a 3D model of the analysed volume by the CT software.

The same heat treatment identified for the joined sample was also used to produce a dry pressed glass-ceramic pellet, using uniaxial pressure of 12 MPa, to thermo-mechanically characterise GC2 glass-ceramic. The coefficient of thermal expansion (CTE) and the dilatometric softening point of as-cast GC2 glass and as-joined glass-ceramic were measured using a dilatometer (Netzsch, DIL 402 PC) equipped with an alumina sample holder, at a heating rate of 5 °C/min, applying a constant compressive force, between the sample and the piston of 0.25 N.

Some joined samples were cross-sectioned and prepared for SEM and EDS analyses, while others were subjected to ageing treatment at 700 °C for 500 h in a muffle furnace (Carbolite Gero, Hope Valley, UK). This temperature was chosen based on the results obtained by Koszelow et al. [9] focused on the corrosion study of the same Fe22Cr porous alloy up to 900 °C. Some joint samples underwent tensile testing before and after thermal ageing using a method modified from the ASTM C633-01 standard. The tests were carried out using a Syntech 10/D machine (MTS Systems Corporation, Minnesota, USA). Each joint was adhered to two loading fixtures (Fig. 1) by using Araldite® 2015 epoxy resin and thermally treated at 85 °C for 1h to crosslink. The cross-head speed was set to 0.5 mm/min. The tensile strength was calculated by dividing the maximum force by the area of the joint which measured 11 mm  $\times$  11 mm. A field-emission scanning electron microscope (FESEM; SupraTM 40, Zeiss, Oberkochen, Germany) equipped with an energy dispersive X-ray analyser (EDS, Bruker, Germany) was used to characterise the morphology of the samples, which were previously polished using SiC papers (grit size 600–4000) and coated with Cr. A benchtop scanning electron microscope (SEM, JCM-6000 plus, Jeol, Peabody, Massachusetts, USA) was used to observe the fractured surface of the samples following mechanical testing. X-ray diffraction (XRD) analysis of the fractured surface of a joined sample after ageing was conducted using an X'Pert Pro MRD diffractometer, with  $\text{Cu K}\alpha$  radiation (PANalytical X'Pert Pro, Philips, Almelo, The Netherlands), and with the aid of X-Pert HighScore software, while the phases were identified using the JCPDS database provided by PDF-4 ICDD (International Centre for Diffraction Data, Newton Square, Pennsylvania, the USA).

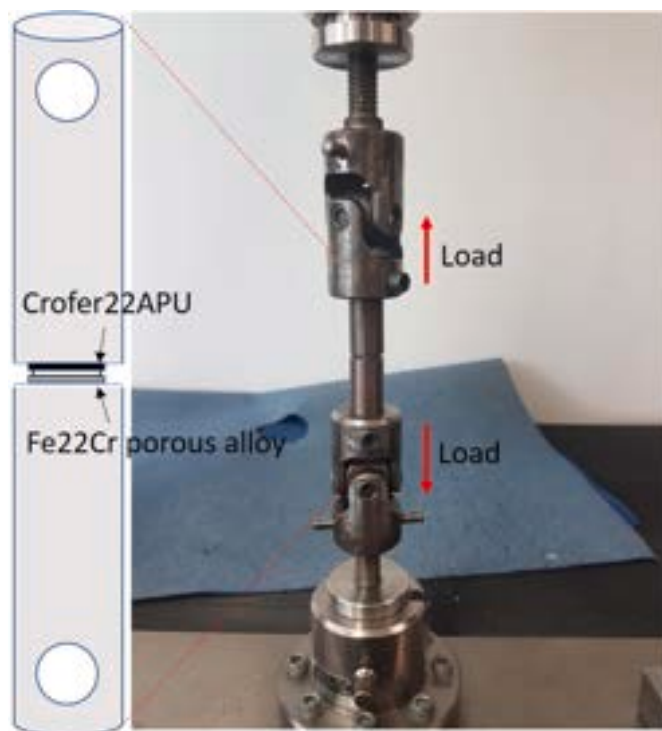


Fig. 1. Configuration used for the mechanical tensile test.

### 3. Results and discussion

Fig. 2 reports the experimental curves obtained from heating stage microscopy (HSM) analyses of the as-cast GC2 glass powder pellets on the porous Fe22Cr alloy (curve 1) and on an inert  $\text{Al}_2\text{O}_3$  support (curve 2), where the linear shrinkages % are plotted against the temperature. The first two characteristic temperatures are the points at which linear shrinkage of the glass starts ( $T_g$ ) and assumes the maximum value ( $T_{ms}$ ):

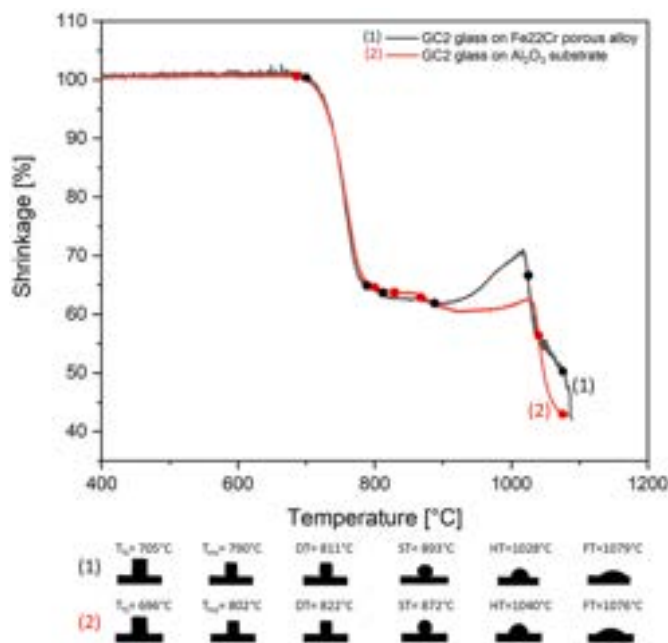


Fig. 2. Heating Stage Microscopy (HSM) curves of the GC2 glass (5 °C/min heating rate) on the Fe22Cr porous alloy (curve 1) and on the inert  $\text{Al}_2\text{O}_3$  support (curve 2); characteristic temperatures of GC2 glass identified with HSM are shown below the figure.

they are 705 °C and 790 °C on the porous alloy, 696 °C and 802 °C on the  $\text{Al}_2\text{O}_3$  substrate. The temperature at which the first signs of softening are observed (DT) was identified at 811 °C (onto Fe22Cr) and 822 °C (onto  $\text{Al}_2\text{O}_3$ ), while the sphere temperature (ST) was at 893 °C on the porous alloy and 872 °C on  $\text{Al}_2\text{O}_3$ , where the height of the sample is equal to the width of the base. The half-sphere temperature (HT), which is the temperature at which the height of the sample is half the width of the base, was measured at 1028 °C on the Fe22Cr porous alloy and at 1040 °C on the inert substrate. Finally, the flow temperature (FT) was evident at 1079 °C and 1076 °C; the latter is the temperature at which the height of the sample drops to below one-third of the base. A visible plateau between 800 and 1000 °C was observed and this represents the crystallization phenomenon that occurs. A significant expansion of the glass powder pellet is visible for the GC2 glass onto the Fe22Cr porous alloy, which is evidently absent on the inert substrate; this is likely due to gaseous species developed at T higher than 920 °C, determined by the oxidation of the porous alloy during the GC2 viscous flow sintering. Based on these observations, the conditions for joining the porous samples to the bulk alloys were determined to be a temperature of 950 °C with a dwelling time of 1h in air. This sinter-crystallization heat treatment led to the formation of GC2 glass-ceramic with  $\text{BaSi}_2\text{O}_5$  as crystalline phase ( $\text{CTE} \sim 12.5 \times 10^{-6} \text{ K}^{-1}$ ), obtained by the partial devitrification of the GC2 parent glass [32].

In order to evaluate the thermo-mechanical properties of the microstructure obtained with the above-mentioned joining thermal treatment, dilatometry was used to measure the coefficient of thermal expansion (CTE) of the GC2 glass-ceramic as well as that of the parent glass (Fig. 3). The CTE value of the GC2 as-cast glass is  $9.2 \times 10^{-6} \text{ K}^{-1}$  between 200 and 500 °C, while the glass transition temperature ( $T_g$ ) and the dilatometric softening point are 665 °C and 688 °C respectively (Fig. 3, curve 1). It can be observed from the dilatometric analysis of the GC2 glass-ceramic that  $T_g$  is slightly lower (658 °C) with respect to the original glass and within experimental error, while the softening point is the same. However, there was evidence of an increase in the coefficient of thermal expansion of the glass-ceramic ( $10.7 \times 10^{-6} \text{ K}^{-1}$ ) in comparison with that of the GC2 glass as suggested by the change in the slope of the curve (Fig. 3, curve 2). The transformation of the parent glass into a glass ceramic led to a significant improvement of the CTE in the view of the thermomechanical compatibility of the final joined structure, since the CTEs of both the substrates to be joined (Crofer22-APU and Fe22Cr) are around  $11 \times 10^{-6} \text{ K}^{-1}$  (200–700 °C).

The sandwiched samples were processed, using the procedure described in the experimental section.

As observed in Fig. 4 a, the SEM image of the cross-section of the joined sample showed excellent adhesion of the GC2 glass-ceramic with

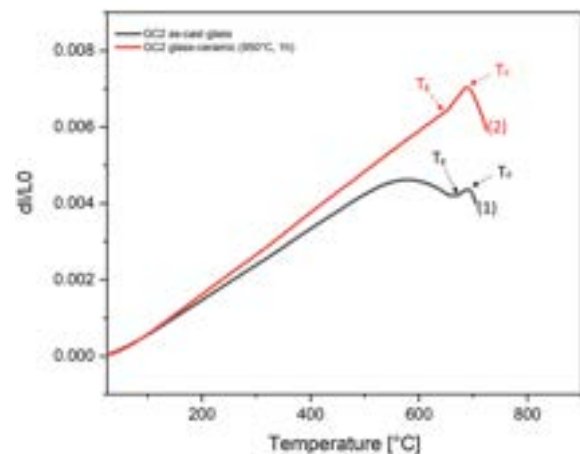
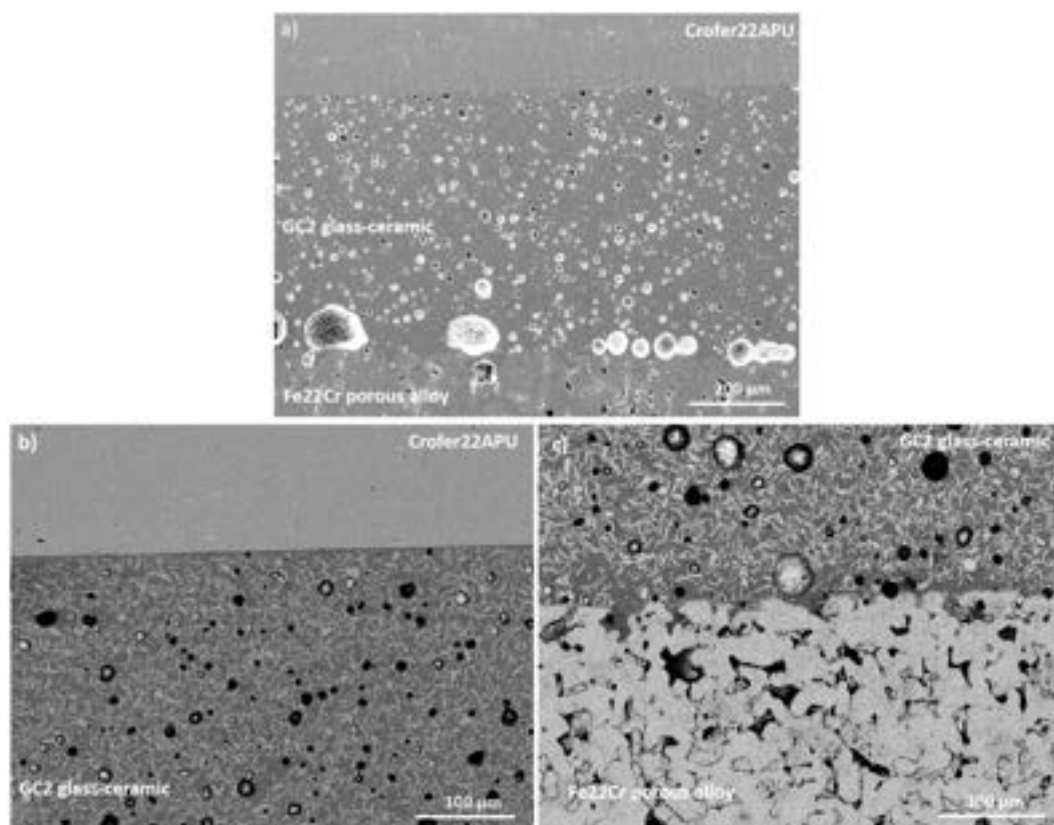
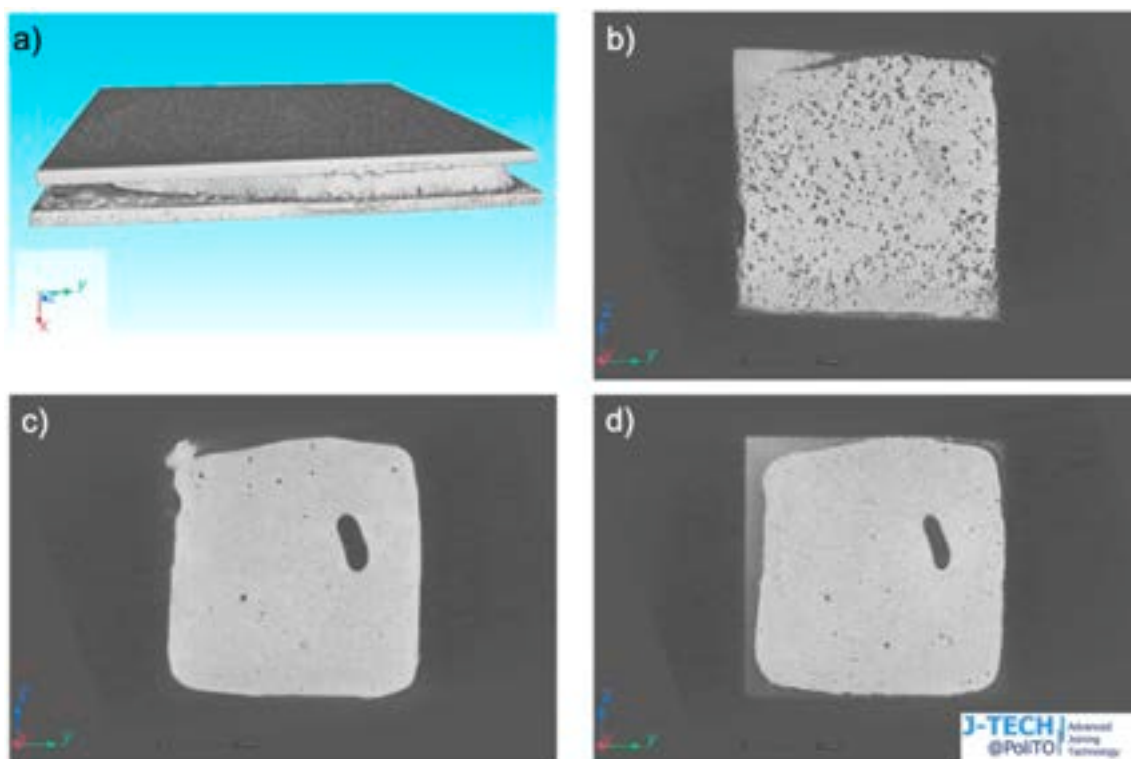


Fig. 3. Dilatometric curves of the GC2 as-cast glass (curve 1) and GC2 glass-ceramic obtained after sinter-crystallization at 950 °C for 1h (curve 2); 5 °C/min heating rate.



**Fig. 4.** SEM images of the cross-section of (a) Crofer22APU/GC2 glass-ceramic/Fe22Cr porous alloy, (b) Crofer22APU/GC2 glass-ceramic interface (back-scattered) and (c) GC2 glass-ceramic/Fe22Cr porous alloy interface (back-scattered) obtained after sinter-crystallization at 950 °C for 1 h.



**Fig. 5.** CT-scan of a Crofer22APU/GC2 glass-ceramic/Fe22Cr porous alloy joined sample thermally treated at 950 °C for 1 h. (a) 3D-model; sectioning plane (b) close to the porous alloy, (c) in the middle of the glass-ceramic, (d) close to Crofer22APU. The big pore on the right could be due to the manual slurry method used to produce the joined specimen.



both the porous and dense metal alloys. No cracks or delamination are visible at the glass-ceramic/substrates interface resulting in a continuous joint along the entire length of the interface. Furthermore, there was no evidence of any reactions taking place by the interaction between the Crofer22APU/porous alloy and the glass (Fig. 4 b,c); an average joint thickness of 520  $\mu\text{m}$  was obtained using a pressure of 1.5 kPa. The presence of a few closed pores, homogeneously distributed in the glass-ceramic, could probably be due to the manual slurry method used to produce the joined specimens. On the other side, the larger voids observed only at the Fe22Cr porous alloy/GC2 glass-ceramic interface is probably due to gaseous species released from the porous substrate during sintering which occurred by viscous flow. Further SEM investigation carried out on a Crofer22APU/GC2 glass-ceramic/Crofer22APU joint (not reported here), showed the absence of these such big voids at both dense alloy/glass-ceramic interfaces, thus confirming that the bigger porosity is due only to the presence of the Fe22Cr porous alloy.

Most of the porosity was concentrated at the porous alloy/GC2 glass-ceramic interface as evidenced by SEM as well as computed tomography (CT) that was carried out on a joined sandwich-like specimen (Fig. 5). In Fig. 5a, a reconstructed 3D model of the sample is shown, while in the other images (Fig. 5 b-d), 3 cross-sections are represented at a different distance from the porous alloy surface; these scans were taken close to the Fe22Cr/GC2 glass-ceramic interface (Fig. 5b), in the middle of the joining area (Fig. 5c) and finally further from the interface with the porous alloy. It is evident that most voids are located at the Fe22Cr/GC2 glass-ceramic interface, while in the other sections very few pores are shown.

More details concerning the Fe22Cr porous alloy/GC2 glass-ceramic interface are shown in FE-SEM images on a cross-sectioned joined sample in Fig. 6. Close inspection at the interface shows that, despite the presence of pores that are concentrated in the lower part of the joining area, no cracks are located both in the joining area and at the interface. Strong adhesion between the GC2 glass-ceramic and the porous

substrate can be observed (Fig. 6a). The distribution of the crystalline phases produces a dense network of needle-like interlocked crystallites embedded in the residual glassy phase. EDS analysis in Fig. 6d (spectrum 1) revealed the presence of Ba, Si and O, indicating the crystallization of a  $\text{BaSi}_2\text{O}_5$  crystalline phase, homogeneously dispersed within the darker glassy matrix which reasonably shows a higher level of Al and Ca and a lower content of Ba and Si (spectrum 2); this hypothesis was supported by XRD diffraction pattern of GC2 glass-ceramic after joining heat treatment at 950  $^\circ\text{C}$ , 1h in air, as reported by Smeacetto et al. [32]. As shown in Fig. 6c and the corresponding EDS in Fig. 6d (spectrum 3), the glass infiltrates the porous alloy very well during the sinter-crystallization treatment; infiltration distance levels of up to 50  $\mu\text{m}$  from the GC2 glass-ceramic/Fe22Cr porous alloy interface are evident.

Tensile testing was used to evaluate the mechanical properties of the joined samples. The tests carried out on as-joined Crofer22APU/GC2 glass-ceramic/Fe22Cr porous alloy samples showed an average tensile strength of  $7.4 \pm 0.5$  MPa (identified with  $\sigma_m$  in Fig. 7). This value is slightly higher than the tensile strength of the majority of glass-ceramic sealants reported in the literature (3.8–6.3 MPa) and used for joining Crofer22APU and Crofer22H [33].

Macrographs of the fracture surface of 3 as-joined specimens are shown in Fig. 7. While most of the fractured area of the Fe22Cr porous substrate in Fig. 7 seems to show exposed metal alloy, however, EDS analyses (not reported here) revealed many parts of the surface covered by the GC2 glass-ceramic; in some areas, large sections (in white) of the GC2 glass-ceramic suggest the presence of cohesive failure, while small white specks show evidence of fractured glass-ceramic that had impregnated the pores of the Fe22Cr substrate. Inspection of the opposite part shows small fractured black specks of Fe22Cr embedded in the GC2 glass-ceramic. These observations suggest that the impregnation of the glass-ceramic into the Fe22Cr porous alloy enhances the interfacial strength. Indeed, part of the failure seems to be occurring in the porous

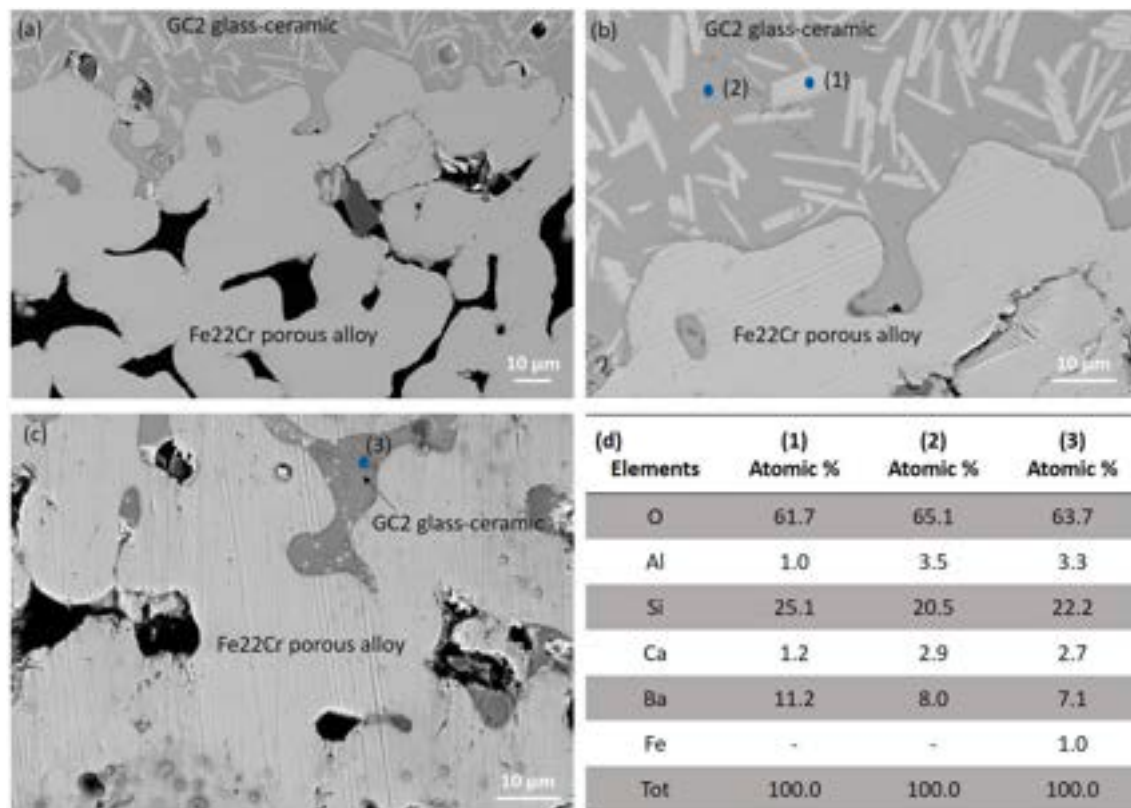


Fig. 6. Cross-section FE-SEM images at lower (a) and higher (b) magnification of the Fe22Cr porous alloy/GC2 glass-ceramic interface after sinter-crystallization at 950  $^\circ\text{C}$  for 1h; (c) infiltration of the glass-ceramic in the porous alloy of the joined sample; (d) EDS analyses of the GC2 glass-ceramic in the joining area.

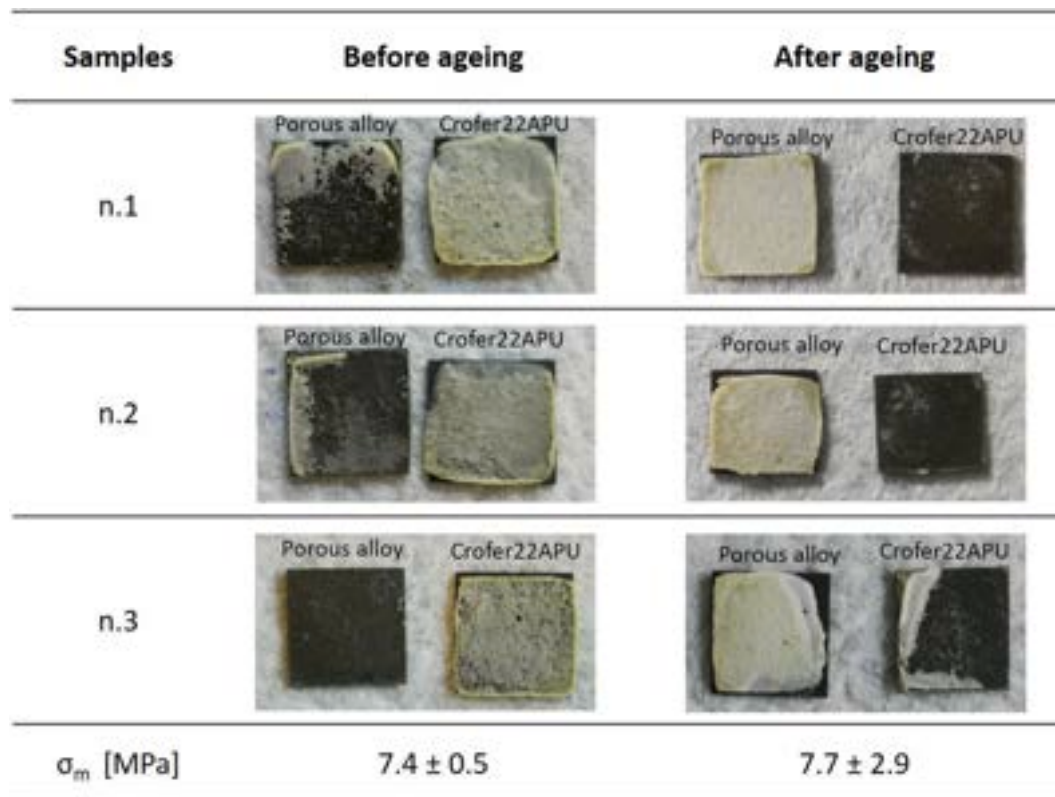


Fig. 7. Macrographs of as-joined and aged Crofer22APU/GC2glass-ceramic/Fe22Cr samples after tensile testing.

Fe22Cr just beyond the area of GC2 impregnation due to stress concentration in the porous alloy (due to the absence of GC2 glass-ceramic). Overall there is mixed adhesive/cohesive failure, where the adhesive failure is mainly localised at the porous/GC2 interface. Fig. 8a shows a magnified fracture surface of the glass-ceramic on the Crofer22APU side after mechanical testing; the bright phase well visible in the back-scattered SEM image identified by the EDS analysis as  $\text{BaCrO}_4$ , was mainly located on the edges of the joined area and was present on both the porous and the dense metal alloy.

Fig. 9 shows a cross-section of a joined sample after ageing at 700 °C for 500 h. There was no evidence of cracks following ageing, thus implying that detrimental thermal stresses did not occur. In addition, the microstructure of the GC2 glass-ceramic did not seem to be affected by the heat treatment (Fig. 9a). However, Fig. 9b shows evidence of the formation of an oxidation scale on the pores surface; oxidation was also

apparent at the GC2 glass-ceramic/porous alloy interface (Fig. 9c). Due to the large surface/volume ratio of the porous samples, there is a risk that oxide formation (typically  $\text{Cr}_2\text{O}_3$  [34]) can potentially lead to depletion of Cr within the porous alloy. In a previously cited work [9], the surface of the same porous alloy, which was exposed to a temperature of 700 °C for 100hrs, did not show any significant microstructural changes in comparison to alloy samples that had not been aged. The weight gain at 700 °C after 100 h was reported to be around 1%. However, a sample that had been exposed to 750 °C for the same time, experienced a weight gain of ~2.5% and was characterised by changes at the surface; a small amount of oxide had clearly formed at the surface which exhibited signs of greater roughness which may have resulted by the fact that the surface of the porous alloy was slightly rough. From Fig. 9d the formation of a darker layer covering the Fe22Cr porous alloy following ageing is apparent. Based on the results of the EDS analysis the

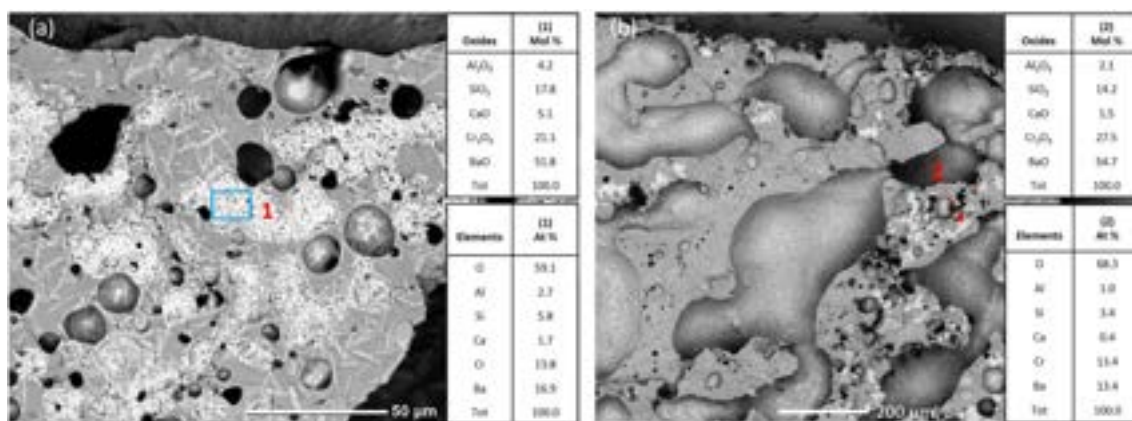
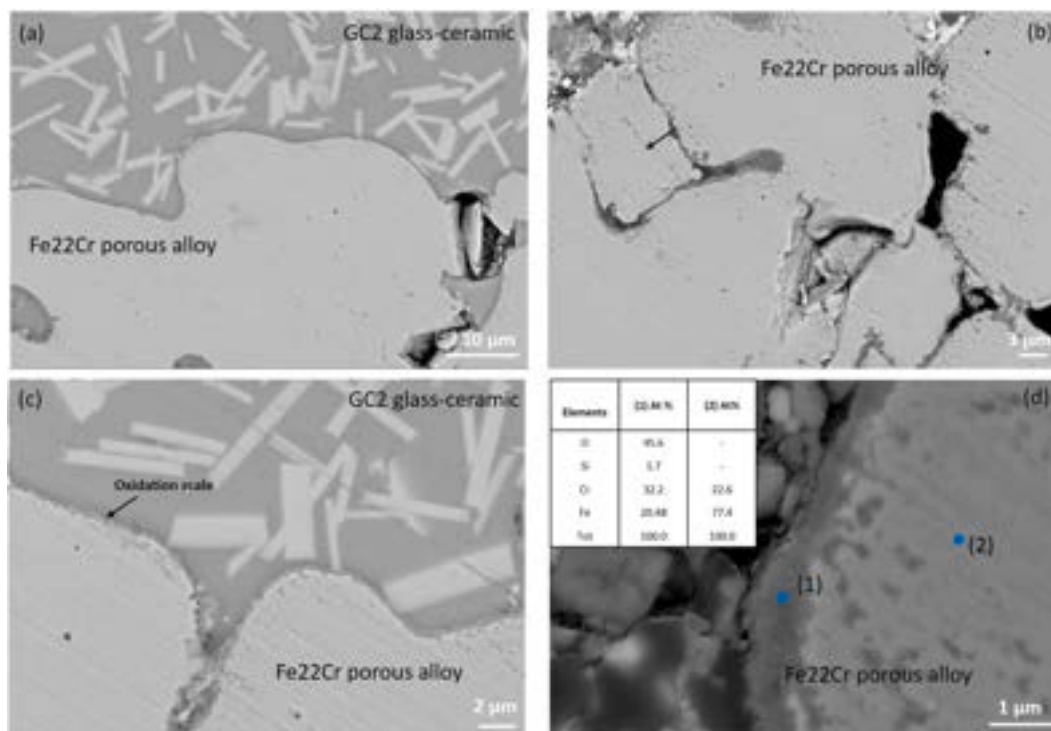


Fig. 8. SEM images of top views of fracture surface of an as-joined (a) and an aged (b) Crofer22APU/GC2glass-ceramic/Fe22Cr porous alloy sample after mechanical testing (Crofer22APU side); EDS analyses carried out on the fracture surfaces in the joining area.



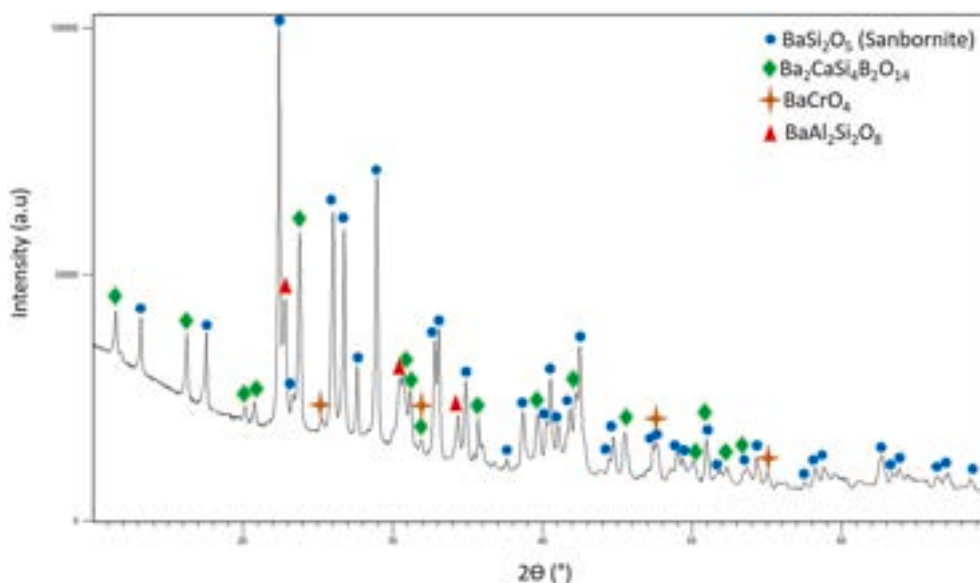
**Fig. 9.** FE-SEM images of a cross-section after ageing at 700 °C for 500hrs: (a,c) Fe22Cr porous alloy/GC2 glass-ceramic interface and (b) Fe22Cr porous alloy; (d) higher magnification of Fe22Cr porous alloy and EDS analysis carried out on the porosity edge of the porous alloy.

scale seems to be composed of a mixed Fe and Cr-based oxide and, since the latter is visible also further from the glass-ceramic/Fe22Cr porous alloy interface, it could be due to a longer ageing heat treatment (700 °C for 500hrs).

The results of mechanical testing for the thermally-aged samples exhibited an average tensile strength of  $7.7 \pm 2.9$  MPa, a value that was similar to the as-joined samples. Inspection of the macrographs in Fig. 7 shows that the samples suffered a completely or mainly adhesive failure. Fig. 8b shows a higher magnification of the fracture surface of the Crofer22APU after ageing at 700 °C for 500 h following mechanical testing. The EDS analysis showed high atomic% of Ba and Cr and therefore the presence of barium chromate can be hypothesized also

after ageing.

XRD analysis that was carried out on the Crofer22APU side (on the porous side, the remaining glass-ceramic layer was not enough) after ageing and mechanical testing, is shown in Fig. 10. The main peaks matched with those of the orthorhombic barium silicate (Sanbornite with chemical formula  $\text{BaSi}_2\text{O}_5$ , PDF card n. 01-071-1441), which was the main phase present after ageing. Prior to the ageing treatment, the only phase that was present was  $\text{BaSi}_2\text{O}_5$  as previously reported for the as joined glass-ceramic system before ageing heat treatment [32]. However, following ageing, new phases emerged like those reported in previous studies with similar glasses [25], where the formation of additional Ba–Ca–silicate phases that were not homogeneously



**Fig. 10.** XRD pattern of the fracture surface (Crofer22APU side) of a Fe22Cr/GC2 glass-ceramic/Crofer22APU joined sample after ageing at 700 °C for 500 h.



distributed within the microstructure was observed. In the present work a secondary phase identified as the barium calcium boron silicate (named Itsiite [35], crystal system: tetragonal; space group: I-42m)  $\text{Ba}_2\text{CaSi}_4\text{B}_2\text{O}_{14}$ , with PDF card n. 04-021-1159 was found. In addition, some low-intensity peaks were identified as the  $\text{BaCrO}_4$  phase, confirming the EDS analyses carried out at the same fracture surface. Finally, the three peaks at about  $2\theta = 22.8^\circ$ ,  $2\theta = 30.2^\circ$  and  $2\theta = 34.5^\circ$  could likely be attributed to  $\text{BaAl}_2\text{Si}_2\text{O}_8$  (ref. code 00-012-0725). In the present work, the glass-ceramic joining material was subjected to a thermal ageing temperature that was  $40^\circ\text{C}$  higher than the GC2 glass-ceramic  $T_g$  value. These findings, while preliminary, suggest that this system is prone to further devitrification at temperatures slightly above the  $T_g$ . Despite this, the mechanical behaviour of the joints is not affected by this microstructural rearrangement. Further research should be undertaken to investigate the thermomechanical behaviour at temperatures higher than  $700^\circ\text{C}$ .

#### 4. Conclusions

The possibility of using porous metal alloys provides interesting engineering features thanks to their functional porosity, which make these candidate materials for metal-supported solid oxide cells. The development of a dense to a porous joint can play a key role in the manufacture of reliable, efficient and durable metal-supported SOCs. The novelty of this study concerns the joining of porous stainless steel to a dense one with a glass-ceramic obtained from sinter-crystallization of a glass sealant. Different aspects concerning the interfacial issues and mechanical properties were discussed, evaluating an optimal adhesion and mechanical stability in Crofer22APU/GC2 glass-ceramic/Fe22Cr porous alloy joints, before and after thermal ageing carried out at  $700^\circ\text{C}$  for 500hrs. The morphological analysis found no defects or cracks at the porous alloy/glass-ceramic interface, neither in the as-joined samples nor in samples after ageing at  $700^\circ\text{C}$  for 500 h. However, at this temperature, the porous alloy started to experience the formation of an oxidation scale at the interface between the Fe22Cr porous alloy and the GC2 glass-ceramic, as well as around the wall of the pores of the porous alloy. The mechanical strength of the joined samples was not affected by thermal ageing ( $7.4\text{ MPa} \pm 0.5$  before and  $7.7\text{ MPa} \pm 2.9$  after ageing).

The current study provides the first assessment concerning the joining of a porous to a dense alloy using glass-ceramics and makes the groundwork for future research into MS-SOC development.

#### Declaration of competing interest

The authors declare that they have no known competing financial interests or personal relationships that could have appeared to influence the work reported in this paper.

#### Acknowledgments

DK and SM acknowledge the support of National Science Centre Poland (NCN) Sonata Bis 8 project number 2018/30/E/ST8/00821 “High-temperature corrosion studies and development of oxidation lifetime model of alloy powders and sintered porous alloys: effects of composition and microstructure”.

#### References

- J.E. Hammer, S.J. Laney, R.W. Jackson, K. Coyne, F.S. Pettit, G.H. Meier, The oxidation of ferritic stainless steels in simulated solid-oxide fuel-cell atmospheres, *Oxid. Metals* 67 (2007) 1–38, <https://doi.org/10.1007/s11085-006-9041-y>.
- N.J. Magdefrau, L. Chen, E.Y. Sun, M. Aindow, Effects of alloy heat treatment on oxidation kinetics and scale morphology for crofer 22 APU, *J. Power Sources* 241 (2013) 756–767, <https://doi.org/10.1016/j.jpowsour.2013.03.181>.
- P. Alnegren, M. Sattari, J. Froitzheim, J.E. Svensson, Degradation of ferritic stainless steels under conditions used for solid oxide fuel cells and electrolyzers at varying oxygen pressures, *Corrosion Sci.* 110 (2016) 200–212, <https://doi.org/10.1016/j.corsci.2016.04.030>.
- B. Timurkutluk, S. Toros, S. Onbilgin, H.G. Korkmaz, Determination of formability characteristics of Crofer 22 APU sheets as interconnector for solid oxide fuel cells, *Int. J. Hydrogen Energy* 43 (2018) 14638–14647, <https://doi.org/10.1016/j.ijhydene.2018.04.243>.
- S. Fontana, R. Amendola, S. Chevalier, P. Piccardo, G. Caboche, M. Viviani, R. Molins, M. Sennour, Metallic interconnects for SOFC: characterisation of corrosion resistance and conductivity evaluation at operating temperature of differently coated alloys, *J. Power Sources* 171 (2007) 652–662, <https://doi.org/10.1016/j.jpowsour.2007.06.255>.
- D.N. Boccaccini, H.L. Frandsen, B.R. Sudireddy, P. Blennow, H. Persson, K. Kwok, P. Vang Hendriksen, Creep behaviour of porous metal supports for solid oxide fuel cells, *Int. J. Hydrogen Energy* 39 (2014) 21569–21580, <https://doi.org/10.1016/j.ijhydene.2014.07.138>.
- M. Stange, C. Denonville, Y. Larring, A. Brevet, A. Montani, O. Sicardy, J. Mougins, P.O. Larsson, Improvement of corrosion properties of porous alloy supports for solid oxide fuel cells, *Int. J. Hydrogen Energy* 42 (2017) 12485–12495, <https://doi.org/10.1016/j.ijhydene.2017.03.170>.
- E. Stefan, C. Denonville, Y. Larring, M. Stange, R. Haugsrud, Oxidation study of porous metal substrates for metal supported proton ceramic electrolyzer cells, *Corrosion Sci.* 164 (2020), 108335, <https://doi.org/10.1016/j.corsci.2019.108335>.
- D. Koszelow, M. Makowska, F. Marone, J. Karczewski, P. Jasiński, S. Molin, High temperature corrosion evaluation and lifetime prediction of porous Fe22Cr stainless steel in air in temperature range  $700\text{--}900^\circ\text{C}$ , *Corrosion Sci.* 189 (2021), <https://doi.org/10.1016/j.corsci.2021.109589>.
- V. Venkatachalam, S. Molin, M. Chen, I. Smirnov, P.O. Larsson, P.V. Hendriksen, N. Bonanos, Optimization of ferritic steel porous supports for protonic fuel cells working at  $600^\circ\text{C}$ , *Mater. Sci. Technol. Conf. Exhib.* 2 (2014) 1231–1239, 2014, MS T 2014.
- Y. Xing, S. Baumann, D. Sebold, M. Rüttinger, A. Venskutonis, W.A. Meulenbergh, D. Stöver, Chemical compatibility investigation of thin-film oxygen transport membranes on metallic substrates, *J. Am. Ceram. Soc.* 94 (2011) 861–866, <https://doi.org/10.1111/j.1551-2916.2010.04171.x>.
- J.A. Calles, R. Sanz, D. Alique, Influence of the type of siliceous material used as intermediate layer in the preparation of hydrogen selective palladium composite membranes over a porous stainless steel support, *Int. J. Hydrogen Energy* 37 (2012) 6030–6042, <https://doi.org/10.1016/j.ijhydene.2011.12.164>.
- J.A. Glasscock, L. Mikkelsen, Å.H. Persson, G. Pećanac, J. Malzbender, P. Blennow, F. Bozza, P.V. Hendriksen, Porous Fe21Cr7Al1Mo0.5Y metal supports for oxygen transport membranes: thermo-mechanical properties, sintering and corrosion behaviour, *Solid State Ionics* 242 (2013) 33–44, <https://doi.org/10.1016/j.ssi.2013.04.006>.
- S. Linderoth, Solid oxide cell R&D at Risø National Laboratory and its transfer to technology, *J. Electroceram.* 22 (2009) 61–66, <https://doi.org/10.1007/s10832-008-9458-6>.
- M.C. Tucker, Progress in metal-supported solid oxide fuel cells: a review, *J. Power Sources* 195 (2010) 4570–4582, <https://doi.org/10.1016/j.jpowsour.2010.02.035>.
- M.C. Tucker, G.Y. Lau, C.P. Jacobson, L.C. DeJonghe, S.J. Visco, Stability and robustness of metal-supported SOFCs, *J. Power Sources* 175 (2008) 447–451, <https://doi.org/10.1016/j.jpowsour.2007.09.032>.
- M.C. Tucker, Durability of symmetric-structured metal-supported solid oxide fuel cells, *J. Power Sources* 369 (2017) 6–12, <https://doi.org/10.1016/j.jpowsour.2017.09.075>.
- J.W. Fergus, Sealants for solid oxide fuel cells, *J. Power Sources* 147 (2005) 46–57, <https://doi.org/10.1016/j.jpowsour.2005.05.002>.
- M.K. Mahapatra, K. Lu, Seal glass for solid oxide fuel cells, *J. Power Sources* 195 (2010) 7129–7139, <https://doi.org/10.1016/j.jpowsour.2010.06.003>.
- N. Mahato, A. Banerjee, A. Gupta, S. Omar, K. Balani, Progress in material selection for solid oxide fuel cell technology: a review, *Prog. Mater. Sci.* 72 (2015) 141–337, <https://doi.org/10.1016/j.pmatsci.2015.01.001>.
- R.N. Singh, Sealing technology for solid oxide fuel cells (SOFC), *Int. J. Appl. Ceram. Technol.* 4 (2007) 134–144, <https://doi.org/10.1111/j.1744-7402.2007.02128.x>.
- F. Smeacetto, A. De Miranda, A. Chrysanthou, E. Bernardo, M. Secco, M. Bindi, M. Salvo, A.G. Sabato, M. Ferraris, Novel glass-ceramic composition as sealant for SOFCs, *J. Am. Ceram. Soc.* 97 (2014) 3835–3842, <https://doi.org/10.1111/jace.13219>.
- M.K. Mahapatra, K. Lu, Glass-based seals for solid oxide fuel and electrolyzer cells - a review, *Mater. Sci. Eng. R Rep.* 67 (2010) 65–85, <https://doi.org/10.1016/j.mser.2009.12.002>.
- S.M. Gross, T. Koppitz, J. Rimmel, J.B. Bouche, U. Reisgen, Joining properties of a composite glass-ceramic sealant, *Fuel Cell. Bull.* (2006) 12–15, [https://doi.org/10.1016/S1464-2859\(06\)71320-7](https://doi.org/10.1016/S1464-2859(06)71320-7), 2006.
- J. Schilm, A. Rost, M. Kusnezoff, S. Megel, A. Michaelis, Glass ceramics sealants for SOFC interconnects based on a high chromium sinter alloy, *Int. J. Appl. Ceram. Technol.* 15 (2018) 239–254, <https://doi.org/10.1111/jiac.12811>.
- H. Javed, A.G. Sabato, K. Herbrig, D. Ferrero, C. Walter, M. Salvo, F. Smeacetto, Design and characterization of novel glass-ceramic sealants for solid oxide electrolysis cell (SOEC) applications, *Int. J. Appl. Ceram. Technol.* 15 (2018) 999–1010, <https://doi.org/10.1111/jiac.12889>.
- A.G. Sabato, A. Chrysanthou, M. Salvo, G. Cempura, F. Smeacetto, Interface stability between bare, Mn–Co spinel coated AISI 441 stainless steel and a diopside-based glass-ceramic sealant, *Int. J. Hydrogen Energy* 43 (2018) 1824–1834, <https://doi.org/10.1016/j.ijhydene.2017.11.150>.

- [28] J. Schilm, A. Rost, M. Kusnezoff, A. Michaelis, Sealing glasses for SOFC - degradation behaviour, in: *Adv. Solid Oxide Fuel Cells V*, 2010, pp. 183–193, <https://doi.org/10.1002/9780470584316.ch17>.
- [29] D. Udomsilp, J. Rechberger, R. Neubauer, C. Bischof, F. Thaler, W. Schafbauer, N. H. Menzler, L.G.J. de Haart, A. Nenning, A.K. Opitz, O. Guillon, M. Bram, Metal-supported solid oxide fuel cells with exceptionally high power density for range extender systems, *Cell Reports Phys. Sci.* 1 (2020), <https://doi.org/10.1016/j.xcrp.2020.100072>.
- [30] A. Drewniak, D. Koszelow, P. Błaszczak, K. Górnicka, K. Jurak, H. Javed, A. G. Sabato, P. Jasiński, S. Molin, F. Smeacetto, Glass-ceramic sealants and steel interconnects: accelerated interfacial stability and reactivity tests at high temperature, *Mater. DES* 212 (2021), <https://doi.org/10.1016/j.matdes.2021.110259>.
- [31] M. Ferraris, S. De la Pierre, A.G. Sabato, F. Smeacetto, H. Javed, C. Walter, J. Malzbender, Torsional shear strength behavior of advanced glass-ceramic sealants for SOFC/SOEC applications, *J. Eur. Ceram. Soc.* 40 (2020) 4067–4075, <https://doi.org/10.1016/j.jeurceramsoc.2020.04.034>.
- [32] F. Smeacetto, A. Chrysanthou, A.G. Sabato, H. Javed, S.D. la Pierre, M. Salvo, M. Ferraris, Glass-to-metal seals for solid oxide cells at the Politecnico di Torino, an overview, *Int. J. Appl. Ceram. Technol.* 19 (2022) 1017–1028, <https://doi.org/10.1111/ijac.13949>.
- [33] B. Cela Greven, S. Gross-Barsnick, T. Koppitz, R. Conradt, F. Smeacetto, A. Ventrella, M. Ferraris, Torsional shear strength of novel glass-ceramic composite sealants for solid oxide fuel cell stacks, *Int. J. Appl. Ceram. Technol.* 15 (2018) 286–295, <https://doi.org/10.1111/ijac.12819>.
- [34] L. Wang, W. Yang, Z. Ma, J. Zhu, Y. Li, First-principles study of chromium diffusion in the ferritic Fe-Cr alloy, *Comput. Mater. Sci.* 181 (2020), 109733, <https://doi.org/10.1016/j.commatsci.2020.109733>.
- [35] A.R. Kampf, R.C. Peterson, B.R. Joy, Itsiite,  $\text{Ba}_2\text{Ca}(\text{BSi}_2\text{O}_7)_2$ , a new mineral species from Yukon, Canada: description and crystal structure, *Can. Mineral.* 52 (2014) 401–407, <https://doi.org/10.3749/canmin.52.3.401>.

## 6. Conclusions

The dissertation describes the research regarding the porous ferritic alloys high-temperature oxidation. The set of five publications, included in this work, presents the comprehensive study of porous alloys oxidation kinetics, morphology changes and lifespan prediction. The two hypotheses (presented in Section 2) were proved and elaborated on in the attached publications.

The first hypothesis was: **It is possible to create a lifespan prediction model for porous ferritic chromia-forming alloys based on short-term oxidation exposure experiments at high-temperatures.**

In the first publication [DK1], a simple lifespan prediction model for porous chromia-forming ferritic alloys was proposed based on the short-term oxidation tests and post-mortem analysis of exposed Fe<sub>22</sub>Cr samples. The model took into consideration the specific surface area of porous alloy as well as the Cr reservoir in the alloy's particles. Then, based on the change of slope that was detected for samples oxidized at 900°C, the 6 % of weight gain was established as the threshold level for the possible lifespan of the alloy.

The model was validated based on long-term cyclic oxidation experiments that were performed at temperatures ranging from 600°C to 900°C for up to 6000 h for three different porous alloy compositions: Fe<sub>20</sub>Cr, Fe<sub>22</sub>Cr, and Fe<sub>27</sub>Cr [DK3]. The lifespan of ~3000 h predicted by the model for Fe<sub>22</sub>Cr oxidized at 700°C was confirmed by long-term tests. However, as the model relies on extrapolation of weight gain curve in a log-log plot, its uncertainty was found to be relatively high.

In order to enhance understanding of microstructural changes in the porous alloys occurring at high-temperature oxidation environment, a detailed synchrotron X-Ray tomography study was performed [DK2]. It allowed for the separation and quantification of porosity, metallic core, and oxide scale phases. Moreover, the tomographic study provided information that can improve the lifespan prediction model of the porous alloys by determining the breakaway corrosion formation regions.

The second hypothesis was: **It is possible to extend the lifespan of porous ferritic chromia-forming alloys operating at high temperatures by performing an initial pre-oxidation process.**

This hypothesis was proved based on comprehensive corrosion experiments which took into consideration different pre-oxidation conditions [DK4]. It was confirmed that the temperature of the pre-oxidation process is a crucial parameter for the positive effect on porous alloy's lifespan. Moreover, the pre-oxidation performed at 900°C leads to significant increase of porous alloy lifespan (additional ~2000 h of lifespan).

The possible application of pre-oxidized porous Fe<sub>22</sub>Cr alloy was investigated by considering porous-to-bulk ferritic alloys joining using Si-based glass-ceramic [DK5]. The stability of as-fabricated system, which can be compared with sealing system in MS-SOC stack, was confirmed at 700°C, which is the typical operating temperature of IT-SOCs.

Researching the impact of high temperature oxidation process on porous alloys yielded promising results, but also showed that there are still many details that need to be investigated. The proposed lifespan prediction model does not take into consideration, for example, various particles size which constitute the porous alloy microstructure. Furthermore, there is still lack of information about the impact of initial porosity on the alloys' lifespan. The application of porous alloys in metal-supported solid oxide cells requires additional study regarding gas permeability throughout the alloy structure as well as the electrical conductivity measurements. Nevertheless, the results presented in the dissertation provide an essential data of high-temperature oxidation of porous ferritic chromia-forming alloys and its possible lifespan in devices operating at elevated temperatures.

My original achievements which have been highlighted in the thesis are:

- Formulating the lifespan prediction model of porous alloys based on short-term isothermal oxidation experiments
- Determining the microstructure changes such as porosity, oxide scale thickness, and specific surface area of porous alloys in high-temperature oxidation conditions
- Validating the proposed lifespan prediction model via long-term oxidation tests
- Confirming that pre-oxidation process performed at 900°C can lead to lifespan extension of porous alloys

## 7. References

- [1] G.Y. Lai, High-Temperature Corrosion and Materials Applications, ASM International, 2007. <https://books.google.pl/books?id=tfDwOe7xWeQC>.
- [2] C.A.C. Sequeira, High Temperature Corrosion: Fundamentals and Engineering, Wiley, 2019. <https://books.google.pl/books?id=HL59DwAAQBAJ>.
- [3] G.D. Smith, B.A. Baker, Nickel and Its Alloys, Mech. Eng. Handb. Mater. Mech. Des. Third Ed. 1 (2006) 256–277. <https://doi.org/10.1002/0471777447.ch6>.
- [4] High Temperature WILEY SERIES IN CORROSION, n.d.
- [5] S. Kumar Bohidar, R. Dewangan, K. Kaurase, Advanced Materials used for different components of Gas Turbine, Artic. Int. J. Sci. Res. Manag. 1 (2013) 2321–3418. [www.ijssrm.in](http://www.ijssrm.in).
- [6] G. Tammann, Über Anlauffarben von Metallen, Zeitschrift Für Anorg. Und Allg. Chemie. 111 (1920) 78–89. <https://doi.org/10.1002/zaac.19201110107>.
- [7] G. Tammann, W. Köster, Metallographische mitteilungen aus dem institut für physikalische chemie der universität göttingen. cv. die geschwindigkeit der einwirkung von sauerstoff, schwefelwasserstoff und halogenen auf metalle, Zeitschrift Für Anorg. Und Allg. Chemie. 123 (1922) 196–224.
- [8] N.B. Pilling, The oxidation of metals at high temperature, J. Inst. Met. 29 (1923) 529–582.
- [9] L.B. Pfeil, The oxidation of iron and steel at high temperatures, J. Iron Steel Inst. 119 (1929) 501–560.
- [10] C. Wagner, Beitrag zur Theorie des Anlaufvorgangs, Zeitschrift Für Phys. Chemie. 21B (1933) 25–41. <https://doi.org/10.1515/zpch-1933-2105>.
- [11] J. Eklund, I. Hanif, S. Bigdeli, T. Jonsson, High temperature corrosion behavior of FeCrAlSi model alloys in the presence of water vapor and KCl at 600 °C – The influence of Cr content, Corros. Sci. 198 (2022) 110114. <https://doi.org/10.1016/j.corsci.2022.110114>.
- [12] Y. Peng, M.A. Imam, R.G. Reddy, High-temperature corrosion model of Incoloy 800H alloy connected with Ni-201 in MgCl<sub>2</sub>-KCl heat transfer fluid, High Temp. Mater. Process. 42 (2023). <https://doi.org/10.1515/htmp-2022-0291>.
- [13] A.S. Khanna, High Temperature Oxidation, Second Edi, Elsevier Inc., 2012. <https://doi.org/10.1016/B978-1-4377-3455-3.00005-5>.
- [14] A.S. Khanna, High-temperature oxidation, Handb. Environ. Degrad. Mater. Third



Ed. 2 (2018) 117–132. <https://doi.org/10.1016/B978-0-323-52472-8.00006-X>.

- [15] R.W. Revie, Uhlig ' S Corrosion Handbook the Electrochemical Society Series, 2011.
- [16] W. Gao, Z. Li, Developments in high-temperature corrosion and protection of materials, 2008.
- [17] T.H.E. Society, O.F. Chemical, Metallurgical processes, Vacuum. 7–8 (1959) 216. [https://doi.org/10.1016/0042-207x\(59\)90795-x](https://doi.org/10.1016/0042-207x(59)90795-x).
- [18] B.H.A. Mii, THEORY OF OXIDATION AND TARNISHING OF METALS. I. T h e Linear, P a r a b o l i c a n d L o g a r i t h m i c, (1942) 391–411.
- [19] J.T. Waber, On the cubic law of oxidation, J. Chem. Phys. 20 (1952) 734–735. <https://doi.org/10.1063/1.1700525>.
- [20] S. Bose, Chapter 4 - OXIDATION, in: S.B.T.-H.T.C. Bose (Ed.), Butterworth-Heinemann, Burlington, 2007: pp. 29–52. <https://doi.org/https://doi.org/10.1016/B978-075068252-7/50005-6>.
- [21] R. Ghez, On the Mott-Cabrera oxidation rate equation and the inverse-logarithmic law, J. Chem. Phys. 58 (1973) 1838–1843. <https://doi.org/10.1063/1.1679440>.
- [22] C.S. Tedmon, The effect of li on the high temperature oxidation of Fe-25 Cr alloy, Corros. Sci. 7 (1967). [https://doi.org/10.1016/s0010-938x\(67\)80091-x](https://doi.org/10.1016/s0010-938x(67)80091-x).
- [23] W. Gao, Z. Li, Developments in high-temperature corrosion and protection of materials, 2008.
- [24] D.J. Young, Alloy Oxidation II, 2016. <https://doi.org/10.1016/b978-0-08-100101-1.00006-6>.
- [25] M. Nanko, D.T.M. Do, Oxide nano-rod array structure via a simple metallurgical process, IOP Conf. Ser. Mater. Sci. Eng. 20 (2011). <https://doi.org/10.1088/1757-899X/20/1/012012>.
- [26] R.N. Hajra, H. Tripathy, C. Sudha, N. Vijayashanthi, S. Raju, S. Saroja, Effect of sigma phase on thermophysical properties of Fe55Cr45 alloy, Intermetallics. 112 (2019) 106552. <https://doi.org/10.1016/j.intermet.2019.106552>.
- [27] E. Zanchi, J. Ignaczak, B. Kamecki, P. Jasiński, S. Molin, A.R. Boccaccini, F. Smeacetto, Manganese–cobalt based spinel coatings processed by electrophoretic deposition method: The influence of sintering on degradation issues of solid oxide cell oxygen electrodes at 750°C, Materials (Basel). 14 (2021). <https://doi.org/10.3390/ma14143836>.

- [28] J. Ignaczak, L. Zeng, D.F. Sanchez, M. Makowska, K. Górnicka, K. Lankauf, J. Karczewski, P. Jasiński, S. Molin, Fe-modified  $\text{Mn}_2\text{CuO}_4$  spinel oxides: coatings based on abundant elements for solid oxide cell interconnects, *Int. J. Hydrogen Energy*. 8 (2023). <https://doi.org/10.1016/j.ijhydene.2023.06.041>.
- [29] H. Wang, Q. Zhao, H. Yu, Z. Zhang, H. Cui, G. Min, Effect of aluminium and silicon on high temperature oxidation resistance of Fe-Cr-Ni heat resistant steel, *Trans. Tianjin Univ.* 15 (2009) 457–462. <https://doi.org/10.1007/s12209-009-0079-1>.
- [30] G. Azimi, M. Shamanian, Effect of silicon content on the microstructure and properties of Fe-Cr-C hardfacing alloys, *J. Mater. Sci.* 45 (2010) 842–849. <https://doi.org/10.1007/s10853-009-4008-4>.
- [31] A. Purniawan, H. Irawan, S.T. Wicaksono, Microstructure and Adhesion Properties Post-Annealed Metallic Coating of FeCrBmnsi on Tube and Internal Structure Coal-Fired Boiler, *IPTEK J. Proc. Ser.* 0 (2017) 98. <https://doi.org/10.12962/j23546026.y2017i1.2200>.
- [32] L. Aries, J. Roy, S. El Hajjaji, L. Alberich, P.V. Hernandez, P. Costeseque, T. Aigouy, Preparation and high-temperature behaviour of electrolytic alumina film on Fe-Cr-Al stainless steel, *J. Mater. Sci.* 33 (1998) 429–433. <https://doi.org/10.1023/A:1004384116409>.
- [33] D. Pilone, F. Felli, U. Bernabai, FeCrAl Alloys Produced by Roll-Bonding and Annealing of Al(RE)-Clad Stainless Steel: How Addition of Hf and Zr Affects their Oxidation Behaviour, *Mater. Sci. Forum.* 604–605 (2008) 133–137. <https://doi.org/10.4028/www.scientific.net/msf.604-605.133>.
- [34] J. Masalski, J. Gluszek, J. Zabrzski, K. Nitsch, P. Gluszek, Improvement in corrosion resistance of the 316L stainless steel by means of  $\text{Al}_2\text{O}_3$  coatings deposited by the sol-gel method, *Thin Solid Films*. 349 (1999) 186–190. [https://doi.org/10.1016/S0040-6090\(99\)00230-8](https://doi.org/10.1016/S0040-6090(99)00230-8).
- [35] M.C. Tucker, Progress in metal-supported solid oxide fuel cells: A review, *J. Power Sources*. 195 (2010) 4570–4582. <https://doi.org/10.1016/j.jpowsour.2010.02.035>.
- [36] H. Dawson, U. Kingdom, A. Energy, Friction Stir Welding of ODS Steels for Future Generation Nuclear Reactors A thesis submitted to the University of Manchester Huw Dawson School of Materials, (2018).
- [37] Thesis, M. Siyah, Title of the Thesis: Surface modification of stainless steel 316

alloy using bio materials coating, 2018.  
<https://doi.org/10.13140/RG.2.2.15130.26567>.

- [38] V.G. Efremenko, Y.G. Chabak, A. Lekatou, A.E. Karantzalis, A. V. Efremenko, High-Temperature Oxidation and Decarburization of 14.55 wt pct Cr-Cast Iron in Dry Air Atmosphere, *Metall. Mater. Trans. A Phys. Metall. Mater. Sci.* 47 (2016) 1529–1543. <https://doi.org/10.1007/s11661-016-3336-7>.
- [39] M. Chen, H. Alimadadi, S. Molin, L. Zhang, N. Ta, P. V. Hendriksen, R. Kiebach, Y. Du, Modeling of Ni Diffusion Induced Austenite Formation in Ferritic Stainless Steel Interconnects, *J. Electrochem. Soc.* 164 (2017) F1005–F1010. <https://doi.org/10.1149/2.1711709jes>.
- [40] Z. Tokei, K. Hennesen, H. Viefhaus, H.J. Grabke, Diffusion of chromium in ferritic and austenitic 9-20 wt-% chromium steels, *Mater. Sci. Technol.* 16 (2000) 1129–1138. <https://doi.org/10.1179/026708300101507055>.
- [41] E. Stefan, C. Denonville, Y. Larring, M. Stange, R. Haugsrud, Oxidation study of porous metal substrates for metal supported proton ceramic electrolyzer cells, *Corros. Sci.* 164 (2020) 108335. <https://doi.org/10.1016/j.corsci.2019.108335>.
- [42] L. Niewolak, E. Wessel, L. Singheiser, W.J. Quadackers, Potential suitability of ferritic and austenitic steels as interconnect materials for solid oxide fuel cells operating at 600 °C, *J. Power Sources.* 195 (2010) 7600–7608. <https://doi.org/10.1016/j.jpowsour.2010.06.007>.
- [43] A.M. Huntz, A. Reckmann, C. Haut, C. Sév rac, M. Herbst, F.C.T. Resende, A.C.S. Sabioni, Oxidation of AISI 304 and AISI 439 stainless steels, *Mater. Sci. Eng. A.* 447 (2007) 266–276. <https://doi.org/10.1016/j.msea.2006.10.022>.
- [44] A. Bautista, F. Velasco, M. Campos, M.E. Rabanal, J.M. Torralba, Oxidation behavior at 900°C of austenitic, ferritic, and duplex stainless steels manufactured by powder metallurgy, *Oxid. Met.* 59 (2003) 373–393. <https://doi.org/10.1023/A:1023000329514>.
- [45] E.W. Hart, On the Role of Dislocations THE, *Acta Metall.* 5 (1957) 597.
- [46] T. Suzuoka, Lattice and Grain Boundary in Polycrystals, *Trans. JIM.* 2 (1961).
- [47] R.E. Lobnig, H.P. Schmidt, K. Hennesen, H.J. Grabke, Diffusion of cations in chromia layers grown on iron-base alloys, *Oxid. Met.* 37 (1992) 81–93. <https://doi.org/10.1007/BF00665632>.
- [48] S.C. Tsai, A.M. Huntz, C. Dolin, Growth mechanism of Cr<sub>2</sub>O<sub>3</sub> scales: Oxygen and chromium diffusion, oxidation kinetics and effect of yttrium, *Mater. Sci. Eng.*

- A. 212 (1996) 6–13. [https://doi.org/10.1016/0921-5093\(96\)10173-8](https://doi.org/10.1016/0921-5093(96)10173-8).
- [49] P. Kofstad, K.P. Lillerud, Chromium transport through Cr<sub>2</sub>O<sub>3</sub> scales I. On lattice diffusion of chromium, *Oxid. Met.* 17 (1982) 177–194. <https://doi.org/10.1007/BF00738381>.
- [50] P. Kofstad, Defects and transport properties of metal oxides, *Oxid. Met.* 44 (1995) 3–27. <https://doi.org/10.1007/BF01046721>.
- [51] B.K. Kim, Y.S. Ko, I.H. Jung, H.N. Han, K.W. Yi, D.I. Kim, Role of the alloy grain boundaries in the high-temperature oxidation and Cr volatilization of 22 wt% Cr ferritic stainless steel for SOFC applications, *Corros. Sci.* 213 (2023) 110940. <https://doi.org/10.1016/j.corsci.2022.110940>.
- [52] K.D. Ralston, N. Birbilis, Effect of grain size on corrosion: A review, *Corrosion.* 66 (2010) 0750051–07500513. <https://doi.org/10.5006/1.3462912>.
- [53] A. Bahmani, S. Moradi, M. Lotfpour, H.T. Jeong, W.J. Kim, Effect of grain size on the corrosion resistance of the Fe<sub>41</sub>Mn<sub>25</sub>Ni<sub>24</sub>Co<sub>8</sub>Cr<sub>2</sub> high entropy alloy, *Corros. Sci.* 230 (2024). <https://doi.org/10.1016/j.corsci.2024.111892>.
- [54] P.S. Liu, G.F. Chen, Application of Porous Metals, *Porous Mater.* (2014) 113–188. <https://doi.org/10.1016/b978-0-12-407788-1.00003-4>.
- [55] O. Stepanov, N. Rydalina, E. Antonova, The use of porous metals in heat exchangers, *IOP Conf. Ser. Mater. Sci. Eng.* 890 (2020). <https://doi.org/10.1088/1757-899X/890/1/012150>.
- [56] H. Nakajima, Fabrication, properties and application of porous metals with directional pores, *Prog. Mater. Sci.* 52 (2007) 1091–1173. <https://doi.org/10.1016/j.pmatsci.2006.09.001>.
- [57] D.J.L. Brett, A. Atkinson, N.P. Brandon, S.J. Skinner, Intermediate temperature solid oxide fuel cells, *Chem. Soc. Rev.* 37 (2008) 1568–1578. <https://doi.org/10.1039/b612060c>.
- [58] A. Holt, P. Kofstad, Electrical conductivity and defect structure of Cr<sub>2</sub>O<sub>3</sub>. II. Reduced temperatures (<~1000°C), *Solid State Ionics.* 69 (1994) 137–143. [https://doi.org/10.1016/0167-2738\(94\)90402-2](https://doi.org/10.1016/0167-2738(94)90402-2).
- [59] P. Pavlasek, J. Rybař, S. Ďuriš, J. Palenčar, Effects of Quartz Glass Insulation on Platinum Gold Thermocouples, *Meas. Sci. Rev.* 19 (2019) 209–212. <https://doi.org/10.2478/msr-2019-0027>.
- [60] B. Timurkutluk, S. Toros, S. Onbilgin, H.G. Korkmaz, Determination of formability characteristics of Crofer 22 APU sheets as interconnector for solid oxide fuel

- cells, *Int. J. Hydrogen Energy*. 43 (2018) 14638–14647. <https://doi.org/https://doi.org/10.1016/j.ijhydene.2018.04.243>.
- [61] Y.C. Zhang, X.T. Yu, W. Jiang, S.T. Tu, X.C. Zhang, Y.J. Ye, Creep fracture behavior of the Crofer 22 APU for the interconnect of solid oxide fuel cell under different temperatures, *Int. J. Hydrogen Energy*. 45 (2020) 4829–4840. <https://doi.org/10.1016/j.ijhydene.2019.12.009>.
- [62] B. Öztürk, A. Topcu, S. Öztürk, Ö.N. Cora, Oxidation, electrical and mechanical properties of Crofer®22 solid oxide fuel cell metallic interconnects manufactured through powder metallurgy, *Int. J. Hydrogen Energy*. 43 (2018) 10822–10833. <https://doi.org/10.1016/j.ijhydene.2018.01.078>.
- [63] H. Shahbaznejad, H. Ebrahimifar, A study on the oxidation and electrical behavior of crofer 22 APU solid oxide fuel cell interconnects with Ni-Co-CeO<sub>2</sub> composite coating, *J. Mater. Sci. Mater. Electron*. 32 (2021) 7550–7566. <https://doi.org/10.1007/s10854-021-05470-z>.
- [64] M. Palcut, L. Mikkelsen, K. Neufeld, M. Chen, R. Knibbe, P.V. Hendriksen, Corrosion stability of ferritic stainless steels for solid oxide electrolyser cell interconnects, *Corros. Sci*. 52 (2010) 3309–3320.
- [65] Ł. Mazur, S. Molin, J. Dąbek, K. Durczak, M. Pyzalski, T. Brylewski, Physicochemical properties of Mn<sub>1.45</sub>Co<sub>1.45</sub>Cu<sub>0.1</sub>O<sub>4</sub> spinel coating deposited on the Crofer 22 H ferritic steel and exposed to high-temperature oxidation under thermal cycling conditions, *J. Therm. Anal. Calorim*. 147 (2022) 5649–5666. <https://doi.org/10.1007/s10973-021-10884-2>.
- [66] B. Talic, V. Venkatachalam, P.V. Hendriksen, R. Kiebach, Comparison of MnCo<sub>2</sub>O<sub>4</sub> coated Crofer 22 H, 441, 430 as interconnects for intermediate-temperature solid oxide fuel cell stacks, *J. Alloys Compd*. 821 (2020). <https://doi.org/10.1016/j.jallcom.2019.153229>.
- [67] H. Farnoush, M. Farnak, H. Abdoli, A fluid-flow approach in oxidation evaluation of SUS 430 steels coated by Fe/Mn-modified MnCo<sub>2</sub>O<sub>4</sub> for solid oxide fuel cell application, *Int. J. Hydrogen Energy*. 52 (2024) 905–915. <https://doi.org/https://doi.org/10.1016/j.ijhydene.2023.06.221>.
- [68] J. Li, Y. Zhang, K. Zhao, S.P. Jiang, M. Chen, An investigation of Cr vaporization from SUS430 metallic interconnect and deposition on (La,Sr)MnO<sub>3</sub> cathode of intermediate temperature solid oxide fuel cells, *J. Power Sources*. 579 (2023) 233285. <https://doi.org/https://doi.org/10.1016/j.jpowsour.2023.233285>.

- [69] C. Jia, Y. Wang, S. Molin, Y. Zhang, M. Chen, M. Han, High temperature oxidation behavior of SUS430 SOFC interconnects with Mn-Co spinel coating in air, *J. Alloys Compd.* 787 (2019) 1327–1335. <https://doi.org/10.1016/j.jallcom.2019.01.015>.
- [70] S. Opakhai, K. Kuterbekov, Metal-Supported Solid Oxide Fuel Cells: A Review of Recent Developments and Problems, *Energies.* 16 (2023). <https://doi.org/10.3390/en16124700>.
- [71] R. Wang, Z. Sun, J.-P. Choi, S.N. Basu, J.W. Stevenson, M.C. Tucker, Ferritic stainless steel interconnects for protonic ceramic electrochemical cell stacks: Oxidation behavior and protective coatings, *Int. J. Hydrogen Energy.* 44 (2019) 25297–25309. <https://doi.org/https://doi.org/10.1016/j.ijhydene.2019.08.041>.
- [72] M.C. Tucker, Progress in metal-supported solid oxide electrolysis cells: A review, *Int. J. Hydrogen Energy.* 45 (2020) 24203–24218. <https://doi.org/10.1016/j.ijhydene.2020.06.300>.
- [73] M. Reisert, V. Berova, A. Aphale, P. Singh, M.C. Tucker, Oxidation of porous stainless steel supports for metal-supported solid oxide fuel cells, *Int. J. Hydrogen Energy.* 45 (2020) 30882–30897. <https://doi.org/10.1016/j.ijhydene.2020.08.015>.
- [74] N. Shaigan, W. Qu, D.G. Ivey, W. Chen, A review of recent progress in coatings, surface modifications and alloy developments for solid oxide fuel cell ferritic stainless steel interconnects, *J. Power Sources.* 195 (2010) 1529–1542. <https://doi.org/10.1016/j.jpowsour.2009.09.069>.
- [75] M.C. Tucker, Progress in metal-supported solid oxide fuel cells: A review, *J. Power Sources.* 195 (2010) 4570–4582. <https://doi.org/10.1016/j.jpowsour.2010.02.035>.
- [76] S. Molin, B. Kusz, M. Gazda, P. Jasinski, Evaluation of porous 430L stainless steel for SOFC operation at intermediate temperatures, *J. Power Sources.* 181 (2008) 31–37. <https://doi.org/10.1016/j.jpowsour.2007.10.009>.
- [77] S. Molin, M. Gazda, P. Jasinski, High temperature oxidation of porous alloys for solid oxide fuel cell applications, *Solid State Ionics.* 181 (2010) 1214–1220. <https://doi.org/https://doi.org/10.1016/j.ssi.2010.06.049>.
- [78] M.C. Tucker, Development of High Power Density Metal-Supported Solid Oxide Fuel Cells, *Energy Technol.* 5 (2017) 2175–2181. <https://doi.org/10.1002/ente.201700242>.



- [79] D.J. Young, A. Chyrkin, W.J. Quadakkers, A Simple Expression for Predicting the Oxidation Limited Life of Thin Components Manufactured from FCC High Temperature Alloys, *Oxid. Met.* 77 (2012) 253–264. <https://doi.org/10.1007/s11085-012-9283-9>.
- [80] P. Huczowski, N. Christiansen, V. Shemet, J. Piron-Abellan, L. Singheiser, W.J. Quadakkers, Oxidation Induced Lifetime Limits of Chromia Forming Ferritic Interconnector Steels, *J. Fuel Cell Sci. Technol.* 1 (2004) 30. <https://doi.org/10.1115/1.1782925>.
- [81] C. Asensio-Jimenez, L. Niewolak, H. Hattendorf, B. Kuhn, P. Huczowski, L. Singheiser, W.J. Quadakkers, Effect of Specimen Thickness on the Oxidation Rate of High Chromium Ferritic Steels: The Significance of Intrinsic Alloy Creep Strength, *Oxid. Met.* (n.d.) 1–14. <https://doi.org/10.1007/s11085-012-9323-5>.
- [82] P. Huczowski, V. Shemet, J. Piron-Abellan, L. Singheiser, W.J. Quadakkers, N. Christiansen, Oxidation limited life times of chromia forming ferritic steels, *Mater. Corros.* 55 (2004) 825–830. <https://doi.org/10.1002/maco.200303798>.
- [83] M.C. Tucker, Progress in metal-supported solid oxide electrolysis cells: A review, *Int. J. Hydrogen Energy.* 45 (2020) 24203–24218. <https://doi.org/https://doi.org/10.1016/j.ijhydene.2020.06.300>.
- [84] A. Chyrkin, S.L. Schulze, J. Pirón-Abellán, W. Bleck, L. Singheiser, W.J. Quadakkers, Oxidation limited lifetime of Ni-base metal foams in the temperature range 700-900°C, *Adv. Eng. Mater.* 12 (2010) 873–883. <https://doi.org/10.1002/adem.201000139>.
- [85] D. Koszelow, M. Makowska, F. Marone, J. Karczewski, P. Jasinski, S. Molin, High Temperature Corrosion Evaluation and Lifetime Prediction of Porous Fe22Cr Stainless Steel in Air in Temperature Range 700-900°C, *Corros. Sci.* 189 (2021) 109589. <https://doi.org/10.1016/j.corsci.2021.109589>.
- [86] D. Paganin, S.C. Mayo, T.E. Gureyev, P.R. Miller, S.W. Wilkins, Simultaneous phase and amplitude extraction from a single defocused image of a homogeneous object, *J. Microsc.* 206 (2002) 33–40. <https://doi.org/10.1046/j.1365-2818.2002.01010.x>.
- [87] R. Wang, Z. Sun, U.B. Pal, S. Gopalan, S.N. Basu, Mitigation of chromium poisoning of cathodes in solid oxide fuel cells employing CuMn1.8O4 spinel coating on metallic interconnect, *J. Power Sources.* 376 (2018) 100–110. <https://doi.org/10.1016/j.jpowsour.2017.11.069>.

- [88] J. Froitzheim, H. Ravash, E. Larsson, L.G. Johansson, J.E. Svensson, Investigation of Chromium Volatilization from FeCr Interconnects by a Denuder Technique, J. Electrochem. Soc. 157 (2010) B1295. <https://doi.org/10.1149/1.3462987>.

## 8. List of figures

Figure 1. Schema of the oxide scale growth at high-temperature in oxygen atmosphere.....	15
Figure 2. Ellingham diagram [17]. .....	19
Figure 3. Comparison of oxide scale growth that follow linear and parabolic rate law. ....	21
Figure 4. A) Weight gain data presented as square weight change with respect to the initial surface area, B) Arrhenius plot. ....	22
Figure 5. Comparison of oxidation behavior of Fe-Cr-Li and Fe-Cr alloys at 1100°C [22].....	23
Figure 6. A schematic representation of the high-temperature corrosion components [23].....	24
Figure 7. Schematic model of inward and outward oxidation process. IOZ is internal oxidation zone, A(B) is alloy consist of solvent A and solute B, and $J_x$ is diffusion flux of x species [25]. ....	25
Figure 8. Fe-Cr phase diagram [36]. ....	27
Figure 9. Crystal structure of ferritic and austenitic alloys [37]. ....	28
Figure 10. Arrhenius plot of oxidation for 439 and 304 steel [43]. ....	29
Figure 11. Different diffusion routes in two neighboring grains at high temperature. ....	30
Figure 12. SEM image of A) porous, B) dense chromia-forming alloy cross-section. ....	33
Figure 13. SEM image of porous Fe22Cr alloy A) before oxidation, B) after oxidation at 900°C for 30 h. ....	33
Figure 14. Schematic representation of electrolyte-supported solid oxide cell, anode-supported solid oxide cell and metal-supported solid oxide cell [68]. ....	35
Figure 15. SEM image of a, b) polished cross-section of MS-SOFC structure after sintering and before catalyst infiltration, and c) cathode pore after infiltration of LSM [76]. ....	37

Figure 16. The lifespan prediction model applied for ferritic alloys based on the specimen thickness [78]. .....	39
Figure 17. Calculated lifespan for various metal foams based on the average particle radius at different temperatures compared with experimental data [82]. .....	40
Figure 18. A balance prepared to Archimedes liquid displacement measurements. .	46
Figure 19. Fe22Cr alloy sheet (left) and set of samples obtained by cutting the 1 cm edge squares (right). .....	46
Figure 20. Diagram of the experimental setup featuring the reactor containing a sample and the denuder tube [86]. .....	51